UNIVERSITY OF OKLAHOMA

GRADUATE COLLEGE

THE TRICUSPID VALVE: MECHANICS, MICROSTRUCTURE, MODELING, AND SIMULATION

A DISSERTATION

SUBMITTED TO THE GRADUATE FACULTY

in partial fulfillment of the requirements for the

Degree of

DOCTOR OF PHILOSOPHY

By

DEVIN WILLIAM LAURENCE
Norman, Oklahoma
2022

THE TRICUSPID VALVE: MECHANICS, MICROSTRUCTURE,

MODELING, AND SIMULATION

A DISSERTATION APPROVED FOR THE
SCHOOL OF AEROSPACE AND MECHANICAL ENGINEERING

BY THE COMMITTEE CONSISTING OF

Dr. Chung-Hao Lee, Chair

Dr. Handan Acar

Dr. Kuang-Hua Chang

Dr. Chenkai Dai

Dr. Ryan Baumwart

To my family

Without your love and support, this would not be possible.

Table of Contents

List of Figures

List of Tables

Acknowledgments

I would like to first extend my sincerest gratitude to my research advisor, Dr. Chung-Hao Lee. You have provided endless support and guidance over the past five years as I have grown from beginning my undergraduate research journey to now completing my Dissertation. The countless research experiences that we have shared are something that I will always cherish and remember as I progress through my career. I am forever thankful for my time in the Biomechanics and Biomaterials Design Laboratory at the University of Oklahoma.

I would like to also express my sincerest gratitude to my Dissertation committee members: Dr. Handan Acar, Dr. Kuang-Hua Chang, Dr. Chenkai Dai, and Dr. Ryan Baumwart. You all have been wonderful mentors throughout my time at the University of Oklahoma, and I am forever grateful for your guidance, collaborations, time, and considerations for my education.

My time in the laboratory has also been blessed by numerous friendships. These include my original M.S. compatriots: Samuel Jett and Robert Kunkel; my current Ph.D. gang: Colton Ross and Sergio Pineda-Castillo; the past M.S. students: Luke Hudson and Ryan Bodlak; and several wonderful undergraduates: Katherine Kramer, Michael Barber, and Brennan Mullins.

Last, but certainly not least, my sincerest thank you to my parents Shannon and Lisa, my sister Keely, my partner in crime Katherine, and my closest of friends Dillon, Jordan, Jonathan, Lawrence, Taylor, and Ben. Your support has helped make all of this possible.

Thank you.

Vita

2014-2018	B.S., School of Aerospace and Mechanical Engineering, University of Oklahoma (OU)
2018	Grand Prize, Oklahoma Research Day at the Capitol
2018-2019	Research Assistant, Biomechanics and Biomaterials Design Laboratory, OU
2018-2019	M.S., School of Aerospace and Mechanical Engineering, OU *Thesis*: *Investigations of the Tricuspid Heart Valve Function: An Integrated Computational-Experimental Approach*
2019-2022	National Science Foundation Graduate Research Fellow
2019	First Place Poster Award, OU-OUHSC Biomedical Engineering Symposium
2019	OU Gallogly College of Engineering (GCoE) Ph.D. Recruitment Fellowship
2019	Thomas Milam Sr. Endowed Fellowship
2019	First Place Award, Summer Biomechanics, Bioengineering, and Biotransport Conference (SB^3C) M.S.-Level Poster Competition
2020	Second Place Award, SB^3C Ph.D.-Level Poster Competition
2020	Featured Cover Art, *International Journal for the Numerical Methods in Biomedical Engineering*, Vol. 36, Issue 7
2021-2022	American Heart Association & Children's Heart Foundation Predoctoral Fellow
2022	OU GCoE Dissertation Excellence Award

Publications

2022

Casey KM, **Laurence DW**, Tang M, Lee C-H, "Mechanical and collagen microstructural characterizations of tricuspid valve leaflet microdissected layers," *Journal of Visualized Experiments*, 180:e63522, 2022.

Hudson LT, **Laurence DW**, Lau HM, Mullins BT, Doan DD, Lee C-H, "Linking collagen fiber architecture to tissue-level biaxial mechanical behaviors of porcine semilunar heart valve cusps," *Journal of Mechanical Behavior of Biomedical Materials*, 125:104907, 2022.

2021

Laurence DW, Lee C-H, Johnson EL, Hsu M-C, "An *in-silico* benchmark for the tricuspid valve – Geometry, finite element mesh, Abaqus simulation, and result data set," *Data in Brief*, 39:107664, 2021.

Laurence DW, Homburg H, Yan F, Tang Q, Fung K-M, Bohnstedt BN, Holzapfel GA, and Lee C-H, "A pilot study on biaxial mechanical, collagen microstructural, and morphological characterizations of a resected human intracranial aneurysm tissue," *Nature Scientific Reports*, 11:3525, 2021.

Laurence DW, and Lee C-H, "Determination of a strain energy density function for the tricuspid valve leaflets using constant invariant-based mechanical characterizations," *Journal of Biomechanical Engineering*, 143(1):121009, 2021.

Ross CJ, **Laurence DW**, Echols AL, Babu AR, Gu T, Duginski GA, Johns CH, Mullins BT, Casey KM, Laurence KA, Amini R, Fung K-M, Mir A, Burkhart HM, Wu Y, Holzapfel GA, Lee C-H, "Effects of enzyme-based removal of collagen and elastin constituents on the biaxial mechanical responses of porcine atrioventricular heart valve anterior leaflets," *Acta Biomaterialia*, 135:425-440, 2021.

Johnson EL, **Laurence DW**, Xu F, Crisp CE, Mir A, Burkhart HM, Lee C-H, and Hsu M-C, "Parameterization, geometric modeling, and isogeometric analysis of tricuspid valves," *Computer Methods in Applied Mechanics and Engineering*, 384:113960, 2021.

He Q, **Laurence DW**, Lee C-H, and Chen J-S, "Manifold learning based data-driven modeling for soft biological tissues," *Journal of Biomechanics*, 117:110124, 2021.

2020

Laurence DW, Johnson EL, Hsu M-C, Baumwart R, Mir A, Burkhart HM, Holzapfel GA, Wu Y, and Lee C-H, "A pilot *in silico* modeling-based study of the pathological effects on the biomechanical function of tricuspid valves," *International Journal for Numerical Methods in Biomedical Engineering*, 36, e3346, 2020.

Ross CJ, **Laurence DW**, Hsu M-C, Baumwart R, Zhao YD, Mir A, Burkhart HM, Holzapfel HA, Wu Y, and Lee C-H, "Mechanics of porcine heart valves' strut chordae tendineae investigated as a leaflet-chordae-papillary muscle entity," *Annals of Biomedical Engineering*, 48, 1463-1474, 2020.

Duginski GA, Ross CJ, **Laurence DW**, Johns CH, and Lee C-H, "An investigation of the effect of freezing storage on the biaxial mechanical properties of excised porcine tricuspid valve anterior leaflets," *Journal of the Mechanical Behavior of Biomedical Materials*, 101, 103438, 2020.

Hudson LT, Jett SV, Kramer KE, **Laurence DW**, Ross CJ, Towner RA, Baumwart R, Lim KM, Mir A, Burkhart HM, Wu Y, and Lee C-H, "A pilot study on linking tissue mechanics with load-dependent collagen microstructures in porcine tricuspid valve leaflets," *Bioengineering*, 7(2), 60, 2020.

2019

Kramer K, Ross C, **Laurence DW**, Babu A, Wu Y, Towner R, Mir A, Burkhart HM, Holzapfel GA, and Lee C-H, "An investigation of layer-specific tissue biomechanics of porcine atrioventricular heart valve leaflets," *Acta Biomaterialia*, 96, 368-384, 2019.

Ross C, **Laurence DW**, Richardson J, Babu A, Evans L, Beyer E, Wu Y, Towner R, Fung K-M, Mir A, Burkhart H, Holzapfel G, and Lee C-H, "An investigation of the glycosaminoglycan contribution to mechanical behaviors of porcine atrioventricular heart valve leaflets," *Journal of the Royal Society Interface*, 16(156), 20190069, 2019.

Laurence DW, Ross C, Jett SV, Johns C, Echols A, Baumwart R, Towner R, Liao J, Bajona P, Wu Y, and Lee C-H, *"*An investigation of regional variations in the biaxial mechanical properties and stress relaxation behaviors of porcine atrioventricular heart valve leaflets*,"* *Journal of Biomechanics*, 83:16-27, 2019.

Ross C, **Laurence DW**, Wu Y, and Lee C-H, *"*Biaxial mechanical characterization of atrioventricular heart valve leaflets*,"* *Journal of Visualized Experiments*, 146, 2019.

Laurence DW, Ross CJ, Jett SV, Johns C, Echols A, Baumwart R, Towner RA, Liao J, Bajona P, Wu Y, and Lee C-H, "Regional biaxial mechanical data of the mitral and tricuspid valve anterior leaflets," *Data in Brief*, 24:103961, 2019.

Lee C-H, **Laurence DW**, Ross CJ, Kramer KE, Babu AR, Johnson EL, Hsu M-C, Aggarwal A, Mir A, Burkhart HM, Towner RA, Baumwart R, and Wu Y, "Mechanics of the tricuspid valve – From clinical diagnosis/treatment, *in-vivo*, and *in-vitro* investigations, to patient-specific biomechanical modeling, *Bioengineering*, 6(2), 46, 2019.

2018

Kunkel R, **Laurence DW**, Wang J, Robinson D, Scherrer J, Wu Y, Bohnstedt BN, Chien A, Liu Y, and Lee C-H, *"*Synthesis and characterization of bio-compatible shape memory polymers for the development of intracranial aneurysms embolic devices*,"* *Journal of Mechanical Behavior of Biomedical Materials*, 88:422-430, 2018.

Jett SV, **Laurence DW**, Kunkel R, Babu AR, Kramer K, Baumwart R, Towner R, Wu Y, and Lee C-H, ***"***An investigation of the anisotropic mechanical properties and anatomical structure of porcine atrioventricular heart valve leaflets***,"*** *Journal of Mechanical Behavior of Biomedical Materials*, 87:155-171, 2018.

Jett SV, **Laurence DW**, Kunkel R, Babu AR, Kramer K, Baumwart R, Towner R, Wu Y, and Lee C-H, *"*Biaxial mechanical data of porcine atrioventricular valve leaflets*,"* *Data in Brief*, 25:358-363, 2018.

Selected Presentations

2022

Laurence DW, Casey KM, and Lee C-H, "The Mechanical Behaviors and Collagen Fiber Architectures of the Tricuspid Valve Leaflet Layers", World Congress of Biomechanics, July 10-14, 2022.

Laurence DW and Lee, C-H, "An Experimental Approach to Quantify the Pre-Strains of the Tricuspid Heart Valve Leaflets", Summer Biomechanics, Bioengineering, and Biotransport Conference 2022, June 20-23, 2022.

2021

Laurence DW, "Synthesizing Experimental and Computational Mechanics to Understand the Biomechanics of the Tricuspid Valve," Iowa State University Richard and Carol Pletcher Seminar Series, November 16, 2021.

2020

Laurence DW, He Q, Lee C-H, and Chen J-S, *"Modeling the Porcine Mitral Valve Posterior Leaflet Using Manifold Learning-Based Data-Driven Mechanics,"* Summer Biomechanics, Bioengineering, and Biotransport Conference 2020, June 17-20, 2020.

2019

Laurence DW, Johnson EL, Hsu M-C, Mir A, Burkhart HM, Wu Y, and Lee C-H, *"Finite element-based computational studies of the healthy and diseased tricuspid valve function,"* Biomedical Engineering Society (BMES) Annual Meeting 2019, Philadelphia, PA, October 16-19, 2019.

Laurence DW, Johnson, E, Hsu M-C, Mir A, Burkhart HM, Wu Y, and Lee C-H, *"Finite element biomechanical investigations of pathological effects on organ-level tricuspid valve function,"* 6th International Conference on Computational and Mathematical Biomedical Engineering, Japan, June 10-12, 2019.

Laurence DW, Johnson, E, Hsu M-C, Mir A, Burkhart HM, Wu Y, and Lee C-H, *"Finite element simulation framework for investigating pathological effects on organ-level tricuspid valve biomechanical function,"* Summer Biomechanics, Bioengineering, and Biotransport Conference 2019, Seven Springs, PA, June 25-28, 2019.

2018

Laurence DW, Wu Y, and Lee C-H, *"Development of a Multiscale Computational Modeling Framework for the Tricuspid Valve – Linking Valvular Interstitial Cell Mechanobiology with Organ-Level Function,"* World Congress in Computational Mechanics 2018, New York, NY, July 23-27, 2018.

Laurence DW, Wu Y, and Lee C-H, *"Development of a Multiscale Computational Model for the Tricuspid Valve – Linking Valvular Interstitial Cell Mechanobiology with Organ-Level Function,"* Engineering Mechanics Institute (EMI) Conference 2018, Cambridge, MA, May 29 – June 1, 2018.

Laurence DW, Mobaraki M, Towner R, and Lee C-H, *"Development of a Novel Integrated MRI-Beating Heart Model for Investigations into Pathophysiological Factors linked to Tricuspid Regurgitation,"* National Conference on Undergraduate Research 2018, Edmond, OK, April 4-7, 2018.

Laurence DW, and Lee C-H, *"An Integrated Experimental-Computational Approach for Development of an Atrioventricular Heart Valve-Specific Multiscale Computational Model,"* Research Day at the Capitol (RD@C) Competition, Oklahoma City, OK, March 26-27, 2018.

Abstract of the Dissertation

The Tricuspid Valve: Mechanics, Microstructure, Modeling, and Simulation

by

Devin William Laurence

Doctor of Philosophy in Mechanical Engineering

University of Oklahoma, Norman, OK, 2022

Dr. Chung-Hao Lee, Chair

The objectives of this research include: (1) experimentally characterizing the multi-scale properties of the tricuspid valve (TV) leaflets, (2) linking the mechanical and microstructural properties of the TV leaflets to their intrinsic microstructure and morphology, (3) developing new *in-silico* methods for modeling the TV leaflet mechanical behaviors, and (4) providing the first benchtop characterization and *in-silico* implementation of TV leaflet pre-strains.

We first characterize the properties of tricuspid valve leaflets at the tissue, mesoscale, and microstructural scales. The tricuspid valve leaflets are mechanically characterized using our established biaxial testing protocols to elucidate how the choice of specimen size influences

the observed mechanical behaviors. Then, we employ our polarized spatial frequency domain imaging device to analyze the intrinsic collagen fiber architecture of each leaflet. Our results demonstrate that the leaflet mechanical behaviors are linked to the underlying collagen fiber architecture, which adapts to the applied loading. Finally, one representative specimen for each tricuspid valve leaflet is imaged using a confocal microscope with multiphoton imaging and second harmonic generation. From the resulting high-fidelity reconstructed microstructures, we note that the four layers of the tricuspid valve leaflets contains unique leaflet-specific arrangements of collagen and elastin fibers.

As an extension of the multi-scale characterizations, we then experimentally derive the contributions of the tricuspid valve leaflet microstructures to the tissue-level mechanical behaviors. First, the tricuspid valve leaflets are dissected into the composite atrialis/spongiosa layers and the composite fibrosa/venricularis layers. Our mechanical characterization revealed that the isolated composite layers were stiffer than the intact specimen. On the other hand, the mesoscale polarized spatial frequency domain imaging results show that the composite leaflet layers had more flexible collagen fiber architectures that reacted more to applied tensions than the intact specimens. Next, we use an iterative enzyme-digestion procedure to understand how the collagen fibers and elastin fibers contribute to the tricuspid valve leaflet mechanical. The collagen-digested leaflets were more compliant in their high-tensile mechanical behaviors due to the removal of the primarily load bearing constituent—collagen. In contrast, the elastin-digested specimens were significantly stiffer than the control specimens, suggesting that elastin may play an important role in mediating the recruitment of collagen fibers and the transition to the high-tensile mechanical behaviors.

We next shift our focus to *in-silico* developments and provide two new studies on modeling the mechanical behaviors of the tricuspid valve leaflets. In the first study, a constant invariant-based mechanical characterization is used to isolate the contributions of the first invariant and the fourth pseudo-invariant to the leaflet mechanical behaviors. These data are fit with three candidate strain energy density functions to evaluate their fitting efficacy. Our analyses reveal that an exponential strain energy density function is more suited for capturing the tricuspid valve leaflet mechanical behaviors. Interestingly, the coupling between the invariants is crucial to capturing the leaflet behaviors, and this must be considered in future constitutive modeling developments. For the second study, we focus on an emerging topic in the soft tissue biomechanics community: data-driven material modeling. This new approach is promising since it does not require the *a priori* definition of a constitutive law and instead relies on large collections of experimental data. We compare this emerging modeling technique with common structural constitutive models used for the atrioventricular heart valve leaflets and find that it provides excellent predictions of the leaflet behaviors provided sufficient model training data.

We conclude this dissertation by experimentally characterizing the tricuspid valve leaflet pre-strains, which are an important consideration when linking *in vitro* properties with *in vivo* function. First, the pre-strains of all three tricuspid valve leaflets are characterized using stereo cameras equipped with a direct linear transformation and the reproducing kernel shape function method. Our results reveal that there are indeed pre-strains embedded within the tricuspid valve leaflets that are released upon dissection of the tissue from their *in-situ* anatomy. In addition to the pre-strain quantification, we compare different stress-free reference configurations to determine which may provide mechanical behaviors closest to those *in vivo*. Interestingly, we

found that our existing preconditioning method does not appropriately restore the *in vivo* leaflet behaviors as expected, and, instead, the post-preconditioned configuration results in stiffer, more anisotropic material behaviors. In the second portion of this investigation, we implement pre-strains into a simplified tricuspid valve finite element benchmark we develop to evaluate new computational methods. The finite element simulations reveal that the pre-strains significantly altered tricuspid valve behaviors: at 20% pre-strain, the leaflet stresses nearly doubled and there was the significant formation of valvular regurgitation.

CHAPTER 1 Introduction

1.1 Motivation

The tricuspid valve (TV) has seen a significant increase of interest within the soft tissue biomechanics community since the first biaxial mechanical characterization study of Amini *et al*. in 2016 [5]. For example, the scientific community has used *in vitro* benchtop characterizations, *in-silico* numerical investigations, and *in vivo* animal works to better understand the TV properties. It has become increasingly evident that the TV properties across the length scales are interconnected and play essential roles in healthy TV function. However, limited attention has been devoted to connecting the TV multi-scale properties or appropriately bridging the gaps between *in vitro*, *in vivo* and *in-silico* investigations.

The TV is a complex structure with relevant properties that span several length scales. At the *organ-level*, the TV is motivated by the hemodynamics within the right ventricle (RV) to seal the orifice between the right atrium (RA) and RV. This organ-level behavior dictates the *tissue-level* mechanical environment of the TV structures. For example, the leaflets must be compliant to cyclically open and close within the span of one heartbeat (0.5-1 s), but they must provide sufficient stiffness to withstand physiological stresses (~125 kPa). These tissue mechanical behaviors are governed by the underlying *mesoscale* leaflet properties. Particularly, the collagen fiber architecture provides material stiffness to the leaflets throughout loading, and its preferred orientation and dispersion drives material anisotropy. Finally, the underlying valvular interstitial cells probe the surrounding extracellular matrix and monitor mechanical

and biochemical cues. In pathological conditions, the valvular interstitial cells trigger biosynthetic processes to alter the tissue mechanical behaviors and restore tissue homeostasis. The interconnected nature of these properties is essential for holistically understanding the TV in healthy and diseased conditions.

Investigations that explore the multi-scale properties of the TV require the combination of *in vitro*, *in-silico*, and *in vivo* methods. Although several studies have successfully leveraged these various methods for the TV tissues, there are currently no studies that have experimentally or numerically characterized their intrinsic pre-strains. These pre-strains are present in all *in vivo* soft tissues and are released upon dissection of the tissue from its *in-situ* environment. Thus, the pre-strains are an important linkage between *in vitro* and *in vivo* material behaviors that must be considered when predicting the TV function using *in-silico* methods.

1.2 Objective and Scope

The objective of this dissertation is three-fold: (1) to perform multi-scale characterizations of the TV leaflets that links their mechanical properties, mesoscale collagen fiber architecture (CFA), and microstructural morphology, (2) to develop new methods for *in-silico* modeling of the TV leaflet mechanical behaviors, and (3) to experimentally characterize the TV leaflet pre-strains and understand their *in vivo* implications. These developments are summarized as follows:

(1) *Experimental characterization of the TV leaflet properties across the length scales*

In this work, we first use our established biaxial testing protocols to characterize the mechanical properties of the TV leaflets and understand how the selected specimen size influences the observed properties. We then relate the observed mechanical properties to the underlying mesoscale CFA properties using our in-house polarized spatial frequency domain imaging (pSFDI) device. Finally, we employ confocal microscopy with multiphoton imaging and second harmonic generation (SHG) to elucidate the tissue microstructure.

(2) *Biaxial mechanical characterizations of the TV leaflets to elucidate the microstructural contributions*

Following our baseline characterizations of the multi-scale TV leaflet properties in **Research Task (1)**, we experimentally connect the TV leaflet mechanical behaviors and microstructure. First, we use our established leaflet layer micro-dissection technique to separate TV leaflets into two set of composite layers. These mechanical and CFA properties of these tissues are then characterized and compared to the intact TV leaflets. Next, we use an iterative enzyme-based approach to elucidate the role of collagen and elastin fibers in the TV leaflet mechanical behaviors. These findings are compared with our previous investigation that used a similar iterative enzyme degradation approach for the glycosaminoglycans (GAGs).

(3) *Development of novel methods for modeling the TV leaflet mechanical properties*

The next **Research Task** focused on developing new methods for modeling the

mechanical behaviors of the TV leaflets. We first perform constant invariant-based mechanical characterizations to isolate the contributions of the first invariant and the fourth pseudo-invariant to the tissue's mechanical behaviors. This mechanical data is then used to evaluate the efficacy of three strain energy density functions. For the second portion of this **Research Task**, we compare an emerging data-driven biomechanics method with well-established constitutive models typically used for the atrioventricular heart valve leaflets. One benefit of this new approach is its ability to work directly with experimental data without requiring the definition of a strain energy density function (SEDF) form.

(4) *Benchtop characterization and in-silico implementation of TV leaflet pre-strains*

We conclude this work by experimentally characterizing the TV leaflet pre-strains in four configurations: (i) the explanted TV configuration, (ii) the dissected specimen configuration, (iii) the mounted leaflet configuration, and (iv) the post-preconditioned configuration. These four candidate reference configurations, in addition to the *ex vivo* heart, are next evaluated to understand how they influence the characterized leaflet mechanical behaviors. Finally, we establish a simplified finite element benchmark for the TV that allows for easier *in-silico* computational developments and investigations. This benchmark framework is employed to understand how the experimentally characterized pre-strains influence *in-silico* predictions of the TV function.

The remainder of this dissertation is organized as follows. Chapter 2 provides a literature review of the recent developments for the TV from the soft tissue biomechanics community.

We also use this chapter to the define key continuum mechanics variables used throughout the remainder of the text. In Chapter 3, we characterize the multi-scale properties of the TV leaflets using *in vitro* mechanical characterizations, pSFDI quantifications, and confocal microscopy. These findings are supplemented by Chapter 4, where we relate the TV leaflet microstructures, mechanical properties, and CFAs. In Chapter 5, we explore two potential avenues for modeling the TV leaflet mechanical behaviors: (i) constant invariant-informed SEDF selection and (ii) data-driven material modeling. Chapter 6 concludes the technical chapters by experimentally characterizing and computationally exploring the TV leaflet pre-strains. Finally, concluding remarks and suggested future research avenues are provided in Chapter 7.

CHAPTER 2 Literature Review

2.1 The Tricuspid Valve Anatomy, Function, and Disease

2.1.1 Tricuspid Valve Anatomy and Function

The TV regulates the blood flow within the right side of the heart. Functionally, the TV is analogous to a check valve, where the TV allows blood flow from the atrium to the ventricle during diastole and prevents the undesired retrograde blood flow into the atrium during systole. This cyclic opening and closing of the TV are facilitated by the four primary sub-valvular components—the three TV *leaflets* that seal the atrial-ventricular orifice at systole, the rigid ring-like TV *annulus* that affixes the TV leaflets to the surrounding heart chambers, and the array of string-like *chordae tendineae* that pin the TV leaflets to the *papillary muscles* on the RV wall.

2.1.2 Tricuspid Valve Disease

Any alterations to the geometry and function of the TV sub-valvular components may cause retrograde blood flow, which is commonly known as tricuspid regurgitation (TR). TR is a complex valvular heart disease that can be classified based on the underlying etiology: (i) *primary* TR occurring when the regurgitation is due to structural alterations of the TV leaflets (e.g., the Ebstein's anomaly or chordae rupture-induced tricuspid leaflet flail) [10]; (ii) *secondary* TR arising from alterations to the surrounding heart anatomy caused by different etiologies (e.g., pulmonary hypertension, papillary muscle displacement, and annular dilation) [15, 111, 150].

Clinical research suggests that secondary TR accounts for approximately 70-80% of all TR cases [36]. Likewise, much of the clinical effort has been focused on establishing reliable surgical repair techniques to restore the diseased TV into the normal valve function. There are two prominent techniques for the TV surgical repair, including the ring annuloplasty [24, 45] and the De Vega suture valvuloplasty [9, 33, 34], both with a common goal of restoring the annulus dimension and geometry to address TR caused by the annular dilation. These techniques are generally successful immediately after the TV repair, but the recurrence of TR has been disappointing, i.e., recurrence rate approaching 16-18% at 5-8 years following the initial surgery [59, 118]. This undesired TR recurrence suggests that other factors, besides annular dilation, warrant more clinical attention. Although there is an apparent need for improving the long-term outcomes of the current therapeutics, the TV has been historically considered as the "*forgotten valve*". This could be attributed to the common sentiment among cardiologists and cardiac surgeons that TR would naturally regress after correcting the concomitant left-sided lesion [20]. However, Dreyfus *et al*. (2005) [36] and Anyanwu *et al*. (2010) [11] suggested that the lack of timely clinical actions addressing TR may be inadequate, and that the TR, *left untreated*, will continue to worsen the prognosis and significantly affect the quality of life of the patient. These new fundamental clinical viewpoints sparked interests in studying the TV for the clinical community and, more recently, the soft tissue biomechanics community.

2.2 Major Challenges and Questions

2.2.1 Biomechanics-Focused Challenges & Questions

From 1990-2015, the mitral valve (MV) in the left side of the heart was the primary focus of the two atrioventricular heart valves. Much of our current understanding stems from these seminal studies, such as the mechanical properties [51, 52, 105, 115], microstructural morphology [76, 137], collagen fiber architecture [90, 93, 95] or valvular interstitial cell-regulated biosynthetic response [14, 116, 127]. It is logical to expect the TV displays similar properties as the mitral valve because they share the same *in vivo* roles of regulating the blood flow between the atria and the ventricles. However, there are several inherent differences in their respective *in vivo* environments, including the significantly higher systolic transvalvular pressure for the MV (i.e., 120 mmHg) compared to the TV (i.e., 25 mmHg), and the different numbers of valve leaflets (two for the MV vs. three for the TV). It is, thus, likely that the properties of the TV sub-valvular components differ from the previous observations for the MV counterparts, leading to the following three motivating questions. First, *what are the mechanical properties of the TV sub-valvular components*? The mechanical properties of the TV may be more compliant due to the less-demanding *in vivo* transvalvular pressures, yet anatomical differences, such as the different numbers of leaflets, may obscure this. Second, *what is the microstructural morphology of the TV sub-valvular components*? Differences (or similarities) in the mechanical properties between the two atrioventricular heart valves may be attributed to the underlying microstructures and tissue morphology. Third, *are the valvular interstitial cell-regulated biosynthetic responses altered due to lower transvalvular pressure for the TV*? A previous study highlighted the lower stiffness of the TV valvular interstitial cells

(VICs) that, when combined with the reduced *in vivo* pressure, may have notable implications for the cellular biosynthetic response to pathological loading. Answering these questions will provide a better fundamental understanding of the function and physiopathology of the TV that will enable the improvements of the existing clinical remedies for TR.

2.2.2 Clinical Challenges and Questions

Currently, there are several clinical remedies to address the complex nature of TR. One of the most prominent devices is the annuloplasty ring, which seeks to restrict the annulus size (i.e., circumference), restore the leaflet coaptation, and prevent further TR. This leads to several questions to ideally improve the long-term treatment outcomes. First, *how do the individual valvular pathologies alter the TV function and mechanical environment*? Since the current gold standard for TR only addresses the annular dilation, and there is a long-term recurrence of TR, it is possible that other valvular pathology factors should be also addressed. Second, *what is the ideal therapeutic option, or combination of therapeutic methods, that best address TR for a given patient's pathological conditions*? Several factors may obscure this decision, such as the patient's unique TV geometry and the severity of the TR. Also, it is unsure what the target is for a successful TR repair—should it be a certain reduction in the annulus size, the amount of leaflet coaptation, and/or the homeostatic (or healthy) leaflet stresses and strain? *In-silico* modeling has emerged as a platform that could be used to address these questions; however, the fundamental questions must be carefully answered before the *in-silico* simulations can be confidently and reliably used in these clinically relevant applications.

For correcting TR, it is largely recommended that repair be performed whenever possible, as valvular replacement is associated with high mortality [4, 66]. In the case of TV repair, the preferred correction method is to reduce the tricuspid annulus size to facilitate a larger coaptation area of the TV leaflets through either suture valvuloplasty or ring annuloplasty. In the valvuloplasty procedure, a suture is fed through the annulus and pulled to constrict the valve, while in ring annuloplasty a pre-sized rigid or flexible band is sutured to the commissure points of the annulus to change the annulus shape and size. Previous clinical studies have shown that suture annuloplasty is much less effective than ring annuloplasty in preventing recurrent TR; however, some clinicians still perform suture annuloplasty for its procedural simplicity and satisfactory intermediate-term treatment outcome [78, 151]. Comparing the rigid and flexible rings used in TV annuloplasty repair, rigid rings provide the benefit of retaining the 3D annulus shape and increasing leaflet coaptation; however, these devices have the consequences of restricted annular contraction and an increased chance of ring dehiscence. In contrast, flexible rings have a reduced risk of ring dehiscence and better annular contraction. Nevertheless, they lose the 3D annulus shape and carry an increased potential for the sub-optimal leaflet coaptation [3]. While TV annuloplasty is generally successful, there is the potential for recurrent TR in the long term, and researchers have recommended the TV annuloplasty ring devices be further improved through the consideration of anisotropic material properties to better retain natural valve contraction, and customization of the ring to each patient's annulus geometries and pathological conditions [104].

2.3 In-Vitro, Ex-Vivo, and In-Vivo Characterizations of the Tricuspid Valve

2.3.1 The Tricuspid Valve Leaflets

The three TV leaflets, namely the anterior leaflet (AL), posterior leaflet (PL), and septal leaflet (SL), function collectively to seal the orifice between the RA and the RV during systole (**Figure 2-1**(a)). These leaflets are attached to the surrounding heart tissue through the ring-like TV annulus and a series of string-like chordae tendineae that insert into the ventricular surface (**Figure 2-1**(b)). From the microstructural point of view, these TV leaflet tissues are composed primarily of collagen fibers, elastin, GAGs and proteoglycans, and a population of smooth muscle-like VICs. Morphologically, these constituents are arranged into four distinct layers, described from the atrial to the ventricular surfaces: (i) the *atrialis* (A), composed of circumferentially-oriented elastin; (ii) the *spongiosa* (S), containing non-fibrous GAGs and proteoglycans; (iii) the *fibrosa* (F), a collagen-rich layer; and (iv) the *ventricularis* (V), which is composed primarily of radially-oriented elastin fibers [74, 107] (**Figure 2-1**(c)). In addition to these four morphologically distinct tissue layers, the VICs are distributed throughout the TV tissue that are responsible for the biosynthetic regulation of the tissue extracellular matrix. This section summarizes several recent experimental investigations from our lab, which aid in advancing our understanding of the TV leaflets mechanical, collagen fiber architectural, and morphological properties.

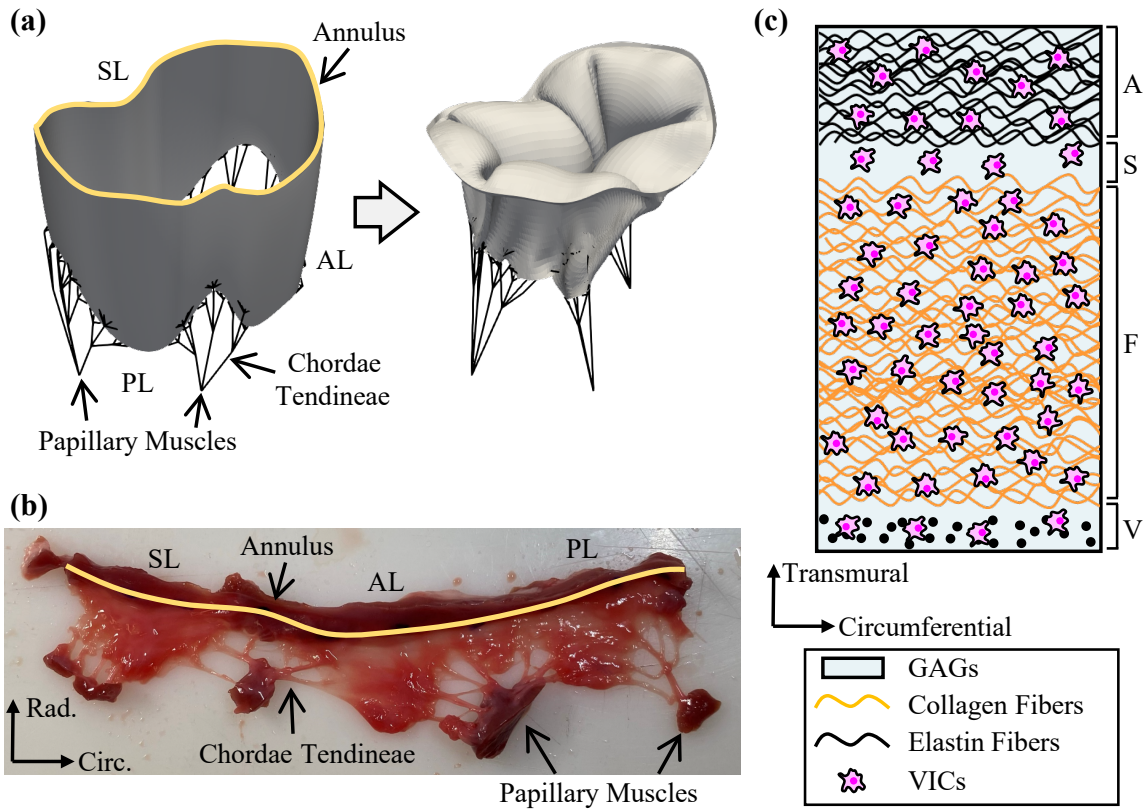

Figure 2-1. (a) Schematic of the sub-valvular components of the tricuspid heart valve at diastole *left* and at systole *right* adopted from the finite element simulation of Laurence *et al*. (2020) [84]**,** (b) a representative excised porcine TV showing the three TV leaflets, the TV annulus, the chordae tendineae, and papillary muscles, and (c) illustration of the four distinct tissue layers and VICs of the TV leaflets.

2.3.2 *In Vitro* Mechanical Characterizations of the TV Leaflets

Two approaches have been employed to characterize the mechanical behavior of the TV leaflets. The first is planar biaxial mechanical testing in which orthogonal tensile loads are applied to the tissue specimen using sutures or thin tines [135]. Our lab has extensively used this experimental method to characterize the planar biaxial mechanical responses of the TV

leaflet tissues, which provide useful information for developing TV-specific constitutive models under the hyperelasticity framework (see also Section 2.4). One inherent limitation of this testing method is the lack of mimicking the *in vivo* loading environment for the tissue. With this in mind, the second characterization approach emulates the *in vivo* loading environment via an *in vivo* animal model [136] or an *in vitro* testing apparatus [122]. This approach provides richer information of the *in vivo* functioning environment of the TV. The following focuses primarily on the recent studies from our lab on the TV leaflet tissue biomechanics, and briefly reviews the studies that maintained the entire TV apparatus within an *in vitro* or *in vivo* biomechanical characterization pipeline.

Mechanical characterizations of the TV leaflets were first provided by Heyden *et al*. (2015) [57], where the authors provided a survey of the mechanical properties for the leaflet tissues from all four cardiac heart valves. Shortly thereafter, Khoiy *et al*. (2016) [5] provided the pioneering biaxial mechanical characterization of porcine TV leaflets. Their results highlighted the nonlinear and anisotropic mechanical responses for all three TV leaflets. Interestingly, each leaflet had its distinct mechanical behavior, as later echoed by Meador *et al*. (2020) [107] and Pham *et al*. (2017) [114] for ovine and human TVs, respectively. TV leaflet-specific mechanical responses stem from the unique microstructural differences, yet the comprehensive understanding of the intricate mechanics-microstructure interrelationship remains elusive.

Recently, our lab expanded these fundamental characterization studies by developing a comprehensive experimental procedure to systematically examine the mechanical behaviors of the TV leaflets in response to varied biaxial loading conditions, as well as the time-

dependent mechanical response of the tissue [67, 133]. Our investigations using this approach can be generally classified into *bulk-tissue* and *microstructurally focused* characterizations. The former includes characterizations of the loading-rate effect, the species differences, and spatial variations in the characterized tissue mechanical properties, while the latter seeks to understand how the microstructural constituents, such as the GAGs or collagen fibers, contribute to the TV leaflet tissue's biaxial mechanical properties. Collectively, these recent results of our lab have provided an extensive understanding of the mechanical behaviors of the three TV leaflets. The comprehensive biomechanical database we established is useful for informing the development of constitutive models in predictive computational modeling of the TV *in vivo* function (see Sections 2.4 and 2.5). Our experimental methods and the key findings of these studies are further elaborated as follows.

Bulk-Tissue Characterizations

Our lab first aimed to establish a comprehensive biaxial mechanical characterization framework and explore how the strain rate, testing temperature, species, and age influence the observed mechanical behaviors [67, 133]. Like the previous studies [5, 57, 114], we found that the three TV leaflets had distinct, nonlinear and anisotropic mechanical responses (**Figure 2-2**(a)-(b)). Interestingly, the adult ovine specimens were more compliant than their juvenile counterparts, but stiffer than the adult porcine specimens, indicating species and age are important factors for *in vitro* biomechanical characterizations. Moreover, the mechanical response for all three TV leaflets became stiffer with an increased loading rate, with the differences found to be statistically insignificant. This observation agrees with the typical viscoelastic theory for soft tissues [47]. Finally, the peak radial stretches became larger as the

temperature increased, which no obvious microstructural connection was made. Our study provided a fundamental overview of the TV leaflet mechanical responses and explored how several experimental factors influence the observed mechanical behaviors.

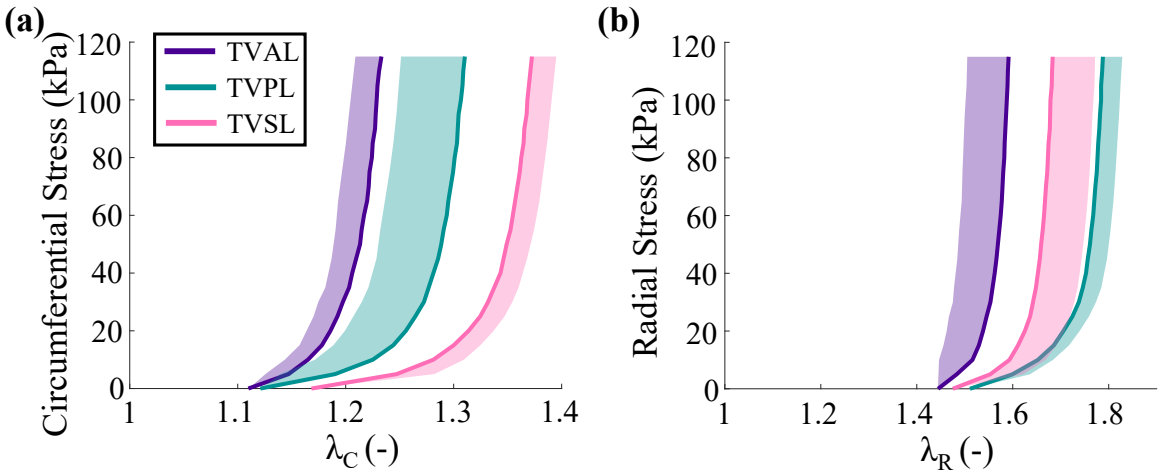

Figure 2-2. Characterized biaxial mechanical behaviors of the three TV leaflets [67]: stress-stretch data in the tissue (a) circumferential, and (b) radial directions. Results are presented as mean ± SEM (only half error bars are plotted).

The general consensus within the heart valve biomechanics community is to use the central region of the tissue for biaxial mechanical characterizations [5, 52, 115]. This experimental setup is chosen to avoid chordae insertions that may affect the characterize mechanical properties of the TV leaflet tissues. However, it relies on an assumption that the mechanical properties of the central region accurately represent the entire TV leaflet specimen. Although this assumption may be reasonable for certain applications, no studies have quantified the regionally varying mechanical properties to evaluate the efficacy of this assumption. In

Laurence *et al*. (2019) [82], our lab used a modified experimental technique to characterize the mechanical properties for six smaller regions of the porcine TV AL. From this study, we found that the central regions (i.e., Regions B and E) are more anisotropic compared to the edge regions (i.e., Regions A, C, D, and F). This observation was supported by the quantified *anisotropy index* (*AI*, defined as the ratio of the peak radial stretch to the peak circumferential stretch) (**Figure 2-3**(a)). Interestingly, we also found that all the six tissue regions appeared to exhibit similar deformations after the specimen was preconditioned (**Figure 2-3**(b)). Based on Y.C. Fung's seminal quasi-linear viscoelasticity theory for soft tissues [47], this post-preconditioning tissue deformation can be viewed as the tissue's *in vivo* functioning deformation, and our novel findings imply the assumption of *homogeneous mechanical properties* commonly adopted in heart valve computational modeling is valid, considering the post-preconditioned (PPC) state as the reference configuration (i.e., the stress-free configuration). These observations of our work underscore the importance of the chosen stress-free reference configuration [124], and partially verify the previous assumptions that the heart valve leaflet's mechanical properties are *spatially heterogeneous* [8, 119, 121, 136].

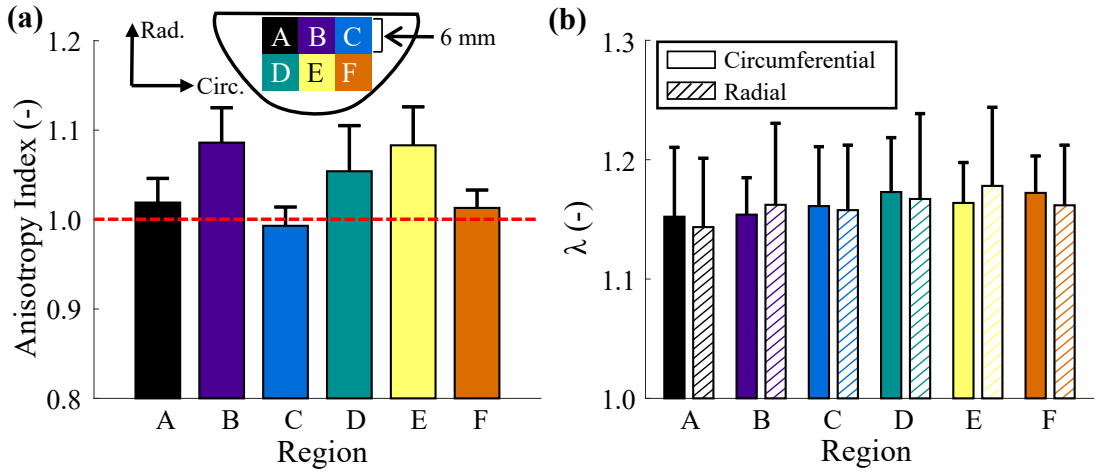

Figure 2-3. Quantified regional variations in the TVAL biaxial mechanical properties [82]: (a) The *AI* for the six leaflet regions, and (b) the circumferential (i.e., solid bars) and radial (i.e., patterned bars) tissue deformations for the six regions. Values are in mean ± SEM.

The tissues used in our mechanical characterizations are typically stored in a −14 °C freezer between dissection and testing. In Duginski *et al*. (2020) [38], our lab sought to understand how this temporary freezer storage may influence the TV leaflet's mechanical responses, since the existing literature for various tissues (e.g., cartilage, skin or aortic tissues) had conflicting conclusions. In this study, the fresh TVAL specimens were first biaxially characterized using our typical experimental protocols. The tested tissue was then frozen in a −14 °C freezer for 48 hours and was subsequently tested using the same experimental characterization. Despite the relatively short duration, the freezer storage appeared to make the leaflet's mechanical response slightly *stiffer* and *more anisotropic*, although we only found a statistically significant difference in the low-tensile mechanical response of the radial tissue direction. This suggests that the short storing period may slightly alter the TV leaflet mechanical response, but in a non-significant manner. Another recent study by Salinas *et al*. (2020) [139] showed opposite

trends (i.e., more compliant tissue behaviors) following a freezing period of 1-3 days at −80 °C. Thus, it is important to emphasize that the freezing-storage method for the TV leaflets should be carefully selected, and it is valuable to examine the differences in the characterized tissue's mechanical behaviors arising from the selected freezer storage technique.

Microstructurally Focused Characterizations

Our lab further elucidated the contributions of microstructural constituents to the TV leaflet mechanical responses. Ross *et al*. (2019) [133] used an iterative experimental technique to investigate of role the GAGs in the TV leaflet tissue biomechanics, where the untreated (i.e., control) specimen was biaxial characterized, then treated with an enzyme solution consisting of hyaluronidase and chrondroitinse to obtain the treated specimen (**Figure 2-4**(a)), and finally biaxial characterized. This approach enabled us to understand the differences in the mechanical behaviors, *by using the same specimen*, considering the removal of >60% of the GAG content. The tissue's deformations were larger following the enzyme degradation treatment (**Figure 2-4**(b)-(c)). Interestingly, we further found that the enzyme degradation-induced discrepancy was primarily attributed to the preconditioning effect. We also conducted stress relaxation tests in the same study and found a reduced stress relaxation following the removal of the GAGs. This study highlights the intricate contributions of the GAG content to the TV leaflet's biaxial mechanical and viscoelastic properties.

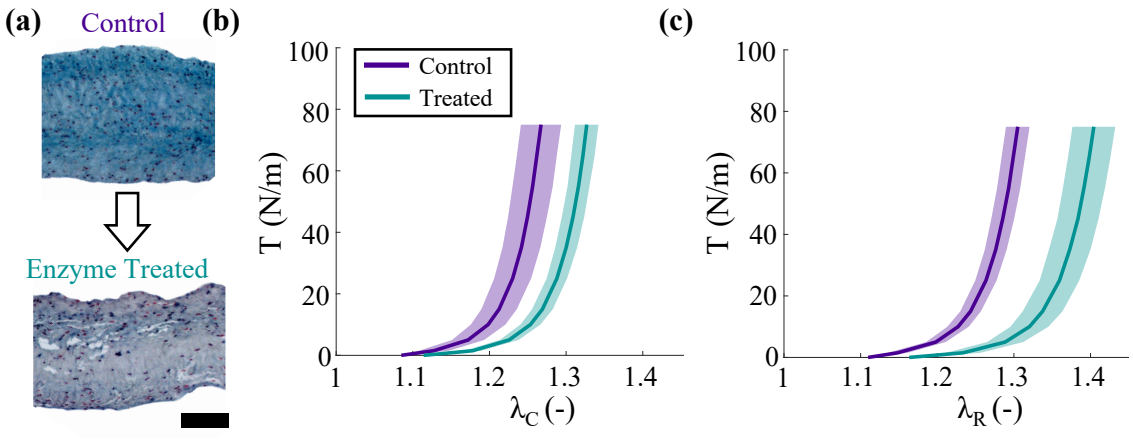

Figure 2-4. (a) Comparison of the TV leaflet's microstruture (*top*) before and (*bottom*) after the enzyme degradation. Tension vs. stretch responses in the tissue's (b) circumferential, and (c) radial directions before and after the enzyme degradation treatment. Results are presented in mean ± SEM. Data are taken from [133].

In Kramer *et al*. (2019) [74], our lab used another experimental method to understand the interrelationship between the tissue mechanics and its underlying microstructure for the TV. This approach utilized a micro-dissection procedure to separate the tissue layers of the TVAL and characterize the biaxial mechanical properties of the separated tissue layers. Because the spongiosa layer lacks the structural constituents (such as collagen or elastin fibers) to bear substantial mechanical loading and the ventricularis layer is typically very thin, the TVAL was dissected into two composite layers: namely (i) A/S—the combined atrialis and spongiosa layer; and (ii) F/V—the combined fibrosa and ventricularis layer. These two composite layers were biaxially characterized, and we arrived at two primary observations. Firstly, the tissue deformations with respect to the PPC configuration were nearly isotropic and much smaller than the anisotropic preconditioning deformations. Secondly, the A/S and F/V layers had

similar tissue deformations with respect to the preconditioned configuration, with most of the differences in the observed mechanical response stemming from preconditioning (**Figure 2-5**). The latter observation contradicts an assumption that the fibrosa layer behaves similarly to the intact layer; however, similar investigations for the aortic valve (AV) leaflets supported our observation and suggested the isotropic behavior of the separated fibrosa is due to the release of inter-layer attachments [146, 155, 156]. Although the observations from Kramer *et al*. provided an understanding of the layer-specific biomechanical functions of the TV leaflets, this study did not make a direct comparison of the mechanical properties to the intact leaflet (i.e., before micro-dissection).

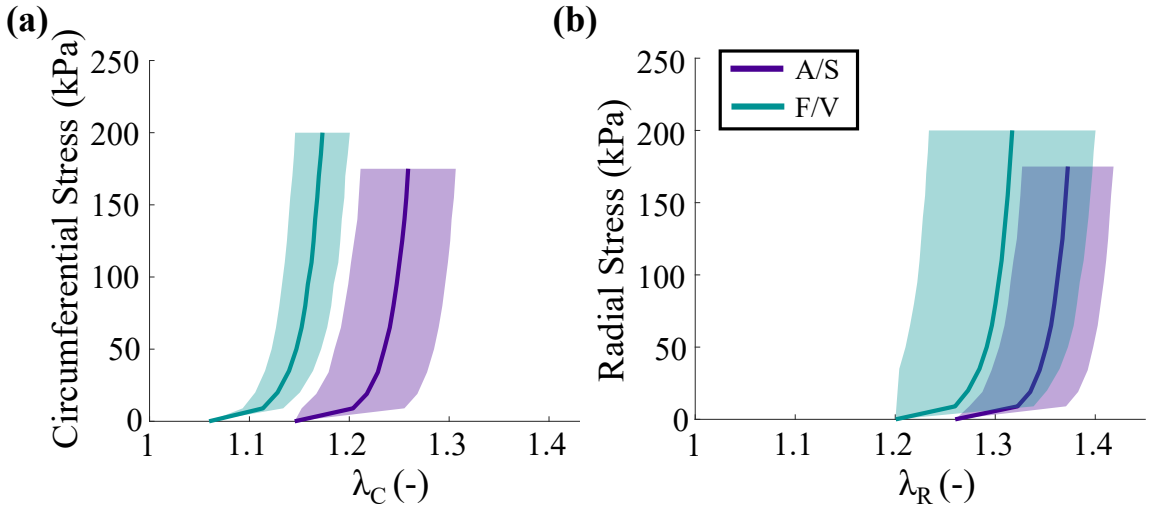

Figure 2-5. Biaxial mechanical results for the separated tissue layers of the TVAL in the (a) circumferential, and (b) radial directions [74]. Values are in mean ± SEM.

2.3.3 *In Vitro* Microstructural Characterizations of the TV Leaflets

In additional to characterization of the mechanical properties of the TV leaflets, studies on the mesoscopic quantification of the TV leaflet tissues can further unveil the complex underlying microstructure. Specifically, these observations focus primarily on examining the CFA of the TV leaflets, i.e., the reorientation and realignment of the collagen fiber networks in response to the applied mechanical loading [37, 93, 95, 107]. Techniques, such as small-angle light scattering [113, 152], SHG [117] and two-photon fluorescent microscopy [107], have provided insight to the microstructural components of the TV leaflets. For example, the collagen fibers of the cardiac heart valve leaflets were shown to align predominantly in the circumferential direction in the unloaded state, with varying degrees of fiber dispersion and crimping across different layers of the tissue. In one study, Meador *et al*. (2020) [107] performed a detailed microstructural observation of the three TV leaflets using both two-photon fluorescent microscopy and histological quantification. Each microstructural constituent within the TV, including the collagen fibers, elastin, GAGs, and VICs, was found to be heterogeneously distributed with composition differences between the TV leaflets. Although the constituent composition varied from leaflet to leaflet, the CFA was found to be relatively similar, with fibers primarily oriented in the circumferential direction throughout the thickness direction. Depth-discriminated SHG quantification further suggested that the collagen be organized as individual fibers in the atrialis layer with both radial and circumferential orientations, before organizing into higher-order sheets in the F/V layers with a distinct circumferential orientation. Although these studies do not quantify the load-dependent changes in the CFA, the microstructural quantification has improved our understanding of collagen organization and composition within the TV leaflets.

2.3.4 *Ex Vivo* and *In Vivo* Mechanical Characterizations of the TV Leaflets

Previous research efforts to characterize the mechanical properties of the TV leaflets *in vitro* have followed a distinct methodology: excising the TV apparatus and mounting them to a rigid annulus in a ventricular chamber simulator [17]. Although this technique may give insight into the TV leaflet mechanics and coaptation, utilizing a rigid annulus may not be ideal for mimicking the native valve function, primarily due to the dynamic nature of the cardiac valve annulus and the subsequent alterations in the leaflet strain over cardiac cycles. In recent years, significant emphasis has been placed on characterizing the *in vitro* mechanical properties of the TV leaflets through the utilization of this category of characterization devices.

Khoiy *et al*. (2016) [7] took the first step towards characterizations of the *in vitro* mechanical properties of the TV leaflets by quantifying the dynamic deformations of the TV in a beating porcine heart. This was achieved by implementing an *ex vivo* pump apparatus to simulate the right-sided systolic and diastolic pressures exhibited within the cardiac cycle. The use of this system showed that immediately after the coaptation of the TV leaflets, all the leaflet strain values (i.e., circumferential, areal, and radial) increased rapidly and reached their peak values at the maximum right ventricular pressure. Throughout the cardiac cycle, the maximum principal strain remained evenly distributed throughout the leaflet, increasing until reaching the maximum right ventricular pressure, with the strain values as high as 12%. Overall, the strains were shown to be minuscule during diastole and increased during systole. Heterogeneity in the spatial distribution of the circumferential and radial strains was also observed for the TV SL, matching similar trends when the biaxial testing methods are employed. Khoiy *et al*. (2018) [6] later expanded this study to investigate the role of the chordae tendineae rupture in the

disturbance of annular function and leaflet coaptation. When the chordae tendineae was ruptured, the flow into the RA was found to decrease by 26% and the maximum right ventricular pressure decrease by 17%, highlighting the importance of the sub-valvular components in relation to the proper leaflet coaptation and TV function.

Apart from using an intact TV geometry under the *in vitro* apparatus, a deeper understanding of TV leaflet function has been underscored by the recent investigations of the *in vivo* TV leaflet mechanics. Mathur *et al*. (2019) [103] examined the TV leaflet strains in a beating ovine heart, suturing sonomicrometry crystals to the belly and free-edge portions of each TV leaflet, as well as to the TV annulus. A fiducial marker array was constructed for tracking the deformation of the TV leaflets and for calculating the *in vivo* leaflet strains. It was found that the strains are qualitatively different between the belly region and the free edges, with positive strains at systole and little change during diastole in the belly region of each leaflet, whereas the areal and circumferential strains were small at the free edges. Conclusively, no distinct common strain pattern was observed across all the three TV leaflets, although heterogeneity was noted for all strain evaluations (i.e., areal, radial, and circumferential). This study did, however, confirm the anisotropy of the quantified strains within each leaflet, with larger strain in the tissue's radial direction than the circumferential direction. Utilizing the technique, Mathur *et al*. (2020) [104] later investigated the effects of the De Vega valvuloplasty on the leaflet tissue mechanics when different degrees of cinching were applied. With each degree of cinching, the De Vega technique reduced the range of motion and angular velocity of the TV AL, and, therefore, reduced the areal and radial strains, especially in the belly region of the leaflet. The circumferential strain remained similar throughout each cinching level. These

observations concluded that the area strain in the leaflet's belly region was driven by the reduction in radial strains, leading to the reduced chordal tethering (**Table 2-1**). Furthermore, this mechanical interaction resulted in a reduced range of motion for leaflet coaptation. These investigations are integral for understanding their role in leaflet coaptation and mechanics within the native valve after operation.

Table 2-1. Mean strain values relative to baseline at end-diastole (ED) and end-systole (ES) for each level of De Vega (DV) cinching [103].

		DV1		DV2		DV3		DV4		DV5	
Strain		ED	ES	ED	ES	ED	ES	ED	ES	ED	ES
Circ.	Mean	2.45	0.37	1.03	1.12	1.86	-2.68	2.90	-2.13	2.77	-0.71
	STD	5.22	4.76	10.32	10.72	8.88	8.28	9.43	11.72	8.97	18.20
Rad.	Mean	-3.73	-1.24	-0.94	1.99	-6.61	-8.49	-0.24	-9.8	-2.11	-12.63
	STD	12.14	5.51	10.01	14.68	11.12	9.87	21.56	14.21	22.90	16.30
Areal	Mean	-3.89	-4.86	-2.36	-8.33	-8.15	-19.00	-10.29	-24.53	-11.15	-30.22
	STD	17.37	16.21	20.99	20.54	20.89	21.98	37.47	32.03	28.36	36.12

2.3.5 The Tricuspid Valve Chordae Tendineae

The TV chordae tendineae affix the leaflets to the right ventricular walls at the papillary muscle tips, providing supporting forces to the leaflets during systolic closure. The morphology of the TV chordae tendineae have received sparse attention in the previous literature as compared to their mitral valve counterparts, despite the noticeable differences between the two atrioventricular heart valves (e.g., anatomy, mechanical loading environment, etc.). Silver *et al*. (1971) [141] conducted a pioneering study on the TV chordae morphology by analyzing human cadaveric hearts and provided a categorization system that is widely used to date. In

their work, they described three primary subsets of the chordae tendineae based on the leaflet insertion locations: (i) the noticeably thicker *struct chordae* that attach to the central, belly region of the TVAL; (ii) the *basal chordae*, affixing at the annulus-leaflet transition (i.e. the base of the leaflet); and (iii) the *marginal chordae*, connecting to the free edge of the leaflets. While the classification system proposed by Silver *et al*. (1971) provides the basis naming convention for many other studies, researchers have adopted their own categorization schemes due to contentions such as whether the strut chordae exist for all the three TV leaflets. For example, some researchers have opted for labeling the chordae based on their cross-sectional area (i.e., small, medium, or large) [144], or using a more detailed scheme by considering the gross structure, insertion locations, and branching patterns, resulting in over 11 types of TV chordae [53]. While these earlier works provided valuable insight to the anatomical trends in TV chordae morphology, moving forward it is important to adopt a unified and consistent classification/naming convention for the TV chordae tendineae. By using different chordae naming conventions, it becomes difficult to make direct comparisons of the findings between different studies. For example, how do the "*strut chordae in the TVAL*" differ from a "*medium chordae in the central region of the same leaflet*"?

Additionally, a key aspect of the TV chordae morphology that requires more attention is the comparison between different species. The potential discrepancies in the TV chordae morphology across different animals may affect the translation of research findings from the animal works into the biomechanical understanding of the human chordae. Previous studies have shown more chordae in the porcine TV than the human or ovine TV [53, 67, 141], however other inter-species comparisons are limited or non-existent (e.g., differences in the

branching patterns, insertion locations). The few interspecies comparisons in the previous works necessitates more comprehensive future works to better understand the differences in TV morphology, including the comparisons of: (i) the tissue donors' ages, (ii) the healthy/diseased state of the valves, and (iii) the chordae branching patterns and insertion locations.

2.3.6 *In Vitro* Mechanical Characterizations of the TV Chordae

Uniaxial Mechanical Characterizations

The chordae tendineae primarily undergo uniaxial loading in the valve apparatus, and as such the *in vitro* mechanical characterizations of the chordae tendineae generally involves uniaxial tensile loading. In the chordae characterization experiments, the central segment of the tissue was typically used and mounted between the crossheads of a servo-hydraulic testing device. Then, the chordae were preconditioned via cyclic uniaxial tensions followed by either repeated loading and unloading cycles to a targeted stress or loading the chordae until rupture. In a recent study from our lab, we took a different approach to the aforementioned chordae testing setup that may better emulate the *in vivo* function of the TV apparatus. In this work, we preserved the insertion to the leaflet and the papillary muscle, and mounted the leaflet-chordae-papillary muscle entity to a tine-based uniaxial testing system for characterizing the uniaxial mechanical properties of the tissue (**Figure 2-6**(a)). Utilizing the uniaxial mechanical testing of the TV chordae, several key comparisons can be made between: (i) different species, (ii) different leaflet insertion locations, and (iii) different experimental boundary conditions.

First, it was observed that the porcine and ovine chordae exhibit similar extensibility in the TVAL (porcine: 1-3% vs. ovine: 2-3% at a 1 MPa Cauchy stress), and that for the TVSL and

TVPL, the porcine chordae were 80-95% more extensible than the ovine chordae [117, 144]. The differences in the tensile properties between the porcine and ovine TVAL and the TVPL/TVSL chordae demonstrate a need for further corroborations of these findings. Second, it has been shown that the strut chordae are generally less extensible than the marginal or basal chordae, and that the marginal and basal chordae appear to have similar tensile characteristics. Third, it has been found that there is an insignificant trend between the TV chordae extensibility and the cross-sectional area; however, chordae with a cross-sectional area >0.404 mm^2 were shown to have significantly smaller low-tension tangent stiffness than the thicker chordae [144]. Fourth, comparing our study [132] considering the porcine TV strut chordae as a leaflet-chordae-papillary muscle entity (**Figure 2-6**(b)) to an earlier work via the clamp-based testing method [117], similar tensile properties were found from both tissue mounting approaches. Although the two testing methods yielded similar uniaxial tissue mechanical behaviors, advantages were demonstrated in the approach using the leaflet-chordae-papillary muscle entity, including the ability to analyze the leaflet and papillary muscle contributions to the chordae stretch, and the ability to image the load-dependent changes in the CFA at the chordae-leaflet insertion.

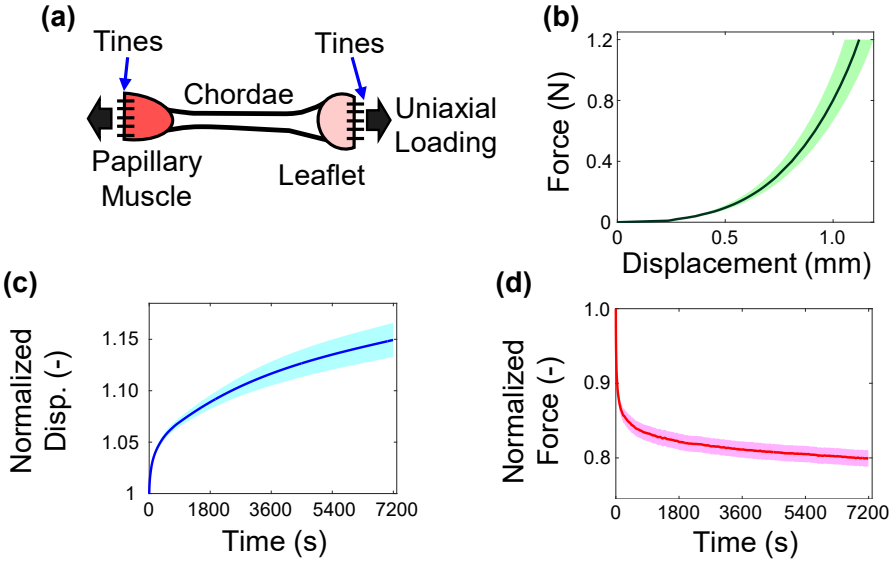

Figure 2-6. (a) Schematic of the chordae tendineae tested as a holistic chordae-leaflet-papillary muscle entity using a tine-based mounting system. Mechanical characterization results [132]: (b) uniaxial tension, (c) 2-hour creep, and (d) 2-hour stress relaxation. Results are presented as mean ± SEM.

While the leaflet-chordae-papillary muscle entity approach is a step closer to emulating the *in vivo* deformation of the chordae, even more physiologically representative mechanics could be realized through the use of a right heart simulator, however no studies have been performed in this manner to date. In addition, other useful studies of tissue biomechanics for the TV chordae would involve understanding the effects of disease on the tissue's uniaxial mechanics. One such study was performed by Lim *et al*. (1983) [97] on the tensile behaviors of a myxomatous human TV chordae and they found that the diseased chordae was more extensible and ruptured at a much lower stress than the healthy chordae. This is a relatively outdated study, and limitations include: (i) only one chordae was tested, (ii) preconditioning was not performed,

and (iii) optical strain tracking via fiducial markers was not used, resulting in less accurate measurements of the tissue deformation. Further investigations are warranted to obtain better information about the changes in the mechanical properties and the underlying microstructure of the diseased TV chordae.

Viscoelastic Properties

Although comprehensive investigations of the quasi-elastic tensile properties of TV chordae are available in the literature, there have been relatively fewer studies on quantification of the viscoelastic properties for the TV chordae. In our lab, we are currently investigating the viscoleastic properties of the TVAL strut chordae through creep and stress relaxation tests. For creep testing, the leaflet-chordae-papillary muscle entities were subjected to a 1.2 N force, and the force was maintained through increasing applied displacements over the course of 90 minutes (**Figure 2-6**(c)). In stress relaxation testing, the specimens were displaced and held at the displacement associated with a 1.2 N force over a 90-minute duration (**Figure 2-6**(d)). These viscoelastic characterizations are useful for understanding the time-dependent behaviors of the chordae, which will be valuable in the refinement of TV computational models when the rate-dependent responses of the TV chordae are imperative.

2.3.7 *In Vitro* Microstructural Quantifications of the TV Chordae

In addition to understanding the biomechanical behaviors of the TV chordae, there have been some studies investigating the mesoscale properties and microstructure of the chordae segment or the chordae-leaflet insertion. For visualizing the microstructure of the chordae segments, previous works have used methods such as histology [117, 144], fluorescent dye staining [144],

SHG imaging [144], transmission electron microscopy [96] or scanning electron microscopy [96]. It was found, from these studies, that the TV chordae are composed of dense collagen fiber bundles that are undulated at their unloaded state, together with inter-dispersed elastin and interstitial cells. On the outer surface of the chordae is the endothelial cell layer where the cell nuclei are fairly circular in shape. Moving from the outer surface to the center, the cell nuclei become more elongated and undulated and the collagen fibers and cell nuclei become more directly aligned along the primary axis. Depictions of the depth-discriminated collagen microstructure and the cells of the TV chordae are shown in **Figure 2-7**. Another earlier work on the microstructure also noted the vasculature present in the TV chordae, indicating another potential function of the tissue to provide nutrients to the TV leaflets [39]. Nevertheless, this finding has not been corroborated in recent studies, and additional research efforts are warranted to better understanding this observation.

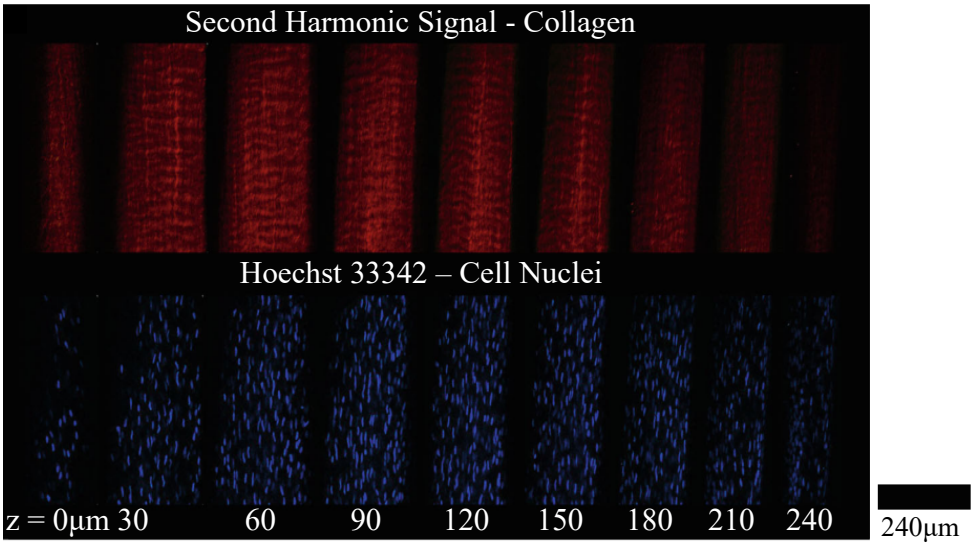

Figure 2-7. SHG imaging results reveal the unidirectional, wavy CFA of the chordae at varying tissue depths, while fluorescent dye staining (Hoechst 333432) allows visualization of the cell nuclei through the thickness of the tissue (images adapted from Smith *et al*. (2020) [144]).

The TV chordae-leaflet insertion is of particular interest in previous studies due to the complexity of the transition between the leaflet and chordae collagen fiber networks. To better understand and quantify the load-varying CFA changes in the TV chordae-leaflet insertion, in our lab, we utilized the pSFDI collagen imaging modality [130] (**Figure 2-8**). We found that with an increased loading (up to 1.2 N), the collagen fibers of the TV chordae-leaflet insertion did not undergo significant reorientation, but underwent significant increases in the DOA, indicating that the uncrimping of the collagen fibers may be the primary mechanism by which the chordae-leaflet insertion bears loading. Furthermore, the changes in the DOA at the leaflet insertion demonstrated the spatial variations in the tissue's collagen microstructure. In contrast, another preliminary study used X-ray diffraction to image the TV chordae-leaflet insertion and

noted higher molecular strains at the chordae-leaflet insertion than the chordae segment or the leaflet region [102]. From these findings, it is observed that the complexity of the chordae-leaflet insertion microstructure facilitates the distribution of forces from the leaflet to the chordae and papillary muscles, however the microstructural complexity may also cause some adverse fiber-to-fiber interactions that can lead to tissue rupture.

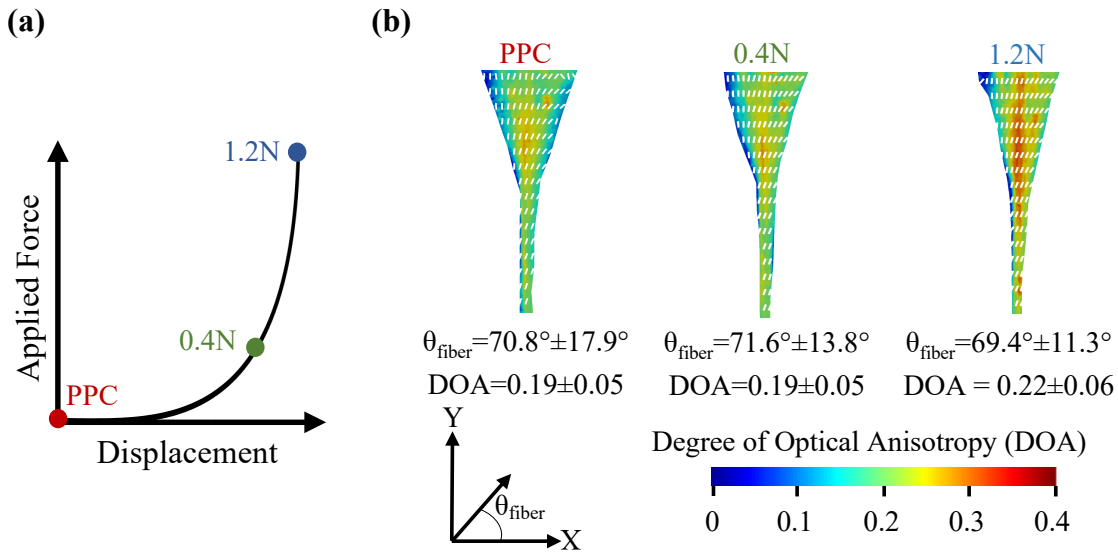

Figure 2-8. Quantification of the load-dependent CFA for a representative TV chordae-leaflet insertion using our integrated opto-mechanical instrument [130]: (a) applied force vs. tine displacement with three configurations used to perform pSFDI-based collagen microstructural imaging (i.e., PPC, 0.4 N, and 1.2 N loading states), and (b) results of collagen fiber orientation and degree of optical anisotropy (DOA). Values are presented as mean ± SEM, and white dashed lines denote the quantified fiber orientations.

2.4 Constitutive Modeling of the Sub-Valvular Components

The continuum mechanics theory presented in this sub-section defines invariants and tensors that are used throughout this dissertation. These definitions are assumed throughout unless otherwise defined.

2.4.1 Continuum Mechanics and Hyperelasticity Theory Framework

Constitutive modeling for soft biological tissues, such as the TV leaflets or chordae tendineae, is typically formulated under the hyperelasticity theory [58]. First, a strain energy density function (SEDF) W is chosen that relates the tissue deformations to the stresses of the material:

$$W = W(I_1, I_2, I_3, I_4, I_5) \tag{2.1}$$

Herein, $I_1 = \mathrm{tr}(\mathbf{C})$, $I_2 = \frac{1}{2}[\mathrm{tr}(\mathbf{C})^2 - \mathrm{tr}(\mathbf{C}^2)]$, and $I_3 = \det(\mathbf{C})$ are the first three invariants of the right Cauchy-Green deformation $\mathbf{C} = \mathbf{F}^T\mathbf{F}$, $I_4 = \mathbf{N}\cdot(\mathbf{C}\mathbf{N})$, and $I_5 = \mathbf{N}\cdot(\mathbf{C}^2\mathbf{N})$ are the pseudo-invariants of $\mathbf{C}$, and $\mathbf{F}$ is the deformation gradient that maps the tissue from its undeformed to deformed configurations. Note that the incompressibility condition is often assumed for modeling soft cardiovascular tissues, which reduces Eq. (2.1) to a function of two invariants I_1, I_2 and two pseudo invariants I_4, I_5.

The stress-strain relationship of the material is then established via

$$\boldsymbol{\sigma} = 2J^{-1}\mathbf{F}\left(\frac{\partial W}{\partial \mathbf{C}}\right)\mathbf{F}^T - p\mathbf{I} \tag{2.2}$$

where $\boldsymbol{\sigma}$ is the Cauchy stress, p is the penalty to enforce incompressibility, and $\mathbf{I}$ is the second-order identity tensor. The parameters of the selected SEDF form are typically

determined by nonlinear least-squares regression to the mechanical testing data [1].

The deformation gradient $\mathbf{F}$ and Cauchy stress $\boldsymbol{\sigma}$ can be easily transformed into other strain and stress measures. For the tissue strains, $\mathbf{F}$ can be transformed into the right Cauchy-Green deformation $\mathbf{C} = \mathbf{F}^T\mathbf{F}$, the left Cauchy-Green deformation $\mathbf{B} = \mathbf{F}\mathbf{F}^T$, and the Green-Lagrange strain $\mathbf{E} = (\mathbf{F}^T\mathbf{F} - \mathbf{I})/2$. On the other hand, the Cauchy stress can be used to compute the first Piola-Kirchhoff stress $\mathbf{P} = J\boldsymbol{\sigma}\mathbf{F}^{-T}$ with $J = \det(\mathbf{F})$ or the second Piola-Kirchhoff stress $\mathbf{S} = J\mathbf{F}^{-1}\boldsymbol{\sigma}\mathbf{F}^{-T}$. In addition to these common continuum mechanics stress measures, the membrane tension can be used for comparing the mechanical behaviors of thin, membranous tissues $\mathbf{T} = \mathbf{P}t$, where t is the tissue thickness.

2.4.2 Modeling of the Tricuspid Valve Leaflets

Constitutive modeling of the mechanical behaviors of the TV leaflets has recently received more and more attention. Khoiy *et al*. (2018) [71] considered a Fung-type SEDF in the modeling of the biaxial mechanical behaviors of the three TV leaflets. The differences in the averaged model parameters and the variances in the estimated model parameters of the three TV leaflets underscored the unique leaflet-specific mechanical properties and inter-specimen variability. Although this work provided the critical first step towards accurately modeling the TV leaflet biaxial mechanical response, the Fung-type SEDF form is a phenomenological model, which does not consider important microstructural information, and may not be the most representative SEDF form for the TV leaflet's mechanical behaviors.

One promising experimental avenue to determine the appropriate SEDF form for the TV

leaflets could be the use of the constant-invariant testing procedure, such as what was previously adopted for the left ventricle myocardium [62] and the MV leaflets [106]. This empirical technique considers carefully designed biaxial mechanical characterization protocols to qualitatively relate the derivatives of the SEDF W with respect to the invariants of $\mathbf{C}$. A series of constant I_1 or I_4 characterizations are used to isolate the contributions of each invariant to the partial derivatives of W and establish an ideal SEDF form for a specific soft tissue. It is imperative that the CFA is preferentially aligned with one of the biaxial testing axes for I_4 to be maintained at a constant value.

2.4.3 Modeling of the Tricuspid Valve Chordae Tendineae

Several SEDF forms have been proposed for modeling the TV chordae tendineae, including the Neo-Hookean, Fung-type, Mooney-Rivlin, Yeoh, and Ogden models (**Table 2-2**). Smith *et al*. (2020) [144] evaluated the effectiveness of each SEDF model for capturing the uniaxial mechanics of the TV chordae and found that all, except the neo-Hookean and Mooney-Rivlin models, can provide good fits with root mean square errors < 0.05. Their study also suggests that the two-term Ogden model would be the most appropriate for describing the TV chordae's mechanical behaviors, as this model avoids over-fitting of the data while preserving model simplicity. This two-term Ogden model, with some minor modifications, was used by both Ross *et al*. (2020) [132] and Pokutta-Paskaleva *et al*. (2019) [117] to model the TV chordae's uniaxial mechanics. The evaluation of the SEDF forms for the TV chordae will be valuable for refining the organ-level simulations of the TV apparatus, resulting in better predicted chordae behaviors and valve closing. While these phenomenological models provide an appropriate description of the TV chordae uniaxial tensile behaviors, they neglect the time-dependent

viscoelastic properties or the microstructural information.

Table 2-2. Constitutive models for the uniaxial properties of the chordae tendineae [144].

Model	SEDF Form
Neo-Hookean model	$W = C_1(I_1 - 3)$
Fung-type model	$W = C_1(\exp\{I_1 - 3\} - 1)/C_2$
Mooney-Rivlin model	$W = C_1(I_1 - 3) + C_2(I_2 - 3)$
Yeoh model	$W = \sum_{i=1}^{N} C_i(I_1 - 3)^i$
Two-Term Ogden model	$W = C_1(\lambda_1^{C_2} + \lambda_2^{C_2} + \lambda_3^{C_2} - 3)/C_2 + C_3(\lambda_1^{C_4} + \lambda_2^{C_4} + \lambda_3^{C_4} - 3)/C_4$

2.5 *In-Silico* Investigations of the Tricuspid Valve

2.5.1 Organ-Level Tricuspid Valve Simulations

In-Silico simulations enable connections between tissue-level mechanical behaviors and *in vivo* valvular function of the TV. Prior studies have simulated the TV function to understand patient-specific healthy TV mechanical environment [73, 147], explore the impact of papillary muscle displacements on the TV function [143], assess the potential of the MitraClip for restoring healthy TV function [32], or evaluate the performance of a new contact algorithm [70]. Interested readers are referred to our recent review article of these *in-silico* studies for more information [89].

Our lab has recently provided the first comprehensive *in-silico* assessment of how the TV pathologies influence the TV function in Laurence *et al*. (2020) [84]. In brief, the TV geometry from Kamensky *et al*. (2018) [70] was used in finite element (FE) analysis to simulate the TV

function, considering four pathological scenarios: pulmonary hypertension, annular dilation, papillary muscle displacement, and rupture of the chordae tendineae. Our simulation results underscored the effects of each valvular pathology on the TV function, for example, how TR could arise from annulus dilation, papillary muscle displacement, and/or the rupture of the chordae tendineae (**Figure 2-9**). Additional quantitative analyses, based on our *in-silico* TV simulations, led to three key observations. Firstly, the geometry metrics, such as the tenting area or the coaptation height, depended on which two TV leaflets were in contact. This has important clinical implications, because there is uncertainty regarding which two leaflets are visualized for the clinical quantification of these metrics [145]. Secondly, the isolated scenario of papillary muscle displacement led to TR, suggesting this pathology may be a new target for clinical intervention rather than considering only the annulus dilation as a TR indicator. Thirdly, the chordae tendineae attached to the TVAL or TVSL may be more important to ensure the proper valve closure. Moreover, the leaflet stresses increased for all four pathological scenarios, which may trigger the cellular biosynthetic response and lead to altered leaflet morphology. This pilot *in-silico* study has provided the simulation-guided assessment of TV pathologies. However, significant improvements and extensions are warranted to translate our model to the real clinical applications, such as a more accurate description about the *in vivo* motions of the TV annulus or papillary muscles.

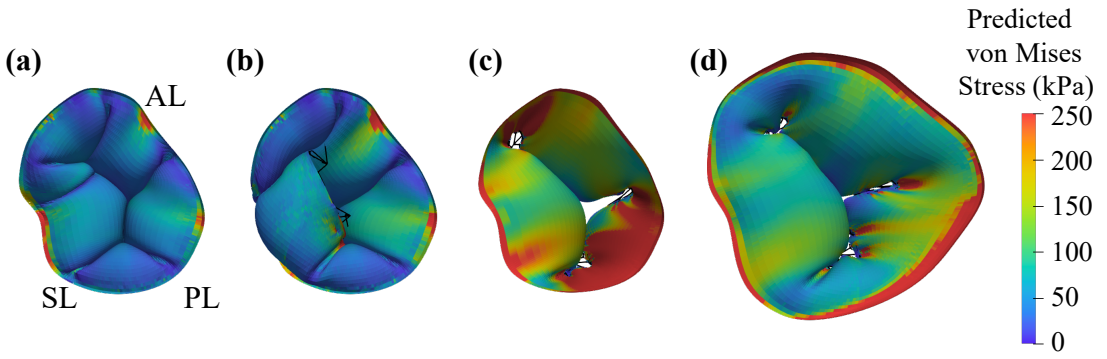

Figure 2-9. FE simulation results for the (a) healthy, and the diseased TVs: (b) chordae rupture, (c) combined flattened annulus and papillary muscle displacement, and (d) combined flattened annulus and annulus dilation [84].

2.5.2 Evaluating the Affine Fiber Kinematics Assumption

Integrating computational and experimental tissue biomechanics enables a cross-validation pipeline for guiding experimental setups and for evaluating the efficacy of a constitutive model to numerically replicate the planar biaxial tests. Thomas *et al*. (2020) [152] performed such an investigation to validate a microstructurally informed constitutive model for the TV leaflets. In their work, they effectively correlated the tissue biaxial mechanical responses with the collagen fiber kinematics by their combined experimental-computational methods. Their study serves as an example of how an integrated experimental-computational approach can validate the numerical implementation of the computational model in simulating TV function. In our lab, we recently performed studies to evaluate the efficacy of the *affine fiber kinematics* (AFK) assumption—an assumption that has been widely accepted in the heart valve computational biomechanics community—by using our pSFDI modality. Preliminary findings of our work

(**Figure 2-10**) suggest that the AFK assumption is a good approximation for TV leaflets under *equibiaxial* tensions, but larger deviations from this assumption were found for *non-equibiaxial* loading protocols. These findings suggest that the AFK assumption may need to be carefully evaluated when it is employed in the organ-level and tissue-level TV simulations to avoid mispredictions of the reorientation and realignment of the underlying collagen fiber networks.

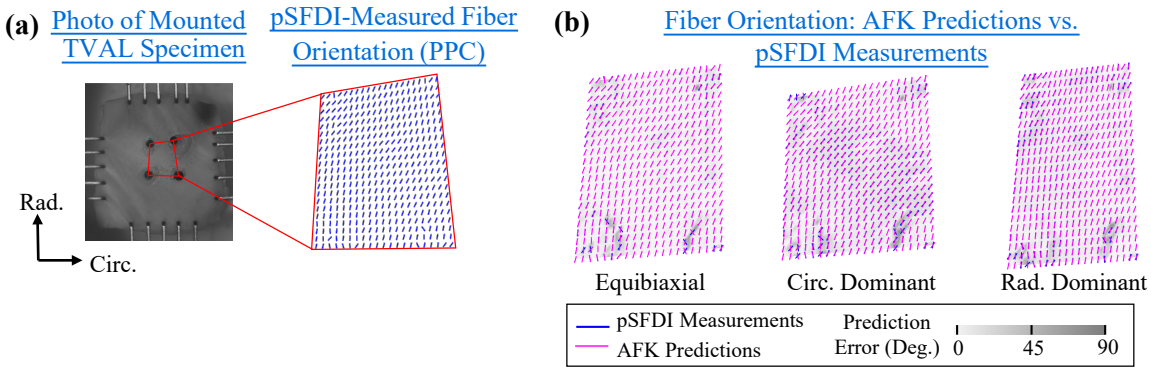

Figure 2-10. (a) The combined pSFDI-biaxial testing approach allowed for (b) validation of the AFK assumption by comparing the fiber orientation angles (denoted by dashed lines) between the pSFDI measurements and the AFK predictions. Data are taken from [134].

2.5.3 Simulating the In-Vitro Biaxial Testing of Heart Valve Leaflets

In-silico simulations are valuable tools to replicate the biaxial mechanical testing experiments. By simulating the biaxial mechanical testing of the TV leaflets, different experimental conditions can be systematically evaluated to determine the optimal setup to more accurately obtain the TV leaflet biaxial mechanical properties. Examples include the simulations of the mitral valve or other biomimetic materials [41, 65, 148], by considering different specimen

geometry (e.g., square vs. cruciform), different boundary (or tissue mounting) conditions (e.g., rotation-allowed suture, rigid tines, or clamps), and the effective mounting size (e.g., 10×10 mm vs. 5×5 mm). We can better ensure accurate material modeling by understanding the effects of various experimental setups on the resultant characterized mechanical properties of the TV leaflet tissues.

2.6 Concluding Remarks

This chapter has summarized recent advancements in our understanding of the TV across the length scales. Various *in vitro*, *ex vivo*, and *in vivo* approaches have enabled researchers to acquire insight into the mechanical and microstructural properties of the TV sub-valvular components. More recently, there has been a shift towards utilizing the rich experimental information to develop robust computational tools for predicting TV function in healthy and diseased states. Despite these tremendous efforts, several avenues require further attention, which are the focus of this dissertation. First, establishing multi-scale connections between the TV leaflet mechanical, mesoscale, and microstructural properties will provide a rich and complete understanding of the TV leaflet behaviors. Second, developing new approaches for modeling the TV leaflet mechanical behaviors will improve *in silico* predictions of the TV behaviors. Third, improving the connection between *in vitro* mechanical characterizations and *in vivo* tissue behaviors through the leaflet pre-strains will allow more accurate predictions of TV functional strains, which play an important role in the cellular biosynthetic behaviors.

CHAPTER 3 Multi-Scale Properties of the TV Leaflets

This chapter summarizes our recent work characterizing the multi-scale properties of the TV leaflets. First, we biaxially test the three TV leaflets and explore how the choice of specimen size influences the observed mechanical properties (Section 3.1). We then relate the observed tissue-level mechanical properties to the mesoscale CFA structures using pSFDI (Section 3.2). The chapter concludes with microstructural investigations of the TV leaflets using confocal microscopy with multiphoton autofluorescence imaging and SHG imaging (Section 3.3). The established properties for the TV leaflets across the length scales may be useful for future developments of multi-scale computational frameworks.

3.1 The TV Leaflet Mechanical Properties

3.1.1 Tissue Acquisition and Preparation

Adult porcine hearts (80-140 kg, 1-1.5 years of age) were obtained from a USDA-approved abattoir (Country Home Meats Company, Edmond, OK) and transported to our laboratory. The hearts were cleaned to remove excess blood and the whole organ was promptly stored in a freezer at −14 °C. The frozen hearts were thawed within a week using a room-temperature water bath, and the three TV leaflets were dissected following our established technique [67, 129]. All three dissected TV leaflets were then temporarily stored in the freezer again until the experimental characterization within 1-3 days. This temporary freezer storage is supported by our previous investigation that found short-term freezer storage of the atrioventricular heart valve leaflets had negligible effects on the characterized mechanical properties [38].

In preparation for biaxial mechanical testing, the excised leaflet was thawed in phosphate buffered saline (PBS). A 11×11 mm specimen was then cut from the central region of each TV leaflet (**Figure 3-1**(a)), and the top-right corner was labelled using a surgical pen for orientation reference. The average thickness of the tissue was determined from three distinct measurements across the specimen via digital caliper (Westward 1AAU4, 0.01 mm resolution). The tissue was next mounted on a BioTester (CellScale, Canada) using BioRakes that delimits a 9×9 mm effective testing region (**Figure 3-1**(b)). Then, four glass beads (300-500 μm) were glued in a square configuration within the central one-third area of the effective testing region for the subsequent computations of the tissue deformation and strains using digital image correlation (DIC). Once the glass beads were affixed to the tissue surface, the specimen was submerged in a $32\,°C$ PBS bath. Although the physiological body temperature is $37\,°C$, our integrated pSFDI system [68] required the testing temperature to be at or below $32\,°C$ for quantifying the collagen fiber architectural properties. Our previous characterization for the atrioventricular valves showed negligible differences in the leaflet mechanical properties arising at differing testing temperatures [67].

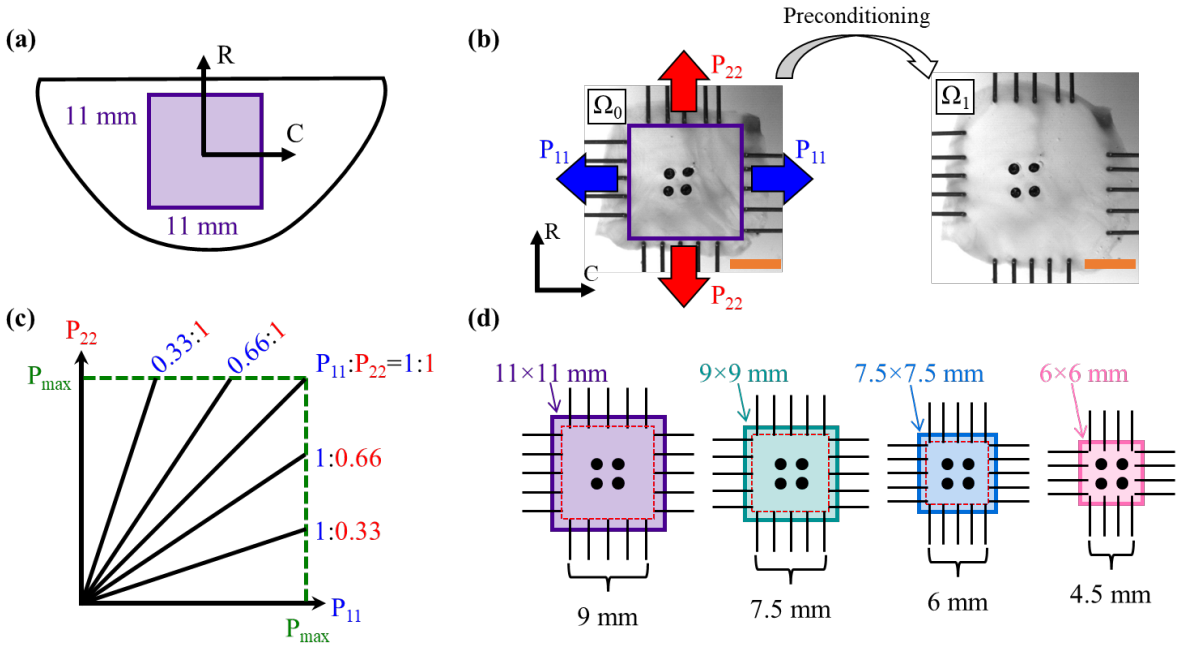

Figure 3-1: (a) The central region of each leaflet was dissected and (b) mounted to the commercial biaxial tester for mechanical preconditioning. (c) Five ratios of the peak physiological stress (115 kPa) were selected for the biaxial mechanical characterizations. (d) The iterative approach for characterizing the effect of specimen size on the observed mechanical properties.

3.1.2 Biaxial Mechanical Characterization

The target peak force f^{target} for the TV leaflet specimen was determined using the approximate maximum physiological stress P^{target} of 115 kPa according to the previous literature [5, 67], the tissue's initial effective edge length L_0, and its initial thickness t_0: $f^{\text{target}} = P^{\text{target}} L_0 t_0$. In the biaxial mechanical testing, the leaflet first underwent force-controlled equibiaxial preconditioning to restore the tissue to its approximate *in vivo* configuration (**Figure 3-1**(b)). This PPC configuration Ω_1 was recorded for subsequent tissue stress/strain analyses. Next, the

tissue was returned to its initial mounted configuration Ω_0, and the functionality of the BioTester was used to determine the biaxial displacements associated with the varying ratios of f^{target}, i.e., $f_{\text{circ}}^{\max} : f_{\text{rad}}^{\max} = 1:1,\ 1:0.66,\ 1:0.33,\ 0.66:1,\ 0.33:1$ (**Figure 3-1**(c)). The specimen was then allowed to rest at Ω_0 for 2-3 min. Finally, the tissue underwent the biaxial mechanical characterization that included three loading/unloading cycles for each of the above-mentioned force ratios (i.e., protocols) at a loading rate of 1.31 N/min.

Throughout biaxial mechanical testing, 1280×960 resolution images were taken using the charge-couple device (CCD) camera, and the load cell forces and tine displacements at 15 Hz. Data from the last loading cycle was used in the subsequent tissue stress/strain analyses and constitutive modeling.

3.1.3 Iterative Approach to Determine the Specimen Size Effect

To investigate the effect of specimen sizes on the characterized mechanical behaviors, a sequential testing procedure was conducted (**Figure 3-1**(d)). Immediately following the mechanical characterization of the 9×9 mm effective testing region, the specimen was unmounted from the BioTester and the BioRake holes were used as guidelines to procure a specimen of 9×9 mm. The 9×9 mm specimen was then mounted to the BioTester with the 2nd effective testing region of 7.5×7.5 mm to repeat the mechanical characterization procedure described in Section 3.1.2. This iterative process was repeated for the 7.5×7.5 mm and 6×6 mm specimen sizes, resulting in characterizations for a total of four effective testing regions: 9×9 mm, 7.5×7.5 mm, 6×6 mm, 4.5×4.5 mm. If possible, the original glass beads from the first specimen size were maintained throughout the iterative procedure. However, sometimes

it was needed that all four glass beads were replaced to keep the fiducial marker array to be within the central $1/3$ of the current specimen size.

3.1.4 Calculations of Tissue Stretches, Stresses, and Other Mechanics Metrics

The time-dependent fiducial marker positions were determined using the DIC functionality of the CellScale LabJoy software. $\mathbf{F}$ was computed using a four-node bilinear finite element and the marker displacements [135].

$$[\mathbf{F}] = [\mathbf{F}(\mathbf{X},t)] = [\mathbf{I}] + \begin{bmatrix} \sum_{I=1}^{4} B_{XI} u_I(t) & \sum_{I=1}^{4} B_{YI} u_I(t) \\ \sum_{I=1}^{4} B_{XI} v_I(t) & \sum_{I=1}^{4} B_{YI} v_I(t) \end{bmatrix} \tag{3.1}$$

Herein, $\mathbf{I}$ is the second-order identity tensor, B_{XI} and B_{YI} are the shape function derivatives of marker *I*, and $u_I(t)$ and $v_I(t)$ are the time-varying *X*- and *Y*-displacements of marker *I* with respect to Ω_0. The tissue total stretches ($\lambda_{\text{circ}}^{0-2}$ and $\lambda_{\text{rad}}^{0-2}$) were determined as the square roots of the principal values of $\mathbf{C}$, which were further decomposed into the *preconditioning* stretches $\lambda_i^{0-2} = \lambda_i^{0-1}\lambda_i^{1-2},\ i = \text{circ},\ \text{rad}$, where the superscripts indicate the configurations (Ω_0 : tissue mounting, Ω_1: PPC, Ω_2: loaded configurations).

The first Piola-Kirchhoff stresses P_{circ} and P_{rad} were determined by

$$[\mathbf{P}] = \text{diag}[P_{\text{circ}}, P_{\text{rad}}] = \frac{1}{t_0 L_0}\text{diag}[f_{\text{circ}}, f_{\text{rad}}] \tag{3.2}$$

where f_{circ} and f_{rad} are the measured forces in the tissue's circumferential and radial directions.

3.1.5 Statistical Analysis

Statistical analysis was performed to determine statistically significant differences in the mechanical behaviors between the different specimen sizes for each TV leaflet. Visualization of the data in MATLAB using quantile-quantile (Q-Q) plots showed the data were not normally distributed (not shown here). Thus, the Wilcoxon signed-rank test was used to evaluate the differences in the total stretches, the preconditioning stretches, and the elastic stretches. The analyses were performed with $p < 0.05$ considered as statistically significant. All data are presented as mean ± standard error of the mean.

3.1.6 The Effect of Specimen Size on the TV Leaflet Equibiaxial Response

The TV leaflets exhibited nonlinear, ansitropic mechanical behaviors for all four specimen sizes under equibiaxial tensions (**Figure 3-2**). Results for other biaxial tension protocols are provided in Appendix B. As expected, the circumferential directions of the leaflets were consistently stiffer than the radial directions, which stems from the underlying CFA (see Section 3.2). Focusing on the largest specimen size (**Figure 3-2**(a)), the TVAL had the stiffest circumferential (1.34±0.05) and radial (1.40±0.08) stretches. On the other hand, the TVPL and TVSL shared similar circumferential behaviors (1.49±0.08 and 1.47±0.07) with the TVPL being slightly stiffer (1.57±0.07) than the TVSL (1.71±0.07) in the radial direction. Our previous study [67] showed similar trends, except the TVSL was stiffer than the TVPL in the radial direction.

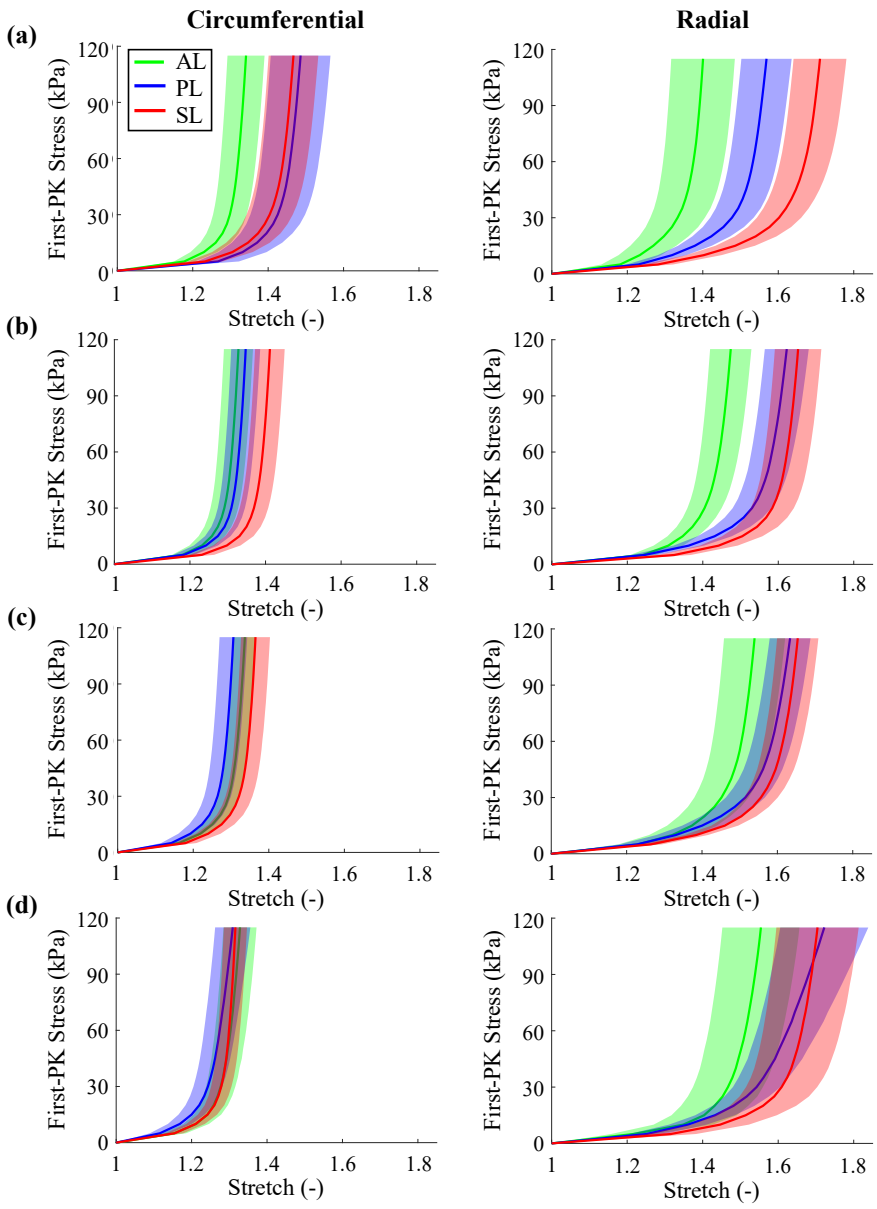

Figure 3-2: Average mechanical behaviors for P_{circ}:P_{rad} =1:1 of the three TV leaflets for the (*left*) circumferential direction and (*right*) radial direction considering: (a) Specimen Size 1 (9×9 mm), (b) Specimen Size 2 (7.5×7.5 mm), (c) Specimen Size 3 (6×6 mm), and (d) Specimen Size 4 (4.5×4.5 mm).

The choice of specimen size has direction-specific and leaflet-specific influences on the biaxial mechanical behaviors. For the circumferential direction, we observed that all three leaflets were stiffer for the smallest specimen size (AL: 1.33±0.04, PL: 1.31±0.05, SL: 1.32±0.03) compared to the largest specimen size (AL: 1.34±0.04, PL: 1.49±0.08, SL: 1.47±0.06). Also, the differences between the three leaflets became negligible by the second specimen size (**Figure 3-2**(b)) and nearly completely vanished by the smallest specimen size (**Figure 3-2**(d)). The specimen size had the opposite effect on the radial tissue behaviors, with all three leaflets exhibiting more compliant radial behaviors at the smallest specimen size (AL: 1.55±0.10, PL: 1.72±0.12, SL: 1.70±0.11) compared to the largest specimen size (AL: 1.40±0.08, PL: 1.57±0.07, SL: 1.71±0.07). However, like the circumferential direction, the leaflet-specific behaviors appear to diminish as the specimen size becomes smaller. Collectively, the observed direction-specific differences for the specimen sizes illustrate an increase in the observed material anisotropy as the tested specimens became smaller.

3.1.7 The Effect of Specimen Size on Computed Stretches

The quantified total stretches, preconditioning stretches, and elastic stretches are presented in **Figure 3-3**. This decomposition of the tissue deformations allows us to better understand the specimen size influence on the TV leaflet mechanical behaviors. For instance, the total stretches shown in **Figure 3-3**(a) echo our observations from Section 3.1.6—the circumferential and radial directions became stiffer and more compliant as the specimens became smaller, respectively. Similar effects were observed for all three stretches of the circumferential direction (top row of **Figure 3-3**), whereas the changes in the stretches of the radial direction appear to originate due to differences in the PPC deformation (**Figure 3-3**(b)).

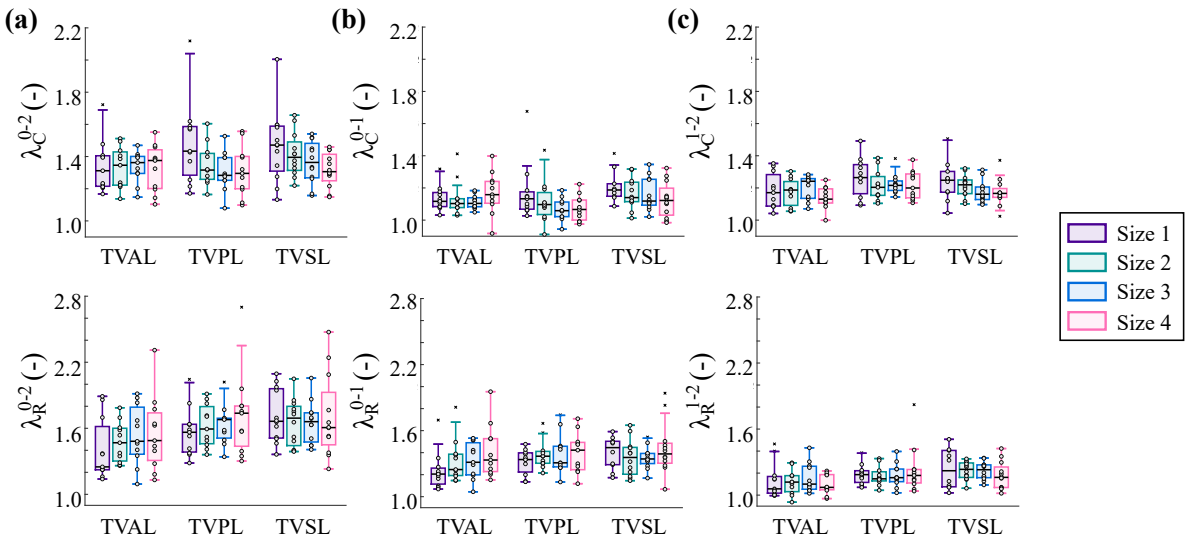

Figure 3-3: Average tissue stretches for the (*top*) circumferential direction and (*bottom*) radial direction: (a) peak tissue stretch λ^{0-2}, (b) PPC stretch λ^{0-1}, and (c) elastic stretch λ^{1-2}.

3.1.8 Discussion

In this sub-section, we have biaxially tested TV leaflets and observed how the choice of specimen size influences the observed mechanical behaviors. Our results showed that the specimen size indeed influenced the TV leaflet mechanical behaviors in a direction-specific manner. Specifically, as the specimen sizes became smaller, the circumferential stretches became stiffer while the radial tissue stretches became more extensible. Further decomposition of the tissue stretches further revealed that the changes to the radial stretch stemmed from the PPC stretch. On the other hand, the changes to the circumferential stretch were similar for the PPC and elastic stretches.

Our findings have significant implications for existing mechanical studies using iterative

experimental protocols. For example, our group has used an iterative enzyme-based approach to characterize how GAGs contribute to the TV leaflet mechanical behaviors [133]. The control tissues were larger than the enzyme-treated tissues in these studies to ensure that previous tine insertion holes did not influence the mechanical behaviors. However, as our present study indicates, this reduction in the specimen size for the enzyme-treated specimens will lead to stiffer circumferential stretches and more compliant radial stretches. It is then possible that the GAGs have a more profound influence on the circumferential tissue behaviors and less of an influence on the radial tissue behaviors.

Beyond the scope of individual experimental investigations, our results also suggest that specimen size must be considered when comparing the mechanical behaviors within the existing literature. Researchers do not typically control for the specimen size across their studies [5, 38, 67, 82, 107, 138, 139], meaning that direct comparisons are inaccurate due to the specimen size effect presented herein. Moreover, studies may use different stress-free reference configurations, such as the mounted specimen, PPC specimen, or the floating specimen. Our findings demonstrate that the specimen size will confound these comparisons, which is further exacerbated by the choice of stress-free reference configuration.

3.2 The Tricuspid Valve Leaflet Mesoscale Properties

3.2.1 Tissue Acquisition and Preparation

The TV leaflets were retrieved from porcine hearts sourced from a local abattoir (Chickasha Meat Co., Chickasha, OK) following our established methods [129]. 12×12 mm square specimens were excised from the central regions of the TVAL (n=19), the TVPL (n=15), and the TVSL (n=14). Each specimen was mounted to our commercial biaxial testing device with an effective edge length of 10×10 mm and biaxially characterized for another investigation (see Section 4.4).

3.2.2 Polarized Spatial Frequency Domain Imaging of the CFA

Following the mechanical characterization, an in-house pSFDI device was used to quantify the load-dependent changes in the tissue's CFA. Details of this system are described previously [68] and our experimental method is described in Appendix C, Step 2. Briefly, a LED-driven, micromirror-based pattern projection system (Texas Instruments, Dallas, TX) emitted cyan light (490 nm wavelength) through a rotating linear polarizer (Thorlabs, Newton, NJ) onto the tissue specimen, which was then reflected back through the same polarizer and captured as an 8-bit grayscale image by a 5-megapixel CCD camera (Basler, Germany). This process was repeated with 5° increments of the rotating polarizer between 0-180 degrees (37 total images). The images were then processed to determine the pixel-wise fiber orientation angle θ_{fiber} and the degree of optical anisotropy (DOA) that is related to the alignment of collagen fibers: smaller DOAs denoting a random fiber network and larger DOAs signifying highly aligned fibers. More information regarding the determination of these parameters from the

experimental data can be found in Section 2.1 of Jett *et al*. 2020 [68]

We considered five leaflet configurations to understand how the leaflet's CFA adapts to applied biaxial mechanical loads. These included the mounted configuration, the PPC configuration, and the three configurations associated with the following ratios of 40 N/m Membrane Tension: $T_{\text{circ}} : T_{\text{rad}} = 1:1,\ 0.5:1,\ 1:0.5$. The leaflet was displaced to each configuration and imaged using the pSFDI technique outlined in the previous paragraph.

3.2.3 Data Analysis

The predicted fiber angle θ_{fiber} at the five configurations were used to generate probability density histograms for the tissue's region of interest (ROI) bounded by the BioRake tines (**Figure 3-4**). Our preliminary data suggested these distributions may follow a bi-modal distribution. Thus, we fit each probability density function with a π-periodic bimodal von Mises probability density function (**Figure 3-4**(b)). The experimental probability density functions were generated using a bin width of 5° and fit using our in-house differential evolution optimization algorithm (DEO) [160]. This fitting process began by generating n_{pop} uniformly distributed parameter sets and computing their residual:

$$f(\theta_{\text{fiber}};\mu_1,\kappa_1,\mu_2,\kappa_2,w) = w g^{von-Mises}(\theta_{\text{fiber}};\mu_1,\kappa_1) + (1-w) g^{von-Mises}(\theta_{\text{fiber}};\mu_2,\kappa_2) \quad (3.3)$$

with

$$g^{von-Mises}(\theta;\mu,\kappa) = \frac{1}{\pi I_0(\kappa)} \exp[\kappa \cos[2(\theta-\mu)]] \quad (3.4)$$

The residuals of all parameter sets were used to update the parameters in an explorative or exploitative manner depending on the data clustering. The DEO algorithm was terminated

when the maximum residual was sufficiently small ($<5\times10^{-7}$) or the difference between two successive generations was negligible ($<1\times10^{-7}$).

The optimal parameters for all specimens were gathered and compared to understand how the leaflet CFA changes in response to the prescribed biaxial tensions (see also [61]). All preferred fiber orientations (θ_1 and θ_2) were shifted to the first quadrant and sorted so that θ_1 was the fiber family closest to the circumferential tissue direction. We also computed the normalize distance between the two fiber families $(\theta_2-\theta_1)/90°$ to understand their relative rotations under the non-equibiaxial mechanical loading.

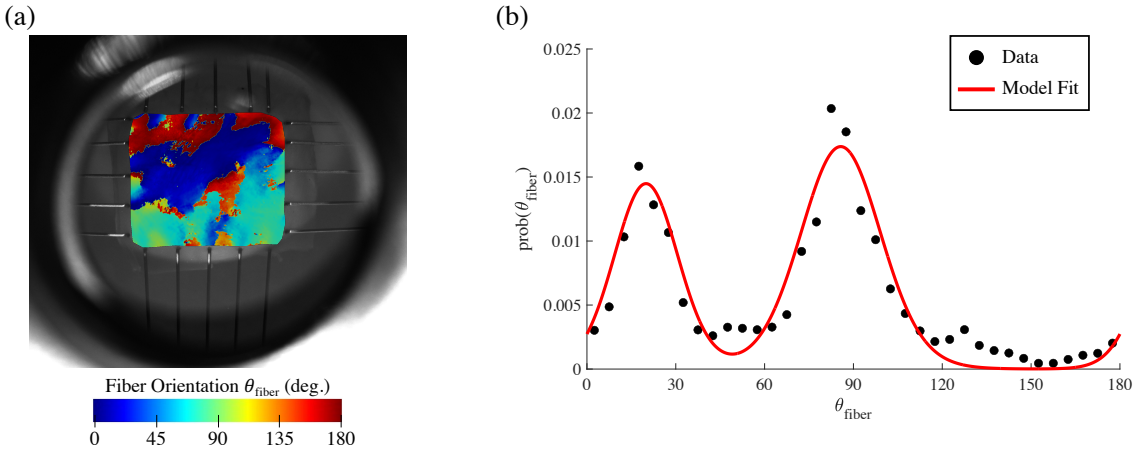

Figure 3-4. (a) pSFDI-predicted collagen fiber orientation plotted on the experimental image for one representative TVAL specimen. (b) Representative collagen fiber orientation probability density function fit with a bimodal von Mises distribution.

3.2.4 Tricuspid Valve Leaflet Collagen Fiber Architectural Properties

The derived bimodal von Mises parameters are presented in **Figure 3-5**. Interestingly, the summarized results show that the three TV leaflets have similar CFAs: the *first fiber family* of each leaflet is approximately aligned with circumferential direction (AL: 27.7°±5.7°, PL: 31.8°±6.2°, SL: 23.9°±7.0°) and the *second fiber family* is aligned near the radial direction (AL: 67.3°±1.7°, PL: 69.6°±7.4°, SL: 64.3°±6.2°). Of the three leaflets, the TVSL has the most unique properties with its first fiber family being more closely aligned with the circumferential direction (23.9°±7.0°) than the TVAL (27.7°±5.7°) or the TVPL (31.8°±6.2°). The fiber family dispersions for all three leaflets suggest that the circumferential fiber family has more variation (6.7°-15.3° vs. 4.1°-9.5°) and the von Mises weights show it is less dominant than its radial counterpart (AL: 0.40±0.06, PL: 0.45±0.07, SL: 0.38±0.06). However, these differences are not statistically significant.

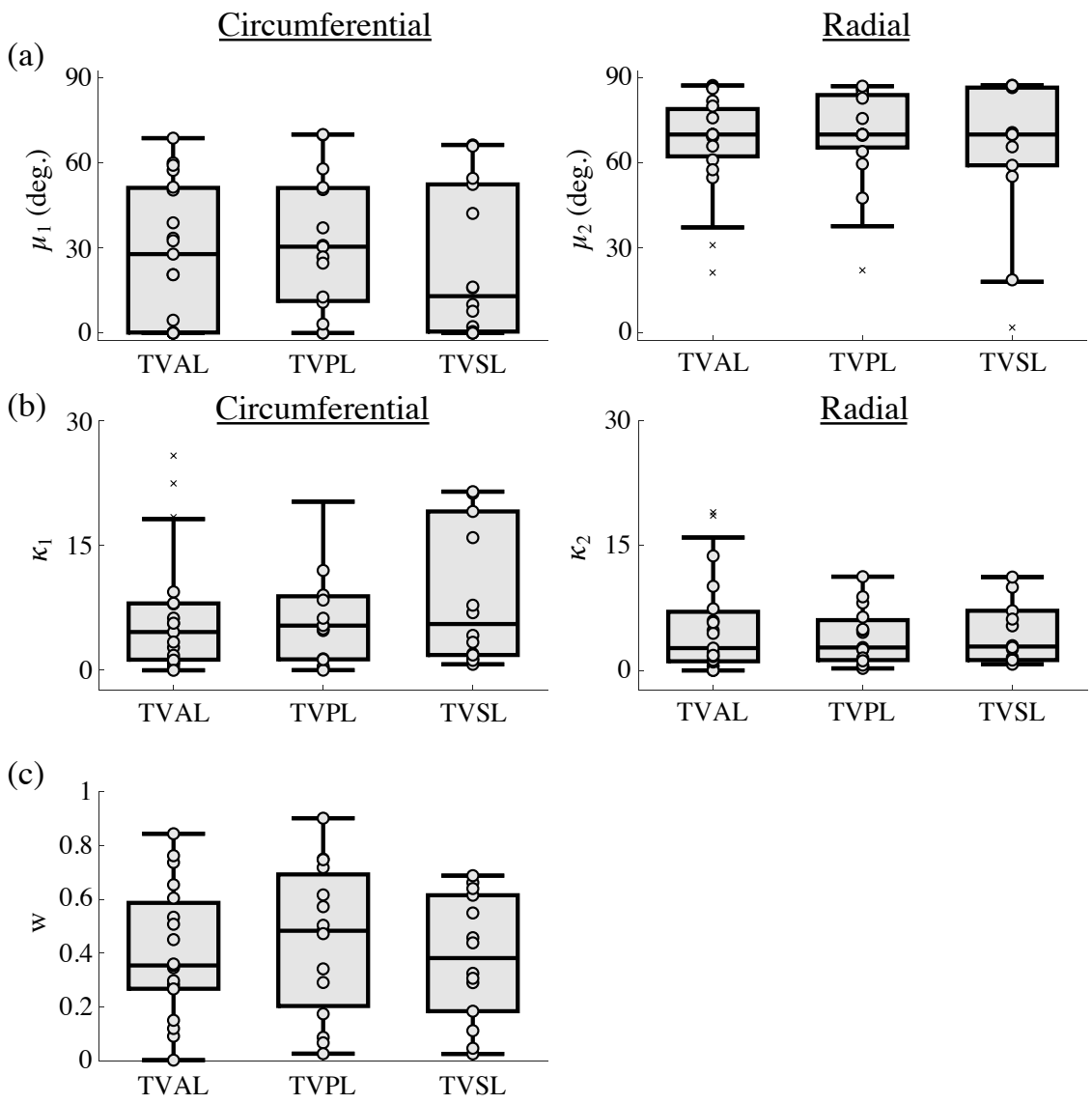

Figure 3-5. Predicted parameters of the bimodal von Mises distribution: (a) fiber family mean orientations, (b) fiber family dispersions, and (c) the weight of the circumferential fiber family.

3.2.5 Quantified Changes of the TV CFA to Biaxial Tensions

The relative rotations of the two fiber families are presented in **Figure 3-6**. These results reveal two interesting observations of the CFA: (i) the two fiber families rotate to be closer following

preconditioning and in the radially dominant configuration and (ii) the changes of the TVAL CFA are smaller than the changes of the TVPL and TVSL CFAs. It is not clear from the pSFDI data why the TVAL shows smaller dynamic adaptations of the CFA in response to the applied loading, but it may stem from its underlying microstructural arrangements (see Section 3.3).

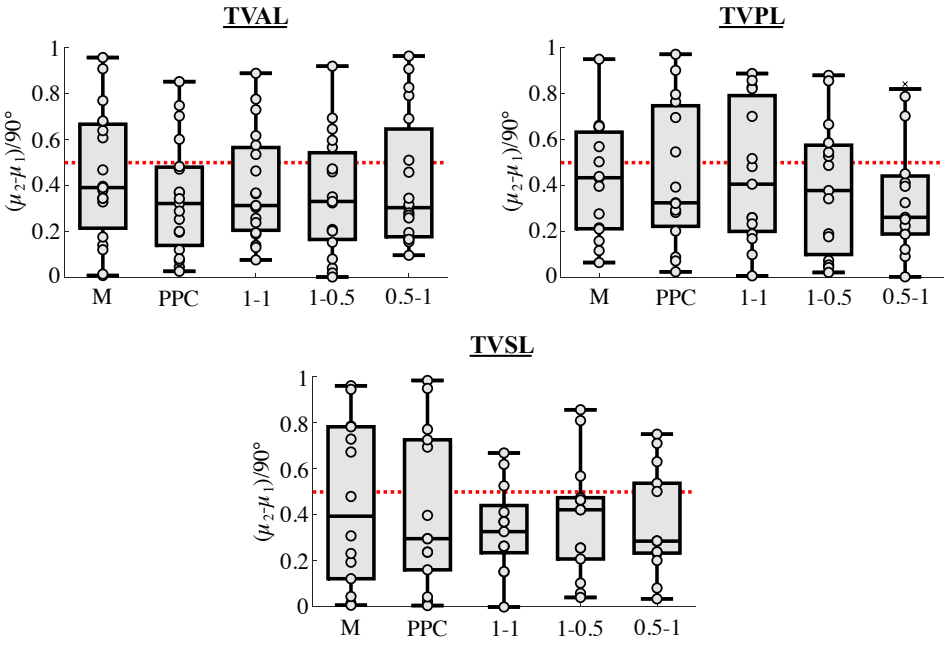

Figure 3-6. Normalized differences of the two fiber families for each TV leaflet in the five key configurations: mounted (M), post-preconditioned (PPC), and three ratios of P_{circ}:P_{rad}.

The von Mises weight *w* of the circumferential fiber family is presented for all three leaflets in **Figure 3-7**. These data can implicitly show which fiber family is most dominant in the given loading configuration—larger values of *w* indicate the circumferential fiber family is more dominant, while smaller values of *w* indicate the radial fiber family is more dominant. We note that, besides the PL, the circumferential fiber family is most dominant under the circumferentially dominant loading protocol (i.e., $P_{\text{circ}} : P_{\text{rad}} = 1 : 0.5$). This expected result

stems from the uncrimping of the circumferential fiber family in response to applied load, which correspondingly increases its birefringence and pSFDI signal across the specimen. Similar to our observations in the previous paragraph for the relative fiber family rotations, we note the TVAL CFA demonstrates smaller changes in response to the applied biaxial tensions.

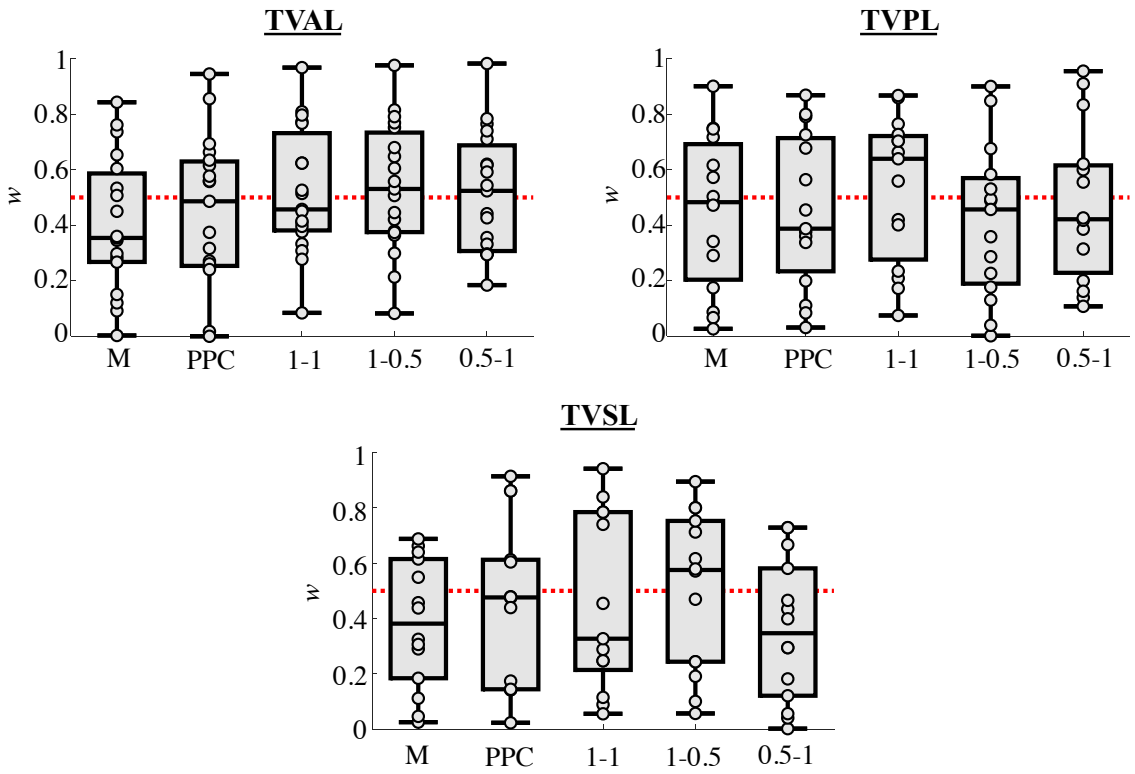

Figure 3-7. Relative weight of the circumferential fiber family in the bimodal von Mises probability density function in five key reference configurations: mounted (M), post-preconditioned (PPC), and three ratios of P_{circ}:P_{rad}.

3.2.6 Discussion

Herein, we have used pSFDI to characterize the CFA of the three TV leaflets and understand how it adapts to applied loading. The CFAs in the mounted configuration show that all three

TV leaflets have two fiber families: one fiber family is found near the circumferential direction (~30°) while a second fiber family is aligned approximately with the radial direction (~70°). Interestingly, the circumferential fiber family exhibits more fiber dispersion than its radial counterpart. We further observed that the three TV leaflets have unique adaptations to applied loading. For instance, the TVAL specimens consistently showed smaller changes to its CFA under applied equibiaxial and non-equibiaxial tensions. The fiber families of the TVPL and TVSL specimens, however, showed larger relative rotations and changes in the fiber family birefringence under the non-equibiaxial tensions. Further microstructural characterizations using confocal microscopy (see Section 3.3) can help clarify these leaflet-specific behaviors.

This novel bimodal von Mises-based analysis of the pSFDI results has also been used for other cardiovascular tissues, and we can use these results for other tissue to contextualize the TV leaflet CFA behaviors. For coronary artery tissues (**Figure 3-8**(a)), we found regional variations in the normalize difference of the two collagen fiber families, with the proximal and medial regions having more well-defined families than the distal region. Our TV leaflet CFA results presented herein are most-similar to the less-organized CFA of the coronary artery distal region. We also investigated the semilunar heart valves and showed the two fiber families of the AV (**Figure 3-8**(b)) were more well-defined than those of the pulmonary valve (PV) (**Figure 3-8**(c)) [61]. It is intriguing that the PV and TV have similar, less well-defined CFAs considering they are under starkly smaller physiological stresses than the AV (25 mmHg vs. 120 mmHg). This observation, in combination with our comparisons to the coronary artery tissues, leads us to believe that the organization of collagen fibers within cardiovascular tissues depends on its physiological environment. The tissues with more demanding physiological

environments, such as the AV leaflets or the proximal/medial regions of the coronary arteries, require well-defined CFAs, whereas tissues with lower-stressed physiological functions (e.g., the TV, the PV, or the coronary artery distal region) have less-defined CFAs.

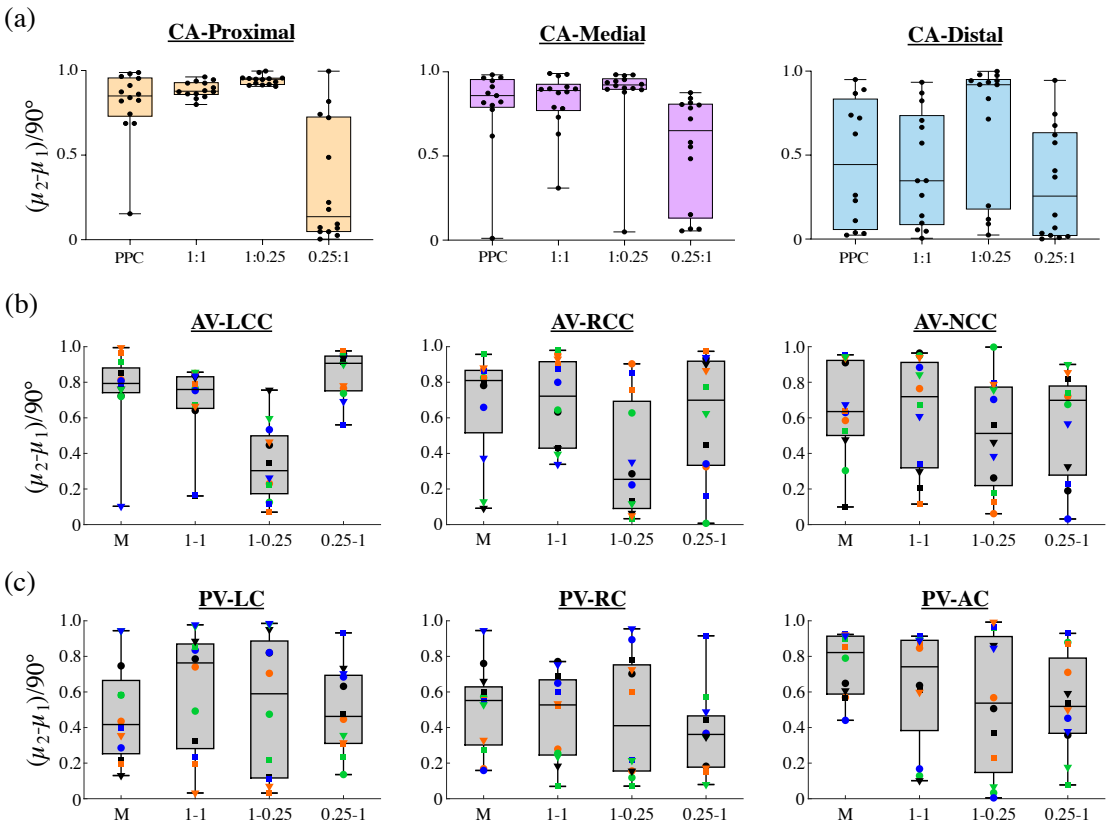

Figure 3-8. Normalized difference between the two collagen fiber families of: (a) coronary artery (CA) tissues, (b) AV tissues, and (c) PV tissues.

3.3 The Tricuspid Valve Leaflet Microstructures

3.3.1 Tissue Preparation and Optical Clearing

One porcine heart was retrieved from a local abattoir (Chickasha Meat Co., Chickasha, OK) and transported to our laboratory. The three TV leaflets were dissected, and one tissue strip was excised from the belly region of each leaflet (n=1 replicate per leaflet). The strips were first submerged in PBS for 3 hours to wash undesired pigments from the tissue (e.g., blood). Next, the specimens underwent a serial ethanol dehydration that included ethanol:PBS (v/v) solutions of 1:1, 3:1, 1:0, and 1:0 for 30 minutes per solution. The dehydrated specimens were optically cleared using 1:2 benzyl alcohol/benzyl benzoate (BABB). To avoid undesired damage to the tissue microstructure, the optical clearing was performed in a graded series of ethanol/BABB (v/v): 1:1, 1:1, 0:1, 0:1 for 30 minutes per solution. Immediately following the optical clearing, a small rectangular specimen was cut from each strip and submerged in a custom reservoir of 100% BABB on a glass slide. Prepared slides were promptly transported to the Samuel Roberts Noble Microscopy Laboratory for the imaging procedures outlined in Section 3.3.2.

3.3.2 Multiphoton Imaging and Analysis

The prepared slides were mounted to the confocal microscope (Leica SP8, Germany) equipped with a multiphoton pulsed laser (Chameleon TI:Sapphire Laser, Coherent Inc., USA) and a 20X glycerol objective. Each specimen was imaged twice to obtain z-stacks of the autofluorescent and SHG signals. The tissues were excited at 830 nm for both imaging processes, with the only difference being the hybrid detector (HyD) settings for capturing

emitted photons: 500-550 nm range for autofluorescence and 410-420 nm range for SHG.

The acquired z-stack images were imported into ImageJ for qualitative analyses. First, the autofluorescence and SHG signals were assigned to green and red look-up tables, respectively. These channels were then superimposed at random locations within the four leaflet layers reveal gross microstructural differences. We also constructed the cross-sectional view of the TVAL specimen to compare it with typical histological findings.

3.3.3 The Microstructure of the Four Tricuspid Valve Leaflet Layers

We observed unique microstructures for each leaflet with some similarities of their respective layers (**Figure 3-9**). For instance, the *atrialis* layer of each leaflet was filled with random networks of elastin fibers (green) and non-structured collagen fibers (red). The non-structured collagen fiber network of the atrialis was starkly different from the aligned, crimped collagen fibers found in the *fibrosa*. This is most obvious for the AL, where the atrialis layer appears to have a fluffy, cloud-like arrangement of collagen fibers and the fibrosa layer collagen fibers form a zebra-like pattern. Unfortunately, the confocal microscope settings employed herein were unable to capture the GAGs of the spongiosa layer, but we did notice the presence of elastin and collagen therein for the TVPL and SL, which was not present for the AL. The confocal imaging was able to capture the thinner and more elastin-rich ventricularis layer.

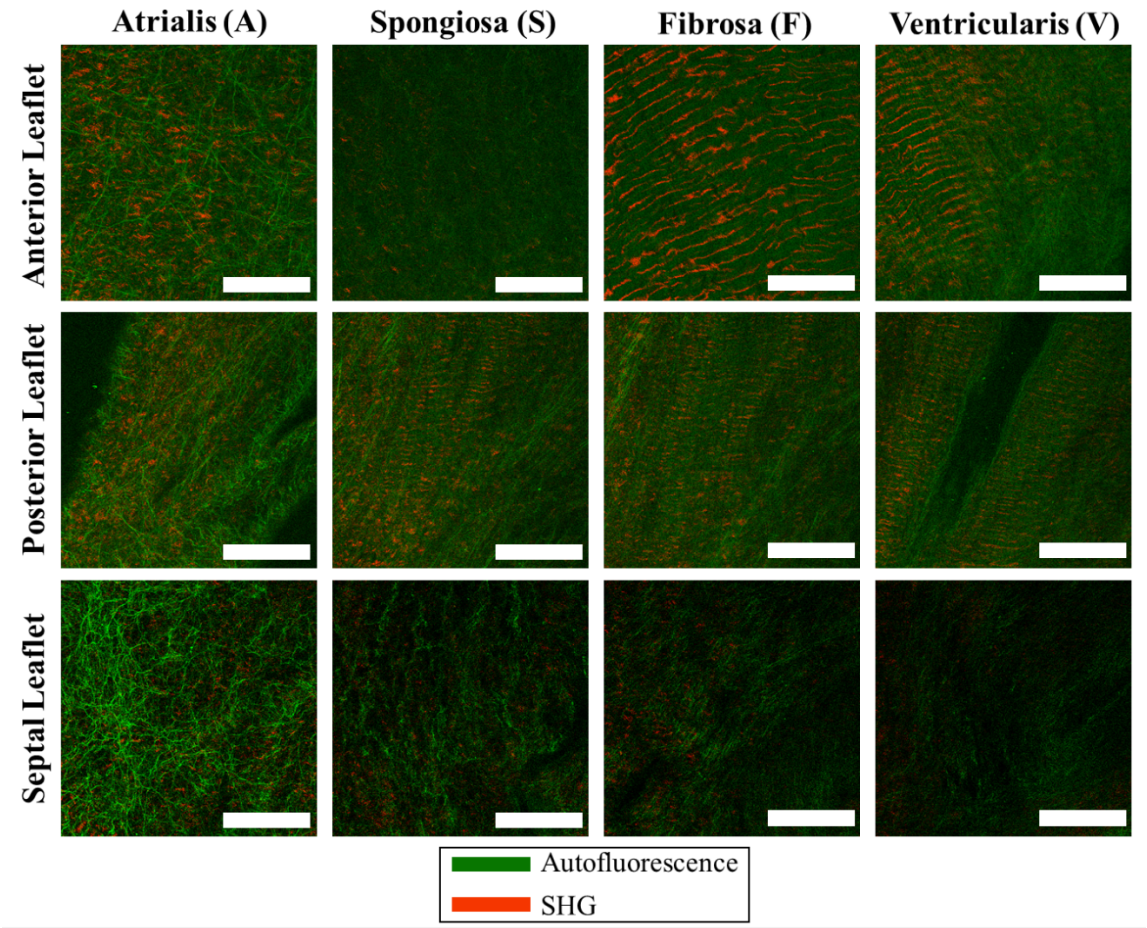

Figure 3-9. Superimposed confocal imaging (*green*) autofluorescence signal and (*red*) SHG signal at random locations within the four morphological layers of the three TV leaflets. Scale bars = 50 μm.

3.3.4 Leaflet Cross-Section Derived from Confocal Microscopy

The cross-section of the confocal *z*-stack for the TVAL is presented in **Figure 3-10**(a). This visualization reveals the expected four-layer microstructure of the TV leaflets (**Figure 2-1** (b)) and highlights the elastin and collagen fibers therein. One benefit of the confocal microscopy versus traditional histology is its ability to observe the structural arrangement of each layer. The cloud-like unstructured collagen fibers of the atrialis are clearly different from the highly

crimped collagen fibers of the fibrosa layer. Interestingly, we can observe a clear lack of signal within the spongiosa layer due to the inability of our confocal settings to capture the autofluorescence of the non-fibrous ground matrix.

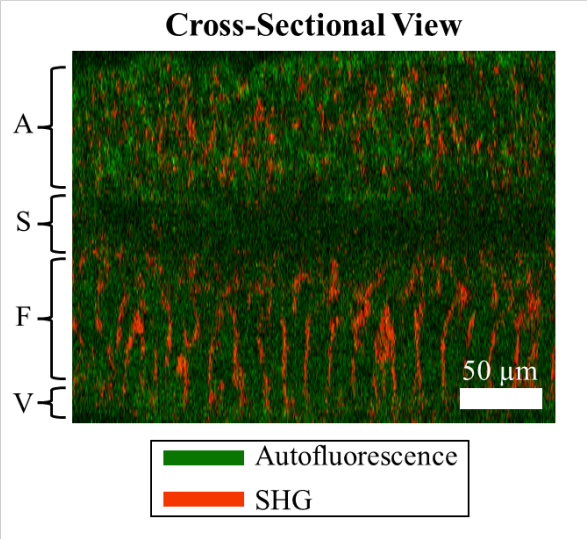

Figure 3-10: Confocal-derived cross-section of the TVAL specimen shown in **Figure 3-9**.

3.3.5 Discussion

In this sub-section, we have elucidated the TV leaflet microstructures using confocal microscopy. The key differences among the leaflets were primarily found in the spongiosa and fibrosa layers. For the spongiosa, the TVAL lacked strong signals of elastin or collagen fibers, whereas the TVPL and TVSL showed sparse fiber networks. It has been reported that the spongiosa is primarily non-fibrous extracellular matrix [60, 74, 107], but our results suggest that the TVPL and TVSL also contain a small degree of structural components. As for the fibrosa, the TVAL and TVPL showed the presence of crimped collagen fibers that were approximately aligned with the circumferential direction, while the TVSL was in an

unstructured arrangement similar to that of the atrialis layer.

The microstructural properties obtained from the confocal imaging can be related to the mesoscale CFA properties reported in Section 3.2. Our pSFDI results showed that the TVAL CFA did not change substantially under applied equibiaxial and non-equibiaxial tensions, which was in contrast to the more flexible CFA of the TVPL and TVSL. The confocal imaging results herein demonstrated that the fibrosa layer of the TVAL included highly crimped and aligned collagen fibers. This collagen fiber arrangement was also present to a lesser extent in the TVPL but was completely lacking in the TVSL. It is possible that this highly structured CFA of the TVAL limits its dynamic adaptations to the applied equibiaxial tension, resulting in the observations from pSFDI.

3.4 Conclusion

This chapter has provided a holistic multi-scale characterization of the TV leaflet mechanical and microstructural properties. First, we use our established *in vitro* biaxial testing procedure to characterize the *tissue-level* mechanical behaviors of the TV leaflets. Our results showed the leaflet behaviors are nonlinear, anisotropic, and depend on the effective specimen size with larger specimens being more *anisotropic*. In the second study, we used a pSFDI system integrated with our biaxial testing device to explore how the TV leaflet CFA changed under applied loading. All three TV leaflets exhibited two families of collagen fibers with one fiber family being approximately aligned with the *circumferential* tissue direction and the second fiber family aligned with the *radial* tissue direction. Interestingly, the CFA of the TVAL showed smaller changes under applied loading than the TVPL and TVSL. Finally, the third

study included two-photon microscopy of optically cleared TV leaflet specimens. The label-free microstructural characterization showed the expected four-layered TV leaflet microstructure. However, in contrast to traditional histology analyses, the SHG modality of the two-photon microscopy elucidated two types of collagen within the tissue microstructure. The fibrosa contained crimped, highly aligned collagen fibers that were starkly different from the amorphous cloud-like collagen fiber structure in the atrialis and ventricularis. Collectively, the experimental discoveries in this chapter provide the first holistic characterization of the TV leaflets across the *tissue-level*, the *mesoscale-level*, and the *microstructure-level*. This information is fundamental for future studies that seek to develop high-fidelity multi-scale simulation tools for the TV leaflets.

CHAPTER 4 Relating TV Leaflet Mechanics and Microstructure

This chapter provides experimental characterizations that seek to understand how the tissue microstructure contributes to the TV leaflet mechanical behaviors. Morphologically, the TV leaflets consist of four distinct layers: the *atrialis*, the *spongiosa*, the *fibrosa*, and the *ventricularis* (see **Figure 2-1**(c)). The first characterization presented herein (Section 4.4) demonstrates how the mechanical behaviors and CFA properties of composite A/S and composite F/V layers differ from the intact leaflet [25, 74]. We then further isolate the contributions of the elastin fibers (Section 4.5) and the collagen fibers (Section 4.6) using an iterative enzyme degradation procedure [131]. For brevity, we first present a general overview of the experimental methods (Sections 4.1-4.3) shared among all the mechanical characterizations before discussing the study-specific findings (Sections 4.4-4.6).

4.1 Tissue Acquisition and Preparation

Healthy porcine hearts (80-140 kg, 1-1.5 year old) were obtained from a USDA-approved slaughterhouse (Chickasha Meat Co., Chickasha, OK) and promptly cleaned of blood clots before being stored in the freezer at −14°C between one and twenty-one days. Freezer storage was used based on previous studies that showed that the TV leaflet mechanical response was not significantly affected by short-term freezer storage [38, 139]. After storage, hearts were thawed and the TVAL was excised and placed back in the freezer until the day of testing. On the day of the mechanical testing, the leaflets were thawed in PBS.

The leaflets were then sectioned into 12×12 mm and 10×10 mm specimens for the layer investigation and enzyme investigations, respectively. Average tissue thicknesses were obtained by taking three leaflet thickness measurements for each specimen using digital calipers (Westward 1AAU4 with 0.01 mm resolution, Grainger, Wake Forest, IL). In our earlier work we found a reasonable correspondence between this contact-based caliper approach and the non-contact thickness measurement methods [67]. After specimen preparation, biaxial mechanical tests were carried out, as discussed next in Section 4.2.

4.2 Biaxial Mechanical Testing

Biaxial mechanical tests were performed to characterize the mechanical responses TV leaflets. The tissues were mounted to a commercial biaxial testing system equipped with 1.5 N load cells (BioTester, CellScale, Canada) using five-tined BioRakes. For the layer investigation, we used an effective testing size of 10×10 mm, whereas our enzyme-focused studies used effective testing size of 7.5×7.5 mm. The tissues were mounted such that the *X*- and *Y*-directions were aligned with the circumferential and radial directions of the tissue, respectively. Four fiducial markers were then placed within the central third of the tissues for later DIC-based quantification of the tissue stretches (see Section 4.3) [12, 142]. The tissues were submerged in deionized (DI) water (layer investigation) or PBS (enzyme invesetigations) throughout testing.

Following our earlier studies [38, 67, 129], biaxial mechanical testing protocols consisted of a preconditioning step to restore the specimens to their approximate *in vivo* configurations, a displacement-controlled biaxial tensile testing step, and a stress relaxation testing step [48]. In

short, during preconditioning the tissues were loaded to a preload of 3% of the targeted membrane tension, followed by a 10-cycle preconditioning protocol up to the peak biaxial membrane tension T_{max}. We selected a peak membrane tension of 40 N/m for the leaflet investigation to emulate the leaflet physiological mechanical environment, and a peak membrane tension of 75 N/m for the enzyme-focused studies to also consider the potential hyper-physiolgoical environment of the constituent-deficient tissues [5, 52]. After preconditioning, the displacements associated with the maximum applied tension were determined for the three biaxial tension ratios: $T_{circ}:T_{rad}=1:1,\ 1:0.5,\ 0.5:1$, and the displacement-controlled biaxial tensile test protocol was carried out with 4 loading/unloading cycles. Throughout the testing, a CCD camera (The Imaging Source, DMK 41AU02) was used to capture 1280×960 images at a rate of 5 Hz, while load cell force readings were recorded at a frequency of 15 Hz.

For the enzyme-focused study, a biaxial stress relaxation protocol was performed in which the tissues were stretched to a configuration associated with the peak biaxial membrane tensions T_{max} and then the displacement held constant for 15 minutes.

4.3 Tissue Stress and Stretch Calculations

We followed our previously developed protocols [67] to calculate the tissue stretches and stresses, as outlined in Section 3.1.4. In short, the coordinates of the four fiducial markers were determined with the DIC module in the LabJoy software of the BioTester. A bilinear finite element with four nodes was used from the marker positions to calculate $\mathbf{F}$ based on the previous literature. Tissue stretches in the circumferential (*X*) and radial (*Y*) directions (i.e.,

λ_{circ} and λ_{rad}) were determined as the square root of the principal values of $\mathbf{C}$.

4.4 Characterization of the Tricuspid Valve Leaflet Composite

4.4.1 Layer Microdissection

The *intact* specimen was unmounted from the biaxial tester to obtain the composite A/S and F/V layers using our established layer microdissection procedure (Appendix C) [25, 74]. First, the intact specimen was pinned to a wax board using four T-pins. A scalpel was then gently rubbed along the tissue to cut through the A/S layers and form a corner. This corner was gradually pulled and separated from the composite F/V using fine-tipped tweezers. Throughout this peeling process, the scalpel was used to form the remaining three corners and cut any undesired interlayer connections. The resulting 4×4 mm A/S and F/V specimens were biaxially tested and imaged using the pSFDI device, as described in Sections 4.2 and 4.4.2.

4.4.2 Polarized Spatial Frequency Domain Imaging

Immediately following biaxial mechanical testing of the intact specimens and composite layers, the specimens were imaged using our integrated pSFDI device. More details are provided in Section 3.2, Appendix C, and our previous publications [25, 68]. The leaflets' CFA properties were determined at five configurations: the *mounted* configuration, the *PPC* configuration, and the peak configurations for each of the biaxial testing ratios (see Section 4.2). Similar to our mesoscale CFA investigation presented in Section 3.2, the pixel-wise fiber orientations were used to construct a probability density function of the complete tissue CFA, which was fit with a π-periodic bimodal von Mises distribution. The resulting model

parameters were analyzed to understand the relative motion and prevalence of the two fiber families.

4.4.3 Determination of Collagen Fiber Ensemble Properties

We were further interested in understanding how the functional mechanical behaviors of the CFA varied between the intact specimens and the composite layers. Towards this end, the stress-stretch data of the equibiaxial loading protocol were fit with a simplified structural model that considers the contributions of the non-fibrous ground matrix (η_m), the elastin fibers (η_e^{circ} and η_e^{rad}), and the collagen fibers (η_c) [41]

$$\begin{aligned}\mathbf{S} = {} & \eta_m\left(\mathbf{I} - C_{33}\mathbf{C}^{-1}\right) + \eta_e^{circ}\left(I_{4,circ} - 1\right)^{d_1}\mathbf{N}_{circ}\otimes\mathbf{N}_{circ} + \eta_e^{rad}\left(I_{4,rad} - 1\right)^{d_2}\mathbf{N}_{rad}\otimes\mathbf{N}_{rad} \\ & + \int_{-\frac{\pi}{2}}^{\frac{\pi}{2}} \Gamma\left(\theta;\mu_\Gamma,\sigma_\Gamma\right) S_{ens}(E_{ens})\mathbf{N}(\theta)\otimes\mathbf{N}(\theta)\,d\theta\end{aligned}, \quad (4.1)$$

where d_1 and d_2 control the non-linearity of the circumferential and radial elastin fiber mechanical behaviors and $\Gamma(\theta;\mu_\Gamma,\sigma_\Gamma)$ is the collagen fiber orientation distribution function represented by a normal distribution with mean μ_Γ and variation σ_Γ. The collagen fiber stress-strain behavior is described by an exponential relationship with parameters *A* and *B*:

$$S_{ens}(E_{ens}) = A\left(e^{BE_{ens}(\theta)} - 1\right). \quad (4.2)$$

This relationship can be used to predict the tissue's mechanical behaviors under various loading conditions; however, for the purpose of this study, we are interested in using it as a surrogate to understand how the behaviors of the collagen fiber ensembles differ among the tested specimens. We first generated the stress-strain response of the collagen fiber ensemble considering from 0 kPa to 250 kPa. We then determined the low-tensile and high-tensile

moduli as the slopes of the linear least squares fit to the data points with stresses <10 kPa and >150kPa, respectively. The fiber ensemble extensibility was taken to be the *x*-intercept of the high-tensile linear least squares regression.

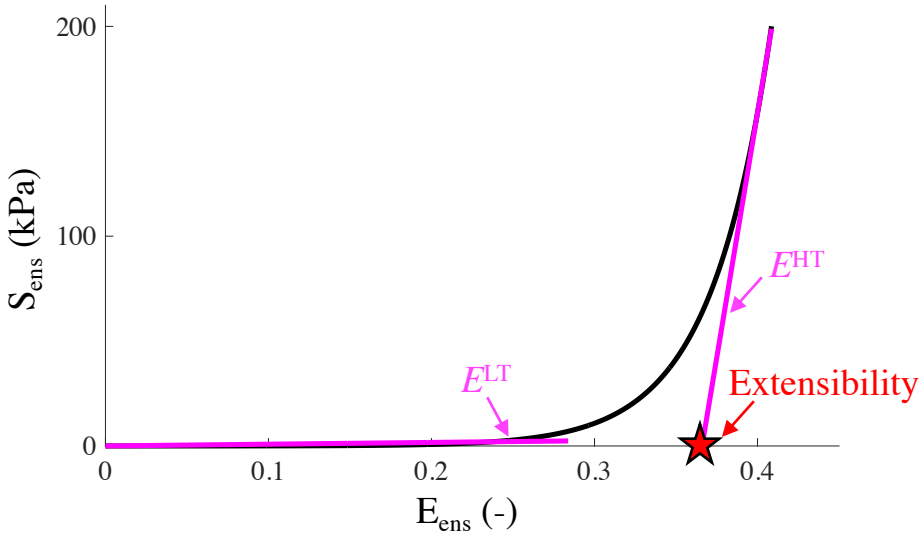

Figure 4-1. Representative collagen fiber ensemble stress-strain data demonstrating the low-tensile modulus E^{LT}, the high-tensile modulus E^{HT}, and the extensibility.

4.4.4 Statistical Analysis

Data are presented as mean ± SEM. Q-Q plots (not shown here) revealed that the data was not normally distributed in general. Thus, two-factor comparisons (layer vs. leaflet) were made using the non-parametric aligned rank transform [158]. Further contrast tests were performed using the aligned rank transform contrasts method [40]. Differences were considered as statistically significant when $p < 0.05$.

4.4.5 Mechanical Behaviors of the Tricuspid Valve Leaflet Layers

The mechanical behaviors of the intact specimens and the composite A/S and F/V layers are presented in **Figure 4-2**. Generally, we note that the A/S and F/V composite layers are stiffer than the intact specimens in both the circumferential and radial directions (p<0.001). These differences are associated with a significant reduction in the material anisotropy for the F/V composite layer (p=0.002) and the areal stretch for both composite layers (p<0.001) compared to the intact leaflet. When comparing the A/S and F/V composite layers, their circumferential stretches are similar (AL: 1.05±0.01 vs. 1.09±0.01, PL: 1.06±0.02 vs. 1.05±0.01, SL: 1.05±0.01 vs. 1.06±0.02), but the radial stretches of the F/V composite layer are smaller (AL: 1.07±0.01, PL: 1.08±0.01, SL: 1.09±0.02) than the A/S composite layer (AL: 1.15±0.03, PL: 1.12±0.02, SL: 1.08±0.01). This leads to less anisotropy and areal stretch for the F/V composite layer. Interestingly, the TVSL composite layers show similar stretches, *AI*s, and areal stretches.

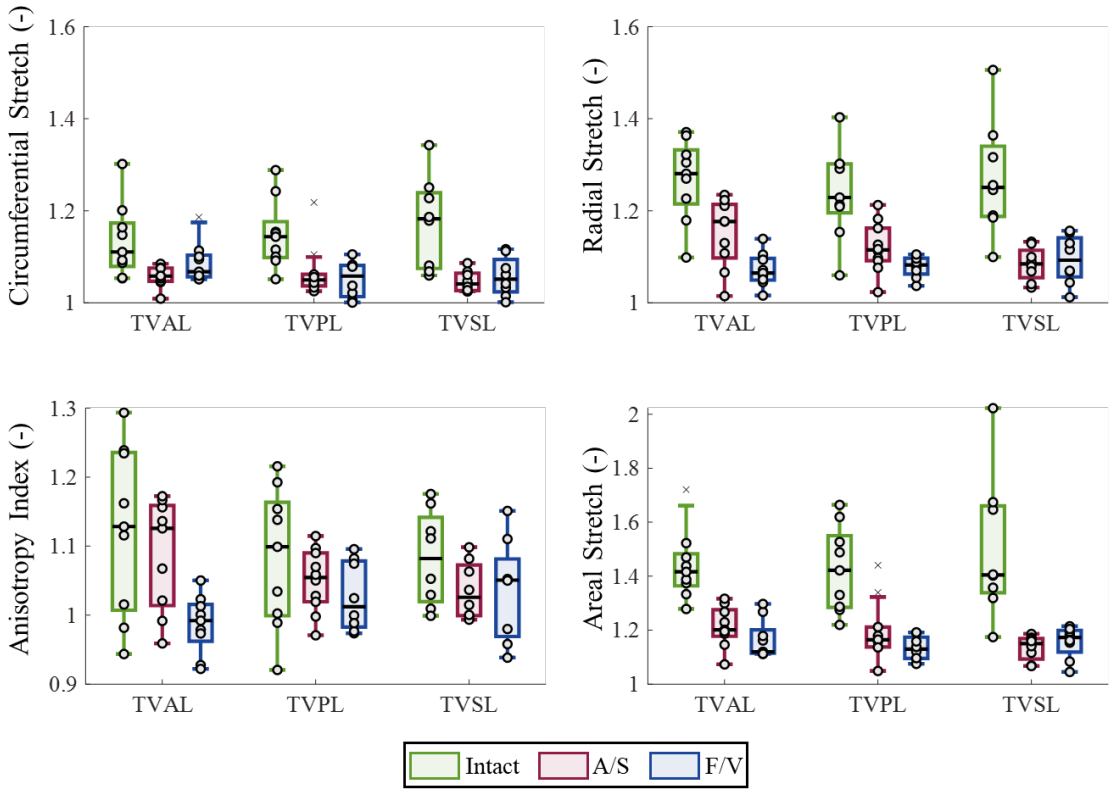

Figure 4-2. Experimentally determined leaflet stretches for the intact leaflets, composite A/S specimens, and composite F/V specimens.

4.4.6 Collagen Fiber Architectures of the Tricuspid Valve Leaflet Layers

Figure 4-3 and **Figure 4-4** present the bimodal CFA properties of the intact TV leaflets and their composite layers. The findings from these results are summarized into three key points. First, the A/S and F/V composite layers of the TVAL (A/S: 0.30±0.06, F/V: 0.37±0.05), TVPL (A/S: 0.40±0.07, F/V: 0.39±0.08), and TVSL (A/S: 0.35±0.06, F/V: 0.39±0.07) show less-defined fiber families when compared to the intact specimens (AL: 0.44±0.07, PL: 0.42±0.06, SL: 0.45±0.10) (**Figure 4-3**). Second, the circumferential fiber family was generally less dominant for the A/S layer (AL: 0.36±0.08, PL: 0.45±0.08, SL: 0.32±0.07) and more dominant

for the F/V layer (AL: 0.61±0.06, PL: 0.42±0.07, SL: 0.47±0.08) when compared to the intact specimens (AL: 0.40±0.06, PL: 0.45±0.07, SL: 0.38±0.06). Third, the load-dependent changes of the layers differed from their intact counterparts. Specifically, the separated composite layers of the TVAL showed larger changes in the normalized distance and *w* under non-equibiaxial loading, whereas the composite layers of the TVPL and TVSL were less responsive to the applied biaxial tensions (i.e., smaller changes in the derived parameters). The exact mechanisms of these differences are unclear and should be further explored using other techniques, such as instant polarized light microscopy [94].

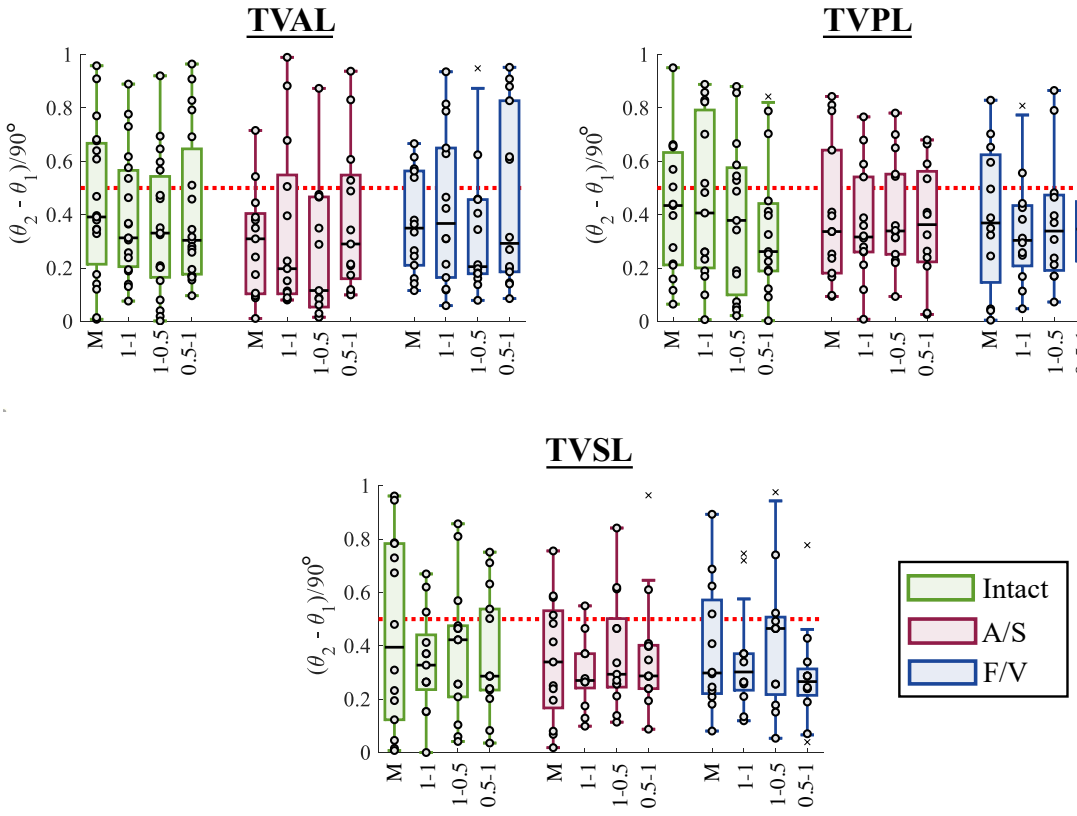

Figure 4-3. Computed normalized differences between the two fiber families for the intact, composite A/S, and composite F/V specimens of all three TV leaflets.

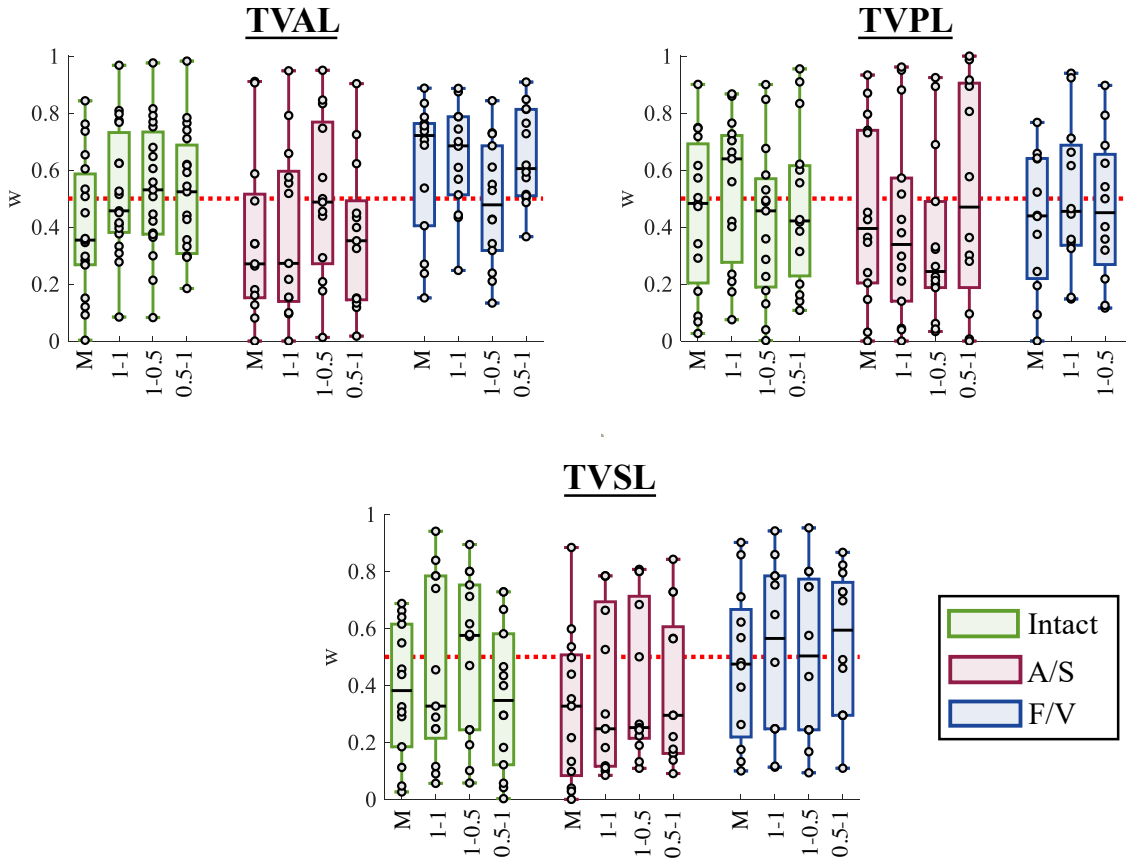

Figure 4-4. Determined bimodal von Mises weight of the circumferential fiber family for the intact, composite A/S, and composite F/V specimens of all three TV leaflets.

4.4.7 Alterations to the Functional Collagen Fiber Architecture Behaviors

The fiber ensemble properties determined via the simplified structural model (see Section 4.4.3) are shown in **Figure 4-5**. We found stiffer low-tensile behaviors for the A/S composite layer (AL: 435.8±158.0 kPa, PL: 611.3±404.2 kPa, SL: 793.8±355.8 kPa) and F/V composite layer (AL: 309.6±121.5 kPa, PL: 501.4±185.3 kPa, SL: 422.3±222.5 kPa) compared to the intact specimen (AL: 43.5±19.7 kPa, PL: 30.0±8.3 kPa, SL: 23.2±8.0 kPa) (**Figure 4-5**(a)). In

the high-tensile region, the F/V composite layer (AL: $1.265\times10^4\pm9.953\times10^2$ kPa, PL: $1.428\times10^4\pm8.405\times10^2$ kPa, SL: $1.495\times10^4\pm1.206\times10^3$ kPa) is notably stiffer than the intact specimen (AL: $1.090\times10^4\pm8.447\times10^2$ kPa, PL: $1.149\times10^4\pm5.928\times10^2$ kPa, SL: $1.051\times10^4\pm1.371\times10^3$ kPa) and A/S composite layer (AL: $1.096\times10^4\pm5.792\times10^2$ kPa, PL: $1.234\times10^4\pm8.539\times10^2$ kPa, SL: $1.276\times10^4\pm2.674\times10^2$ kPa), which have similar behaviors. These differences in the high-tensile response for the F/V composite layer result in a reduced extensibility (AL: 0.078±0.010, PL: 0.062±0.009, SL: 0.077±0.012) compared to the intact specimen (AL: 0.179±0.028, PL: 0.192±0.030, SL: 0.247±0.052). Interestingly, although the high-tensile moduli of the intact specimens and the A/S composite layers are similar, the A/S composite layer has a much smaller extensibility (AL: 0.074±0.008, PL: 0.086±0.017, SL: 0.059±0.008). These differences in the fiber ensemble responses mirror the differences in the tissue stretches presented in Section 4.4.4. This indicates a unique mechanics-microstructure relationship (Section 4.4.5).

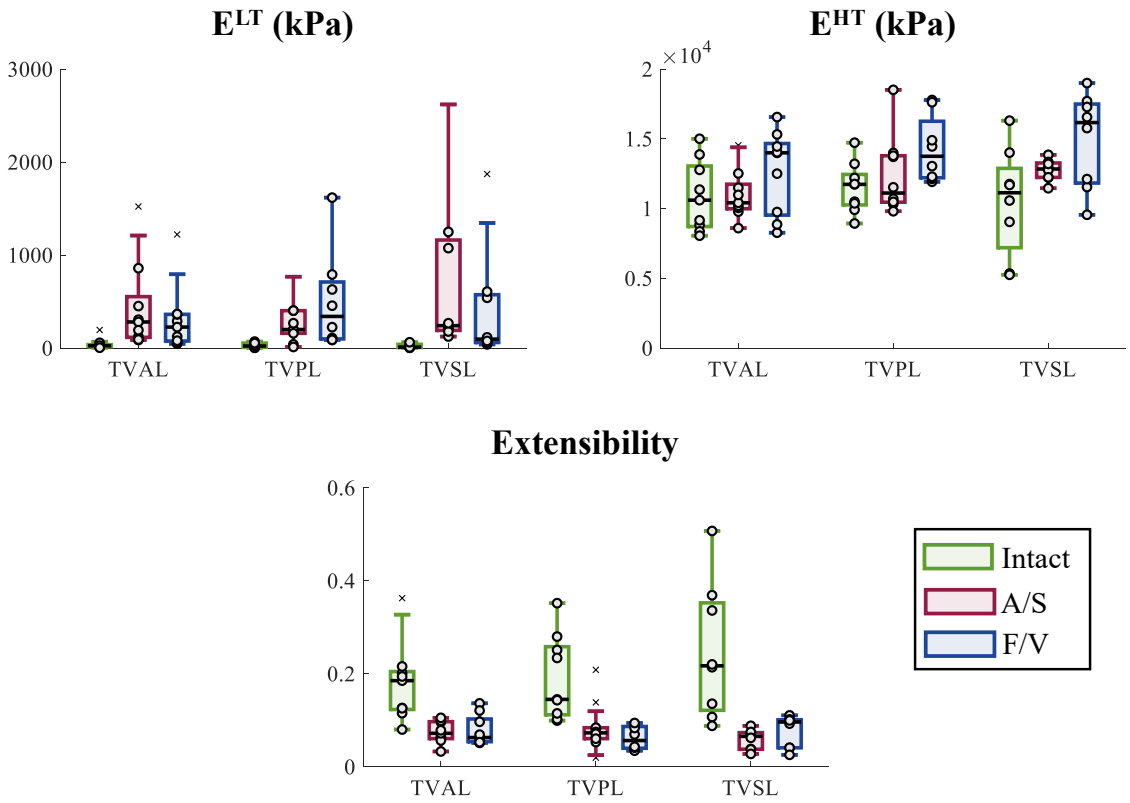

Figure 4-5. Summarized metrics derived from the collagn fiber ensemble stress-strain response for the intact, composite A/S, and composite F/V specimens of all TV leaflets.

4.4.8 Study Limitations

There are a few limitations in this study that can be addressed in future extensions. First, the intact specimens and the A/S and F/V composite layers were tested at different specimen sizes. We showed in Section 3.1 that the specimen size influences the observed mechanical behaviors, with the circumferential direction becoming stiffer and radial direction becoming more compliant as the specimen size decreases. This may confound the exact values of the stretches computed herein, but we noticed significantly smaller stretches for the composite layers that would not be entirely described by the specimen size effect. Future studies can

refine the layer microdissection technique to obtain larger composite layer specimens; however, this will be challenging due to the large contraction of the composite layers we [25, 74] and others [155, 156] have observed following microdissection. Second, the remarkably small size of the composite layers meant the fiducial markers were not adequately placed in the central one-third of the specimen to avoid boundary effects. Future studies can explore the use of speckle tracking or alternative pSFDI-based DIC [35] for determining the tissue strains. Third, we used deionized water throughout all of our experiments, since PBS oftentimes resulted in failed microdissections. A previous study has illustrated the importance of using PBS vs. DI water [138], and future studies can explore the influence of swelling on the composite leaflet layer properties.

4.5 Characterization of the Elastin-Deficient TV Leaflet

4.5.1 Enzymatic Treatment for Elastin Degradation

After biaxial testing of the control leaflets, the specimens were enzymatically treated to degrade a portion of the elastin constituent. The TV leaflets ($n = 18$) were treated in a solution of 60 Units/mL elastase (Worthington Biochemical Corp., #002292) and 0.1 mg/mL trypsin inhibitor (Worthington Biochemical Corp., #003587). The tissues were agitated in a thermal shaker (H5000-H MultiTherm Shaker, Benchmark Scientific, Sayreville, NJ) at 37 °C during the enzymatic treatment. After the tissues had been enzymatically treated for the optimal amount of time to remove >50% of the constituents, the specimens were rinsed thoroughly with PBS at 4 °C and prepared for further biaxial testing, as described in Section 4.2.

4.5.2 Histological Analysis of Constituent Removal

A routine histological analysis was carried out on tissue strips enzymatically digested for 15-minute intervals up to 2-hours to determine the optimal treatment time. Briefly, all tissue strips were fixed for 48 h in 10% neutral buffer formalin at room temperature. Each slice was then paraffinized and sliced at a thickness of 5-7 μm using a microtome (Microm HM 355S, Thermo Scientific). The sections were next deparaffinized, rehydrated, placed on a glass slide and stained to visualize the ECM constituents using Verhoeff elastic-Van Gieson staining (elastin in black).

After staining, a micrograph was taken for each tissue strip using an inverted bright-field microscope (Olympus CKX53) with a 10× objective lens and a 14-megapixel camera. The images were then analyzed using MATLAB (MathWorks, MA) to quantify the change in color intensity of the elastin constituents in the stained specimen. Briefly, a color thresholding was first applied to each micrograph to generate an image that contained only the constituent of interest (i.e., elastin in purple). Then, the constituent-isolated images were converted to grayscale, and the corresponding pixel intensity distribution was used to obtain the average pixel intensity. To finally determine the optimal enzyme treatment time in the intermediate study, the average intensity of the elastin constituent at each treatment timepoint was compared with the control tissue (untreated) as a percentage reduction in the average pixel intensity, representing the change in constituent composition. The histology-based quantification of the tissue composition has been shown to be comparable to other constituent quantification techniques such as hydroxyproline assays (a gold standard) in skin tissue [23].

4.5.3 Histological Results

When comparing the enzymatically treated tissue strips with the control, we observed a percent elastin reduction of almost 100% after a treatment of 45-min in the TVAL samples. We chose the time interval of 90-min to ensure that almost all the elastin has been degraded and to remain consistent with the collagenase-treated tissues (see Section 4.6.3). The percentage composition and percentage elastin reduction for the tissue strips at every 15-min increment can be found in **Table 4-1**, and a representative histological sample from five selected treatment times is shown in **Figure 4-6**. In the treated specimens, the elastin reduction reached ~100%, indicating that all of the elastin present in the tissue was removed by the elastase treatment.

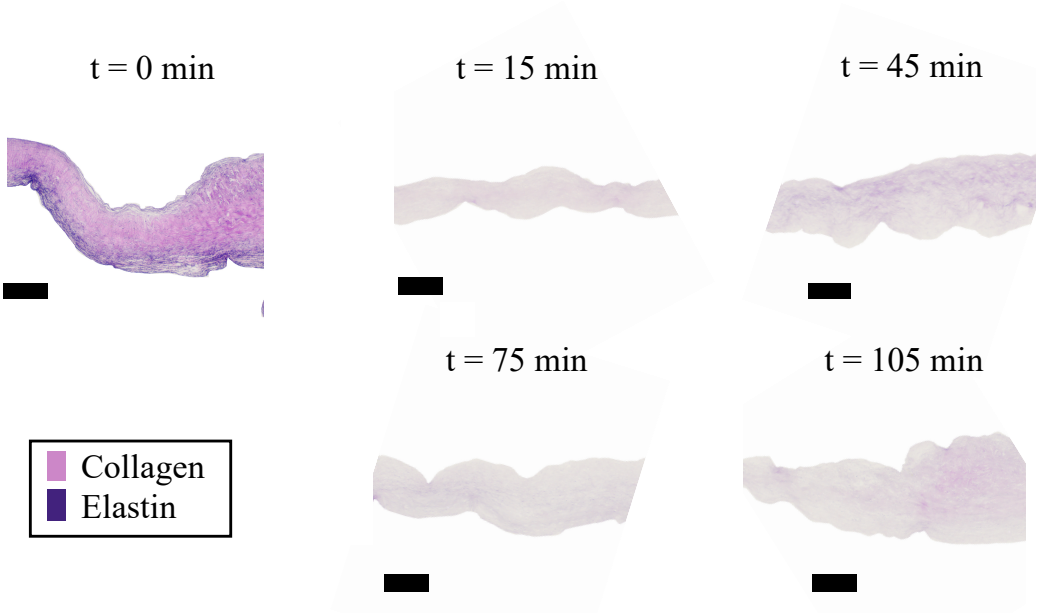

Figure 4-6. Verhoeff-Van Gieson-stained histological images demonstrating the progression of the elastin constituent removal at various enzyme treatment time point. Scale bar 200 μm. The quantified constituent degradation at each analyzed point in time is shown in **Table 4-1**.

Table 4-1. Quantified percentage reduction of elastin in the three control and elastase-treated tissues over a 120-minute treatment time.

Time (min)	Elastin Reduction (%)
0	—
15	+12.2%
30	14.1%
45	~100%
60	~100%
75	~100%
90	~100%
105	~100%
120	~100%

4.5.4 Refined Analysis of the Biaxial Mechanical Data

For quantitative and statistical analyses of the calculated tissue stretches computed in Section 4.3, we further decomposed the total tissue stretches into: (i) the PPC stretch λ^{0-1}, defined as the stretch after PPC (Ω_1) with respect to the undeformed configuration (prior to the preconditioning step) (Ω_0); (ii) the stretch λ^{0-2} between Ω_0 and the maximum tension Ω_2, where the identity is fulfilled: $\lambda^{0-1} = \lambda^{1-2}\lambda^{0-1}$. In addition, the *AI* was used to evaluate the material anisotropy of the tissue, i.e. $AI = \lambda_{\text{rad}}^{0-2}\lambda_{\text{circ}}^{0-2}$. From the biaxial stress-stretch data we have also determined the low-tension elastic modulus E^{LT}, the slope of the stress-stretch curve in the pre-transitional region, by using the first 10-20 data points of the membrane tension-stretch curve; and the high-tension elastic modulus E^{HT}, the slope in the post-transitional region, using the last five data points. In addition, the index of extensibility λ^*, which is the stretch at the intercept of the extended tangent line of the post-transitional region, was

calculated (**Figure 4-7**) [105, 114, 157].

On the other hand, from the biaxial stress relaxation data, the rate change in the membrane tension reduction was quantified using the initial and saturated slopes (dT^1/dt and dT^2/dt), obtained from a linear fit of the first 5-10 data points obtained and the last 250-300 data points (see **Figure 4-7** (e)). To quantitatively assess the shape of the stress-relaxation curve, we have also determined the intersection of the two extended straight lines, which correspond to the initial and the saturated slope and as an indicator for the transition time t_{trans} between the two stress relaxation regimes.

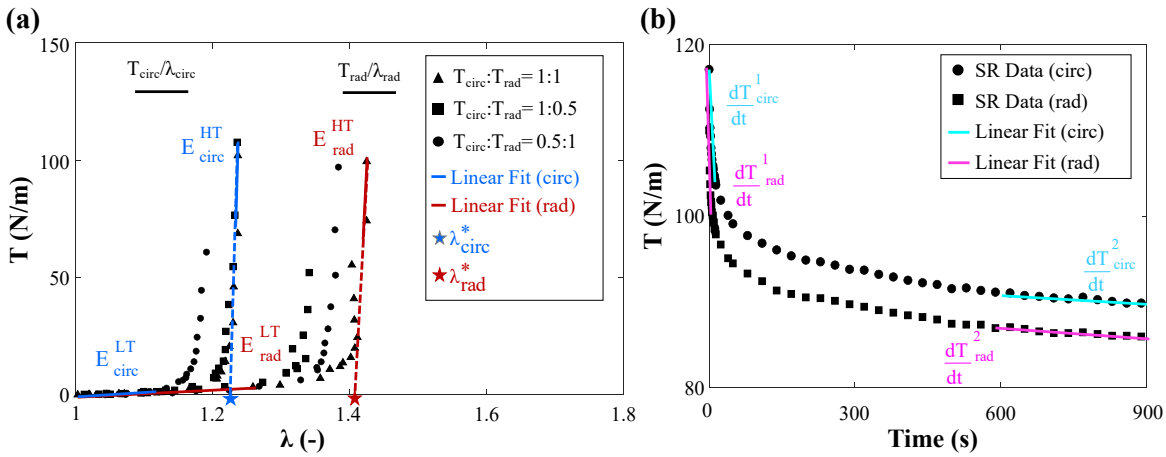

Figure 4-7. (a) Parameters quantified from biaxial tension tests, including the tissue stretch λ, the index of extensibility λ^*, the low-tension modulus E^{LT}, and the high-tension modulus E^{HT}. (b) Parameters quantified from biaxial stress relaxation data, which include the rate of change of membrane tension at the initial and the saturated relaxation regimes, i.e., dT^1/dt and dT^2/dt, respectively. Note: A smaller number of data points are visualized than the actual number of data points analyzed in order to improve visual clarity.

4.5.5 Statistical Analysis

All results are presented as the mean ± standard error of the mean (SEM). Outliers were determined as any values that were removed more than three scaled median absolute deviations from the median. Due to non-normally distributed data, we performed a two-tailed, paired-sample Wilcoxon signed-rank test to assess the significance of the experiments. Comparisons were made between the median values of the parameters of the control group and the treated group. The null hypothesis was that the differences between the control group and the treated group had a median value of zero, i.e., the elastin removal had no statistically significant influence on the tissue mechanics. The parameters compared include: the PPC stretch λ^{0-1}, the stretches λ^{1-2}, the peak stretch λ^{0-2}, the low-tension modulus E^{LT}, the high-tension modulus E^{HT}, the index of extensibility λ^{*}, and the initial and saturated slopes of stress relaxation $\dot{T}^{1}$ and $\dot{T}^{2}$, where the overlying dot signifies the time derivative, i.e., $\dot{T} = \mathrm{d}T / \mathrm{d}t$. For all analyses, differences were considered as statistically significant when $p < 0.05$.

4.5.6 Thickness Measurement

We found no statistically significant difference in the measured tissue thickness between the control and the elastase-treated tissues.

4.5.7 Biaxial Tensile Testing

The results of the biaxial mechanical tests of the control and elastin-deficient tissues are summarized in the **Figure 4-8** and **Figure 4-9**, respectively. The results of the biaxial tests suggest the following observations:

(i) The stretches of the specimens were significantly reduced by nearly 100% elastin

removal, especially in the radial direction.

(ii) Elastin deficiency causes significant increases in the low- and high-tension tissue stiffness.

(iii) Elastase-based enzymatic removal of elastin reduces the *AI*: $-20.3 \pm 4.8\%$ change ($p = 0.002$).

Particularly the TVAL specimens showed a significant decrease in radial tissue stretch: $-9.7 \pm 3.8\%$ for $\lambda_{\text{rad}}^{1-2}$ ($p = 0.008$). The tissue stretch values for the other two load ratios ($T_{\text{circ}} : T_{\text{rad}} = 0.5:1$ and $1:0.5$) showed a similar decreasing trend (**Figure 4-8**). From the derived biaxial test parameters (**Figure 4-9**), the moduli E^{LT} and E^{HT} showed previously insignificant changes for TVAL under equibiaxial loading before and after the removal of elastin. However, we observed significant decreases in the moduli under *non-equibiaxial* loading, which suggests that elastin removal induces changes in the directional coupling of the tissue (**Figure 4-9**). In addition, λ_{rad}^{*} decreased under equibiaxial loading: $-20.2 \pm 4.1\%$ ($p = 0.001$). Similar changes in the extensibility index were observed under non-equibiaxial loading scenarios (**Figure 4-9**).

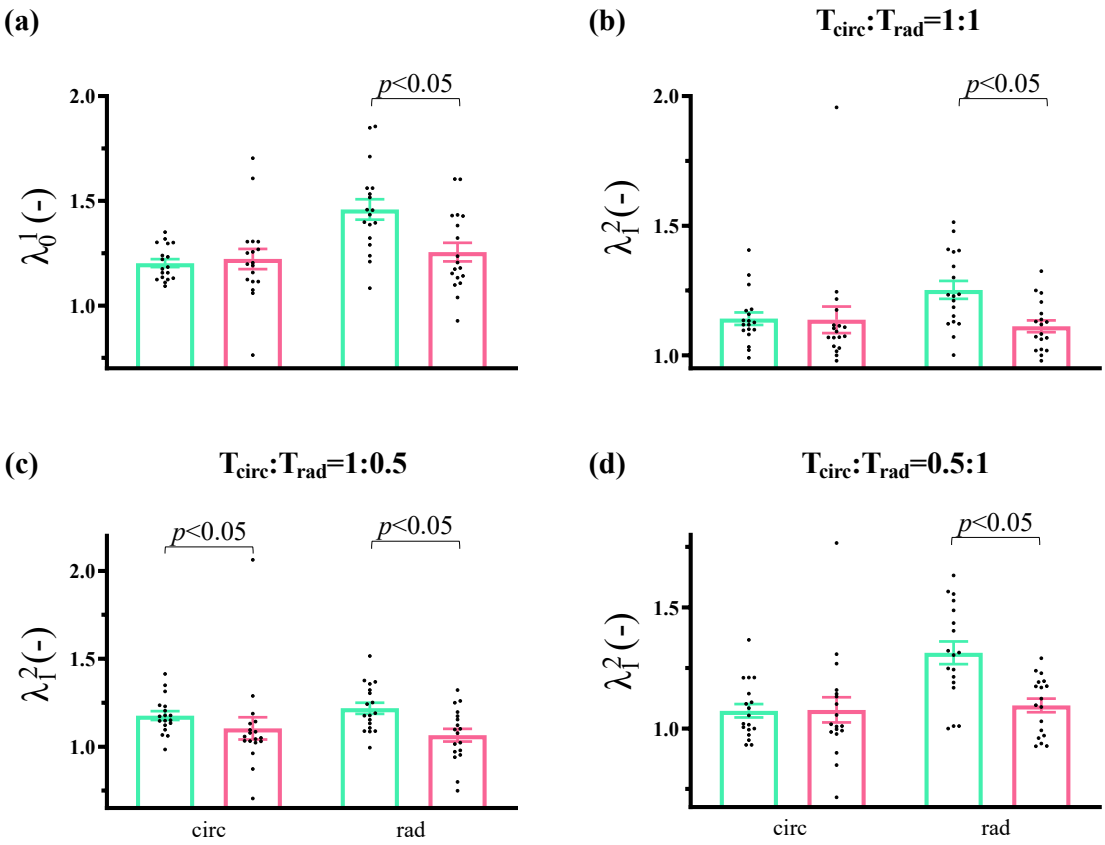

Figure 4-8. (a) Preconditioning stretch λ^{0-1} of the control (blue) and elastase-treated (pink) specimens. Stretch λ^{1-2} of the specimens at the three biaxial tensions protocols: (b) $T_{\text{circ}} : T_{\text{rad}} = 1:1$, (c) $T_{\text{circ}} : T_{\text{rad}} = 1:0.5$, and (d) $T_{\text{circ}} : T_{\text{rad}} = 0.5:1$ ($n = 18$).

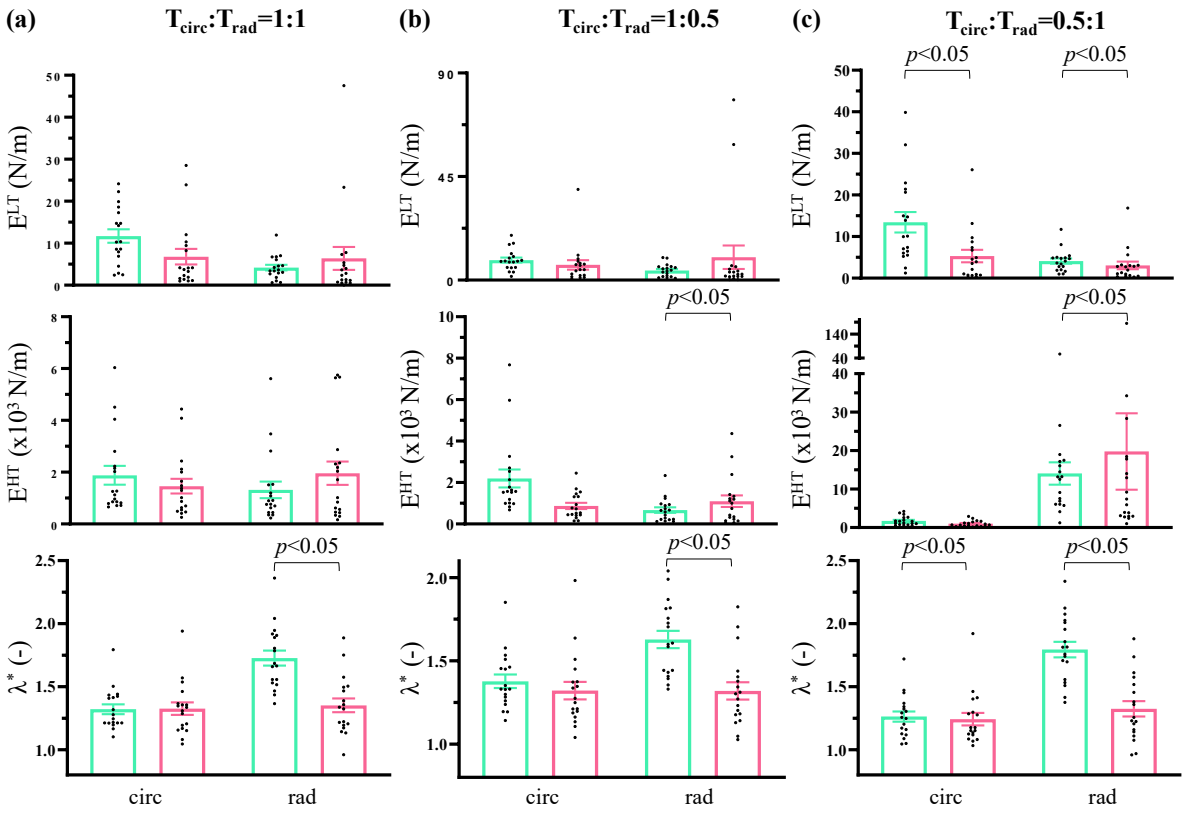

Figure 4-9. Comparison of (a) the low-tension modulus E^{LT}, (b) high-tension modulus E^{HT}, and (c) the index of extensibility λ^* between the control (blue) and elastase-treated (pink) specimens ($n = 18$) with three different biaxial tensions ($T_{\mathrm{circ}} : T_{\mathrm{rad}} = 1:1,\ 0.5:1,\ 1:0.5$).

4.5.8 Biaxial Stress Relaxation

Results from biaxial stress relaxation tests of the control and the elastin-deficient tissue are summarized in **Figure 4-10**. At each of the points in time analyzed, there was a statistically significant increase in the percentage reduction in stress reduction in both the circumferential and radial directions (**Figure 4-10**(a),(b)). For the initial and saturated slopes of the stress relaxation, we observed a significant decrease between the control and the treated tissues: $-69.3 \pm 3.9\%$ for $\dot{T}^2_{\mathrm{circ}}$ ($p < 0.001$), and $-64.1 \pm 6.5\%$ for $\dot{T}^2_{\mathrm{rad}}$ ($p < 0.001$). These results

indicated that the enzymatic removal of elastin resulted in a decrease in both the overall stress reduction and the initial and saturated slopes, suggesting the critical role of elastin in the viscoelastic behavior of TVAL tissues.

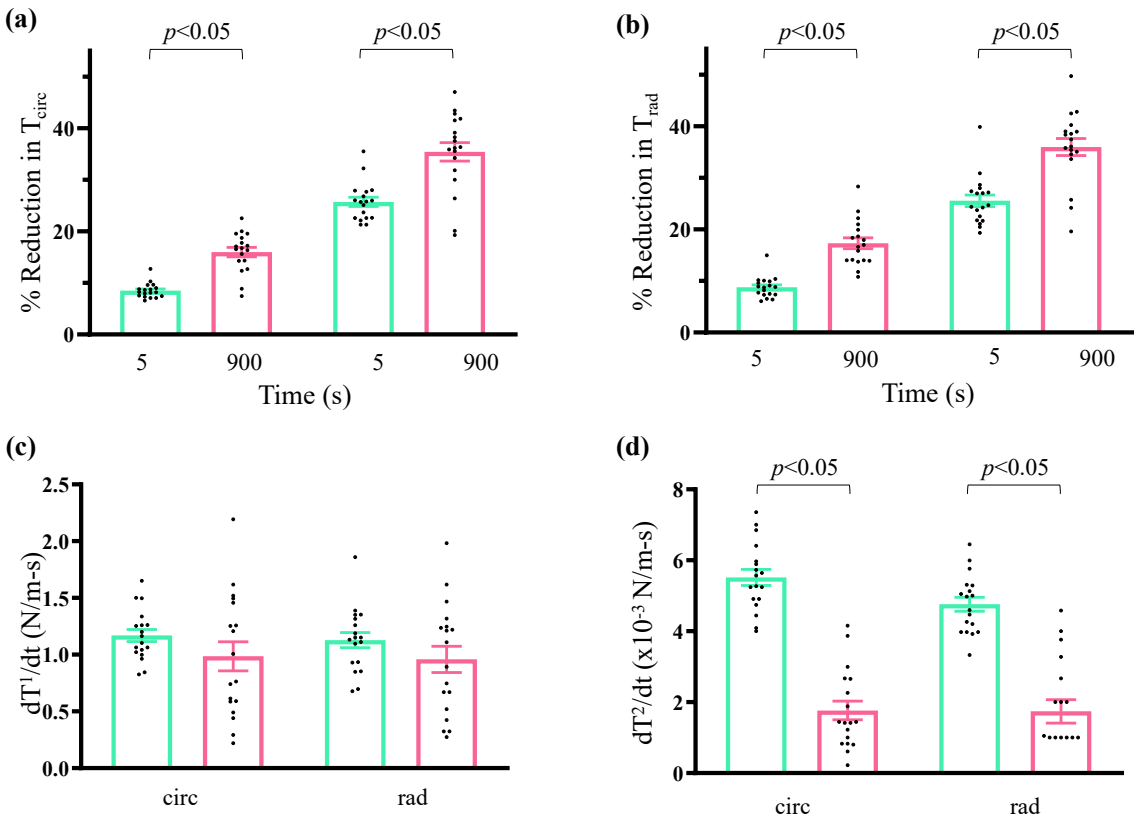

Figure 4-10. Stress relaxation results of the control (blue) and elastase-treated (pink) specimens ($n = 18$). Membrane tension reduction in (a) the circumferential direction, and (b) the radial direction, and (c) the initial and (d) the saturated slopes of the stress relaxation reduction behavior.

4.5.9 Study Limitations

There are several limitations in the present study. First, there is a possibility that the elastase

used in this study could damage the non-targeted ECM components (e.g., degrading elastin due to collagenase). After a quantitative examination of the stained tissue strips from the interim study, however, we observed, on average, minimal changes in the non-targeted ECM components after the enzyme treatment (<25%), also due to regionally different ECM densities. Second, while porcine hearts are very similar to human hearts in size, structure, and function hearts [49], the results of this study may not be immediately applicable to human applications. Third, due to staining quality difficulties from a commercial supplied, it was not possible to perform a histological analysis on every sample. Although we controlled many of the factors that would affect the histological results of our study (e.g., lighting, section thickness, staining, etc.). Because of the inherent nature of the experimental technique the potential for small variations in quality between the tissues still exists.

We also recognize the potential damage to constituents caused by freezer storage. However, we only observed constituent degradation and made comparisons between control (untreated) and enzyme-treated tissues, while no intermediate freezer storage was used during any of our mechanical experiments and enzyme treatments. Finally, other possible limitations include the use of two different effective testing regions, the use of a contact-based thickness measurement tool, a limited number of loading ratios, and a relatively short stress relaxation protocol. For more details on these limitations and how we have addressed them, see our previous works [38, 67, 129, 133].

4.6 Characterization of the Collagen-Deficient TV Tissue

4.6.1 Enzymatic Treatment for Collagen Degradation

After biaxial testing of the control leaflets, the specimens were enzymatically treated to degrade a portion of the collagen constituent. For this enzyme digestion study, TV tissues ($n = 16$) were treated with collagenase (Worthington Biochemical Corp., #LS004176) at a concentration of 96 Units/mL. The tissues were agitated in a thermal shaker (H5000-H MultiTherm Shaker, Benchmark Scientific, Sayreville, NJ) at 37 °C during the enzymatic treatment. After the tissues had been enzymatically treated for the optimal amount of time to remove >50% of the constituents, the specimens were rinsed thoroughly with PBS at 4 °C and prepared for further biaxial testing, as described in Section 4.2.

4.6.2 Histological Analysis of Constituent Removal

A routine histological analysis was carried out on tissue strips enzymatically digested for 15-min intervals up to 2-h to determine the optimal treatment time. Briefly, all tissue strips were fixed for 48-h in 10% neutral buffer formalin at room temperature. Each slice was then paraffinized and sliced at a thickness of 5-7 μm using a microtome (Microm HM 355S, Thermo Scientific). The sections were next deparaffinized, rehydrated, placed on a glass slide and stained to visualize the ECM constituents using Masson's trichrome staining (collagen in dark blue).

After staining, a micrograph was taken for each tissue strip using an inverted bright-field microscope (Olympus CKX53) with a $10\times$ objective lens and a 14-megapixel camera. The images were then analyzed using MATLAB (MathWorks, MA) to quantify the change in color intensity of collagen constituents in the stained specimen. Briefly, a color thresholding was

first applied to each micrograph to generate an image that contained only the constituent of interest (i.e., collagen in blue). Then, the constituent-isolated images were converted to grayscale, and the corresponding pixel intensity distribution was used to obtain the average pixel intensity. To finally determine the optimal enzyme treatment time in the intermediate study, the average intensity of the collagen constituent at each treatment timepoint was compared with the control tissue (untreated) as a percentage reduction in the average pixel intensity, representing the change in constituent composition. The histology-based quantification of the tissue composition has been shown to be comparable to other constituent quantification techniques such as hydroxyproline assays (a gold standard) in skin tissue [23].

4.6.3 Histology Assessment

When we compare each enzyme-treated tissue strip with the control, we observed a percentage collagen reduction of $20.0 \pm 6.3\%$ after a treatment of 15-min, $39.6 \pm 5.2\%$ after a treatment of 45-min, and $46.2 \pm 17.2\%$ after a treatment of 90-min. From this in-house study, we chose a treatment time of 90-min to keep the overall experimental procedure to a reasonable time (i.e., less than 8-h for each specimen test set). The compositions and reductions of collagen at each increment of 15-min are given in **Table 4-2**, and the representative histology is shown in **Figure 4-11**.

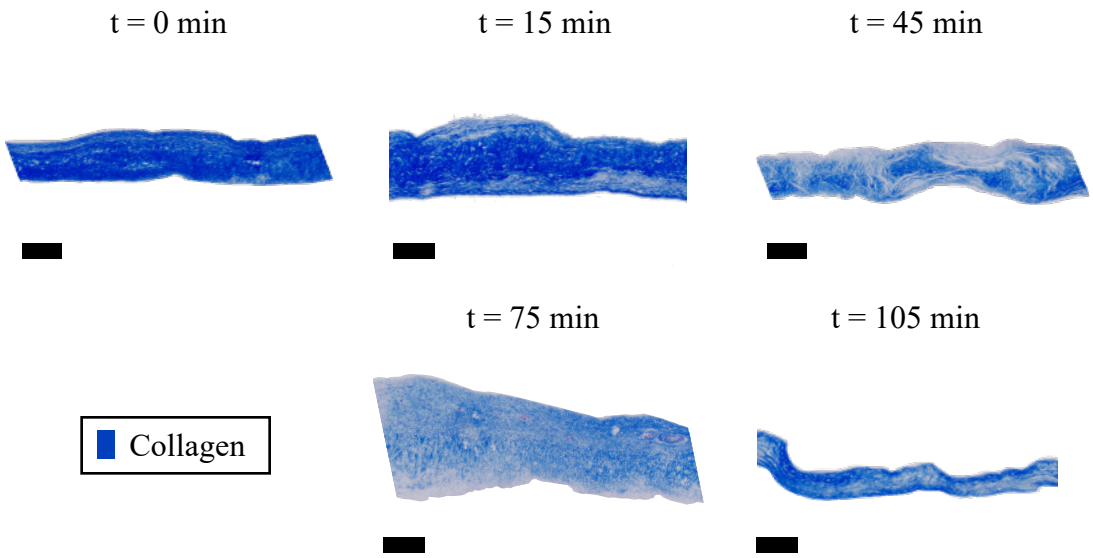

Figure 4-11. Masson's trichrome-stained histological images demonstrating the progression of the collagen constituent removal for one representative TVAL at various enzyme treatment time points. Scale bar 200 µm. The quantified constituent degradation at each analyzed point in time can be found in **Table 4-2**.

Table 4-2. Quantified percentage reduction of the collagen in three control and collagenase-treated TVAL tissues from the intermediate study over a 120 min treatment time. The results are shown as mean ± SEM.

Time (min)	% Collagen Removed
0	—
15	20.0 ± 6.3%
30	10.9 ± 6.7%
45	39.6 ± 5.2%
60	37.4 ± 5.1%
75	43.9 ± 13.9%
90	46.2 ± 17.2%
105	43.0 ± 13.3%
120	43.6 ± 13.2%

4.6.4 Refined Analysis of the Biaxial Mechanical Data

The acquired stress-stretch data from the biaxial tensile tests and stress-time data from the stress-relaxation studies were further analyzed as outlined in Section 4.5.4.

4.6.5 Statistical Analyses

The statistical analyses of the collagen enzyme-digestion investigation were identical to those performed for the elastin enzyme-digestion investigation (see Section 4.5.5).

4.6.6 Thickness Measurement

No statistically significant change in tissue thickness was found after collagen degradation.

4.6.7 Biaxial Tensile Testing

The results of the biaxial mechanical tests of the control and collagen-deficient specimens are summarized in the **Figure 4-12** and **Figure 4-13**. The biaxial test results suggest the following key observations:

(i) Collagen deficiency leads to a significant decrease in the stiffness at the high-tension range during non-equibiaxial loading.

(ii) Collagen deficiency significantly influences the anisotropic nature of the TVAL ($-16.9 \pm 7.4\%$ change in the AI, $p = 0.039$).

We did not observe any statistically significant differences in tissue stretches (λ^{1-2}) after collagen removal. However, we found statistically significant increases in the PPC stretch in the circumferential direction ($\lambda_{\text{circ}}^{0-1}$, $13.9 \pm 0.06\%$, $p = 0.006$). Similar trends were shown in the peak stretch (**Figure 4-12**). Taking into account the derived parameters under equibiaxial loading, E^{LT} decreased by $-36.0 \pm 14.4\%$ in the circumferential direction ($p = 0.008$) for the TVAL specimens, with similar significant changes observed during the non-equibaxial loading scenarios (**Figure 4-13**).

4.6.8 Biaxial Stress Relaxation

The results of the biaxial stress relaxation tests of the control and collagen-deficient tissues are summarized in **Figure 4-14**.

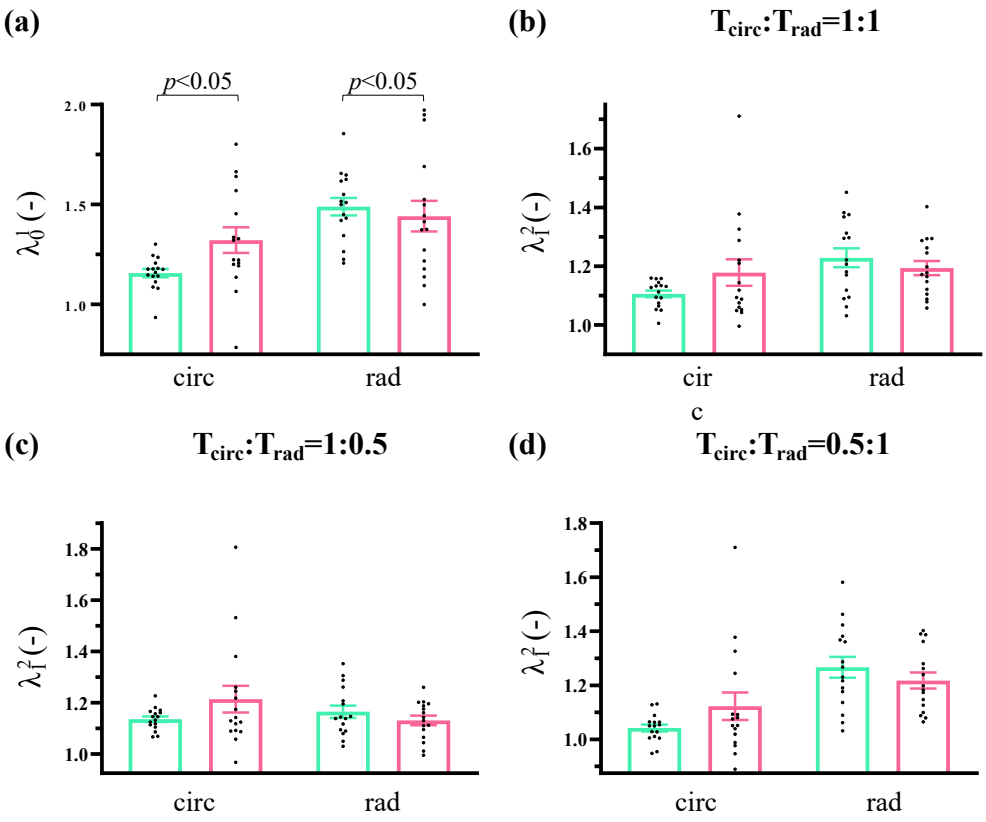

Figure 4-12. (a) Preconditioning stretches λ^{0-1} of the control and collagenase-treated tissues (n=16). Stretches λ^{1-2} at the three biaxial tensions protocols: (b) $T_{\text{circ}}:T_{\text{rad}}=1:1$, (c) $T_{\text{circ}}:T_{\text{rad}}=1:0.5$, and (d) $T_{\text{circ}}:T_{\text{rad}}=0.5:1$.

At each of the analyzed time points, there was a statistically significant increase in the total stress decay in both tissue directions (**Figure 4-14**(a),(b)). We found significant changes in both tissue directions: circumferential $-25.2\pm9.9\%$ ($p=0.011$), and radial $-24.3\pm9.9\%$ ($p=0.026$). These results indicated that collagen removal resulted in a decrease in both stress reduction and saturated slopes, indicating the unique effect of collagen deficiency on the viscoelastic behavior of the TVAL.

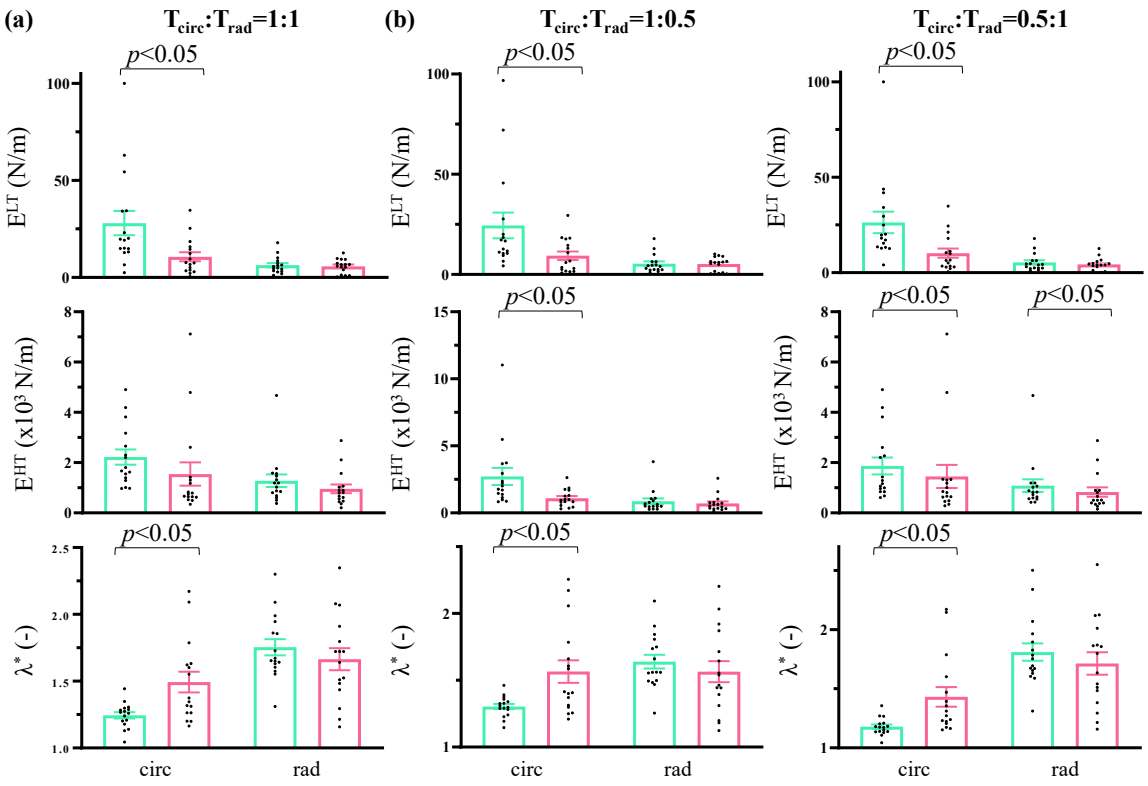

Figure 4-13. Comparisons of: (a) the low-tension modulus E^{LT}, (b) the high-tension modulus E^{HT}, and (c) the index of extensibility λ^* between the control (blue) and the collagenase-treated (pink) TVAL specimens ($n=16$) with three different biaxial tensions ($T_{\mathrm{circ}}:T_{\mathrm{rad}}=1:1,\ 0.5:1,\ 1:0.5$).

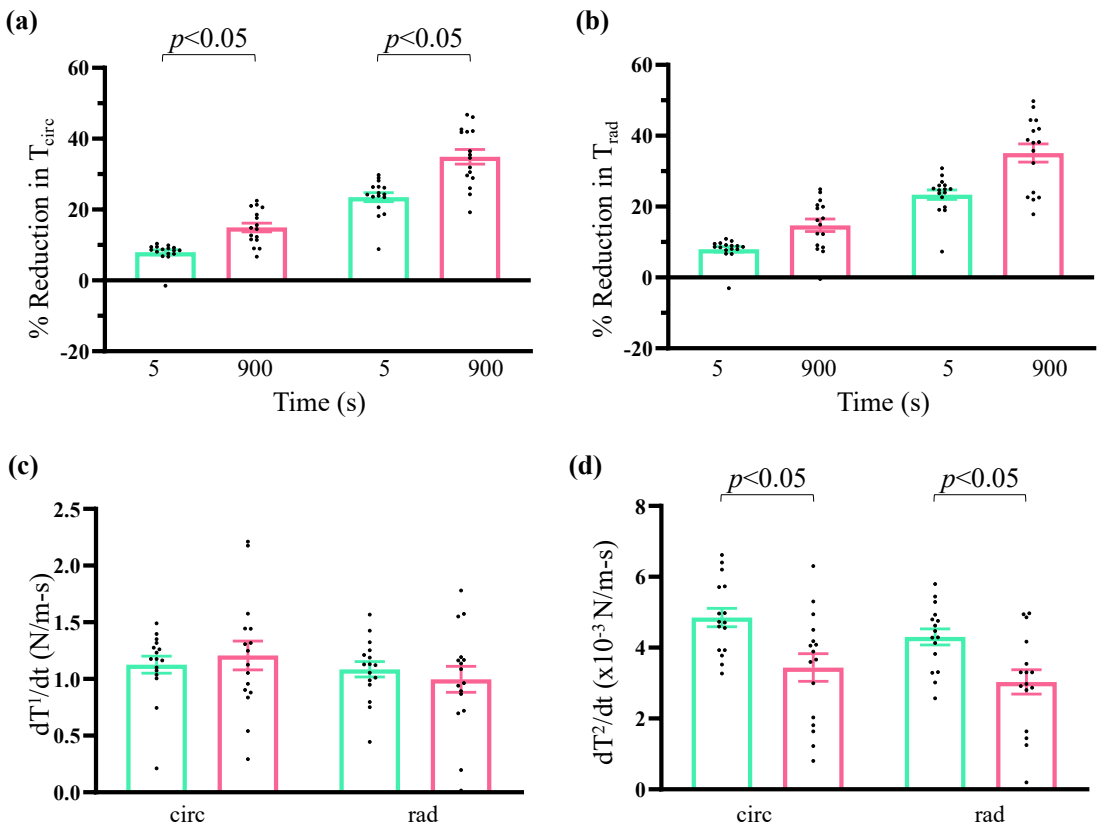

Figure 4-14. Stress relaxation results of the control (blue) and collagenase-treated (pink) TVAL specimens ($n = 16$). Membrane tension reduction in: (a) the circumferential direction, (b) the radial direction, and (c) the initial and (d) the saturated slopes of the stress relaxation reduction behavior.

4.6.9 Study Limitations

The study limitations for this collagen enzyme-digestion study are identical to those presented for the elastin enzyme-digestion study in Section 4.5.9.

4.7 Discussion

4.7.1 Findings from the Layer Investigation

In the investigation of the TV leaflet composite layers (Section 4.4), we provided the first mechanical and microstructural characterization of the A/S and F/V composite layers for all three TV leaflets. Our results showed that the composite layers were generally stiffer than the intact specimens for both tissue directions, which corresponded with lower *AI*s and areal stretches. Of the composite layers, the F/V composite layer exhibited stiffer material behaviors in the radial direction with similar behaviors for the circumferential direction. There were no significant differences between the three TV leaflets despite noticing unique leaflet-specific trends. We then used pSFDI to understand if the mechanical behavior differences could be attributed to the underlying CFA. Although no significant differences were observed between the specimens, we did notice some general trends that suggested variations in CFA properties may result in the different mechanical behaviors. For instance, the collagen fiber family of the F/V composite layers was generally more dominant (as evidenced by the larger w) than the intact and A/S composite layers. This would explain the reduced circumferential tissue stretches but does not directly explain the reduced radial tissue stretches. We therefore employed a simplified structural model to act as a surrogate for elucidating differences in the collagen fiber architectural behaviors (rather than structure). The derived low-tensile modulus was elevated for the both A/S and F/V composite layers, while the high-tensile modulus was only noticeably increased for the F/V composite layer. These differences in moduli were not significant, but collectively resulted in a significant reduction in the fiber extensibility for the A/S and F/V composite layers.

4.7.2 Findings from the Enzyme Degradation Investigations

The most important results of our enzyme-digesetion mechanical characterizations (Sections 4.5 and 4.6) are: (i) We have quantified the effects of enzyme removal on the biaxial tensile properties, whereby collagen-deficient tissue has a lower slope in high-tensile behavior and elastin-deficient tissue is stiffer. (ii) Collagen carries the main high-tension loading, while elastin supports the high- and low-stress valve function. This was demonstrated by the observed decrease in the high-tension elastic modulus for the collagen-removed tissues and the decrease in high- and low-tension moduli for the elastin-removed tissues. These results give an insight into the changes in tissue stress states *in vivo* in the case of microstructural changes caused by TV disease.

4.7.3 Comparison of Collagen-, Elastin-, and GAG-Deficient TV Leaflets

To create a more complete picture of the biomechanical contributions of each constituent to the leaflet biaxial tensile properties, we compared the results of our collagen- and enzyme-digestion studies with our previous glycosaminoglycan removal study [133]. A comparison of the percentage change in tissue stretch before and after enzymatic degradation shows that elastin-deficient tissues showed the greatest change after degradation for all three biaxial tension protocols—a 15.2% difference compared to the 7.0% and 3.3% differences for collagen- and GAG-deficient tissues, respectively (**Figure 4-15**). In addition, elastin removal showed a decrease in tissue extensibility, GAG deficiency showed increased tissue extensibility, and collagen removal showed inconsistent changes in tissue stretch after treatment. Our experimental results show the unique contributions of the microstructural constituents to the overall tensile behavior of the tissue. Although we could not directly

quantify the intricate mechanical coupling relationships between the microstructure components, our results suggested that the collagen fibers, GAGs, and the non-fibrous ECM provide the stiffness to counteract the extensibility of the elastin. Future studies would include the quantification of the coupled behavior of the ECM constituents, e.g., how the hydrophilic GAGs act as a lubricating mediator between the collagen and elastin components and enable a microstructural reorganization under loading.

Comparing the stress relaxation response of the tissues before and after enzymatic removal, both the collagen- and elastin-deficient tissues showed an increased total stress decay behavior, while the GAG-deficient leaflets demonstrated a decreased total stress decay behavior. In addition, in all three scenarios the removal of the ECM component resulted in statistically significant changes to the viscoelastic properties. Furthermore, the collagen- and elastin-deficiencies had a larger impact on the viscoelastic properties of the TV leaflets compared to the GAG deficiency. Visual comparisons of the changes in the PPC stretch, the stretch, and the stress relaxation are shown in **Figure 4-15** and **Figure 4-16**.

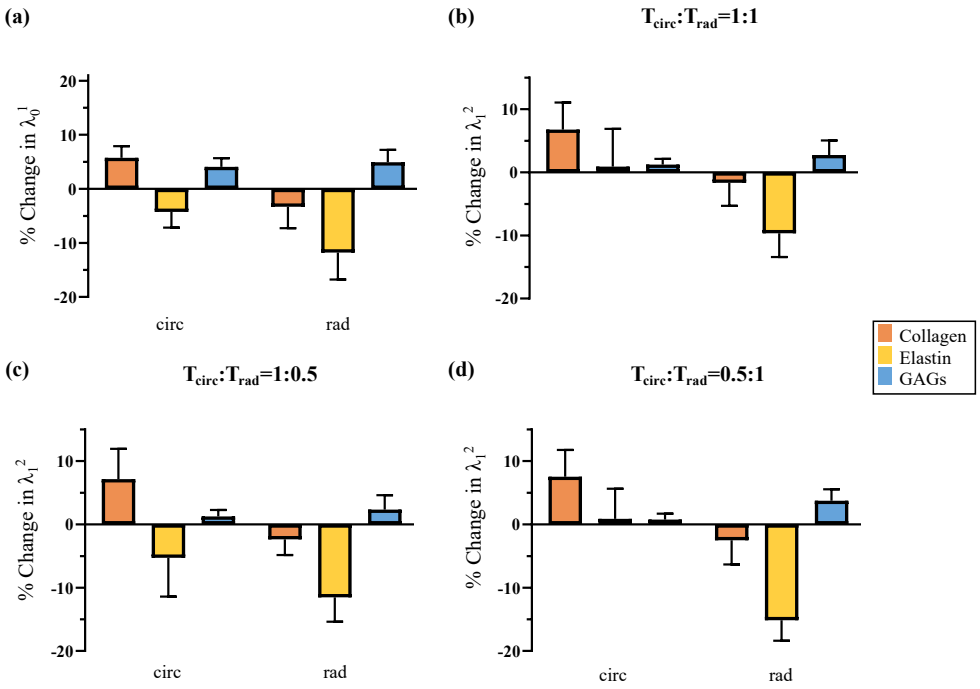

Figure 4-15. Comparisons of the percent change between tissues subjected to collagen-, elastin-, and GAG-removal: (a) the preconditioning stretch λ^{0-1} and (b) the stretch λ^{1-2} at the three biaxial tension protocols. GAG-removal results are from our previous study [133] , with sample sizes ($n = 6$).

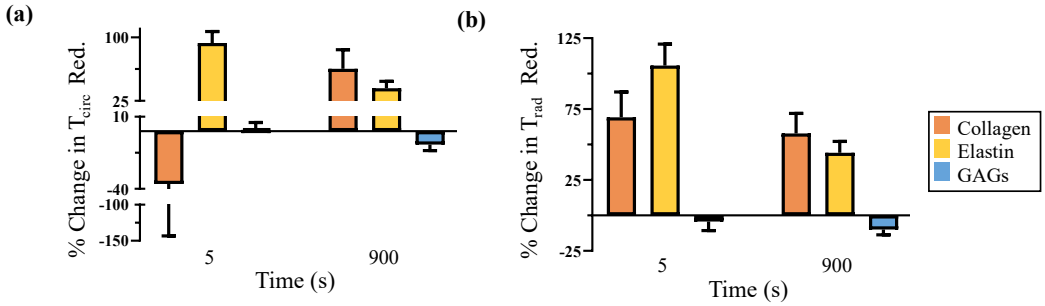

Figure 4-16. Comparison of the percent change between tissues subjected to collagen-, elastin-, and GAG-removal in the stress relaxation behaviors of TVAL specimens. GAG-removal results are from our previous study [133], with sample sizes ($n = 6$).

4.8 Conclusion

This chapter has expanded on the multi-scale experimental characterization of the TV leaflets from Chapter 3 to explore the mechanics-microstructure relationship. First, a layer microdissection protocol was used to separate TV leaflets into their composite A/S and F/V layers for mechanical and pSFDI characterizations. Our findings demonstrated that the isolated composite layers were stiffer than the intact specimens, had larger low-tensile and high-tensile moduli, and more organized CFAs. The second and third investigations used an established enzyme digestion protocol to elucidate how elastin fibers and collagen fibers contributed to TV leaflet mechanics. We found that the collagen fibers primarily contributed to the high-tensile mechanical behaviors, whereas the elastin fibers supported load throughout both the low- and high-tensile regimes. Collectively, the discoveries in this chapter further elucidate the mechanics-microstructure relationship for the TV leaflets. This will be valuable when developing high-fidelity constitutive models, such as those proposed for the mitral valve [161]

CHAPTER 5 Modeling the Tricuspid Valve Leaflet Mechanics

This chapter includes our efforts to improve material modeling for the TV leaflets. We first present our constant invariant-based study that uses carefully designed experiments to isolate the contributions of the I_1 and I_4 to the TV leaflet mechanical behaviors (Section 5.1) [85]. This information is leveraged to determine the most suitable SEDF for the TV leaflets based on its fitting capabilities and model parameter search space. Next, we share our comparison of an emerging data-driven (DD) modeling technique with well-established constitutive models for the heart valve leaflets (Section 5.2) [55]. Our developments herein expand upon the previous works of Amini *et al*. [71] and Laurence [81] and can be employed in future *in-silico* investigations.

5.1 Determination of a SEDF for the TV Leaflets

5.1.1 Study Objective

The objective of this study is to determine a suitable *phenomenological* SEDF form for the TV leaflets using the data from constant invariant-based mechanical characterizations. First, specimens for each TV leaflet ($n = 6$) are characterized using a series of constant I_1 and constant I_4 protocols, and the experimental data is transformed into the partial derivatives of the SEDF. Three candidate SEDF forms are fit to the experimental data using an in-house DEO algorithm to estimate the unknown model parameters. The results from these fits are analyzed to determine the most suitable SEDF form based on: (i) model fitting capability, (ii) model

parameter correlations, and (iii) the well-established *D*-optimality and condition optimality criteria. The advantages and disadvantages of coupling the invariant terms within the SEDF are also discussed to provide our recommendation of the most representative SEDF form for the TV leaflets.

5.1.2 Theoretical Preliminaries

The Strain Energy Density Function

Following prior biomechanical studies for cardiac heart valve leaflets [91, 126, 161], we assume that the TV leaflets are a transversely isotropic and nearly incompressible solid. This allows for defining a SEDF W as a function of the invariants and pseudo-invariants of $\mathbf{C}$:

$$W = W(I_1, I_2, I_3, I_4, I_5), \tag{5.1}$$

Note that the incompressibility condition, i.e., $I_3 = \det(\mathbf{C}) = 1$, reduces Eq. (5.1) to a function of two invariants I_1, I_2 and two pseudo invariants I_4, I_5. Ideally, one could determine an appropriate SEDF of this form for the TV leaflets; however, as shown in the subsequent section, it is infeasible to employ *planar* biaxial testing to fully determine a SEDF that contains invariants more than I_1 and I_4. Thus, we further assume that the SEDF is only a function of I_1 and I_4, resulting in $W = W(I_1, I_4)$. This agrees with the prior assumptions for the constitutive modeling of the heart valve leaflets [88, 106] and is necessary to establish the constant invariant-based mechanical characterization experiment, described next.

Mechanical Characterizations with Planar Biaxial Tensions

The deformation gradient of the TV leaflet undergoing homogeneous planar biaxial deformations is

$$\mathbf{F} = \begin{bmatrix} \lambda_1 & \kappa_1 & 0 \\ \kappa_2 & \lambda_2 & 0 \\ 0 & 0 & \lambda_3 \end{bmatrix}, \tag{5.2}$$

where λ_1 and λ_2 are the tissue stretches in the *X*- and *Y*-axes of the biaxial testing apparatus, respectively, κ_1 and κ_2 denote the in-plane shear deformations, and $\lambda_3 = (\lambda_1\lambda_2)^{-1}$ is the transmural tissue stretch determined as the consequence of enforcing the incompressibility condition. Given the above homogeneous $\mathbf{F}$, $\boldsymbol{\sigma}$ can be computed by

$$\boldsymbol{\sigma} = -p\mathbf{I} + 2W_{,1}\mathbf{B} + W_{,4}(\mathbf{FN}) \otimes (\mathbf{NF}^T). \tag{5.3}$$

Herein, $\mathbf{I}$ is the identity tensor, $\mathbf{N}$ is the fiber orientation at the undeformed (reference) configuration, $W_{,1} = \partial W / \partial I_1$ and $W_{,4} = \partial W / \partial I_4$ are the partial derivatives of W with respect to I_1 and I_4, respectively, and $p = 2W_{,1}(\lambda_1\lambda_2)^{-2}$ is the penalty parameter to enforce the incompressiblity condition as analytically derived from $\det(\mathbf{F}) = 1$.

Computation of the Normal Stress Components and Partial Derivatives of W

Traditionally, Eq. (5.3) is equipped with a pre-defined SEDF to compute tissue stresses for a given deformation. Unlike other soft biological tissues, there is currently no systematic study on the appropriate SEDF form for the TV leaflet tissue. Therefore, the objective of the present work is to use the experimentally measured tissue stretches and stresses to determine a suitable form of *W* for developing TV-specific constitutive models. Towards this end, we assume that

the preferred collagen fiber orientation of the tested leaflet, as denoted by $\mathbf{N}=[1,0,0]^T$, are aligned with the *X*-axis of the biaxial testing system, and that there are minimal shear deformations under the biaxial loading, i.e., $\kappa_1, \kappa_2 \approx 0$, resulting in the following two non-zero components of $\boldsymbol{\sigma}$ as derived from Eq. (5.3):

$$\begin{aligned} \sigma_{11} &= 2W_{,1}[\lambda_1^2 - (\lambda_1\lambda_2)^{-2}] + 2W_{,4}\lambda_1^2, \\ \sigma_{22} &= 2W_{,1}[\lambda_2^2 - (\lambda_1\lambda_2)^{-2}], \end{aligned} \tag{5.4}$$

which can be further rearranged to obtain the relationships for the partial derivatives of *W* [62], i.e.,

$$\begin{aligned} W_{,1} &= \frac{1}{2}\sigma_{22}\xi_2^{-1}, \\ W_{,4} &= \frac{1}{2\lambda_1^2}(\sigma_{11} - \sigma_{22}\xi_1\xi_2^{-1}). \end{aligned} \tag{5.5}$$

In the above relationships, $\xi_1 = \lambda_1^2 - (\lambda_1\lambda_2)^{-2}$ and $\xi_2 = \lambda_2^2 - (\lambda_1\lambda_2)^{-2}$ are the combinations of the tissue stretches. These relationships enable us to directly use the experimental data to compute the partial derivatives of *W* without needing a pre-defined SEDF form.

5.1.3 Preparation of the TV Leaflet Tissue Specimens

Six porcine hearts ($n = 6$) were obtained from a regional tissue vendor (Animal Technologies, Inc., Tyler, TX) overnight on dry ice. On the day of experiments, the hearts were thawed and dissected to acquire the three TV leaflets, which were then frozen for brief storage prior to the mechanical testing within 24 hours [38].

An hour prior to the biaxial mechanical testing, the TV leaflets were thawed in an in-house room-temperature PBS solution. The entire leaflet was promptly mounted to a commercial biaxial testing system—BioTester (CellScale, Canada) —with an effective specimen size of 13×13 mm to first characterize the underlying CFA of the leaflet via an in-house pSFDI device [68] (**Figure 5-1**(a)). In brief, the pSFDI results provided the pixel-wise collagen fiber orientation for the effective region of the TV leaflet, which was transformed into a histogram to determine the probability density distribution of the collagen fiber orientation. Since these histograms did not qualitatively follow a normal distribution, the median fiber orientation was used to represent the specimen's preferred fiber orientation (e.g., $\theta_{\text{fiber}} \approx -16°$ for a representative TV leaflet specimen in **Figure 5-1**(a)).

Once the preferred collagen fiber orientation was determined, the leaflet was unmounted from the biaxial testing device, and an 8×8 mm specimen was excised from the leaflet such that the *X'*-axis of the specimen approximately aligned with the quantified median collagen fiber orientation (**Figure 5-1**(b)). Finally, the specimen was re-mounted to the biaxial testing system using a series of five-tined BioRakes, resulting in a 6×6 mm effective testing size for the subsequent biaxial mechanical characterizations.

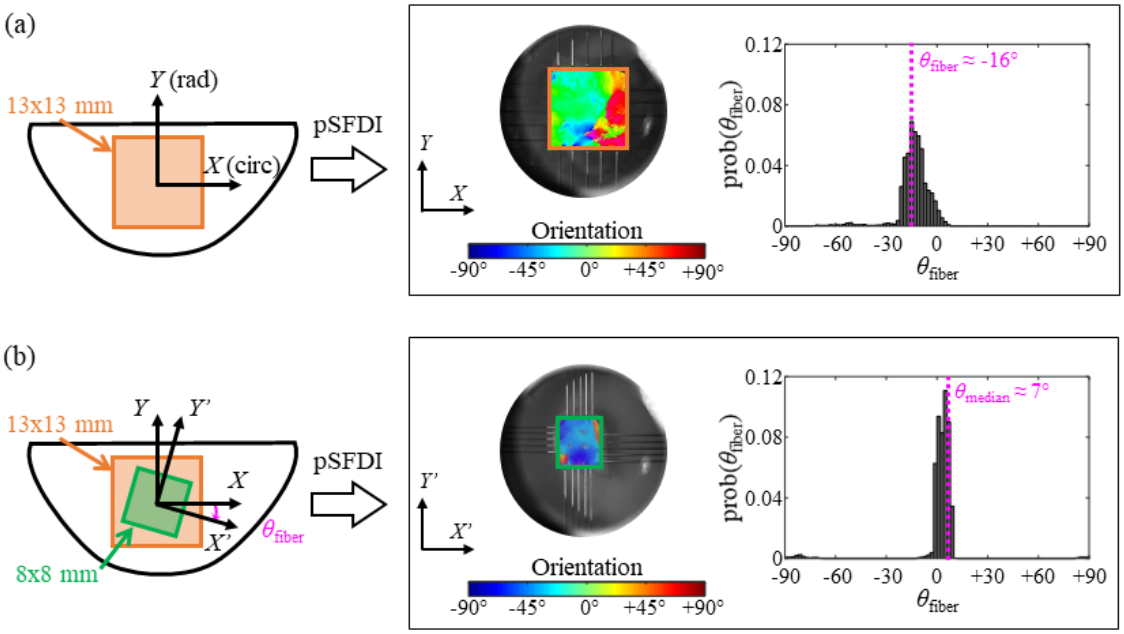

Figure 5-1. Overview of tissue preparation and pSFDI-based collagen fiber architectural quantification. (a) The TV leaflet mounted to the CellScale BioTester to determine the initial fiber orientation from the pSFDI-derived collagen fiber orientation probability density function. (b) An 8×8 specimen oriented with the median fiber angle θ_{fiber} excised from the TV leaflet and mounted to the BioTester for verifying the fiber orientation.

5.1.4 Constant Invariant-Based Biaxial Mechanical Characterizations

The mounted specimens first underwent eight cycles of force-controlled equibiaxial preconditioning to the approximate *in vivo* forces estimated using the Laplace's law in conjunction with the specimen's thickness and effective edge length (6 mm) [67]. The resulting PPC configuration was considered as the reference configuration in the following discussions [29]. Then, a series of constant invariant biaxial tension protocols were performed to experimentally determine the relationships between the partial derivatives of W and the

invariants I_1 and I_4 [62]. Since the specimen was prepared in the way that the preferred collagen fiber direction is aligned with the BioTester's *X*-axis (see **Figure 5-1**(b)), the constant I_4 protocols were achieved by maintaining a constant value of λ_1 throughout the loading. In this work, we considered four constant I_4 protocols in which λ_1 was maintained at fractional values of the peak equibiaxial stretch λ_1^{peak} as determined from the preconditioning step, i.e., $25\%, 50\%, 75\%$, and 100% of λ_1^{peak}, while λ_2 was repeatedly loaded/unloaded to its respective peak equibiaxial stretch λ_2^{peak}. On the other hand, the constant I_1 protocols required more sophisticated loading paths due to the complex nature of $I_1 = \lambda_1^2 + \lambda_2^2 + (\lambda_1\lambda_2)^{-2}$. For simplicity, we selected four target values of I_1 (i.e., $I_1 = 3.1, 3.2, 3.3, 3.4$) and used the following relationship to calculate the λ_2 values required to maintain a constant value of I_1 for a series of linearly increasing/decreasing λ_1:

$$\lambda_2^2 = \frac{1}{2}(I_1 - \lambda_1^2) \pm \sqrt{(I_1 - \lambda_1^2)\lambda_1^{-2}}. \tag{5.6}$$

Each of the constant I_1 protocols and constant I_4 protocols was repeated five times at 1.4%/s. A 3-minute rest period between any two protocols to minimize the potential viscoelastic effects. The linear actuator displacements and load cell force values were continuously recorded at 10 Hz throughout the experiment.

The experimental data from the last cycle were used to compute the tissue stretches and the normal components of the first Piola-Kirchhoff stresses using: $\lambda_i = (L_i + d_i)/L_i$ and $[\mathbf{P}]_{ii} = f_i/(L_i t)$, respectively. Here, subscript i indicates the direction of interest (1:

circumferential or *X'*-direction; 2: radial or *Y'*-direction), L_i are the specimen edge lengths following preconditioning, d_i are the actuator displacements, f_i are the load cell force readings, t is the specimen thickness following PPC, i.e., $t = t_0 / (\lambda_1^{PC} \lambda_2^{PC})$, and t_0 is the specimen thickness at the undeformed (reference) configuration as measured via a non-contact laser displacement sensor (Keyence IL-030, Itaska, IL). The computed $\boldsymbol{\sigma}$ obtained from $\mathbf{P}$ and the tissue stretches were used to calculate the partial derivatives of *W* in Eq. (5.5).

5.1.5 A Smooth Surrogate Function for Data Fitting that Reduces Noise Effects

The computed values of $W_{,1}$ and $W_{,4}$ were plotted against the experimental I_1 protocols and I_4 for the constant I_4 and constant I_1 protocols, respectively (black dots in **Figure 5-2**(a)-(c)). These four plots of the experimental raw data revealed noticeable noise for some specimens and loading protocols, which may negatively impact the quality of the fitting results. Hence, quantile regression was used to fit a third-order polynomial function (the initial surrogate function) to the 50% quantile of the experimental data for each constant invariant protocol. Each fit was qualitatively assessed to observe any potential problems associated with the surrogate function fits, such as undesired oscillations in nearly linearly trends, and to determine if an alternative polynomial order is required. The final surrogate functions were re-sampled at the experimental values of I_1 or I_4 to construct the smooth curves that represent the experimental data (red solid lines in **Figure 5-2**(a)-(c)) while reducing the noise effects.

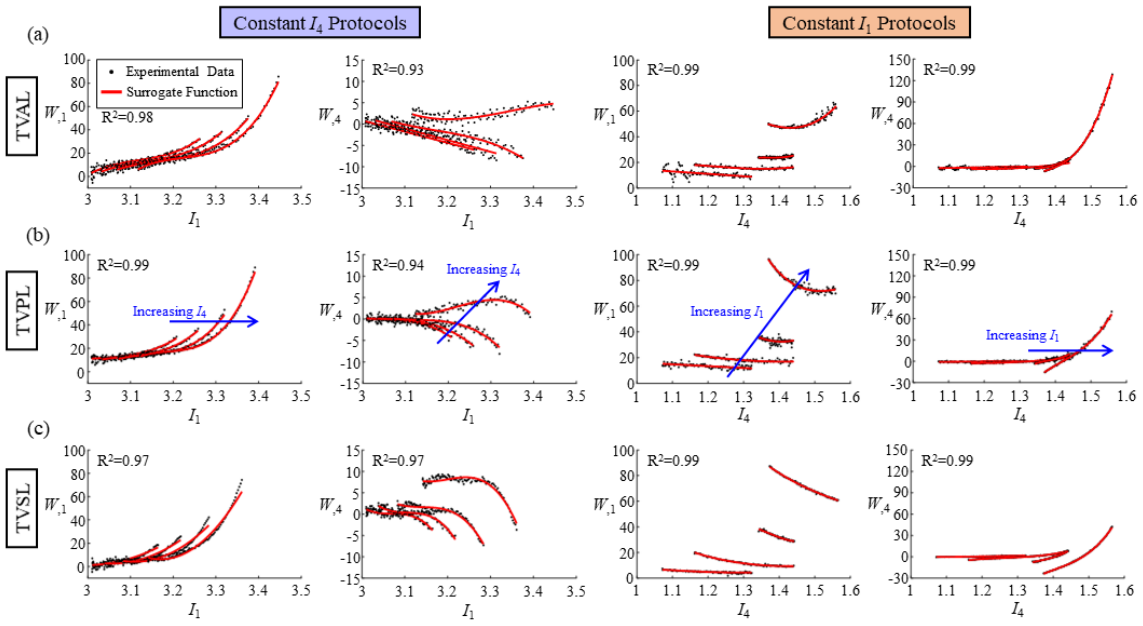

Figure 5-2. Results of constant invariant mechanical characterizations for the representative (a) AL, (b) PL, and (c) TVSL specimens ($W_{,1}$ and $W_{,4}$ are in kPa).

5.1.6 Study Scenarios

We considered two study scenarios to investigate two separate sets of SEDF forms. The first study scenario sought to examine the predictivity for a series of candidate SEDF forms, whereas Study Scenario #2 aimed to evaluate the coupling between the I_1 and the I_4 terms in the SEDF forms.

Study Scenario #1: Evaluating the Candidate SEDF Forms

We considered a series of SEDF forms with their respective model parameters determined by nonlinear least-squares fit to the experimental data from the constant invariant protocols. The first SEDF form is a transversely isotropic version of the Mooney-Rivlin model [109, 128]:

$$W = \sum_{i+j=1}^{3} C_{ij}(I_1 - 3)^i (I_4 - 1)^j \equiv \tilde{\Sigma}_1^3, \tag{5.7}$$

where C_{ij} are the model parameters to be determined, symbol $\tilde{\Sigma}_1^3$ is the concise notation for the summation: $i + j = 1, \ldots, 3$, and its subscript and superscript denote the lower and upper bounds of the summation, respectively. We further considered the second SEDF form that is the exponential version of Eq. (5.7)

$$W = C_{00}(I_1 - 3) + \exp\left[\tilde{\Sigma}_1^3\right]. \tag{5.8}$$

Herein, C_{00} is the model parameter associated with the Neo-Hookean term, and the third SEDF form is chosen as the combination of Eq. (5.7) and Eq. (5.8)

$$W = \tilde{\Sigma}_1^2 + \exp\left[\tilde{\Sigma}_1^2\right] - 1. \tag{5.9}$$

These three SEDF forms were considered in the baseline comparisons (i.e., Study Scenario #1) to assess their applicability to the TV leaflets.

Study Scenario #2: Decoupling of the Exponential SEDF Form

In addition to the comparisons described above, we also sought to further explore the performance of Eq. when the I_1 and I_4 terms were decoupled. First, the summation in Eq. (5.9) can be moved outside of the exponential term (as called as *Decouple I*)

$$W = C_{00}(I_1 - 3) + \sum_{i+j=1}^{3} \exp\left[C_{ij}(I_1 - 3)^i (I_4 - 1)^j\right] - 9. \tag{5.10}$$

Next, the multiplication of the I_1 and I_4 coupling terms within the exponent can be replaced with addition (named as *Decouple II*)

$$W = C_{00}(I_1 - 3) + \sum_{i+j=1}^{3} \exp\left\{C_{ij}\left[(I_1 - 3)^i + (I_4 - 1)^j\right]\right\} - 9. \tag{5.11}$$

Finally, the I_1 and I_4 terms were completely decoupled into separate exponential terms (i.e., *Decouple III*), similar to the form of Choi and Vito [28]

$$W = C_{00}(I_1 - 3) + \sum_{i=1}^{3} \exp\left\{C_i (I_1 - 3)^i\right\} + \sum_{j=1}^{3} \exp \bar{C}_j (I_4 - 1)^j - 6. \tag{5.12}$$

5.1.7 Nonlinear Least-Squares Fitting of the SEDF Forms to Experimental Data

The model parameters for each of the six SEDF forms outlined above were determined via nonlinear least-squares fit to the experimental data using an in-house two-step DEO algorithm [160]. Briefly, n_{pop} parameter sets were generated (based on the best n_{pop} among the $n = 100,000$ randomly generated parameter sets), and the residual was computed for each parameter set by

$$r_j = \sum_{i=1}^{n_{\text{data}}} r_i = \sum_{i=1}^{n_{\text{data}}} (W_{,1}^{\text{exp}} - W_{,1}^{\text{model},j})^2 + (W_{,4}^{\text{exp}} - W_{,4}^{\text{model},j})^2, \tag{5.13}$$

where the superscript denotes either the experimental data or the model predictions, and *j* denotes the current model parameter set. The 10,000 parameter sets with the lowest residuals were selected for use in the model fitting procedure ($n_{\text{pop}} = 1,000$). In each iteration of the DEO algorithm, the n_{pop} residuals and the Euclidian distances to the best parameter set were used to update the parameter sets towards the global minimum. Although global search algorithms, such as the adopted DEO algorithm, are robust and widely used in minimization, they may have difficulty finding a unique minimum when the residual search space near the global minimum is *flat* with small changes in the residual value [1]. The minimization processes were, therefore, repeated $n = 50$ times for each SEDF form to mitigate the potential influence of this inherent limitation of the DEO global optimization algorithm.

5.1.8 Assessments of the SEDF Forms

Three assessments were performed for each of the six studied SEDF forms. First, the distributions of the *coefficients of determination* R^2 were computed for the four plots of the experimental data to evaluate the model fitting capabilities. Second, the $n = 900$ sets of model parameters for each SEDF form were used to determine the Pearson's correlation matrix using the `corr()` function in MATLAB (MathWorks, Natick, Massachusetts), which was subsequently plotted using the `imagesc()` function to visually assess the potential linear relationships between the model parameters. The presence of potential linear relationships may be indicative of more well-defined search space. Finally, the *D*-optimality and condition optimality criteria were computed [80, 110] for each SEDF form with each of the three TV leaflets. Within the realm of soft tissue biomechanics, these optimality criteria have most notably been employed to improve constitutive model fitting [80] and determine appropriate protocols for the mechanical characterization of myocardium tissue [13]. In brief, an in-house MATLAB program was used to compute the Hessian maxtrix $\mathbf{H}$ of Eq. (5.13) for each leaflet specimen considering the parameter set with the smallest residual value. The *D*-optimality criterion was then computed as the $\det(\mathbf{H})$, whereas the condition criterion was computed as $\mathrm{cond}(\mathbf{H})$. The *D*-optimality criterion should be maximized to improve the model fitting as $\det(\mathbf{H})$ represents the inverse of the volume of the confidence region for the model parameters. On the other hand, the condition optimality criterion provides insight into the shape of the confidence region for the model parameters—larger relative values indicate more eccentric (or more non-uniform) confidence regions and smaller relative values for more uniform confidence regions.

5.1.9 Results of the Constant Invariant-Based Mechanical Characterizations

The experimental results for the three representative specimens (one per TV leaflet) are shown in **Figure 5-2**(a)-(c). All the three TV leaflets shared similar trends in the experimental data: (i) $W_{,1}$ increasing nonlinearly as I_1 increased; (ii) $W_{,4}$ decreasing nonlinearly with I_1; (iii) $W_{,1}$ decreasing almost linearly with I_4; (iv) $W_{,4}$ increasing almost linearly as an increasing I_4. These observed trends were generally consistent for all the values considered in the constant I_1 or constant I_4 protocols; however, the experimental trends sometimes deviated from these overall observations at the larger values of the constant invariants. For example, the maximum constant I_1 protocol, i.e., $I_1 = 3.4$, produced more nonlinear behaviors for the representative TVAL and TVPL specimens (**Figure 5-2**(a),(b)) and the nonlinear increasing response was found to be more profound for the representative TVAL specimen (**Figure 5-2**(a)), rather than the linearly decreasing trend in $W_{,1}$ vs. I_4 observed for the other values of constant I_1. The reasoning for this departure is unclear, but, nevertheless, it underscores the complex relationships between the partial derivatives of *W* and the invariants that can be determined from the constant invariant-based mechanical characterizations. In addition to these experimental trends, **Figure 5-2** demonstrates the good-quality fit of the third-order polynomial function to the experimental data.

5.1.10 Study Scenario #1: Evaluating the Candidate SEDF Forms

Three candidate SEDFs were considered in this study scenario—the transversely isotropic version of the polynomial Mooney-Rivlin form (Eq. (5.7)), an exponential version of the polynomial form (Eq. (5.8)), and the combination of the polynomial and exponential form

(Eq. (5.9)). The fitting capabilities of these three SEDF forms were first evaluated by using the distributions of the R^2 values from the nonlinear least-squares fits to the experimental data. Then, the model parameter correlations and the two optimality criteria (i.e., *D*-optimality and condition optimality) were assessed to examine the model parameter search space and confidence regions.

SEDF Fitting Capabilities

Representative best fits of the three SEDF forms in Eqs. (5.7)-(5.9) for the TVPL specimen in **Figure 5-2**(b) are shown in **Figure 5-3**(a)-(c), respectively. Of the three SEDF forms, the exponential SEDF in Eq. (5.8) yielded the best fit to the experimental data of this representative TVPL specimen **Figure 5-3**(b), whereas the polynomial SEDF and the combined polynomial-exponential SEDF had difficulties with fitting to the constant I_4 protocols **Figure 5-3**(a),(c). Moreover, these representative best fits show the inability of the polynomial SEDF form to accurately capture the relationship between $W_{,1}$ and I_1 at the small values of $W_{,1}$ (i.e., the toe region). In contrast, the exponential SEDF, however, can successfully capture this behavior but produces poor fitting at the larger values of $W_{,1}$ for the $I_1 = 3.4$ protocol, which is shared among all three considered SEDF forms.

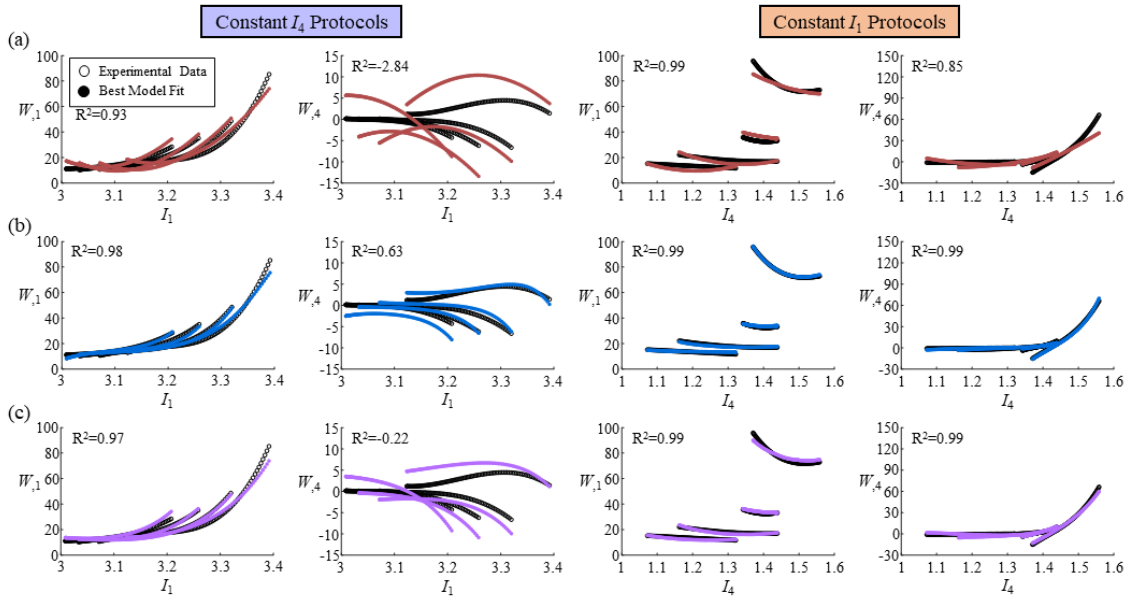

Figure 5-3. Best fits to the representative TVPL (see **Figure 5-2**(b)) for the three SEDF forms: (a) polynomial form in Eq. (5.7), (b) exponential form in Eq. (5.8), and (c) combined polynomial-exponential form in Eq. (5.9). $W_{,1}$ and $W_{,4}$ are in kPa.

We further examined the distributions of the R^2 values as shown in **Figure 5-4**, which provide further insight into the fitting capabilities of the three SEDF forms across different specimens and the corresponding fitting results. These distributions echo the superb performance of the exponential SEDF form for capturing all of the relationships between the partial derivatives of W and the invariants (R^2=0.92-0.99). Further, they also elucidate the disparity between the polynomial SEDF form (R^2=0.91-0.97) and the combined polynomial-exponential SEDF form (R^2=0.91-0.97 vs. R^2=0.65-0.95), which is not directly discernible from the representative fits in **Figure 5-3**. Much of the difference in the fitting capabilities of the considered SEDF forms stems from the $W_{,1}$ vs. I_4 relationship under the constant I_1 protocols. This relationship, interestingly, holds the most qualitative inter-protocol differences as outlined in the previous

subsection (Section 5.1.9), i.e., starkly different relationships between $W_{,1}$ and I_4 under the larger values of constant I_1. Perhaps the unique coupling of the I_1 and I_4 terms in the exponential SEDF form enables this model to more accurately capture these protocol-specific behaviors. This is further explored in Study Scenario #2 (Section 5.1.11), where the decoupled forms of the exponential SEDF are considered.

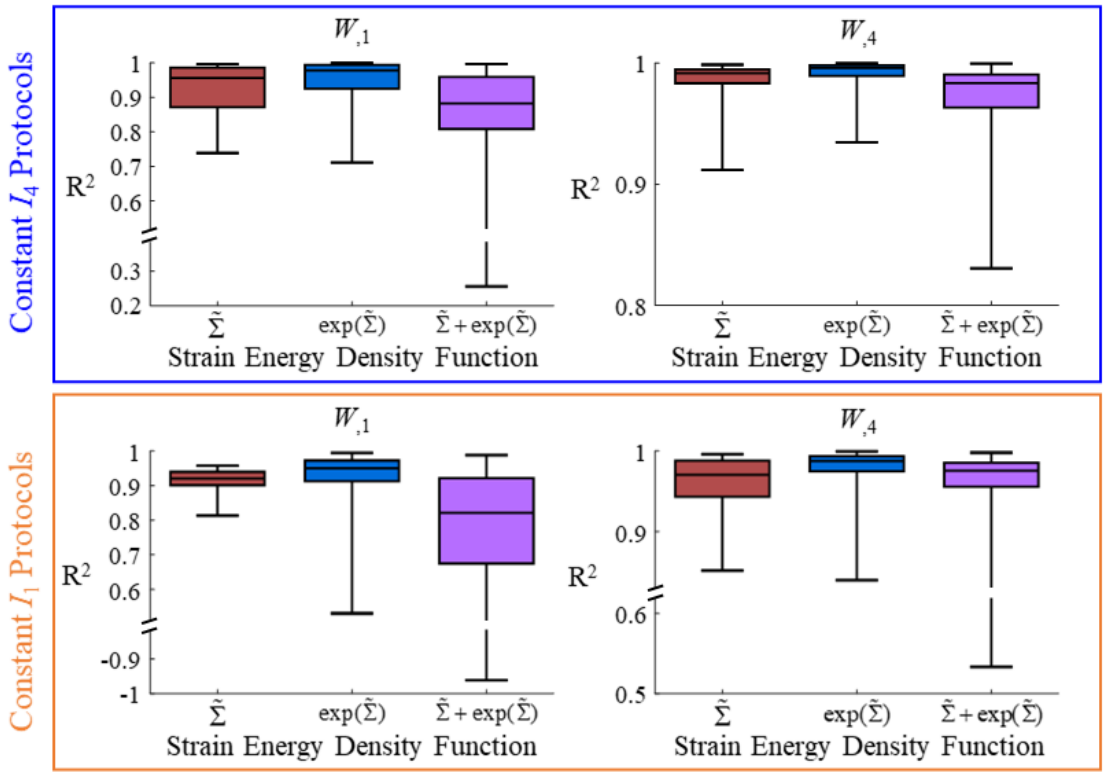

Figure 5-4. Coefficient of determination (R^2) values for the polynomial, exponential, and combined polynomial-exponential SEDF forms, considering all of the experimental data for the three TV leaflets ($n = 6$ each leaflet)

Correlations of the Model Parameters

The fits for the three SEDF forms were further analyzed to determine the Pearson's correlation matrix (**Figure 5-5**). These color maps, which represent the correlation matrix values, provide further insight into the parameter search space near the global minimum. For example, the polynomial SEDF form had a notably larger mean magnitude for the Pearson's correlation coefficients than the exponential SEDF form (0.51 vs. 0.30). A similar trend was shared for the polynomial and exponential components of the combined polynomial-exponential SEDF form (0.51 vs. 0.21), underscoring the intrinsic differences in model parameter correlations between the polynomial form and the exponential form. Nevertheless, the larger mean absolute values suggest that the parameter search space is more well-defined for the polynomial SEDF form. These interpretations are primarily qualitative, and the following assessment of the optimality criteria can elucidate more quantitative information of the model parameter's confidence regions.

Optimality Criteria

The optimality criteria provide insight into the parameter confidence region, such as the volume of the confidence region *D*-optimality criterion) or the eccentricity of the confidence region (condition optimality criterion). The *D*-optimality criterion, which is the most commonly used criterion for design of experiments [13, 80, 110], showed that the mixed polynomial-exponential SEDF form had the smallest parameter confidence volume (i.e., the largest *D*-optimality criterion) for 12 out of 18 specimens and the second-smallest for the remaining 6 specimens. Of the remaining two SEDF forms, the exponential SEDF form had the smallest parameter confidence volume for 6 out of 18 specimens and the second-smallest

for the other 12 specimens, while the polynomial SEDF form consistently had the worst *D*-optimality criterion values. On the other hand, the condition optimality criterion, which is used to determine the eccentricity of the parameter confidence region, shows that the polynomial SEDF form often had the least-eccentric confidence region of the three SEDF forms. This observation may agree with the uniformly larger Pearson's correlation coefficients highlighted in the previous subsection and **Figure 5-5**, and it also follows the prior observation that the exponential SEDF form have an undesired long valley in the model parameter search space near the global minimum.

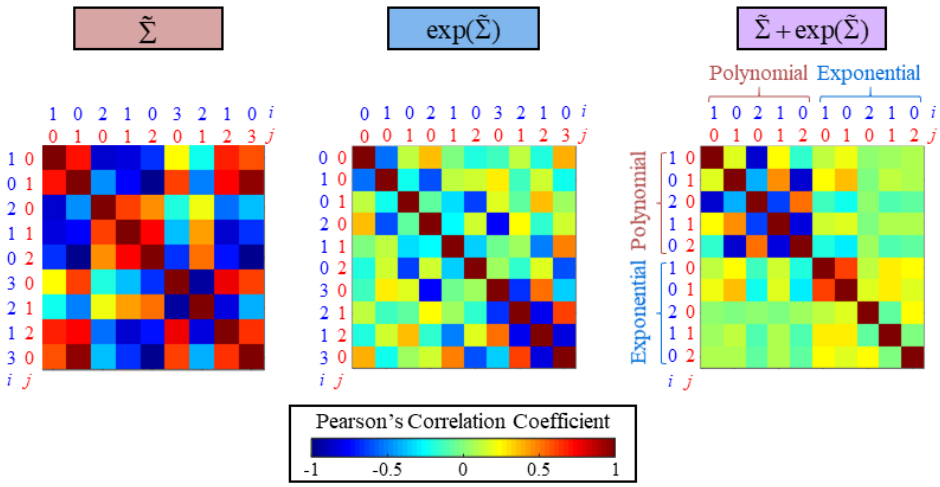

Figure 5-5. Color maps of the Pearson's correlation coefficient for the polynomial SEDF in Eq. (5.7), the exponential SEDF in Eq. (5.8), and the combined polynomial-exponential SEDF in Eq. (5.9).

5.1.11 Study Scenario #2: Decoupling of the Exponential SEDF

We further considered the three decoupled forms of the exponential SEDF

(Eqs. (5.10)-(5.12)) to understand how decoupling the invariant terms within the exponential term influences the model's fitting capabilities, parameter correlations, and optimality criteria.

SEDF Fitting Capabilities

The exponential SEDF in Eq. (5.8) provided the best fit to the representative TVPL specimen as demonstrated in **Figure 5-2**(b) (and the same in **Figure 5-6**(a)), whereas the decoupled SEDF forms had remarked difficulties in capturing the experimental relationships (**Figure 5-6**(b)-(d)). For example, all the three decoupled SEDF forms show the lack of protocol-specific predictions for $W_{,1}$ vs. I_1 in the constant I_4 protocols and $W_{,4}$ vs. I_4 in the constant I_1 protocols, despite a seemingly good representation of the exponential relationships. On the other hand, the predictions for $W_{,4}$ vs. I_1 and $W_{,1}$ vs. I_4 kept their protocol-specific capabilities but became linear and unable to capture the nonlinear relationships.

These observed limitations of the three decoupled SEDF forms to fit the experimental data were also noticeable in the distributions of the R^2 values (**Figure 5-7**). Specifically, the three decoupled SEDF forms showed considerably worse fitting performances for the experimental data for all the TV leaflet specimens (Decouple I-III: R^2=0.79-0.97 vs. 0.74-0.97 vs. 0.75-0.97) compared to the exponential SEDF (R^2=0.92-0.99). It is apparent from these observations that the coupling between the I_1 and I_4 terms is likely critical to the representation of the experimentally quantified behaviors of the TV leaflets. This was alluded to in Study Scenario #1 as one potential reason for the exponential SEDF form out-performing the polynomial SEDF form when predicting protocol-specific behaviors—the disparity is more profound for

the decoupled exponential SEDF forms. Nevertheless, the results show that the decoupled forms may still somewhat capture the experimental trends, which could be beneficial when using traditional planar biaxial mechanical data where the decoupling of the invariants is infeasible.

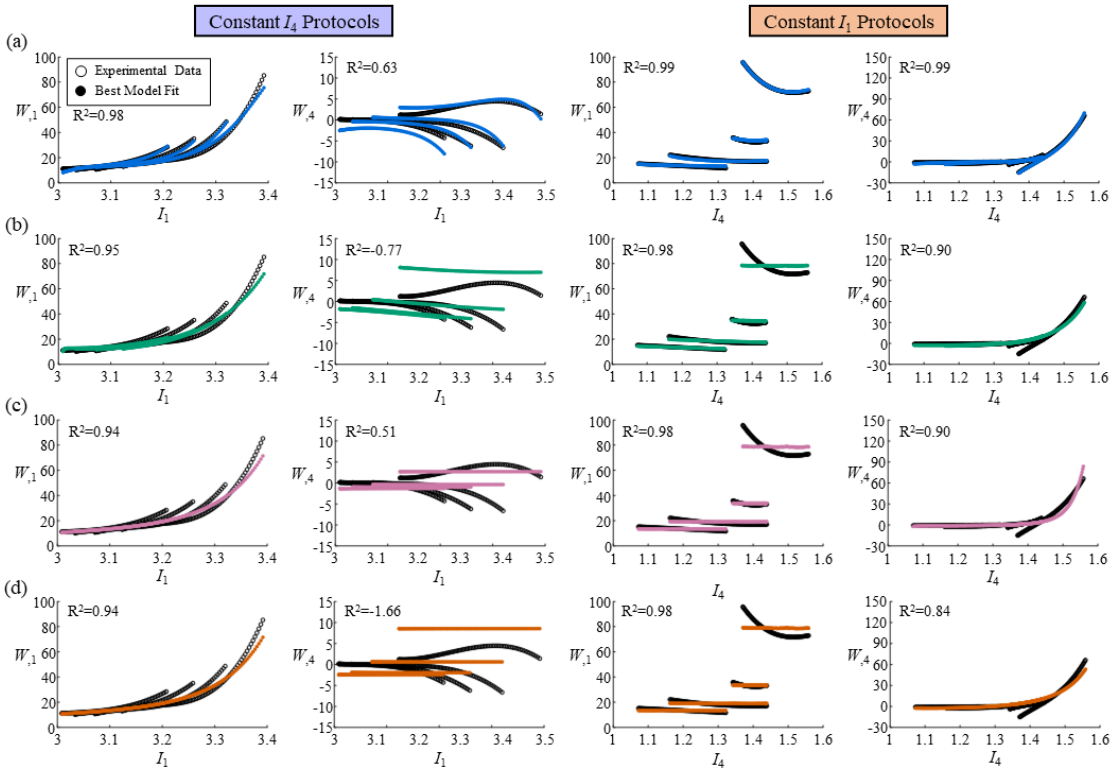

Figure 5-6. The best model fits to the representative TVPL specimen (see **Figure 5-2**), as determined by the smallest residual value, for the (a) exponential SEDF form (Eq. (5.7)), (b) Decouple I SEDF form (Eq. (5.10)), (c) Decouple II SEDF form (Eq. (5.11)), and (d) Decouple III SEDF form (Eq. (5.12)). $W_{,1}$ and $W_{,4}$ are in kPa.

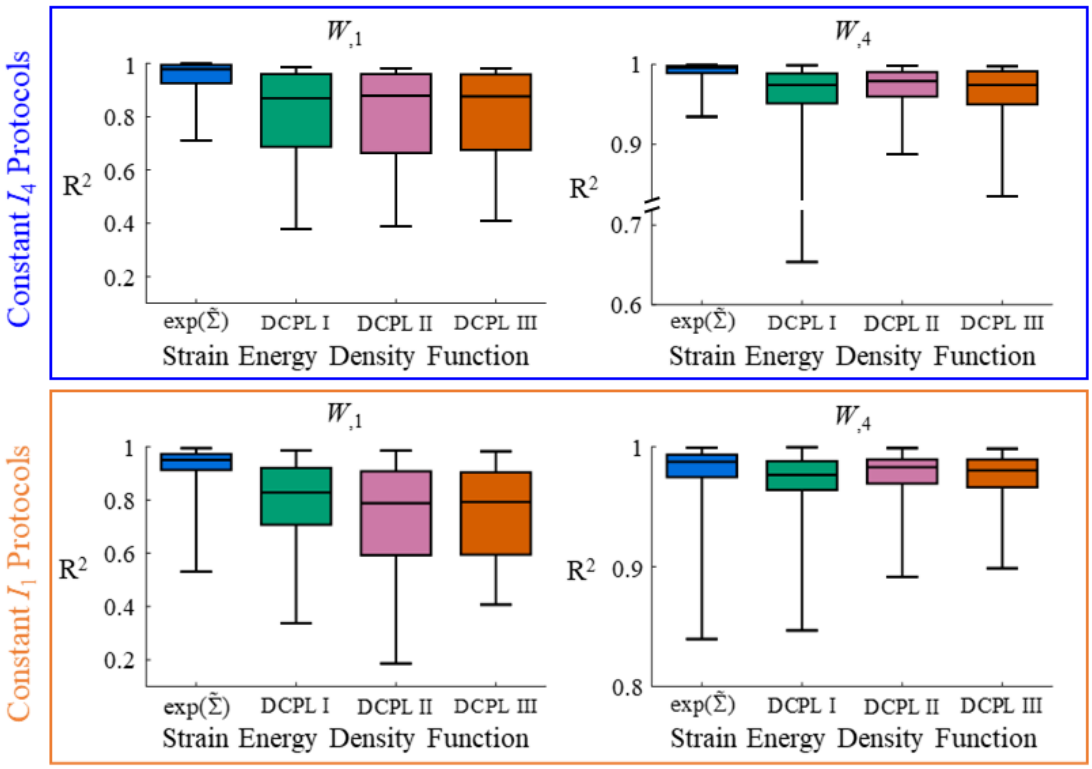

Figure 5-7. The coefficient of determination (R^2) values for the exponential SEDF form in Eq. (5.8) and the three decoupled exponential SEDF forms (Eqs. (5.10)-(5.12)) considering all of the experimental data for the three TV leaflets.

Correlations of the Model Parameters

The color maps of the Pearson's correlation coefficient matrices shown in **Figure 5-8** qualitatively highlight the reduction in the model parameter correlations as the invariant terms were decoupled. Quantitatively, the median magnitude of the Pearson's correlation coefficients reduced from 0.30 for the exponential SEDF form to 0.15, 0.09, and 0.15 for the progressively decoupled exponential SEDF forms (i.e., Decouple I, II, III), respectively. This observation follows the expectation that the decoupled SEDF forms should have fewer model parameter

correlations; however, it is unclear how the reduction in the model parameter correlations alters the residual search space (i.e., the confidence regions), which will be examined next.

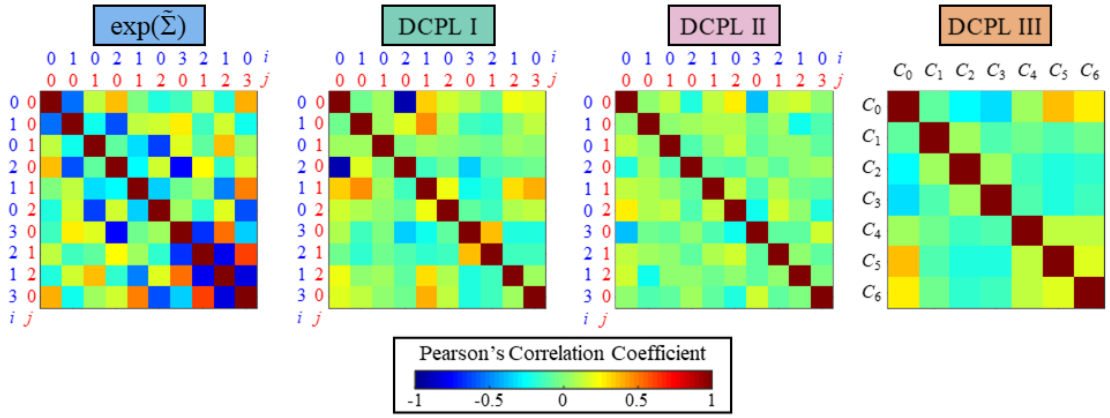

Figure 5-8. Color maps of the Pearson's correlation coefficient for the exponential SEDF form in Eq. (5.8) and the decoupled exponential SEDF forms in Eqs. (5.10)-(5.12).

D-Optimality Criterion

The *D*-optimality and condition optimality criteria for the decoupled SEDF forms provide further quantitative insight into the parameter search space near the global minimum. Although it was unclear in Study Scenario #1 whether the exponential SEDF or the combined polynomial-exponential SEDF had the smallest confidence region (i.e., largest *D*-optimality criterion), the exponential SEDF showed the best criterion values for all the 18 TV leaflet specimens in Study Scenario #2. Interestingly, the most decoupled SEDF form (Decouple III) held the most second-best *D*-optimality criterion for 12 specimens followed by Decouple I for 4 specimens and Decouple II for only two specimens. These observations show no apparent trend in the parameter search space as the SEDF is progressively decoupled—the notably

worse criterion values underscore the value of the coupled I_1 and I_4 terms in the exponential SEDF. Considering the condition optimality criterion, the exponential SEDF also outperforms the decoupled SEDF forms by having the least eccentric search space (i.e., the smallest condition optimality criterion) for 12 of the 18 specimens and the second-least eccentric for the remaining 6 specimens. In contrast to the *D*-optimality, there is a clearly second-best SEDF form candidate: *Decouple III* having the least eccentric search space for 6 specimens and the second-least eccentric for the remaining 12 specimens. These observations indicate the superb performance of the exponential SEDF and highlight the benefits of the coupled I_1 and I_4 terms in the exponential SEDF that reduce the confidence region size and eccentricity of the model parameter search space.

5.1.12 Experimental Observations and Comparisons with Existing Literature

Our constant invariant-based mechanical characterization provided the first-of-its-kind experimental quantification of the relationships between the partial derivatives of W and the invariants I_1 and I_4 for the *TV leaflets*. Similarities in the trends of the experimental data for the $n=18$ tested TV specimens suggest that only one SEDF form must be found to capture the mechanical behaviors of all the three TV leaflets (i.e., no leaflet-specific SEDF forms). Interestingly, the results from the present study have stark differences from the prior constant invariant-based characterization by May-Newman and Yin [106] for the *mitral valve* leaflets, highlighting the tissue-specific nature of the constant invariant characterizations. The mitral valve leaflets showed consistent non-linearly increasing relationships between W and the invariants, whereas our results for the TV leaflets had a mixture of non-linear/linear increasing and decreasing relationships. Some of these differences could be attributed to how the

specimens were prepared in May-Newman and Yin compared to our investigation. For example, we used our in-house pSFDI device to quantify the initial preferred orientation of the CFA, which then informed the orientation of the excised specimen from the central region of the TV leaflets (see **Figure 5-1**). In contrast, May-Newman and Yin assumed the collagen fiber orientation following the native leaflet's fiber architecture and maintained the entire leaflet entity in their testing (i.e., leaflet, annulus, and chordae insertions). The presence of the annulus and chordae insertions may also influence the observed mechanical behaviors of the mitral valve leaflet. Further, assuming a preferred collagen fiber orientation for the mitral valve leaflets is likely reasonable; however, their post-testing histology showed relatively larger inter-specimen and spatially heterogeneous variations in the preferred fiber orientation.

On the other hand, our results herein are more similar to the constant invariant-based mechanical characterization of the *left ventricle myocardial tissue* by Humphrey *et al*. [62]. The primary difference is that the TV leaflets appear to have more non-linear relationships between I_1 and the partial derivatives of *W* for constant I_4 protocols than the left ventricle myocardial tissue. This may be a consequence of different microstructural properties between the two soft tissues—myocardial tissue is well-known to have highly aligned collagen fibers that vary transmurally [13, 159], whereas the TV leaflet CFAs potentially have more splay and spatial heterogeneity [60]. Thus, when the fiber stretch is held constant in the constant I_4 protocols, the cross-fiber stress-stretch relationship may be more linear for the myocardial tissue, leading to more apparently linear relationships between the partial derivatives of *W* and I_1. Future *in-silico* investigations of the constant invariant-based mechanical characterizations could help elucidate the underlying mechanisms of these differences.

5.1.13 The Determined Form of *W* for the TV Leaflets

Prior constant invariant-based mechanical characterization studies made qualitative assessment of the experimental results to determine a more suitable SEDF form for the tissue of interest. For example, Humphrey *et al*. [62] began with a transversely-isotropic version of the Mooney-Rivlin SEDF and employed the observed experimental trends (e.g., linearly increasing relationship between $W_{,1}$ and I_1) to tailor the model form for the myocardial tissue. This approach can successfully lead to an SEDF for the tissue of interest; however, it remains to be answered whether another SEDF form would be more favorable in capturing the mechanical behaviors. We, therefore, adopted an alternative approach, in which we considered three candidate SEDF forms and evaluated their respective performance in fitting to the constant invariant-based experimental data. The distributions of R^2 values in **Figure 5-4** show the superior performance of the polynomial and exponential SEDFs compared to the combined polynomial-exponential SEDF form. Further analyses of the polynomial and exponential SEDF forms based on the well-established optimality criteria [80, 110] revealed that the exponential SEDF had fewer model parameter correlations and larger values of the *D*-optimality and the condition criteria than the polynomial SEDF form. These observations indicate that the exponential SEDF has a smaller but more eccentric model parameter confidence region. The indication of an eccentric model parameter confidence region is supported by a prior investigation highlighted a long, narrow valley in the model parameter search space near the global minimum for SEDFs with an exponential term [1]. Nevertheless, the *D*-optimality criterion is commonly taken as the primary consideration to inform experimental design despite both optimality criteria having implications on how the global search algorithms (e.g., DEO) will perform for fitting the experimental data [110].

Based on these results, it is recommended that a general exponential SEDF form in Eq. (5.8) be used for the TV leaflets because of its favorable fitting performance and model parameter confidence region size, which can be equivalently expressed by:

$$W = C_{00}(I_1 - 3) + \exp\left\{\sum_{i+j=1}^{3} C_{ij}(I_1 - 3)^i (I_4 - 1)^j\right\} - 1 \cdot \tag{5.14}$$

5.1.14 The Importance of Coupling I_1 and I_4

The fundamental investigations of Humphrey and Yin [62, 63] provided the two techniques to determine a SEDF form using experimental data acquired from biaxial mechanical characterizations or constant invariant-based mechanical characterizations. As Humphrey *et al*. [62] pointed out in the latter constant invariant-based investigation, these two approaches can arrive at a unique SEDF form due to the inability of typical biaxial mechanical characterizations to decouple the contributions from the invariants. This inadequacy of the traditional biaxial mechanical characterizations prevents any coupling of the invariants in calibrating the SEDF form, while the constant invariant-based characterizations allow the invariant coupling being considered. We, thus, sought to explore how the coupling of the I_1 and I_4 invariants in the exponential SEDF may alter the model's fitting performance and the confidence region of the model parameters.

Decoupling of the invariants in the exponential SEDF led to a notable reduction in the fitting performance (Decouple I-III: R^2=0.79-0.97 vs. 0.75-0.97 vs. 0.75-0.97) compared to the exponential SEDF (R^2=0.92-0.99). Looking closer at the representative best fits of the decoupled exponential SEDFs (**Figure 5-6**), one will notice that some of the protocol-specific

behaviors ($W_{,1}$ vs. I_1 and $W_{,4}$ vs. I_4) and the non-linearity ($W_{,4}$ vs. I_1 and $W_{,1}$ vs. I_4) cannot be accurately captured by the decoupled SEDF forms. Hence, although the decoupled forms can apparently provide reasonable fits to the experimental data as shown by the median R^2 values, they provide least accurate predictions of the constant invariant-based protocol features that may be more critical to the representation of the tissue's mechanical behaviors. These observations regarding the decoupled forms are unique to the TV leaflets; however, the changes in non-linearity and protocol-specific features arising from the decoupling can guide future SEDF selections for other soft biological tissues.

5.1.15 Study Limitations and Future Extensions

This study is not without limitations. First, although the CFA was characterized using our in-house pSFDI device and careful attention to detail was given to excising the specimen at the median fiber orientation, the CFA may not be perfectly aligned with the BioTester's *X*-axis. This could be due to the spatial heterogeneity in the CFA when excising the specimen from the leaflet or the small rotational errors when mounting the specimen to the CellScale BioTester. Nevertheless, our experimental setup allows us to ensure that all specimens were nearly aligned with the *X*-axis, which is key to our assumptions when determining the analytical form of $W_{,1}$ and $W_{,4}$ and facilitating the constant I_4 protocols. Second, the constant invariant technique employed herein is only valid for tissues with minimal or no transmural variations in the CFA. Although previous studies have demonstrated minimal transmural variations for the TV leaflets [107], this precludes the applicability of this method to other biological tissues with more pronounced transmural variations (e.g., myocardial tissue). Third, the tissue stretches were computed by means of the linear actuator displacements, which may

not be as accurate as the deformation in the center of the specimen where the boundary or loading effects are minimal. All the tested specimens also had an array of four fiducial markers that were used to compute the tissue stretches following our well-established procedure [67, 129]. Our internal study (not presented) that compared the computed stretches between the method of using the linear actuator displacements and the method of the fiducial markers showed negligible differences in the relationships of the partial derivatives of W and the invariants. From this internal study, we elected to use the linear actuator displacements for the tissue stretches, since the constant invariant values are enforced while there may be slight deviations when using the tissue stretches from the fiducial markers. Finally, the DEO algorithm used in this work [160] may possess difficulties finding a unique global minimum for SEDFs with a long valley [1] (e.g., the exponential SEDF form) in the model parameter's search space. We attempted to mitigate this potential limitation by performing numerous minimization procedures ($n = 50$) for each SEDF form, but the influence of this uncertainty in the global minimum on our results was not systematically evaluated.

One primary future extension of this study is fitting the proposed exponential SEDF (Eq. (5.8)) to available biaxial mechanical data for the TV leaflets. This can be done in the conventional manner, such as the prior investigation of Khoiy *et al*. [71], where the SEDF form is fit to the averaged biaxial mechanical data for several specimens. On the other hand, non-parametric bootstrapping [44] can be employed to construct the model parameter likelihoods and compute other meaningful metrics (e.g., the parameter confidence intervals). In addition to the present study using I_1 and I_4, additional constant invariant characterizations can be performed using alternative invariants, such as those proposed by Criscione *et al*. [30]. These

alternative invariants are not covariant unlike the traditional invariants of $\mathbf{C}$ [16], which we expect would improve the robustness of the DEO algorithm-based minimization and potentially the model parameter confidence regions or eccentricity. The exponential phenomenological SEDF form can also be enhanced to consider more rich microstructural information, such as the collagen fiber splay about the preferred direction. Its performance can then be compared to the more complex structurally informed constitutive models, such as those proposed by Zhang *et al*. [161] or Rego and Sacks [126], to determine the further benefits or limitations of this new SEDF form. Ultimately, the exponential SEDF form, together with the optimal model parameters determined in the future extensions, can be employed in *in-silico* simulations of TV function to provide a computationally tractable representation of the TV leaflet's mechanical behaviors.

5.1.16 Conclusion

This study has provided the *first-of-its-kind* constant invariant-based mechanical characterization of the TV leaflets. Our experimental results showed the three TV leaflets shared similar relationships between the partial derivatives of W and the invariants I_1 and I_4, suggesting one SEDF form may suffice to represent all three TV leaflets. Three types of SEDFs—a polynomial SEDF, an exponential SEDF, and a combined polynomial-exponential SEDF—were fit to the experimental data to evaluate their potential use for the TV leaflets. The exponential SEDF form displays a superior performance by providing excellent fits to all of the experimental data (R^2=0.92-0.99) and having a smaller model parameter confidence region, as determined by the *D*-optimality criterion, than the polynomial SEDF with a similar fitting performance (R^2=0.91-0.97). Motivated by the prior investigations of Humphrey and Yin [62,

63] that separately led to candidate coupled and decoupled SEDFs for the myocardial tissue, we further explored how decoupling the invariants in the exponential SEDF could alter the model performance. Interestingly, our results showed that the three decoupled exponential SEDF forms showed a worsened fitting performance than the original exponential SEDF by failing to capture many of the protocol-specific and nonlinear relationships in the experimental data. The further analysis revealed that there was no notable improvement in the confidence region shape or eccentricity of the model parameter space near the global minimum. Thus, although the decoupled SEDF forms could possibly represent the TV leaflet's mechanical responses, they have intrinsic limitations that prevent them from accurately representing the leaflet mechanical behaviors, especially under constant invariant-based mechanical characterizations. It is, thus, recommended to use the generalized exponential SEDF for the TV leaflets. Future extensions of this work will determine the optimal model parameters for the TV leaflets, further enabling *in-silico* simulations of functioning TVs.

5.2 Data-Driven Modeling of Soft Tissue Biomechanics

5.2.1 Study Objective

The objective of this work is to apply DD modeling to soft biological tissues by extending the local convexity DD (LCDD) computational framework [54], which couples manifold learning with nonlinear elasticity, to model a representative mitral valve leaflet's nonlinear anisotropic mechanical responses. Owing to the proposed manifold learning scheme that projects data onto a convex space for dimensional reduction, this method is shown to be robust against noisy data and outliers.

5.2.2 Nonlinear Data-Driven Computational Framework

Overview on the theory

The DD computational framework can be formulated by the following minimization problem

$$\min_{\hat{z}\in E} \min_{z\in C} H(z,\hat{z}), \tag{5.15}$$

where $\mathbf{z}$ and $\hat{z}$ are the *physical state* (e.g., stresses and strains obtained by physical simulations) and the *measured data* (e.g., stresses and strains from experimental measurements), respectively, H is a functional to compute the distance between $\mathbf{z}$ and $\hat{z}$, E is a set of all measurements collected under different experimental protocols, and C denotes the dataset satisfying the equilibrium and compatibility condition (i.e., the strain-displacement relation). The standard solution procedures of this DD problem are based on fixed-point iterations, where the minimization of H with respect to $\mathbf{z}$ and $\hat{z}$ are performed iteratively until the intersection of two datasets in C and E is found within a prescribed tolerance (**Figure 5-9**). The minimization corresponding to the physical state is denoted as the *global step*, whereas the one

associated with the experimental data as the *local step*.

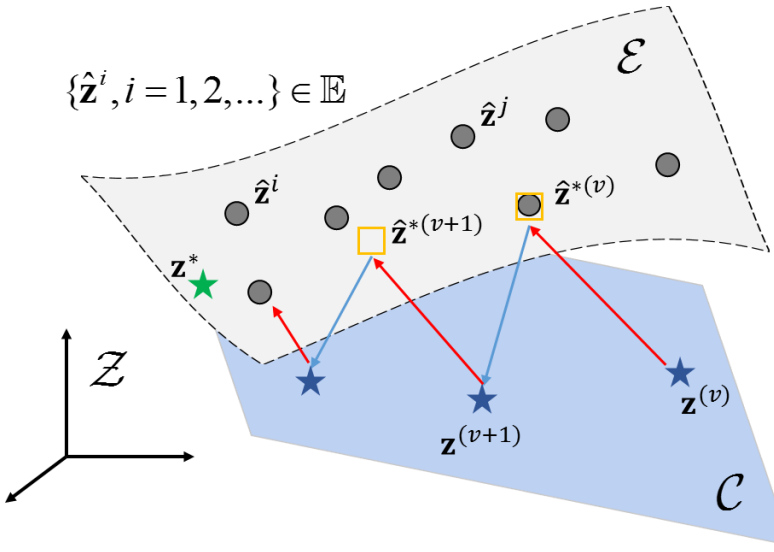

Figure 5-9. Geometric schematic of the proposed LCDD computational framework in Eq. (5.15) solved by an iteration scheme (with v the iteration counter) where $\mathrm{z}^{(v)} \in \mathrm{C}$ (denoted by the blue stars) is the computation state on the physical manifold C at v-th iteration, $\{\hat{\mathrm{z}}^i, i=1,2,...\}$ (denoted by the gray circles) are the collected measurement data stored in E, E is an underlined material manifold (or envelope) constructed based on the data, and Z denote the global phase space. The iteration scheme is decomposed into two update steps: (i) the *local (material) step* where the data solution $\hat{z}^*$ (denoted by the orange squares) is solved by projecting the given computational state onto the manifold E of data set and (ii) the *global (physical) step* where the new computational state is obtained by projecting the given data solution onto C by enforcing the physical constraints. The convergent solution is denoted by z^* (the green stars).

For modeling biological tissues, $\mathbf{E}$ and $\mathbf{S}$ are considered as the strain and stress measures. The functional H involves the strain energy-like and complementary energy-like components, expressed as

$$\mathrm{H}(\mathrm{z},\hat{\mathrm{z}}) = \mathrm{H}((\mathbf{E},\mathbf{S}),(\hat{\mathbf{E}},\hat{\mathbf{S}})) = \int_{\Omega} d_E^2(\mathbf{E},\hat{\mathbf{E}}) + d_S^2(\mathbf{S},\hat{\mathbf{S}})\mathrm{d}\Omega, \tag{5.16}$$

where

$$d_E^2(\mathbf{E},\hat{\mathbf{E}}) = \frac{1}{2}(\mathbf{E}-\hat{\mathbf{E}}):\mathbf{M}:(\mathbf{E}-\hat{\mathbf{E}}), d_S^2(\mathbf{S},\hat{\mathbf{S}}) = \frac{1}{2}(\mathbf{S}-\hat{\mathbf{S}}):\mathbf{M}^{-1}:(\mathbf{S}-\hat{\mathbf{S}})\cdot \tag{5.17}$$

Here, $\mathbf{M}$ is a positive definite coefficient matrix that provides multi-dimensional weights to the distance measure between the experimental stress-strain data $\hat{\mathrm{z}} = (\hat{\mathbf{E}},\hat{\mathbf{S}})$ and the physical stress-strain state $\mathbf{z} = (\mathbf{E},\mathbf{S})$. In the numerical studies for nonlinear materials, $\mathbf{M}$ is defined as a diagonal matrix, in which each diagonal component is the ratio of the standard deviations of the associated components of the stress-strain experimental data. Although being empirical in selecting $\mathbf{M}$, this treatment generally yields satisfactory results in our numerical tests in this study.

To consider large deformations in soft tissue materials, we formulate the DD computational framework based on the finite strain theory [18]. Given a candidate data $(\hat{\mathbf{E}},\hat{\mathbf{S}})$ from the experimental dataset E, the *global step* of the DD solver in Eq. (5.15) is expressed as

$$\min_{\mathbf{u},\mathbf{S}} \int_{\Omega^X} [d_E^2(\mathbf{E}(\mathbf{u}),\hat{\mathbf{E}}) + d_S^2(\mathbf{S},\hat{\mathbf{S}})]\mathrm{d}\Omega, \tag{5.18}$$

$$\text{subject to: } \mathrm{DIV}(\mathbf{F}(\mathbf{u})\cdot\mathbf{S}) + \bar{\mathbf{b}} = \mathbf{0} \text{ in } \Omega^X, \text{ and} \tag{5.19}$$

$$(\mathbf{F}(\mathbf{u})\cdot\mathbf{S})\cdot\mathbf{N} = \bar{\mathbf{t}} \qquad \text{on } \Gamma_t^X. \tag{5.20}$$

Equations (5.19) and (5.20) are the equilibrium equation and the associated natural boundary condition, respectively, $\mathbf{u}$ is the unknown displacement field, $\bar{\mathbf{b}}$ is the body force at the initial

configuration Ω^X, $\bar{\mathbf{t}}$ is the traction on the natural boundary Γ_t^X, and $\mathbf{N}$ is the surface normal on Γ_t^X. Note that in the displacement-based formulation, $\mathbf{F}$ and $\mathbf{E}$ are obtained from $\mathbb{u}$, denoted as $\mathbf{F(u)}$ and $\mathbf{E(u)}$. The constrained minimization problem in Eqs. (5.18)-(5.20) can be solved numerically using the Lagrange multiplier approach with a standard FE or reproducing kernel particle method [26, 27] meshfree numerical solver. The detailed computational formulations are provided in Appendix D.

Computational Algorithm for the Proposed LCDD Nonlinear Solver

The employed DD computational method does not rely on any pre-assumed constitutive model for the relationship between $\mathbb{S}$ and $\mathbf{E}$. Instead, it searches for a stress-strain pair $(\hat{\mathbf{E}},\hat{\mathbf{S}})$ from the experimental measurement set $\mathbb{E}$ that is closest to the physics strain-stress pair $(\mathbf{E},\mathbf{S})$.

In this study, the manifold learning DD solver proposed by [54] is employed to seek for the solution $\hat{\mathbb{z}}^* = (\hat{\mathbf{E}}^*,\hat{\mathbf{S}}^*)$ that minimizes Eq. (5.15) for a given $(\mathbf{E},\mathbf{S})$ obtained from Eqs. (5.18)-(5.20). Because the strain-stress pairs $(\mathbf{E}_\alpha,\mathbf{S}_\alpha)$ are numerically computed at the integration points $\mathbf{X}_\alpha$, the minimization of Eq. (5.15) with the functional in Eq. (5.16) is reduced to the following minimization problem associated to each integration point $\mathbf{X}_\alpha$

$$(\hat{\mathbf{E}}_\alpha^*,\hat{\mathbf{S}}_\alpha^*) = \arg\min_{(\hat{\mathbf{E}}_\alpha,\hat{\mathbf{S}}_\alpha)\in\mathbb{E}_\alpha} d_E^2(\mathbf{E}_\alpha\hat{\mathbf{E}}_\alpha) + d_S^2(\mathbf{S}_\alpha,\hat{\mathbf{S}}_\alpha),\ \alpha = 1,\cdots,m, \tag{5.21}$$

and thus, called the *local step*. In Eq. (5.21), $\mathbb{E}_\alpha$ is the material data space reconstructed by the locally-convex manifold associated with $(\mathbf{E}_\alpha,\mathbf{S}_\alpha)$, m is the total number of integration points employed in the solver. The key idea of the LCDD solver is to construct a locally-convex

subset E_α using k neighboring material data points in E closest to the given local state $(\mathbf{E}_\alpha, \mathbf{S}_\alpha)$, *called k-nearest neighbors*, and solve Eq. (5.21) by using the penalty relaxation and non-negative least squares. In this study, the default value for the number of neighbors is $k = 6$. By imposing suitable smoothness and convexity in the locally convex manifold, LCDD yields stable DD computing results against noisy data and outliers [54]. Note that when the *raw* experimental dataset E is directly used for the *local step* in the solver, the standard distance-minimization DD (DMDD) method [72] is recovered. More details about constructing the locally-convex data set E_α by means of manifold learning can be found in [54].

5.2.3 Application to Tissue Biomechanics of the Heart Valve Leaflet

Tissue Preparation and Biaxial Mechanical Testing

The biaxial mechanical testing data of one representative porcine mitral valve TVPL tissue was used to evaluate the effectiveness of the proposed LCDD modeling. In brief, one porcine heart obtained from a local slaughterhouse (Country Meat Co., Oklahoma) was cleaned and dissected to retrieve the MVPL. The central 10×10 mm section was excised (**Figure 5-10**(a)). Three thickness measurements were taken via a digital caliper (Westward 1AAU4-0.01mm resolution), and the measurements were averaged to obtain the MVPL tissue's thickness t_{MVPL}. The sample was next mounted to the BioTester system equipped with 1.5N load cells (CellScale, Ontario, Canada) by using four BioRakes delimiting a 7.5×7.5 mm effective testing region (**Figure 5-10**(b)). The tissue's circumferential and radial directions were aligned with the BioTester's *X*- and *Y*-directions. The mounted specimen was submerged in a $37\ ^\circ\mathrm{C}$ saline bath and characterized using our previously-developed biaxial mechanical testing protocol for the atrioventricular heart valve leaflets [67, 82, 129]. The biaxial testing consisted

of: (i) ten preconditioning cycles of equi-biaxial tensions ($T_{\text{circ}} = T_{\text{rad}} = T_{\max}$), during which a preload of 1% of $T_{\max}$ were applied, to restore the tissue's *in vivo* configuration [29], and (ii) ten cycles of 11 different biaxial tension protocols (**Table 5-1**). Specifically, there are *nine biaxial tension protocols* (**Figure 5-10**(c)) and *two pure shear protocols* during which the area is kept constant under combined tension-compression loads (i.e., $\lambda_{\text{circ}}\lambda_{\text{rad}} = 1.0$, **Figure 5-10**(d)). Here, λ_{circ} and λ_{rad} are the circumferential and radial stretches, respectively. Note that the MVPL specimen was loaded at 4.42 N/min to $T_{\max} = 100$ N/m according to its physiological condition [52, 56, 75]. $\mathbf{F}$ and $\mathbf{S}$ were computed by

$$\mathbf{F} = \begin{bmatrix} \lambda_{\text{circ}} & 0 \\ 0 & \lambda_{\text{rad}} \end{bmatrix} = \frac{1}{L}\begin{bmatrix} u_x & 0 \\ 0 & u_y \end{bmatrix} \text{ and } \mathbf{S} = \frac{1}{t_{MVPL}}\mathbf{F}^{-1} diag\left(\left[T_{\text{circ}}, T_{\text{rad}}\right]\right), \qquad (5.22)$$

where $L = 7.5$ mm, and u_x and u_y are the *X*- and *Y*-displacements, respectively. Note that the shear component of $\mathbf{E}$ is negligible when using tine-based mounting [77]. The resulting stress-strain data $\hat{\mathrm{z}} = (\hat{\mathbf{E}}, \hat{\mathbf{S}}) = ([\hat{E}_{\text{CC}}, \hat{E}_{\text{RR}}], [\hat{S}_{\text{CC}}, \hat{S}_{\text{RR}}])^T$ were used for the subsequent comparative study.

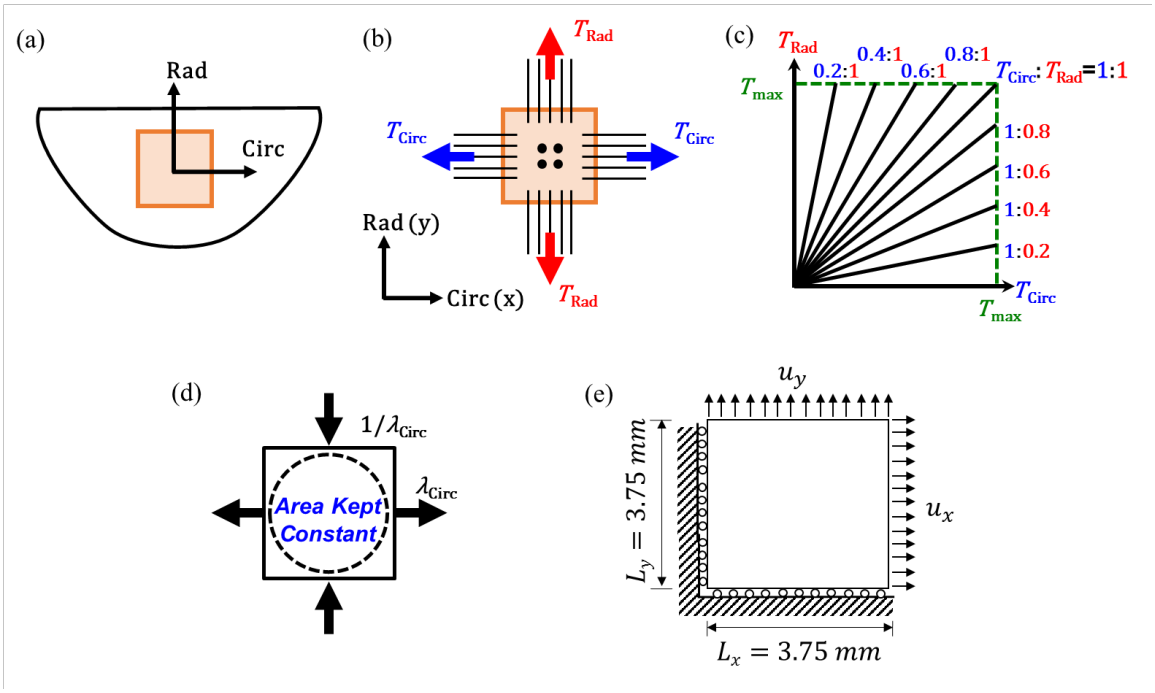

Figure 5-10. (a) Schematic of a MVPL tissue with the central (belly) region highlighted in orange, and (b) tissue specimen mounted to a biaxial testing system with applied tensions T_{circ} and T_{rad}. Schematic of the mechanical testing protocols: (c) biaxial tensions, and (d) pure shear. (e) Schematic of the model of biaxial testing used in DD computations and constitutive modeling.

Table 5-1. Eleven protocols of the conducted biaxial mechanical testing with the experimentally-quantified tissue stretches of a representative MVPL specimen and their equivalent displacements used in the DD computations. (PSX: pure shear in x, PSY: pure shear in y).

ID	Protocol	λ_{circ}	λ_{rad}	u_x (mm)	u_y (mm)
1	1:1	1.333	1.525	2.498	3.983
2	1:0.8	1.342	1.499	2.564	3.744
3	1:0.6	1.355	1.466	2.662	3.498
4	1:0.4	1.369	1.415	2.770	3.110
5	1:0.2	1.388	1.326	2.913	2.442
6	0.8:1	1.313	1.541	2.344	4.055
7	0.6:1	1.275	1.562	2.064	4.215
8	0.4:1	1.213	1.588	1.596	4.409
9	0.2:1	1.109	1.618	0.820	4.635
10	PSX	1.387	0.721	2.903	-2.093
11	PSY	0.620	1.612	-2.847	4.590

Study Scenarios to Validate the Performance of the Proposed LCDD Method

Three study scenarios were considered to evaluate the performance of the proposed LCDD method. Two constitutive models were also used in these study scenarios as a reference for the proposed LCDD method. Selected biaxial testing protocols from the MVPL data were employed for constructing experimental dataset E for LCDD model training and SEDF model parameter calibration, and predictions were made using other protocols that are not used for model training. Note that the simulation results were obtained by using the tissue model's given boundary conditions associated with the testing protocols (**Figure 5-10**(e))**.** The root-mean-

square deviation normalized with respect to the maximum stress of the data (NRMSD) was used as a measure to assess the predictability of each method.

(i) Scenario #1: Protocol 1 for training (*equi-biaxial tension protocol*), and Protocols 3 and 5 for predictions to investigate model's performance in extrapolation with limited information provided.

(ii) Scenario #2: Protocols 10 and 11 (pure shear) for both model training and predictions to examine model's predictability, considering kinematic states with combined compression and tension.

(iii) Scenario #3: Protocols 1, 3, 4, 7, and 8 for training, and predictions for 2, 5, 6, and 9 to study model's interpolative and extrapolative predictabilities.

Constitutive Modeling for Comparisons with the LCDD Method

Two constitutive models were used for the study scenarios described in. The first is a full structural model modified from [161] that does not consider the layer-specific properties

$$\begin{aligned}\mathbf{S}_{FSM} &= \eta_m\left(\mathbf{I}-C_{33}\mathbf{C}^{-1}\right)+\eta_e^{\text{circ}}\left(I_{4,\text{circ}}-1\right)^{d_1}\mathbf{N}_{\text{circ}}\otimes\mathbf{N}_{\text{circ}}+\eta_e^{\text{rad}}\left(I_{4,\text{rad}}-1\right)^{d_2}\mathbf{N}_{\text{rad}}\otimes\mathbf{N}_{\text{rad}}\\ &+\eta_c\int_{-\frac{\pi}{2}}^{\frac{\pi}{2}}\Gamma\left(\theta;\mu_\Gamma,\sigma_\Gamma\right)\left[\int_0^{E_{\text{ens}}(\theta)}\frac{D\left(x;\mu_D,\sigma_D\right)}{\sqrt{1+2x}}\left(\frac{1}{\sqrt{1+2x}}-\frac{1}{\sqrt{1+2E_{ens}\left(\theta\right)}}\right)\right]\mathbf{N}\left(\theta\right)\otimes\mathbf{N}\left(\theta\right)d\theta\end{aligned}. \quad (5.23)$$

Herein, η_m, η_e^{circ}, η_e^{rad}, and η_c are the moduli for the non-fibrous ground matrix, circumferentially-aligned elastin fibers (with orientation $\mathbf{N}_{\text{circ}}=[\cos 0^\circ,\sin 0^\circ]^T$), radially-aligned elastin fibers (with orientation $\mathbf{N}_{\text{rad}}=[\cos 90^\circ,\sin 90^\circ]^T$) and collagen fibers, respectively, d_1 and d_2 describe the nonlinearity of the elastin fiber response, $\Gamma(\theta;\mu_r,\sigma_r)$ is the orientation distribution function with the mean and standard deviation of (μ_r,σ_r),

$E_{\text{ens}}(\theta) = \mathbf{N}(\theta) \cdot [\mathbf{EN}(\theta)]$ is the collagen fiber ensemble strain, and $D(x; \mu_D, \sigma_D)$ is the fiber recruitment function with μ_D and σ_D as the mean and standard deviation.

The second model is the Fung-type strain-based model [153] with the SEDF form

$$W = \frac{c}{2}\left[\exp\left(a_1 E_{\text{CC}}^2 + a_2 E_{\text{RR}}^2 + 2a_3 E_{\text{CC}} E_{\text{RR}}\right) - 1\right], \tag{5.24}$$

where c, a_1, a_2, and a_3 are the model parameters, and E_{CC} and E_{RR} are the circumferential and radial Green strains, respectively (**Figure 5-10**(a),(b)). Note that the shear terms and the higher-order coupling terms could be included in the Fung-type model in Eq. (5.24) for materials subjected to more profound in-plane shear and with extremely large deformation, such as the one in [149].

The constitutive model parameters in Eqs. (5.23)-(5.24) were obtained by nonlinear least-squares fitting to the acquired biaxial testing data using an in-house DEO program [160]. Briefly, n_{pop} uniformly-distributed sets of material parameters were generated, and the residual r_j was computed for each parameter set

$$r_j = \frac{1}{n_{\text{data}}}\left[\sum_{i=1}^{n_{\text{data}}}\left(S_{\text{CC}}^{\text{exp}} - S_{\text{CC},j}^{\text{model}}\right)^2 + \left(S_{\text{RR}}^{\text{exp}} - S_{\text{RR},j}^{\text{model}}\right)^2\right]^{1/2}, \; j = 1, ..., n_{\text{pop}}. \tag{5.25}$$

Herein, n_{data} is the number of experimental data, the superscript denotes either the experimental data or model prediction, and S_{CC} and S_{RR} are the circumferential and radial 2nd Piola-Kirchhoff stresses, respectively. The residual values and the Euclidian distances associated with the current best parameters were used to update the DEO parameters *exploratively* or

exploitatively. This iterative optimization was repeated until the residual threshold was reached $(\max r_j < 5\times10^{-7})$ or the residual difference between any two consecutive iterations was negligible $(<1\times10^{-7})$. The optimal parameters were then used for predictions of other experimental protocols.

5.2.4 Results and Discussion for Study Scenario #1

In this study, Protocol 1 was used for training, and Protocols 3 and 5 were used for prediction validation. Both the proposed LCDD method and the chosen two constitutive models yielded excellent fits to the equi-biaxial tension protocol, whereas the DMDD approach was less accurate in capturing the material's *high-tension* responses (**Figure 5-11**(a)). The predictions for Protocols 3 and 5 (**Figure 5-11**(b),(c)) showed that the performance of the proposed LCDD method is deteriorated as the prediction protocols move beyond the model training range (e.g., NRMSD=0.271 vs. 0.019 for Protocols 5 vs. 1), since insufficient information about the tissue's stress-strain behaviors was used in model training (i.e., only Protocol 1). This trend was shared by the two constitutive models but was less obvious for the full structural model (NRMSD=0.006-0.096) compared to the Fung-type model (NRMSD=0.003-0.265).

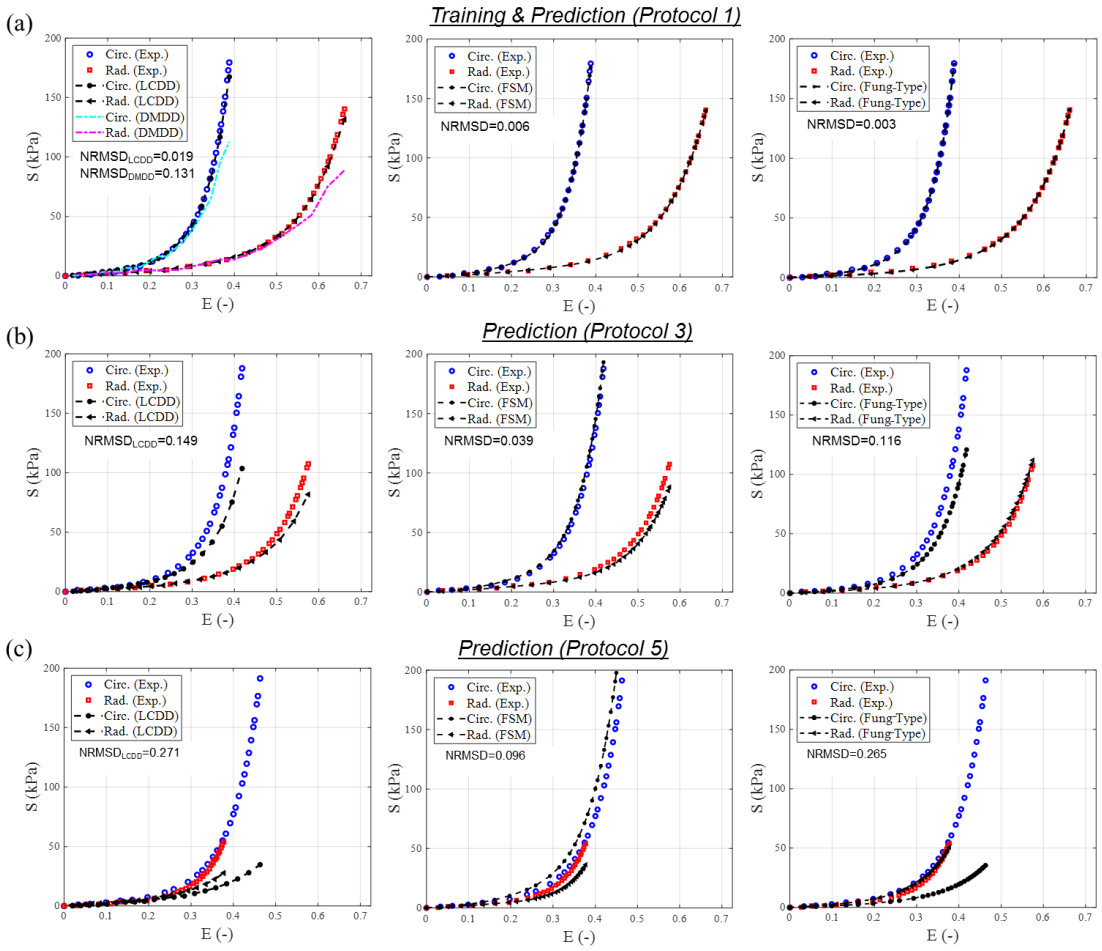

Figure 5-11. Comparison of the training and prediction accuracies among the proposed LCDD nonlinear solver, the DMDD solver, and the constitutive models with the Fung-type SEDF and the modified full structural model : (a) training of the equi-biaxial tension data (Protocol 1) together with its prediction, (b) prediction of Protocol 3, and (c) prediction of Protocol 5.

5.2.5 Results and Discussion for Study Scenario #2

In the first part of this study, both pure shear protocols (Protocols 10 and 11) were used in model training. The proposed LCDD nonlinear solver yielded better predictions than the DMDD approach (NRMSD=0.013-0.030 vs. NRMSD=0.069-0.103, 1st column of **Figure**

5-12(a),(b)). Although both the LCDD and the DMDD approaches could reasonably predict pure shear protocols, the two constitutive models had apparent difficulty capturing the compressive behaviors (2nd and 3rd columns of **Figure 5-12**(a),(b)). This demonstrates the advantage of the DD approaches, in which model predictions are not limited by a pre-defined stress-strain relationship and instead rely on the quality and completeness of the experimental data.

In the second part of this study, *when training with only one pure shear protocol and predicting the same pure shear protocol* (**Figure 5-12**(c),(d)), the proposed LCDD method resulted in excellent fits (NRMSD≤0.016), whereas the DMDD is less accurate in capturing the large pure shear deformation (NRMSD>0.093). The DMDD method appears to have relatively inferior predictability for nonlinear, large-deformation bio-tissues, because its search for the measurement data is based on the *closest* Euclidean distance, which presents difficulties for high-dimensional data. In contrast, the proposed LCDD nonlinear solver improves this weakness through a local manifold learning process. For constitutive modeling, the full structural model exhibits a similar behavior of not capturing the compressive deformations, whereas the Fung-type model successfully captures both pure shear protocols when trained individually.

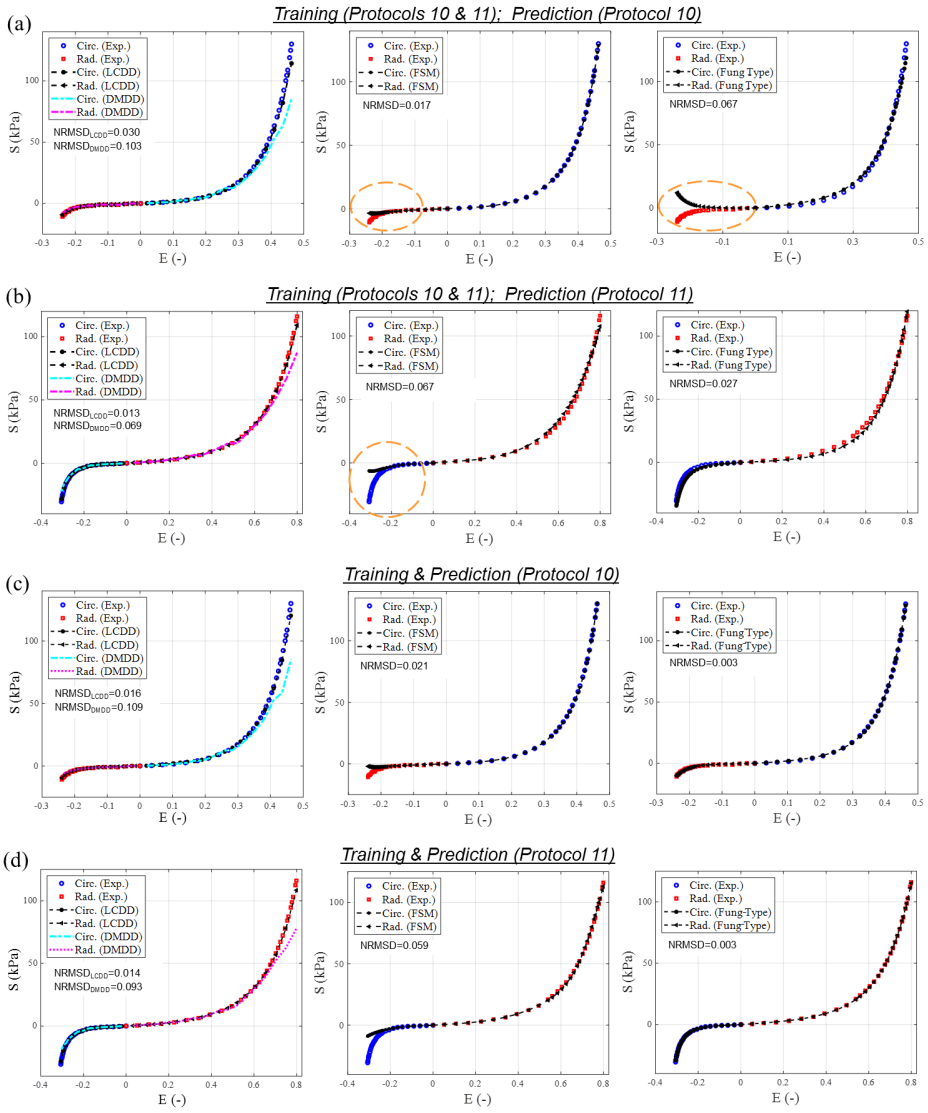

Figure 5-12. Comparison of the prediction performance among the proposed LCDD nonlinear solver, the DMDD solver, and the constitutive models with the Fung-type SEDF and the modified full structural model: (a) training using both Protocols 10 & 11 and the prediction of Protocol 10 (*tension in the circumferential direction and compression in the radial direction*), (b) training using Protocols 10 & 11 and the prediction of Protocol 11 (*tension in the radial direction and compression in the circumferential direction*), (c) training of Protocol 10 together with its prediction, and (d) training of Protocol 11 together with its prediction.

5.2.6 Results and Discussion for Study Scenario #3

In the last comparative study scenario, experimental protocols for training and predictions were selected to test DD methods' prediction ability, when predictions are *within* or *outside* the ranges of training data with mixed biaxial and pure shear deformations. The proposed LCDD method provided a good prediction of training data itself (NRMSD=0.019) as well as *interpolative* predictions of Protocols 2 and 6 (NRMSD=0.022; **Figure 5-13**(a)), but the *extrapolative* predictions were less effective (NRMSD=0.132). The full structural model exhibited an excellent fit to the training data (NRMSD=0.020) as well as the interpolative (NRMSD=0.018) and extrapolative (NRMSD=0.019) predictions when biaxial deformations are considered for both training and predictions. On the other hand, when the two pure shear protocols (Protocols 10 and 11) together with the biaxial deformation protocols were considered in model training, the LCDD predictions provided similar predictivity to the case without pure shear in training. In contrast, the full structural model could not capture the compressive deformations and the overall performance was reduced compared to the case without pure shear in model training (**Figure 5-13**(b)). These results suggest that sufficient coverage of deformation range in the training protocols are required to ensure reliable predictions for the LCDD method. Moreover, the employed constitutive models become less effective when pure shear deformations are included in the training data set due to their specific pre-defined functional forms, while the LCDD method with a direct search of experimental data could be more versatile for general deformation as long as the data set is sufficiently rich.

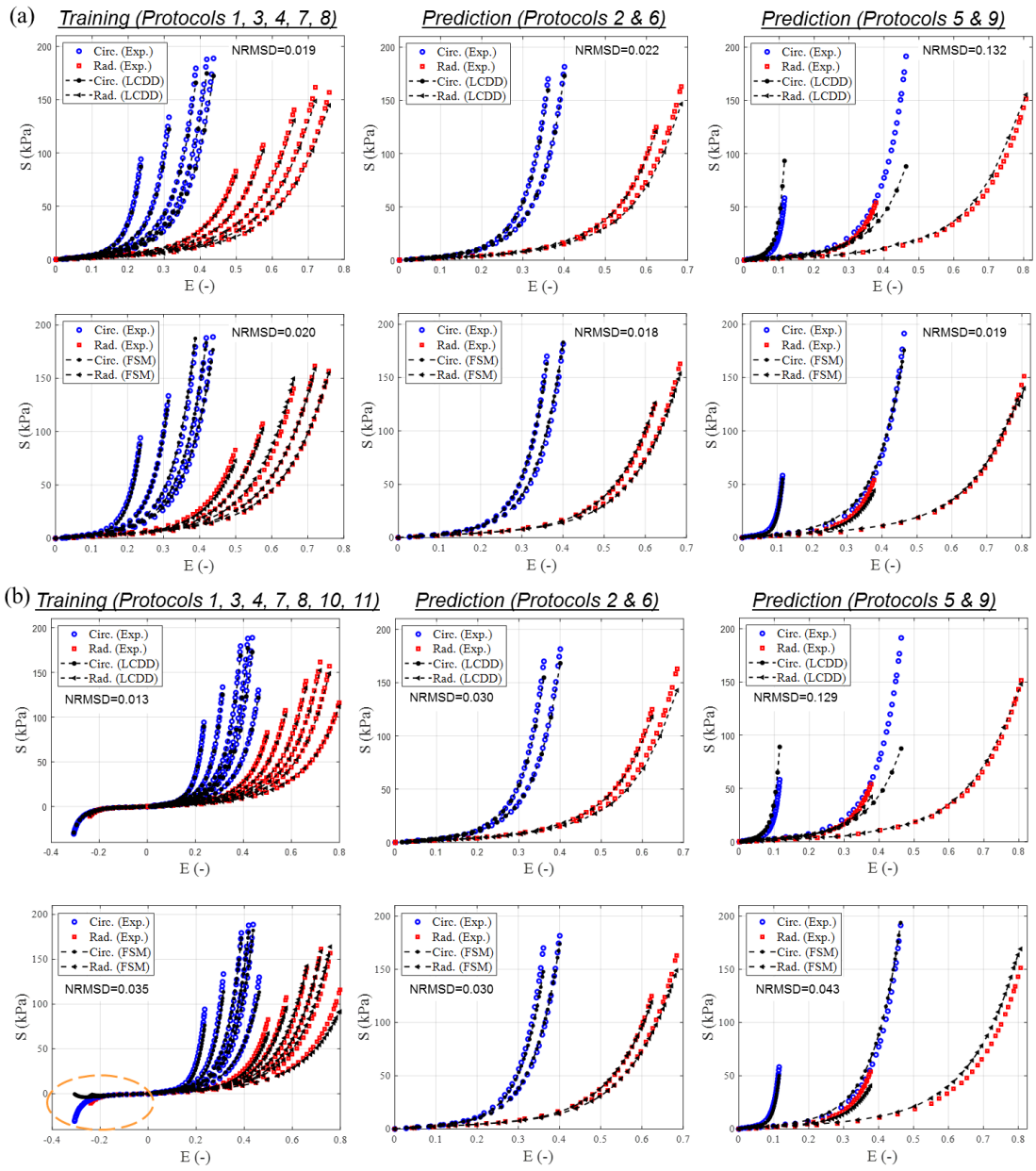

Figure 5-13. Comparison of the interpolative and extrapolative predictability between the proposed LCDD nonlinear solver and constitutive modeling with the modified full structural model: (a) training using Protocols 1, 3, 4, 7, and 8 *without* the pure shear protocols together with its predictions of Protocols 2 & 6 (*interpolative*) and Protocols 5 & 9 (*extrapolative*), and (b) training using Protocols 1, 3, 4, 7, and 8 *together with* the two pure shear protocols together with its interpolative and extrapolative predictions.

5.2.7 Study Limitations and Future Extensions

Several limitations are associated with the present study. While we demonstrated the effectiveness of the proposed LCDD nonlinear solver for soft biological tissues, such as the heart valve leaflet tissue from a single porcine MVPL specimen, further investigations are warranted to incorporate the specimen variations and explore other biological tissues. We could then examine how certain features of the anisotropic database may affect the LCDD predictability, such as data coverage, data density and data distribution. Furthermore, the role of fiber orientation in the LCDD predictive performance may be realized by the specimen-to-specimen fiber orientation variation within the database, and we can explore the method to handle the variation "offline" prior to the simulation. Additionally, how to choose the optimal number of neighbors in the *k*-nearest neighbors algorithm and the optimal M matrix requires more investigations, although our results shown the proposed LCDD approach is less sensitive to these hyperparameters than the DMDD method.

Future extensions are necessary to compare the LCDD method with the constitutive modeling based on other aspects, such as computational cost or applicability to a wider range of specimens. Invariant-based SEDFs determined from rigorous constant-invariant biaxial experiments can also be considered owing to their favorable computational efficiency compared to the two microstructure-informed constitutive models employed in this study. Furthermore, the LCDD method may be integrated with deep learning algorithms to improve model predictability considering data noises and limited experimental data.

5.2.8 Conclusion

In this study, we have applied the LCDD nonlinear solver to modeling biological materials under finite deformations. The proposed LCDD method was used to model a realistic biological tissue – *a porcine MVPL* with the material data collected from biaxial mechanical testing. Our results showed that the proposed nonlinear LCDD method is a promising simulation tool for complex materials, subjected to the availability of good quality data. In all the demonstrated verification and validation cases, our proposed LCDD method consistently outperforms the well-established DMDD method. Further, the LCDD method has comparable performance to the conventional constitutive models in both model training and *interpolative* predictions, but the LCDD method becomes less effective when the prediction is an extrapolation of the training data. The effectiveness of data-driving computational methods relies on the richness and quality of the data. For these reasons, the proposed LCDD nonlinear solver is minimally affected whenever pure shear data are used in model training. For other biaxial deformation cases, the proposed LCDD method can be less accurate than the constitutive models, especially when the prediction constitutes extrapolations from the training data. More investigations on data collection, data processing, and physics-informed machine learning are essential to advance this field.

CHAPTER 6 Linking In-Vitro Behaviors to In-Vivo Function

This chapter focuses on linking the *in vitro* characterizations to the *in-silico* predictions via the leaflet pre-strains. We first present a benchtop characterization of the TV leaflet pre-strains with respect to their *ex vivo* configuration (Section 6.1). This investigation also provides commentary on the choice of stress-free reference configuration when performing biaxial tensile experiments. Next, we establish a simplified *in-silico* benchmark for the TV that can be used for *in-silico* developments within the commercial FE software Abaqus (Section 6.2) [86]. Finally, we demonstrate the value of our established *in-silico* benchmark by predicting how the experimentally derived leaflet pre-strains influence the TV closing behavior (Section 6.3). Collectively, these efforts are a foundational effort towards connecting *in vitro* characterizations to *in vivo* behaviors through *in-silico* predictions in future works.

6.1 Tricuspid Valve Leaflet Pre-Strains

6.1.1 Study Objective

All soft biological tissues are naturally strained in their *in vivo* configurations. Chuong and Fung [29] discovered these pre-strains in their seminal experimental investigation of the arterial opening angles. Despite their conceptual simplicity, pre-strains have profound impacts on soft tissue biomechanics and how we interpret the *in vivo* mechanical behaviors of tissues. For instance, *in vitro* mechanical characterizations use a stress-free reference configuration that does not consider the tissue pre-strains. As a consequence of lacking the consideration of the pre-strains, the subsequent *in-silico* simulations built upon the acquired *in vitro* experimental data would result in very different predictions of the *in vivo* tissue behaviors.

This dilemma leads us to a long-standing question in the soft tissue biomechanics community: *How can we relate the in vitro and in vivo configurations so that reliable in-silico predictions of the soft tissue bio-system can be made possible?*

Thus, the objective of this study is to characterize the *ex vivo* TV leaflet pre-strains. We accomplish this by using a novel approach that combines dual-camera 3D photogrammetry and the reproducing kernel shape function to quantify the TV leaflet strains following dissection from the heart. In brief, 3D photogrammetry is used to determine the 3D locations of a 3×3 grid of fiducial markers associated with three key *in vitro* experimental configurations: the *ex vivo* heart, the explanted valve, and the dissected specimen. The specimens are then mounted to the biaxial tester for force-controlled preconditioning to observe how the typical *in vitro* stress-free reference configuration compares to the *ex vivo* configurations. We further explore how the choice of the reference configuration influences key biomechanics metrics at peak equibiaxial membrane tensions. Finally, we evaluate our results within the context of earlier findings for the other heart valve leaflets and other porcine tissues.

6.1.2 Heart Acquisition and Preparation

Eight adult porcine hearts ($n=8$, 80-140 kg, 1-1.5 years of age) were transported from a local USDA-approved abattoir (Chickasha Meat Company, Chickasha, OK) to our laboratory. The auricles were removed, and the right ventricle was opened by cutting along the posterior-septal commissure to the apex of the heart. The central 10×10 mm testing region of each TV leaflet was delimited by four surgical pen dots, and 9 glass beads (arranged in a 3×3 grid) were

affixed within this region using cyanoacrylate glue (**Figure 6-1**(a)).

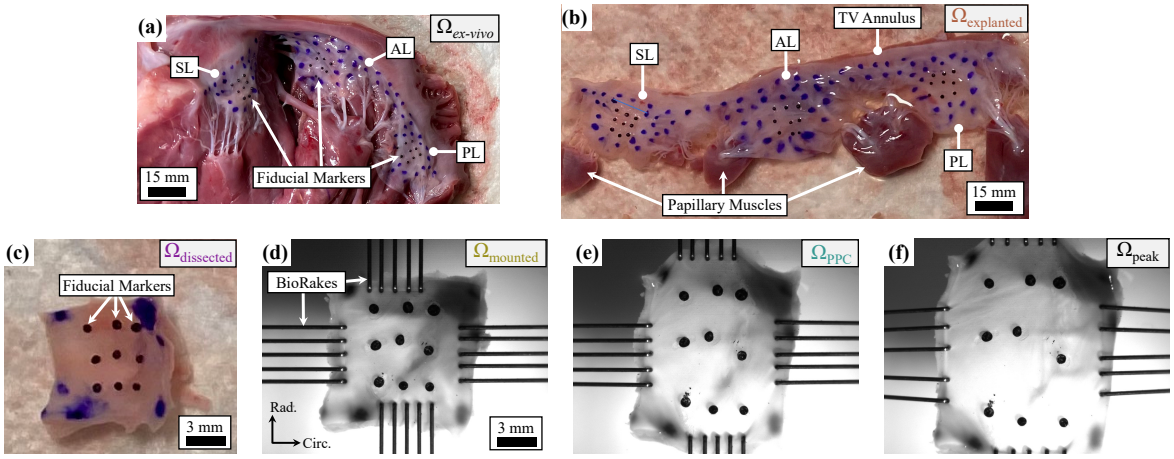

Figure 6-1. Representative experimental images of: (a) the opened right ventricle with fiducial markers affixed to the central region of each TV leaflet (Ω_{exvivo}), (b) the explanted TV while maintaining valvular connections ($\Omega_{explanted}$), (c) the dissected 10×10 mm TVAL specimen ($\Omega_{dissected}$), (d) the specimen mounted to the CellScale BioTester ($\Omega_{mounted}$), (e) the PPC specimen (Ω_{PPC}), and (f) the specimen at peak equibiaxial tensions of 40 N/m (Ω_{peak}).

6.1.3 Reconstruction of Marker 3D Coordinates and Dissection of the TV

Two cameras arranged in a stereo configuration were used to capture images of the TV in three configurations (**Figure 6-1**(a)-(c)): (i) the *ex vivo* configuration ($\Omega_{ex-vivo}$), (ii) the explanted configuration ($\Omega_{explanted}$), and (iii) the dissected specimen configuration ($\Omega_{dissected}$). The opened RV was first placed beneath the cameras to capture images of the *ex vivo* configuration (**Figure 6-1**(a)). Next, the TV, including the annulus and the chordal connections to the papillary muscles, was dissected and floated on a shallow bath of PBS to image the *explanted*

configuration (**Figure 6-1**(b)). Finally, the central 10×10 mm region of each leaflet (i.e., TVAL, TVPL, and TVSL) was excised and floated on the PBS bath to image the *dissected* specimen configuration (**Figure 6-1**(c)).

The two images acquired by dual cameras for each of the above three TV configurations were imported into MATLAB (MathWorks, Natick, MA). The pixel locations (p_i, q_i) of the nine fiducial markers ($i=1\sim9$) captured by the two cameras were obtained using the `drawpolygon()` function in MATLAB. The pixel locations were combined with the calibrated direct linear transformation (see more details in Appendix E) to determine the 3D locations of the fiducial markers (**Figure 6-2**(a)) [64].

6.1.4 Preconditioning Step of Planar Biaxial Mechanical Testing

Then, the 10×10 mm specimen was mounted to a commercial biaxial mechanical testing system (BioTester, CellScale, Ontario, Canada) with an effective testing region of 7×7 mm (**Figure 6-1**(d)). From this *mounted* configuration (Ω_{mounted}), the specimens underwent 10 cycles of force-controlled preconditioning to target equibiaxial membrane tensions of 40 N/m (i.e., 280 mN) [5]. 1280×960 resolution images of the fiducial markers were captured by a CCD camera and the load cell values were recorded throughout testing at 10 Hz. The stress-free configuration following the tenth force-controlled loading cycle was taken as the *PPC* configuration (Ω_{PPC}) [67]. In addition, the configuration associated with the peak biaxial tensions of the tenth loading cycle (Ω_{peak}) was used to analyzed the tissue stretches with respect to each of the five configurations shown in **Figure 6-1**.

6.1.5 Calculation of the Tricuspid Valve Leaflet Pre-Strains

The reproducing kernel (RK) method [26] (Appendix F) was used to determine the deformation gradient $\mathbf{F}$ from the *ex vivo* configuration to the explanted, dissected, mounted, PPC, and peak-tension configurations. The partial derivatives of the RK shape functions ($\Psi_{I,x}$, $\Psi_{I,y}$, and $\Psi_{I,z}$) were combined with the fiducial marker displacement vector $d_I(t) = [u_I(t), v_I(t), w_I(t)]^T$ (**Figure 6-2**(c),(d)) to compute $\mathbf{F}$:

$$[\mathbf{F}] = [\mathbf{F}(\mathbf{X},t)] = [\mathbf{I}] + \begin{bmatrix} \sum_{I=1}^{NP} \Psi_{I,x} u_I(t) & \sum_{I=1}^{NP} \Psi_{I,y} u_I(t) & \sum_{I=1}^{NP} \Psi_{I,z} u_I(t) \\ \sum_{I=1}^{NP} \Psi_{I,x} v_I(t) & \sum_{I=1}^{NP} \Psi_{I,y} v_I(t) & \sum_{I=1}^{NP} \Psi_{I,z} v_I(t) \\ \sum_{I=1}^{NP} \Psi_{I,x} w_I(t) & \sum_{I=1}^{NP} \Psi_{I,y} w_I(t) & \sum_{I=1}^{NP} \Psi_{I,z} w_I(t) \end{bmatrix}. \quad (6.1)$$

The deformation gradient at each of the chosen nine isoparametric locations (**Figure 6-2**(b)) was further transformed into the Green-Lagrange strain $\mathbf{E}$ [125].

The principal values and principal directions of $\mathbf{E}$ were next used to determine the *in-plane* principal strains and the areal strains of the TV leaflets. Due to experimental limitations in quantifying the change in the tissue thickness direction between different configurations, we did not consider or examine the tissue incompressibility that is a common assumption adopted in the heart valve biomechanics literature [126, 161]. Therefore, the principal value aligned with the tissue's transmural direction (determined via its principal direction) was not considered in our overall pre-strain analyses. The remaining in-plane principal values were categorized as the maximum principal strain, E_1, and the minimum principal strain, E_2, which were used to compute the maximum principal shear strain (MPSS) $\gamma = (E_1 - E_2)/2$. Finally,

the associated principal stretches λ_1 and λ_2 were used to compute the areal stretch $\lambda_A = \lambda_1 \lambda_2$, and, subsequently, the areal strain $E_A = (\lambda_A{}^2 - 1)/2$.

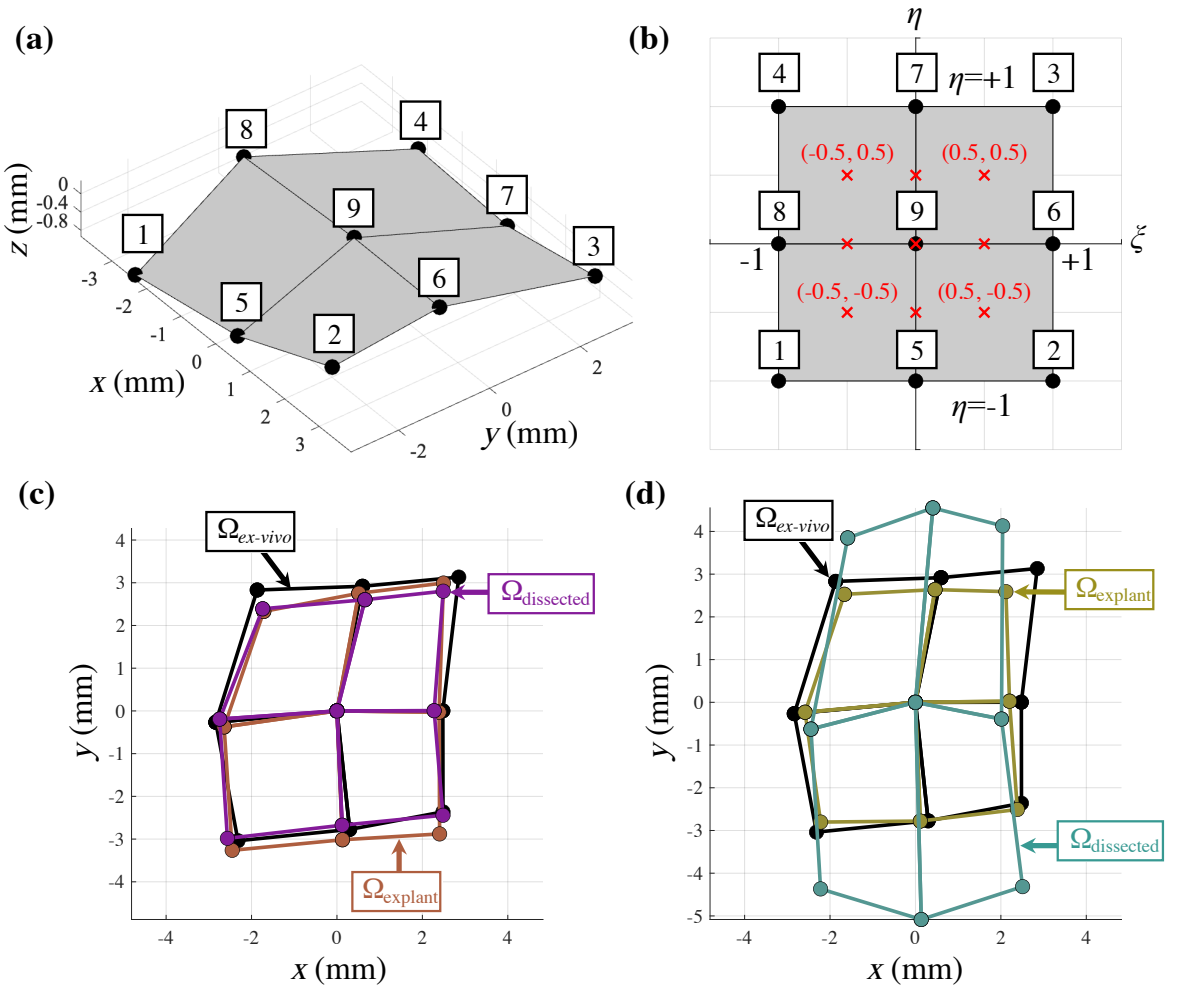

Figure 6-2. (a) Reconstructed 3D locations of the fiducial marker grid using the calibrated direct linear transformation-based photogrammetry (Appendix E). (b) Nine isoparametric locations (red crosses) chosen to evaluate the TV leaflet pre-strains for regional analysis. (c-d) Results of the TV leaflets from a representative porcine heart.

6.1.6 Data Analysis

Analysis I: Ex Vivo Pre-Strains. The primary objective of this study was to quantify the *ex vivo* pre-strains for all the three TV leaflets. Thus, our first analysis aimed to compare the in-plane principal strains and the areal pre-strain between the explanted and dissected configurations at the center of the specimen, i.e. $(\xi, \eta) = (0, 0)$ (**Figure 6-2**(b)). Since our preliminary qualitative assessment revealed that the pre-strains were spatially heterogeneous, we also compared the areal pre-strains among the nine locations defined in **Figure 6-2**(b).

Analysis II: Biaxial Testing Configurations. In addition to quantifying the *ex vivo* TV leaflet pre-strains, we were also interested in understanding the how the mounted and PPC configurations compared to the *ex vivo* configurations. The stress-free reference configuration is an important consideration for mechanical characterizations [8, 29, 67, 107, 124], so it is crucial to understand how these two common reference configurations in the benchtop tissue characterization procedures compare to the more realistic *ex vivo* configuration. Therefore, our second analysis focused on comparing the principal and areal pre-strains for the mounted and PPC configurations. Similar to the analysis of the *ex vivo* pre-strains in *Analysis I*, we compared these values among the nine isoparametric locations as shown in **Figure 6-2**(b).

Analysis III: Stress-Free Reference Configurations. Our final analysis was an extension of *Analysis II* but focused more on understanding what role the *ex vivo* pre-strains play in the characterized tissue mechanical behaviors. To facilitate this comparison, we computed several common biomechanics-based metrics derived from the biaxial mechanical characterizations for the five reference configurations. These included the peak stretches in the circumferential

(λ_{circ}) and radial (λ_{rad}) tissue directions and the *AI* [67, 107].

6.1.7 Statistical Analysis

Data are presented as mean $\pm$ SEM. Q-Q plots (not shown here) revealed that the data was not normally distributed in general. Thus, two-factor comparisons (configuration vs. leaflet) of the principal pre-strains (E_1, E_2), the areal pre-strain (E_A), the leaflet stretches ($\lambda_{circ}, \lambda_{rad}$), and the *AI* were made using the non-parametric aligned rank transform [158]. Further contrast tests were performed using the aligned rank transform contrasts method [40]. The non-parametric Kruskal-Wallis test was also employed to determine statistically significant differences in the computed pre-strains among the nine isoparametric locations. Differences were considered as statistically significant when $p < 0.05$.

6.1.8 Results for Representative TV Leaflet Specimens

The quantified areal pre-strains of one representative porcine heart for the explanted ($\Omega_{explanted}$), dissected ($\Omega_{dissected}$), mounted ($\Omega_{mounted}$), and PPC (Ω_{PPC}) configurations are shown in **Figure 6-3**. These color maps highlight the leaflet-specific and heterogeneous nature of the quantified pre-strains. Further analyses of these results considering all the porcine hearts ($n = 8$) are provided in the following sub-sections.

6.1.9 TV Leaflet Pre-Strains Following Valve Dissection and Biaxial Testing Specimen Excision

The pre-strains presented in **Figure 6-4** show minimal differences between the explanted and

dissected configurations, while **Table 6-1** shows no significant differences between these two configurations. Throughout these comparisons, there was a consistent trend of the TVSL exhibiting more compressive pre-strains compared to the TVAL. This difference was significant for the maximum principal pre-strain ($E_1 = -0.071 \pm 0.044$ vs. 0.13 ± 0.068) and the areal pre-strain ($E_A = -0.244 \pm 0.039$ vs. 0.018 ± 0.082) in the dissected configuration, as well as the areal pre-strain ($E_A = -0.252 \pm 0.041$ vs. -0.033 ± 0.060) in the explanted configuration with respect to Ω_{exvivo}. There were also significant differences when comparing the maximum principal pre-strains of the TVSL in the explanted configuration (-0.070 ± 0.042) to the TVAL in the dissected configuration (0.130 ± 0.068), and when comparing the areal strains of both leaflets in the explanted (septal: -0.252 ± 0.041, anterior: -0.033 ± 0.060) and dissected configurations (septal: -0.244 ± 0.039, anterior: -0.018 ± 0.082). No significant differences were found when comparing the TVPL to the TVSL or AL.

6.1.10 Comparison of the Mounted and PPC Configurations with the *Ex Vivo* Configuration

The comparisons of pre-strains in **Figure 6-5** and **Table 6-1** reveal significant differences between the mounted and PPC configurations. Interestingly, no significant differences were found between the three leaflets within one configuration. For the minimum principal pre-strain, the TVSL (-0.186 ± 0.023) when mounted was significantly lower than the TVAL (0.049 ± 0.070), TVPL (0.002 ± 0.052), and TVSL (-0.027 ± 0.046) at PPC. On the other hand, the maximum principal pre-strains for the TVAL (0.150 ± 0.067), TVPL (0.049 ± 0.033), and TVSL (-0.015 ± 0.039) were significantly smaller in the mounted

configuration than for the TVAL (0.751 ± 0.096) and TVPL (0.754 ± 0.064) leaflets in the PPC configuration. Only the TVSL maximum principal pre-strain (-0.015 ± 0.039) in the mounted configuration was smaller than that for the TVSL (0.419 ± 0.138) in the PPC configuration. In terms of the areal pre-strain, all but the mounted TVAL (0.053 ± 0.092) and PPC TVSL (0.318 ± 0.076) were statistically different. Finally, significant differences in maximum principal shear strain were found between the mounted TVSL (0.086 ± 0.019) and the PPC TVAL (0.351 ± 0.055) and TVPL (0.376 ± 0.038), as well as the mounted TVAL (0.118 ± 0.032) and PPC TVPL (0.376 ± 0.038).

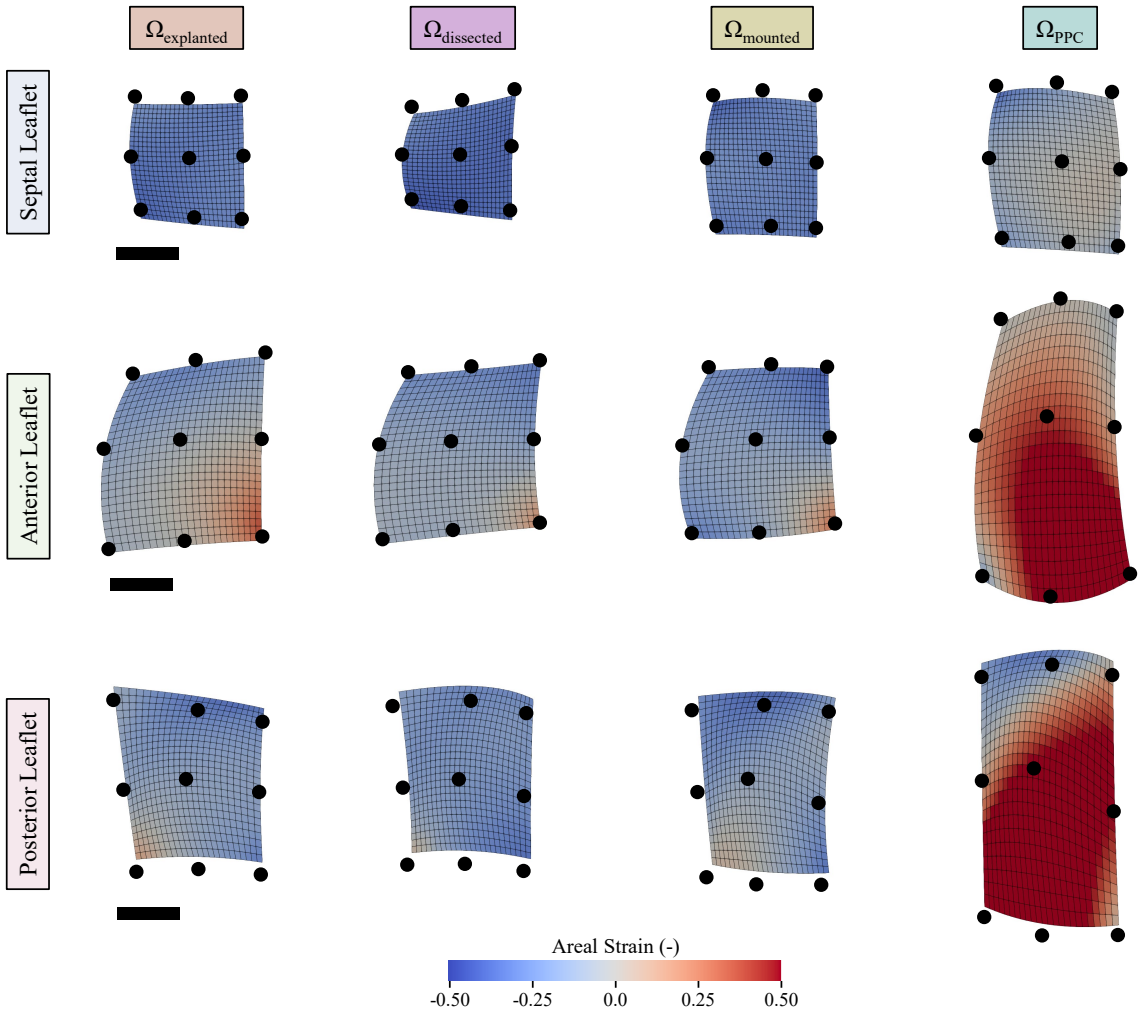

Figure 6-3. Results of the TV leaflets from a representative porcine heart: visualization of the areal pre-strain E_A computed with respect to the explanted configuration ($\Omega_{explanted}$), dissected configuration ($\Omega_{dissected}$), mounted configuration ($\Omega_{mounted}$), and PPC configuration (Ω_{PPC}). Scale bars 2 mm.

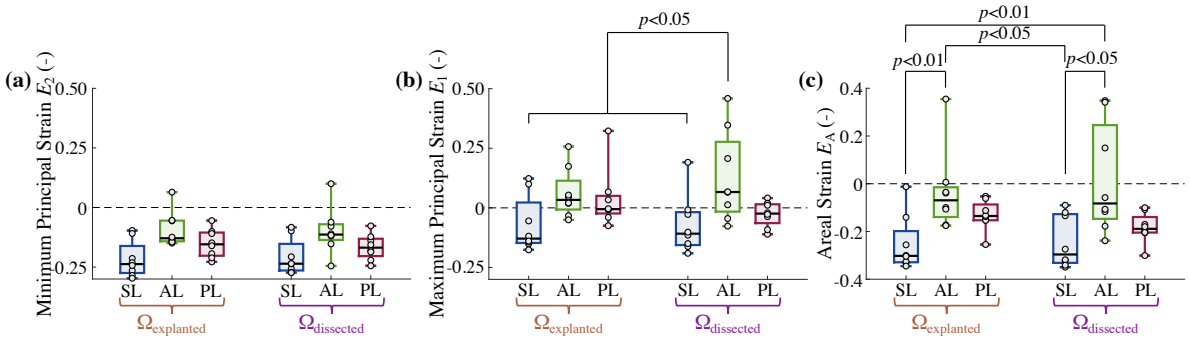

Figure 6-4. Computed pre-strains of the explanted configuration ($\Omega_{\text{explanted}}$) and the dissected configuration ($\Omega_{\text{dissected}}$) with respect to the *ex vivo* configuration (Ω_{exvivo}): (a) the minimum principal strain, (b) the maximum principal strain, and (c) the areal strain.

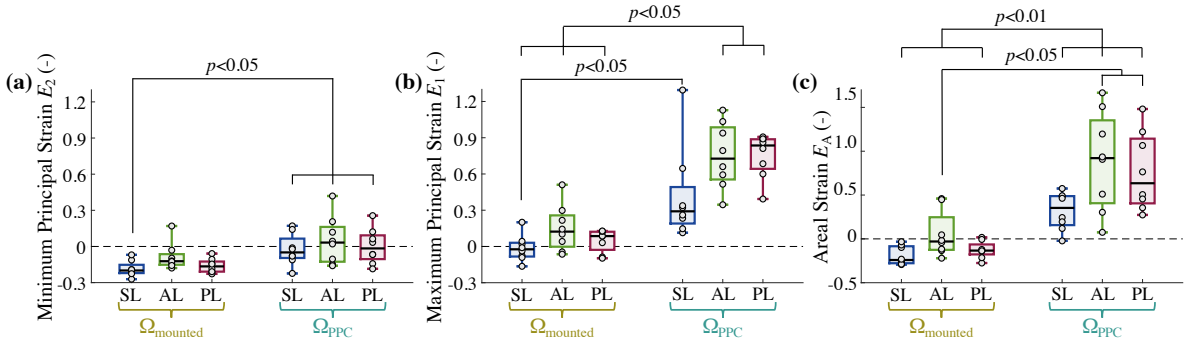

Figure 6-5. Computed pre-strains of the mounted configuration (Ω_{mounted}) and the PPC configuration (Ω_{PPC}) with respect to the *ex vivo* configuration (Ω_{exvivo}): (a) the minimum principal strain (E_1), (b) the maximum principal strain (E_2), and (c) the areal strain (E_A).

Table 6-1. MPSS of the three TV leaflets computed with respect to Ω_{exvivo}.

Leaflet	Configuration			
	Explanted	**Dissected**	**Mounted**	**PPC**
TVSL	0.074 ± 0.021	0.069 ± 0.022	0.086 ± 0.019	0.223 ± 0.084
TVAL	0.076 ± 0.014	0.114 ± 0.032	0.118 ± 0.032	0.351 ± 0.055
TVPL	0.094 ± 0.029	0.070 ± 0.012	0.105 ± 0.018	0.376 ± 0.038

6.1.11 TV Leaflet Biaxial Mechanical Properties Considering *Different Reference Configurations*

The biaxial testing parameters derived with respect to the five reference configurations are presented in **Figure 6-6**. In the tissue's circumferential direction, the only significant differences were found for the TVSL, where the stretches λ_{circ} determined with respect to $\Omega_{dissected}$ (1.486 ± 0.079) and $\Omega_{mounted}$ (1.467 ± 0.075) were significantly larger than those computed with respect to Ω_{exvivo} (1.179 ± 0.058) and Ω_{PPC} (1.169 ± 0.020). On the other hand, the radial stretches λ_{rad} for the TVAL and TVPL determined with respect to Ω_{PPC} (anterior: 1.140 ± 0.022, posterior: 1.127 ± 0.016) were found to be significantly smaller than radial stretches considering the other four configurations (anterior: 1.617-1.741, posterior: 1.741-1.901). The TVSL radial stretches from Ω_{PPC} (1.167 ± 0.032) were only significantly smaller than the stretches determined using $\Omega_{explanted}$ (1.820 ± 0.120) and $\Omega_{dissected}$ (1.710 ± 0.090). Finally, the *AI* became approximately 1.0 for all the three leaflets. This change was significant for the TVAL and TVPL but was not found to be significant for the TVSL.

Specifically, the *AI* for the TVAL was significantly smaller from Ω_{PPC} (0.972 ± 0.032) than Ω_{exvivo} (1.396 ± 0.102) and $\Omega_{\text{explanted}}$ (1.351 ± 0.080). The TVPL anisotropy (0.939 ± 0.006), on the other hand, was significantly different using Ω_{PPC} than all the four remaining configurations (1.238-1.501).

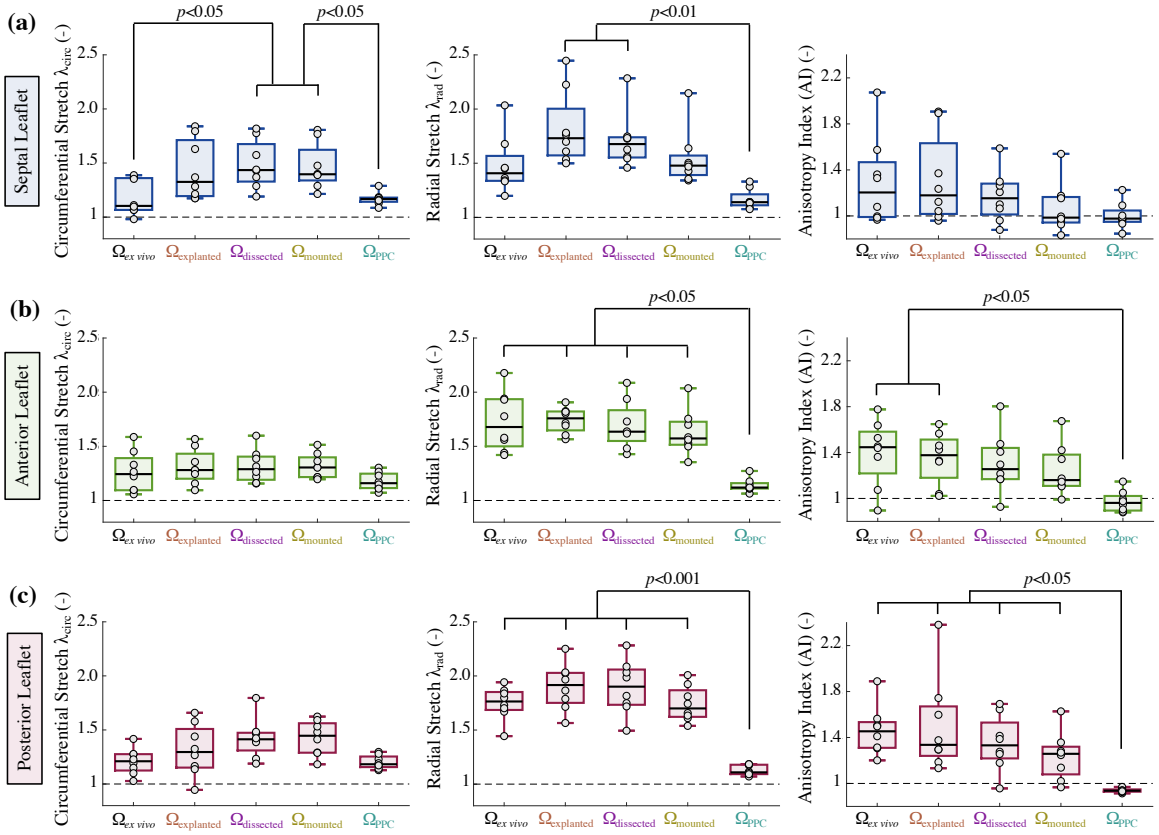

Figure 6-6. (*left*) circumferential stretch λ_{circ}, (*middle*) radial stretch λ_{rad}, and (*right*) *AI* computed with respect to the five reference configurations for: (a) the TVSL, (b) the TVAL, and (c) the TVPL.

6.1.12 Regional Variations in TV Leaflet Areal Pre-Strains

The areal pre-strains E_A of the TV leaflets at the nine isoparametric locations (**Figure 6-2**(b)) are shown in **Figure 6-7** and **Figure 6-8** for the four configurations with reference to Ω_{exvivo}. These results reveal relatively large variations in the pre-strains when compared to the results presented in **Figure 6-4** and **Figure 6-5** for the central location, i.e. $(\xi, \eta) = (0, 0)$ **Figure 6-2**(b). Despite these regional variations, for the explanted areal pre-strains (septal: $+0.021$, anterior: -0.093, posterior: $+0.020$), the dissected areal pre-strains (septal: $+0.019$, anterior: -0.138, posterior: $+0.043$), the mounted areal pre-strains (septal: $+0.061$, anterior: -0.191, posterior: $+0.065$), and PPC areal pre-strains (septal: -0.129, anterior: -0.503, posterior: -0.279), no statistically significant differences were detected.

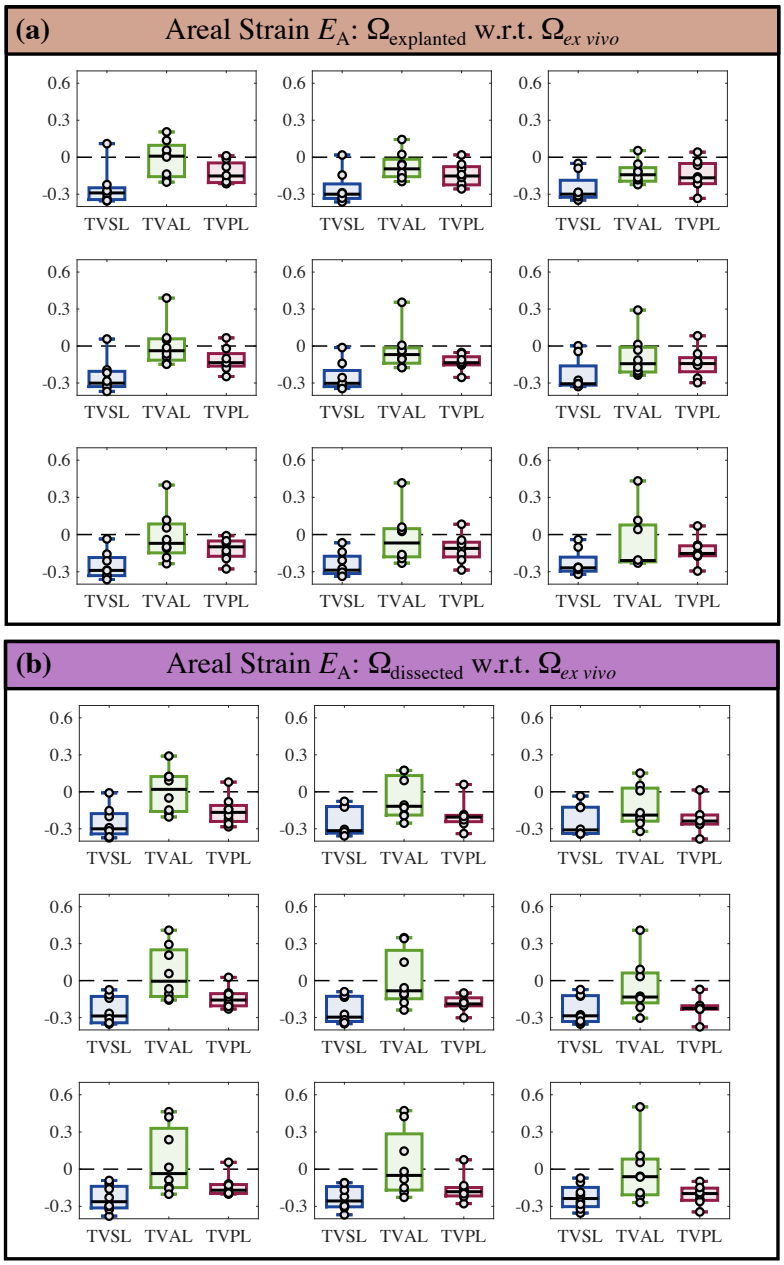

Figure 6-7. Areal pre-strain E_A computed at the nine isoparametric locations (see **Figure 6-2**(b)) for: (a) the explanted configuration ($\Omega_{explanted}$), and (b) the dissected configuration ($\Omega_{dissected}$), with respect to the *ex vivo* configuration (Ω_{exvivo}).

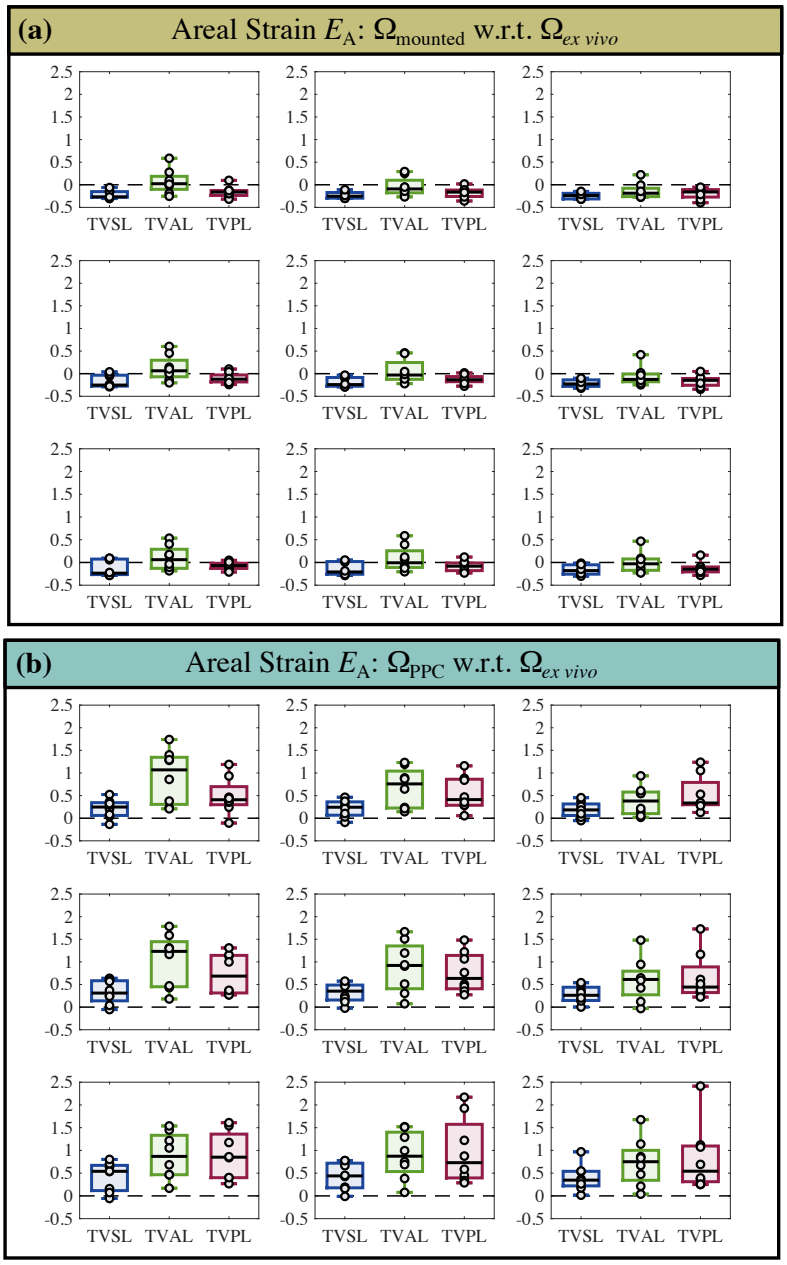

Figure 6-8. Areal pre-strain computed at the nine isoparametric locations (see **Figure 6-2**(b)) for: (a) the mounted configuration ($\Omega_{mounted}$), and (b) the PPC configuration (Ω_{PPC}), with respect to the *ex vivo* configuration (Ω_{exvivo}).

6.1.13 Overall Findings

For the first time, we characterized the *ex vivo* pre-strains for the *TV leaflets*. In the present work, we combined 3D photogrammetry with the reproducing kernel shape function to compute the leaflet pre-strains at four key configurations associated with the common tissue preparation procedures in the *in vitro* mechanical characterization experiments. This integrated approach enabled us to understand the kinematic changes of the central 10×10 mm region for each of the three TV leaflets as it was gradually released from its *ex vivo* configuration and mounted to the biaxial testing device. We further explored how these reference configurations influenced the biaxial mechanical behaviors of the TV leaflets. Specifically, we gained new insights into how the stress-free reference configuration influences the leaflet mechanical properties typically reported in the literature (i.e., λ_{circ}, λ_{rad}, AI).

The Tricuspid Valve Leaflet Pre-Strains

Overall, we found that the three TV leaflets shrunk following excision from the heart. This compressive deformation was smaller in magnitude for the TVAL ($E_A = -0.033$) when compared to the TVSL ($E_A = -0.252$) and TVPL ($E_A = -0.132$). Our previous biaxial mechanical characterization of porcine TV leaflets [67] showed a similar trend with the TVAL being the stiffest among the three TV leaflets. Interestingly, there were much smaller strains following dissection of the central 10×10 mm specimen (E_A=1-5%) compared to when the valve was explanted from the heart. This suggests that most of the pre-strains observed in our experimental setup were due to the release of the annulus and chordae tendineae from their *in situ* connections to the heart chambers.

When the specimens were mounted to the biaxial testing device, we found that they were placed under slight tensile strains from their dissected configurations (E_A=+5-6%). However, this incidental tensile strain during mounting was not sufficient to restore the *ex vivo* leaflet configuration, and all the three leaflets were still mostly under large compressive strains (E_A=-5-19%) This is in accordance with previous suggestions that soft tissues must undergo some type of preconditioning to restore the *in vivo* functioning behaviors [29]. Coincidentally, the equibiaxial force-controlled preconditioning protocol employed herein somewhat restored only the minimum principal pre-strains of the leaflet (E_A=0-5%), but drastically overshot the maximum principal pre-strains (E_A=42-75%). An alternative preconditioning protocol is warranted so that this preconditioning protocol refinement can better restore the pre-strained leaflet configuration for more representative biaxial mechanical characterizations. This protocol could be related to the quantified *in vivo* leaflet strains [7, 103], or simply target the average pre-strains presented in this work.

Qualitative analysis of all our results revealed that the TV leaflet pre-strains were heterogeneous within the fiducial markers. The leaflets oftentimes experienced a combination of compressive and tensile strains when compared to the *ex vivo* configuration, except for the PPC configuration that was primarily large tensile strains. This is in accordance with the previous studies that found heterogeneous leaflet behaviors from refined strain fields [35], varying specimen locations [82], or *in vivo* analyses [103]. However, quantitative analysis showed that the regional differences presented herein were statistically non-significant.

The Impact of Reference Configuration on the Leaflet Biaxial Mechanical Properties

Our use of the reference configurations to determine key biomechanics metrics led us to two key observations. First, the PPC configuration significantly reduced the radial stretch and diminished the mechanical anisotropy (i.e., $AI \approx 1.0$) for the TVAL and TVPL. This is somewhat expected since we also observed large tensile strains for the PPC configuration with respect to the *ex vivo* configuration. However, it is intriguing that the circumferential direction, along with most collagen fibers are aligned [60, 107, 152], experienced no significant changes in the investigated biomechanics-based metrics. Second, the TVSL had a unique combination of changes to the biomechanics-based metrics that did not significantly alter the mechanical anisotropy. Previous studies [60, 107] have also noted distinct microstructural properties for the TVSL, which suggests that the pre-strains may be linked to some unique microstructural feature of the tissue. This is elaborated further next.

Potential Microstructural Drivers of Leaflet Pre-Strains

The leaflet-specific findings found herein may be linked to the underlying leaflet microstructure. Previous imaging studies have noted the TV leaflet collagen fibers are preferentially aligned near the circumferential direction, with less aligned CFAs for the TVSL [60, 107]. The large compressive strains we found for the TVAL and TVPL following valve explantation were approximately aligned with the circumferential direction. On the other hand, the compressive strains for the TVSL were less consistently aligned with the circumferential or radial directions. These findings point to the role of collagen fibers in the leaflet pre-strains, which is in accordance with the fact that collagen fibers are deposited with a pre-stretch during the growth and remodeling process [31, 79]. Further, our results showed that the leaflet radial

stretches computed with respect to the PPC configuration were significantly smaller than with respect to the other configurations. Since the radial direction is orthogonal to the preferred collagen fiber direction, this may have the implications that the collagen fibers may help inhibit the erroneous PPC strains. Future studies can further explore this key connection between tissue microstructure and the observed leaflet pre-strains.

6.1.14 Comparisons with Existing Literature

To the best of our knowledge, no studies have focused on the *TV leaflet* pre-strains. Therefore, this sub-section focuses on placing our findings within the context of the mitral valve, aortic valve, and other porcine tissues.

Experimental Characterizations of the Mitral and Aortic Heart Valves

Amini *et al*. (2012) [8] were the first to quantify the mitral valve anterior leaflet *in vivo* pre-strains using a 2×2 grid of sonocrystals sutured to the central 10×10 mm region of the leaflet. They showed that the leaflet had 16% circumferential pre-strain and 26% radial pre-strain between the "explanted" and *in vivo* configurations. The later investigation by Lee *et al*. (2017) [92] used five sonocrystals in the central region of $n=6$ mitral valve anterior leaflets and found average circumferential and radial pre-strains of 32% and 35% between the *in vivo* and "*ex vivo*" configurations. On the other hand, Aggarwal *et al*. (2016) [2] showed that the aortic valve cusps shrank by ~17% when excised from the heart. Our principal pre-strains (7-21%) are generally smaller than the findings of the mitral valve studies, but in a similar range of the aortic valve investigation. The discrepancies may be attributed to the differences between the heart valves [19, 61, 67], or they could stem from our lack of the *in vivo* unloaded TV

configuration compared to those sonocrystal-based studies. The data of Amini *et al*. (2012) [8] showed an additional 11% circumferential strain and 1% radial strain between the *ex vivo* and *in vivo* configurations, which may serve as a means to bring our pre-strains to a similar level to the mitral valve leaflet counterpart.

Computational Investigations of the Mitral Valve

Rausch *et al*. (2013) [123] incorporated varying levels of the pre-strain into their FE model of a simplified mitral valve geometry. They then used this model to fit the experimental sonocrystal deformations using inverse FE analysis. Their FE model with 30% homogeneous areal pre-strain provided the best predictions of the uniaxial data presented by May-Newman and Yin (1998) [106]. This predicted pre-strain is much larger than our present findings for the TV leaflets as well as the pre-strains presented by Amini *et al*. (2016) [8], but agrees better with the more isotropic pre-strains reported by Lee *et al*. (2017) [92]. More recently, Prot and Skallerud (2017) [120] performed a similar computational investigation using a complete mitral valve apparatus acquired from echocardiographic measurements. They found that an areal pre-strain of 22% could result in non-realistic leaflet motions and incomplete leaflet coaptation. Our experimentally determined TV leaflet pre-strains fall within this threshold, except for the TVSL. Interestingly, this threshold is larger than the experimental findings of Amini *et al*. (2016) [8] and Lee *et al*. (2017) [92], suggesting that the pre-strains are spatially varying to allow the complete mitral valve closure. Finally, the study by van Keele *et al*. (2019) [154] combined the mitral valve computational model developed by Rausch *et al*. (2013) [123] with the mechanobiology model of Loerakker *et al*. [100, 101] to understand if the pre-stretches are related to traction forces generated by cells within the tissue. They found that the

cells generated circumferential and radial pre-strains of 18% and 22%, respectively, which were also much larger than the pre-strains presented herein for the TV leaflets.

Experimental Characterizations of Pre-Strains for other Porcine Tissues

Buganza Tepole *et al*. (2015) [21] used stereo cameras to determine that the pre-strains of porcine skin were on the order of 23%. The authors later refined their approach to consider smaller regions for their pre-strain analysis [22] and discovered substantial variations in the pre-strain that, when averaged, were much larger than their previous findings. For ventricle tissue, Genet *et al*. (2015) [50] used a computational model of the left ventricle wall to understand what the levels of pre-strain generated via growth and remodeling processes could replicate their opening angle experiment. They found that a range of pre-strains (6-17%) led to reasonable predictions of the ventricle opening angle. Finally, Sigaeva *et al*. (2019) [140] recently expanded the seminal work of Chuong and Fung (1986) [29] and found the strains on the order of −7% to +15% throughout the wall of a porcine aorta following incision. Compared to these collective results, it appears that the porcine TV leaflet pre-strains are smaller than the skin pre-strains, in a similar range to the left ventricle pre-strains, and potentially larger than the aorta pre-strains. Differences among the methodologies and techniques may confound these results, and further studies could compare the pre-strains in a more controlled/comparable environment.

6.1.15 Study Limitations

This study is not without limitations. First, we only focused on the pre-strains within the central 10×10 mm of each leaflet. Previous studies have highlighted the spatially varying properties

of the TV leaflets [82]. It is also known that the TV leaflet layers have unique microstructures and mechanical behaviors [74]. Future studies must consider these regional and transmural variations when investigating the pre-strains or when incorporating them into computational models of the TV. Second, user bias in the fiducial marker selection will influence the 3D marker locations determined using photogrammetry. We attempted to limit the influence of such bias by having one user for all porcine hearts ($n = 8$). Our verification of the photogrammetry method presented in Appendix E showed small discrepancies (< 0.5 mm) when comparing the predictions against the ground truth. This user bias may be circumvented via automatic marker selection techniques (e.g., Otsu's method [112]), and the distance errors could possibly be further reduced by expanding on the number of cameras used with the direct linear transformation (see Figure 4 of [21]). Third, we were only able to experimentally characterize the *ex vivo* pre-strains of the TV leaflets. There are pre-strains released by removing the heart from the animal subject [8], and the pre-strains likely released by opening the RV before fiducial marker placement. Future studies should use more controlled animal models in combination with our *ex vivo* techniques to holistically determine the pre-strains of the TV leaflets. Finally, our approach did not allow us to monitor the changes in the leaflet thickness across the configurations considered herein. It is common for heart valve-focused studies to assume that the leaflets are incompressible [126, 162], which should be carefully examined in future studies using our pre-strain quantification process.

6.1.16 Future Extensions

There are several potential extensions of this work in addition to addressing our study limitations (Section 6.1.15). First, we have considered the pre-strains associated with releasing

the tissue from its *in-situ* environment, but not the intrinsic pre-strains at a given location. Future investigations could take inspiration from a recent tympanic membrane study by Livens *et al*. [99] that used micro-incisions to release the local tissue pre-strains, or the work of Buganza Tepole *et al*. [22] that sub-divided their porcine skin specimens to reveal the local pre-strains. Second, there is substantial evidence from our results that the pre-strains are related to the underlying tissue microstructure. This relationship could be explored in future works by combining our novel benchtop method with advanced imaging techniques, such as pSFDI (i.e., CFA) [60], optical coherence tomography (i.e., microstructural morphology) [83] or multi-photon microscopy (i.e., constituent distributions) [107]. Finally, we have shown that equibiaxial force-controlled preconditioning to 40 N/m (280 mN) does not appropriately restore the *ex vivo* pre-strains. An extension of this work could determine better *in vitro* techniques to restore the tissue pre-strains prior to biaxial mechanical characterizations. These could be different biaxial force ratios, force-controlled vs. displacement-controlled preconditioning, and/or a new protocol that applies strains matching our pre-strains presented in this study. These extensions, among others, will significantly advance the field of TV tissue biomechanics and allow accurate pre-strains to be considered in computational predictions of the valvular function.

6.1.17 Conclusion

This study has provided the first benchtop characterization of the TV leaflet *ex vivo* pre-strains. We have shown that the TV leaflets shrink following excision from the *ex vivo* heart, with the TVSL having more compressive changes. These deformations have slight, non-significant spatial variations within the central 10×10 mm leaflet region. Interestingly, no significant

differences have been found between the strains in the explanted or dissected configurations for a given leaflet. This further suggests that most of the pre-strains were released by dissecting the valve from its *in situ* environment. The dissected specimens have then been mounted to a biaxial testing device to understand how the common stress-free configurations for mechanical characterizations compare to the *ex vivo* reference configuration. Upon mounting to the system, the leaflets were placed under slight tensile strains from their dissected configuration but were still compressed from their *ex vivo* configuration. The tensile changes were magnified following equibiaxial preconditioning with significant changes in the maximum principal strain and areal strain. These observed changes at the four configurations have then been placed within the context of common biomechanics-focused metrics obtained during biaxial mechanical testing. One key observation from this analysis has been that the large tensile strains placed on the tissue following preconditioning resulted in significant under-predictions of the radial tissue stretches and material anisotropy. This observation leads us to believe that the employed equibiaxial force-controlled preconditioning protocol is not ideal for restoring the *in vivo* TV leaflet behaviors. Extensions of this work should determine a more appropriate TV-specific preconditioning protocol.

6.2 An *In-Silico* Benchmark for the Tricuspid Valve

The substantial increase of experimental studies for the TV within the past decade has enabled researchers to develop *in-silico* computational frameworks for the TV. These frameworks have provided new insight into how common pathologies influence TV function, the potential of alternative surgical interventions for addressing TR, or the efficacy of new computational

techniques (e.g., contact algorithms). Despite these notable advancements stemming from the *in-silico* developments, there are several limitations that may hinder or prevent future discoveries. For example, variations in TV geometry can drastically influence the closing behavior of the valve and limit comparisons across studies when comparing findings. Furthermore, TV closure is complex with many features (e.g., self-contact or buckling) that can significantly increase computation time. Thus, it would be advantageous to establish an *in-silico* benchmark for the TV that considers a simplified geometry. Such a development would enable consistent comparisons among studies developing new *in-silico* approaches for simulating cardiac valve closure that are computationally-efficient.

6.2.1 Tricuspid Valve Model Geometry and Mesh

The idealized TV geometry shown in **Figure 6-9**(a) was prepared using B-spline curves and surfaces within the Rhino software (Robert McNeel & Associates, Seattle, Washington). Specific details necessary to reproduce the idealized geometry are provided in **Figure 6-10**. In brief, the TV annulus was represented using an oval shape with major and minor axis dimensions of 30 mm and 20 mm, respectively (**Figure 6-9**(b)). A uniform leaflet height of 15 mm was used to generate the leaflet surfaces, and the papillary muscles were located 10 mm below the leaflet free edge (**Figure 6-9**(c)). These dimensions were selected to provide a realistic representation of typical porcine TV dimensions [69, 84].

To create the mesh of the TV geometry, the leaflet surface was discretized into 18,960 shell elements (S4) using an approximate global seed size of 0.25 mm, while each chordae was represented using one 3D truss element (T3D2). We assumed a uniform leaflet thickness of

0.396 mm [70] and a uniform chordae radius of 0.23 mm [70]. The chordae insertions into the leaflets were represented using shared nodes between the chordae and leaflet elements (see **Figure 6-9**).

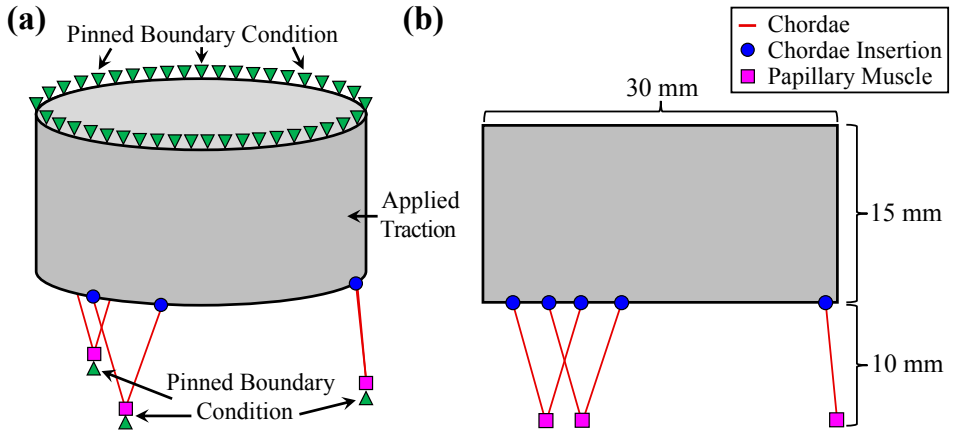

Figure 6-9. The idealized TV geometry: (a) isometric view with labeled boundary and loading conditions and (b) side view showing the dimensions as well as the papillary muscle and chordae insertion locations.

6.2.2 Material Models

In accordance with the previous cardiac valve biomechanics studies (e.g.,[161]), we assume the TV leaflets are transversely isotropic an incompressible solids [58]. Hence, the TV leaflets were modeled using the Lee-Sacks hyperelastic SEDF [88]

$$W = \frac{c_0}{2}(I_1 - 3) + \frac{c_1}{2}\left(\delta e^{c_2(I_1-3)^2} + (1-\delta)e^{c_3(I_4-1)^2} - 1\right) - p(J-1) \qquad (6.2)$$

Herein, $c_0 = 10\,\text{kPa}$, $c_1 = 0.209\,\text{kPa}$, $c_2 = 9.046$, and c_3 are the material parameters [69], and δ represents the collagen fiber alignment where $\delta = 0$ indicates perfectly aligned collagen

fibers (i.e., anisotropic material) and $\delta = 1$ indicates randomly oriented collagen fibers (i.e., isotropic material) [88]. For the purpose of this TV *in-silico* benchmark, we only considered the *isotropic* component of Eq. (6.2) (i.e., $\delta = 1$) so the I_4 term in Eq. (6.2)vanishes. However, the CFA information, such as that acquired via pSFDI [68], could be incorporated into the material model, rendering the *anisotropic* material behaviors typically observed in planar biaxial mechanical characterizations. $p = 2(\partial W / \partial I_1) / (\mathbf{C}^{-1})_{33}$ is analytically determined by considering the tissue incompressibility and assuming a plane stress condition.

The chordae were modeled as a Saint Venant-Kirchhoff material without the Poisson effect:

$$S_{11} = (\lambda + 2\mu)E_{11}, \tag{6.3}$$

where λ and μ are the Lamé constants. Considering a Young's modulus *E*=40 MPa and a Poisson's ratio $\upsilon = 0$ [70], the Lamé constants are $\lambda = 0$ MPa and $\mu = 20$ MPa.

The implementations of the material models within the Abaqus `VUMAT` subroutine were verified using the analytical solutions for a chordae undergoing uniaxial tension (Eq. (6.3)) and TV leaflet undergoing equibiaxial tensions. The analytical stresses for the leaflets were computed using

$$\mathbf{S} = 2\frac{\partial W}{\partial \mathbf{C}} = -p\mathbf{C}^{-1} + 2\frac{\partial W}{\partial I_1}\mathbf{I} + 2\frac{\partial W}{\partial I_4}\mathbf{m}\otimes\mathbf{m}, \tag{6.4}$$

considering the SEDF in Eq. (6.2), with $\mathbf{m}$ describing the preferred collagen fiber orientation, which was not considered in this exploratory study. The analytical stresses for the chordae were computed using the stress-strain relationship in Eq. (6.3). The agreement between the FE and analytical stresses for both the TV leaflet (**Figure 6-11**(a)) and the chordae (**Figure**

6-11(b)) indicated successful implementation of the material models in the `VUMAT` subroutine.

6.2.3 Boundary and Loading Conditions

Three simplifications were made regarding the boundary and loading conditions. First, for simplicity we assumed the TV annulus and chordae tendineae were pinned throughout the simulation, although these are dynamic structures during *in vivo* cardiac function [42, 46]. Second, the time-varying transvalvular pressure typically experienced by the TV leaflets (see Figure 5 of [7]) was simplified as a linear increase to 25 mmHg over 0.005 s that was maintained for a total simulation time of 0.4 s. The simulation was performed using Abaqus Explicit dynamics with a viscous damping pressure of 5×10^{-6} MPa·s and a maximum time step of 1×10^{-6} s in adaptive time stepping to ensure proper convergence.

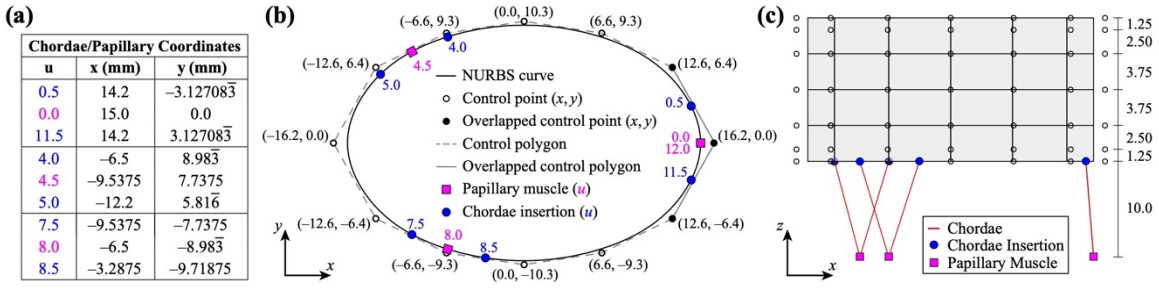

Figure 6-10. Definition of the idealized TV geometry: (a) Table of chordae insertions and papillary muscle parametric coordinates (u) and corresponding X- and Y-coordinates, (b) top view showing the oval-shaped valve curve, control points, and papillary muscle and chordae insertion locations, and (c) side view showing the distance between control points. All X-, Y-, and Z-coordinate and distances are in millimeters (mm). The knot vectors are {-3, -2, -1, 0, 1, 2, 3, 4, 5, 6, 7, 8, 9, 10, 11, 12, 13, 14, 15} and {0, 0, 0, 0, 1, 2, 3, 4, 4, 4, 4} in the circumferential and vertical directions, respectively.

6.2.4 Visualization of the Simulation Results

Additional steps were performed to visualize the simulation results stored in the Abaqus `*.odb` binary file. First, the results from each output frame were converted to an ASCII `.txt` file by running a custom batch file in the command prompt. Next, the ParaView `*.vtk` file for each frame was generated by running an in-house MATLAB script. The resulting `.vtk` file can be opened using the ParaView `Visualize.pvsm` state file for customizable visualization (see **Figure 6-12**) of the simulation results.

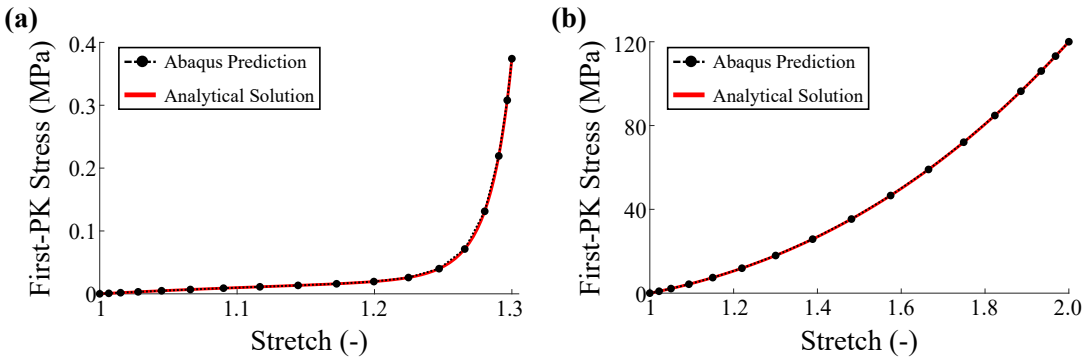

Figure 6-11. Verification of the `VUMAT` subroutines: (a) the TV leaflet under equibiaxial tension, and (b) the TV chordae under uniaxial stretching.

It is important to note the localized buckling of the TV leaflets in this *in-silico* benchmark may result in multiple simulation solutions. This could stem from differences between computers, variations in domain discretization (not employed herein), possible machine errors, or the use of different simulation approaches. We have not yet observed this phenomenon in our *in-silico* benchmark. However, the companion article [69], which employed isogeometric analysis,

demonstrated multiple solution configurations considering varying levels of mesh refinement.

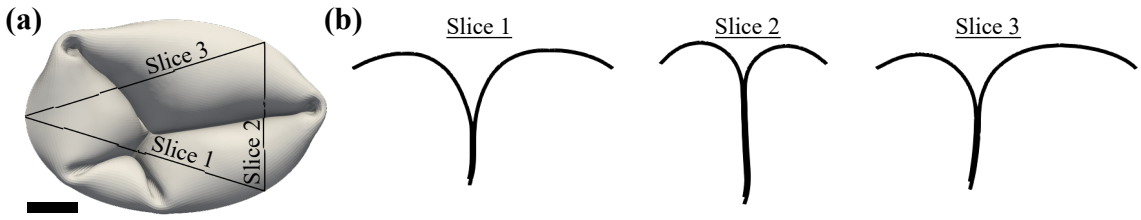

Figure 6-12. ParaView visualization of the Abaqus simulation result: (a) top view with labeled slice views and (b) various slice views. Scale bar = 5 mm.

6.3 *In-Silico* Consideration of Tricuspid Valve Leaflet Pre-Strains

6.3.1 Implementation of Pre-Strains into the Finite Element Simulations

We then aimed to use the developed *in-silico* benchmark to understand how the experimentally determined pre-strains influence *in-silico* predictions of the TV behavior. In brief, we used a three-step simulation process to embed the leaflet pre-strains into the FE simulations before simulating the valve closure. First, the TV nodes were imported into MATLAB and uniformly contracted by the circumferential and radial pre-strains outlined in Section 6.3.2. This contracted geometry was then imported into Abaqus for the first-step simulation whereby the nodes were displaced to their original configuration. This step embeds the pre-strains into the FE simulation. Finally, the TV closure was simulated via the boundary and loading conditions outlined in Section 6.2.3. Through this three-step process, we can explore how various degrees of isotropic or anisotropic pre-strains influence the predicted TV function.

6.3.2 Study Scenarios

We considered several *isotropic* and *anisotropic* combinations of circumferential and radial pre-strains. Past studies have shown the heart valve leaflet pre-strains can be as large as 30-35%; however, our preliminary simulations showed that 25% pre-strain was sufficient to capture a wide range of pre-strain effects. Thus, we considered all combinations of 5%, 10%, 15%, 20%, and 25% circumferential/radial pre-strains.

6.3.3 Influence of Pre-Strains on the Predicted Valve Behavior

The predicted systolic TV configurations for various isotropic combinations of pre-strains are shown in **Figure 6-13**. We observe the leaflet stresses increase with increased pre-strain, which is likely due to the inherent initial pre-stress within the leaflets stemming from the pre-strains. The model considering no pre-strains has a leaflet belly stress on the order of 60 kPa, which approximately doubles to 100 kPa when 20% pre-strain is implemented into the model. Additionally, the systolic TV configuration changed substantially across the simulation scenarios. The simulation scenario considering no pre-strains had atypical protrusions of the leaflets above the annulus near the commissures. This strange, closed configuration was remediated by incorporating 5% pre-strain, and the leaflets were no long protruding above the annulus. Interestingly, when considering 20% pre-strain, there is a large regurgitant orifice that forms in the center of the TV. The changes to the geometry with respect to the circumferential and radial pre-strains are further discussed in Section 6.3.4.

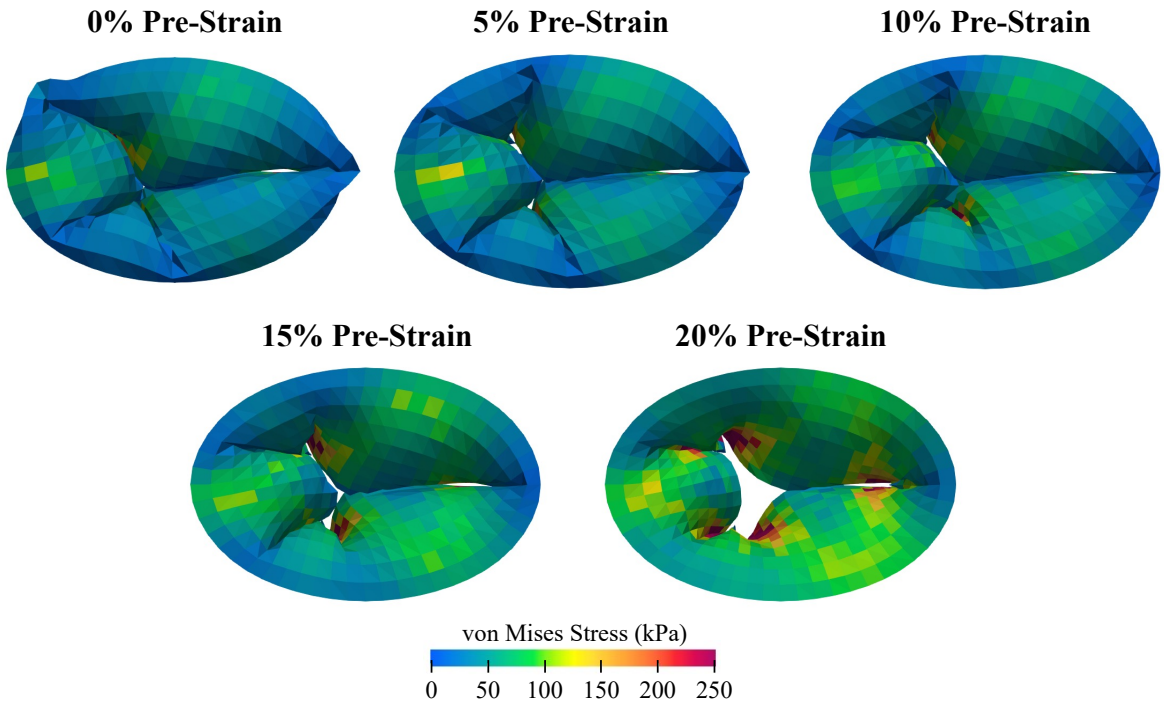

Figure 6-13. FE predictions of the TV closure considering four levels of isotropic pre-strains.

6.3.4 Alterations to the Leaflet Coaptation

The isolated effects of circumferential and radial pre-strains on Slice View 2 (**Figure 6-12**) are shown in **Figure 6-14**. The increasing pre-strains restrict the TV leaflet closure, resulting in coaptation farther below the annulus plane and less leaflet contact area. The effects of radial pre-strains appear to influence the closed TV geometry more, although the circumferential pre-strains still restrict the leaflet motion to some degree.

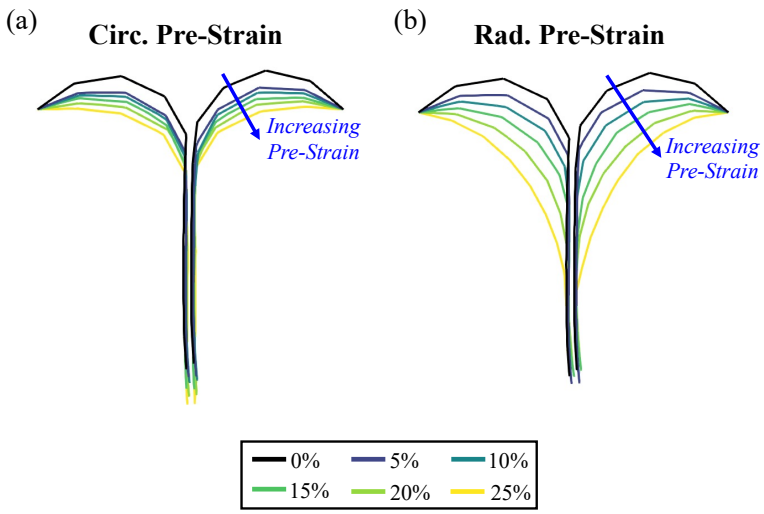

Figure 6-14. Predicted changes in the coaptation for Slice View 2 (see **Figure 6-12**) considering isolated pre-strains in the (a) circumferential direction and (b) radial direction.

6.3.5 Discussion

This study has provided the first *in-silico* simulations of the TV function considering leaflet pre-strains. Our simulations show that the pre-strains can nearly double the predicted leaflet stresses and lead to noticeable regurgitation. Furthermore, we have isolated the effects of circumferential and radial pre-strains, and our simulations suggest that radial pre-strains have more influence on the closed TV geometry. The *ex vivo* pre-strain quantification presented in Section 6.1 demonstrated that the TV leaflets can express pre-strains on the order of 5-20% when dissected from the heart. However, our simulations herein showed large variations in the valve behavior across this range of pre-strain. The *in-silico* prediction with 5% pre-strain mitigated some of the unrealistic leaflet excursion above the annulus plane, whereas 20% pre-strain resulted in significant TR. Therefore, it is likely that the pre-strains are valve-specific and require a specific combination of leaflet-specific pre-strains to prevent regurgitation.

Future studies should explore these ideas considering leaflet-specific pre-strains embedded within realistic TV geometries whose systolic configuration can be verified against imaging data.

CHAPTER 7 Conclusions and Future Work

7.1 Conclusions

The results presented in this dissertation sought to enhance our understanding of the TV leaflet multi-scale properties and intrinsic pre-strains. We first provided novel multi-scale characterizations of the TV leaflet mechanical properties, CFA properties, and microstructural properties. Then, we further evaluated the role of the tissue microstructure in the TV leaflet mechanical behaviors. We next turned our attention towards *in-silico* developments by first developing new approaches for modeling the TV leaflet mechanical behaviors. Finally, we linked our *in vitro* characterizations to the *in vivo* TV functioning behaviors by providing the first quantification of the TV leaflet pre-strains. The role of these pre-strains was further explored in our established *in-silico* benchmark for the TV. The research developments and key observations are summarized below.

7.1.1 Multi-Scale Experimental Characterizations of the Tricuspid Valve Leaflets

We characterized the properties of the TV leaflets at the tissue-level, the mesoscale-level, and the microstructural level. First, we characterized mechanical properties of the three TV leaflets and observed that the properties changed when varying the effective specimen size (Section 3.1). Next, we characterized the TV CFA at the mesoscale using our integrated opto-mechanical device that leverages pSFDI (Section 3.2). Our results showed that the TV leaflets have two fiber families: one circumferential fiber family that was oriented 25°-30° from the circumferential direction and another radial fiber family aligned approximately with the radial direction. These fiber families were observed to rotate under various biaxial tensions, although

less than the more well-defined fiber families of the AV cusps and the coronary arteries. Finally, we used a confocal microscope with multiphoton imaging and SHG to visualize the microstructure of all three TV leaflets (Section 3.3). The SHG revealed there were two structural arrangements of collagen found in the leaflets: (i) the *atrialis* included disorganized, cloud-like collagen fibers and (ii) the *fibrosa* contained highly crimped and circumferentially aligned collagen fibers. On the other hand, the autofluorescence signal from multiphoton imaging revealed random networks of elastin fibers in the *atrialis* and the *ventricularis* layers.

7.1.2 Experimentally Relating the Tricuspid Valve Leaflet Mechanical Behaviors to the Underlying Microstructure

We further leveraged our established biaxial testing protocols to elucidate how the TV leaflet microstructures contributed to the bulk tissue mechanical behaviors. First, we separated all three TV leaflets into their composite A/S layers and composite F/V layers. Subsequent biaxial mechanical characterizations showed that the composite layers were stiffer and less anisotropic than the intact tissue. Interestingly, the pSFDI characterization showed no obvious differences between the intact tissues and their composite layers. However constitutive model-based analysis revealed that the collagen fiber ensembles of the TV composite layers were mechanically stiffer. This difference should be explored further. In addition to the layer investigation, we used an iterative enzyme-based approach to explore how the collagen and elastin fibers independently contribute to the TV leaflet mechanical behaviors. Most notably, our investigation showed that tissues with degraded collagen fibers were more compliant in the high-stress region, while tissues with degraded elastin were stiffer. These findings supplement our previous enzyme-based investigation of how GAGs contribute to the TV

leaflet mechanical behaviors. Through our investigations we have provided a holistic relationship between the TV leaflet mechanical behaviors and their underlying microstructural constituents and morphology.

7.1.3 Modeling of the Tricuspid Valve Leaflet Mechanical Behaviors

For modeling the TV leaflet mechanical behaviors, we first explored the use of constant invariant mechanical characterizations to determine a SEDF for the TV leaflets. The results from our mechanical characterization suggested that one SEDF was sufficient to describe the mechanical behaviors of all three leaflet. We then determined the most appropriate SEDF for the TV leaflets from three candidate models: (i) a polynomial SEDF, (ii) an exponential SEDF, and (iii) a combined polynomial-exponential SEDF. Our fitting and optimality criteria analysis revealed that the exponential SEDF was best suited for the TV leaflets due to its superb fitting capabilities and well-defined parameter space. Furthermore, we presented findings that suggest the coupling of model parameters within the exponential term is important for accurately capturing the leaflet behaviors. In addition to our constant invariant characterizations, we applied an emerging LCDD modeling technique to the atrioventricular heart valve leaflets and compared its performance with a well-established structural constitutive model. This novel approach directly employed the experimental data to model the leaflet mechanical behaviors rather than relying on a specific constitutive model form. We showed that, provided sufficient data for training, the LCDD method provided superb fits and predictions of various biaxial tension protocols typically employed in soft tissue biomechanical characterizations.

7.1.4 Experimental Characterization and *In-Silico* Consideration of TV Leaflet Pre-Strains

We further sought to link our *in vitro* experimental findings to the *in vivo* TV behaviors through *in-silico* simulations. Inspired by previous characterizations for the mitral valve leaflets, we provided the first benchtop characterization of the TV leaflets. Our findings showed the leaflets were pre-strained in their *in-situ* configurations, which were immediately released following TV excision from the heart. We then leveraged our established biaxial testing protocols to explore how the choice of stress-free reference configuration influenced the observed *in vitro* mechanical behaviors. The most intriguing finding was that, when computed with respect to the *post-preconditioning* configuration, the leaflet stretches were significantly smaller and more isotropic than when considering any other configuration. This observation has significant implications for TV biaxial mechanical characterizations and suggests that our preconditioning protocol must be revisited to better restore the realistic leaflet functioning behaviors. We then established a simplified *in-silico* benchmark for the TV leaflets for evaluating new computational methods (e.g., contact algorithms). In particular, we used this benchmark to explore how the experimentally derived pre-strains could influenced the predicted TV behaviors. Interestingly, for the simplified TV geometry, the pre-strains had profound impacts on the FE predictions: (i) the leaflet stresses nearly doubled with 20% pre-strain and (ii) the pre-strains significantly altered the closed TV geometry, resulting in severe TR with 20% pre-strain. Our further analysis revealed that the radial pre-strains may have larger impacts on the TV behaviors.

7.2 Recommendations for Future Research

We conclude this dissertation by recommending the following topics for future research studies:

(1) *Development of a multi-scale in-silico framework for the soft biological tsisues*

The investigations in Chapters 3 and 4 provided multi-scale connections between the TV leaflet mechanical properties, mesoscale CFA, and microstructural morphology. This information can be used to develop a multi-scale *in-silico* framework for soft tissue biomechanics that successfully links organ-level behaviors to microstructural phenomena. Our methods are easily applicable to other soft tissues besides the TV leaflets, providing a versatile multi-scale characterization framework. For example, see our recent multi-scale characterization of one resected human intracranial aneurysm tissue. Researchers could employ the developed multi-scale frameworks to understand how variations in tissue microstructure or diseased conditions alter tissue function.

(2) *Enhanced confocal microscopy characterization of the TV leaflets*

In Chapter 3, we used confocal microscopy with a refined optical clearing method to image the microstructures of TV leaflets via autofluorescence and SHG. This investigation provided rich information of the TV leaflet layered morphology, but we were unable to differentiate between various microstructures due to the lack of biomarkers. Future investigations may consider incorporating various dyes or immunohistochemical markers to delineate the elastin fibers, VICs, or other non-fibrous constituents (e.g., GAGs) in the autofluorescence signals. Additionally, we only imaged non-fixed TV leaflets and did not explore the load-dependent properties. Our

mesoscale CFA results from Chapter 3 highlighted that the birefringent collagen fibers adapted to applied loading, and confocal microscopy can be used to better understand these behaviors. Particularly, researchers can seek to understand the contributions of the cloud-like collagen fibers of the *atrialis* and the highly crimped, aligned collagen fibers of the *fibrosa*.

(3) *Refined experimental investigations linking TV microstructure to mechanics*

The mechanical and CFA characterizations presented in Chapter 4 linked the TV leaflet mechanics and microstructure. These studies provided basic insight into how the constituents contribute to the bulk TV leaflet mechanical behaviors; however, there are several refinements that could enhance the value of the data. For example, we characterized the tissues following 2-hour enzymatic degradation of collagen and elastin to remove >50% of either constituent, but the enzymatic degradation was a gradual process. One future study could investigate the changes in TV leaflet mechanical behaviors following smaller treatment times to provide a refined relationship between tissue microstructural constituent fractions and bulk tissue mechanical behaviors. This information could be leveraged to develop material models that provide accurate predictions of the mechanical behaviors considering fractional values of each constituent. Moreover, our studies have only focused on the isolated contribution of GAGs, collagen fibers, and elastin fibers, but the results from our layer investigation suggested that the interactions between constituents are important to recover the complete TV leaflet mechanical behaviors. Another future extension of this work could consider combining degradation steps to enzymatically digest several

constituents and better isolate the contribution of a given non-degraded constituent. This work could be supplemented using our described confocal microscopy to further understand the associate changes at the microstructural level.

(4) *In vivo characterization of in-silico implementation of the TV leaflet pre-strains*

Chapter 6 included the first benchtop characterization and *in-silico* implementation of the TV leaflet pre-strains. One limitation of our investigation was the lack of *in vivo* information for the leaflets. Specifically, a previous study for the mitral valve showed that there were non-negligible pre-strains removed when excising the heart from its *in vivo* configuration. Future investigations should refine our presented technique to consider the *in vivo* configuration through image-based analysis or the *in vivo* implantation of sonocrystal fiducial markers. Moreover, the acquired information could be embedded within *in-silico* frameworks for the TV leaflet, such as those proposed in **Future Extension** Item (1). This additional step would help complete the link between *in vitro* characterizations and *in vivo* tissue function and provide more realistic predictions of the TV function.

APPENDIX A Nomenclature

Table A-1: Description of the abbreviations used throughout the Dissertation.

Group	Abbreviation	Description
Anatomy	AV	Aortic Valve
	MV	Mitral Valve
	MVPL	Mitral Valve Posterior Leaflet
	PV	Pulmonary Valve
	RA	Right Atrium
	RV	Right Ventricle
	TV	Tricuspid Valve
	TVAL	Tricuspid Valve Anterior Leaflet
	TVPL	Tricuspid Valve Posterior Leaflet
	TVSL	Tricuspid Valve Septal Leaflet
	TR	Tricuspid Regurgitation
Confocal Microscopy	BABB	Benzyl Alcohol/Benzyl Benzoate
	HyD	Hybrid Detector
Constitutive Modeling	$\mathbf{C}$	Right Cauchy-Green Deformation
	δ	Degree of Anisotropy
	DEO	Differential Evolution Optimization
	DD	Data-Driven
	DMDD	Distance-Minimization Data-Driven
	$\mathbf{E}$	Green-Lagrange Strain
	E_{ens}	Fiber Ensemble Strain
	$\mathbf{F}$	Deformation Gradient
	Γ	Fiber Orientation Distribution Function
	$\mathbf{I}$	Identity Tensor
	I_1	First Invariant of $\mathbf{C}$
	I_2	Second Invariant of $\mathbf{C}$

	I_3	Third Invariant of **C**
	I_4	Fourth Pseudo-Invariant of **C**
	I_5	Fifth Pseudo-Invariant of **C**
	LCDD	Locally Convex Data-Driven
	N	Preferred Fiber Orientation
	N_{pop}	Number of Parameter Sets in Population
	P	First Piola Kirchhoff Stress
	S	Second Piola Kirchhoff Stress
	SEDF	Strain Energy Density Function
	S_{ens}	Fiber Ensemble Stress
	W	Strain Energy Density
	$W_{,1}$	Partial Derivative of W w.r.t. I_1
	$W_{,4}$	Partial Derivative of W w.r.t. I_4
Heart Function	ED	End Diastole
	ES	End Systole
Mechanical Testing	AI	Anisotropy Index
	circ	Circumferential Leaflet Direction
	E^{HT}	High-Tensile Modulus
	E^{LT}	Low-Tensile Modulus
	κ	Tissue Shear Deformation
	L	Tissue Effective Edge Length
	λ	Tissue Stretch
	MPSS	Maximum Principal Shear Stress
	PPC	Post-Preconditioning
	PSX	Pure Shear Loading in the X-direction
	PSY	Pure Shear Loading in the Y-direction
	rad	Radial Leaflet Direction
	t	Tissue Thickness
	T	Membrane Tension
Numerical Methods	FE	Finite Element

	RK	Reproducing Kernel
Microstructure	A	Atrialis
	AFK	Affine Fiber Kinematics
	CFA	Collagen Fiber Architecture
	DOA	Degree of Optical Anisotropy
	DLP	Digital Light Processing
	F	Fibrosa
	GAG	Glycosaminoglycan
	pSFDI	Polarized Spatial Frequency Domain Imaging
	S	Spongiosa
	SHG	Second Harmonic Generation
	θ_{fiber}	Preferred Fiber Orientation
	V	Ventricularis
	VIC	Valvular Interstitial Cell
Other	2D	Two-Dimensional
	3D	Three-Dimensional
	CCD	Charge-Coupled Device
	DI	Deionized
	DIC	Digital Image Correlation
	NRMSD	Normalized Root-Mean Square Error
	PBS	Phosphate Buffered Saline
	Q-Q	Quantile-Quantile
	ROI	Region of Interest
	SEM	Standard Error of the Mean
	USDA	United States Department of Agriculture

APPENDIX B The Effect of Specimen Size on TV Leaflet Non-Equibiaxial Mechanical Behaviors

This appendix presents the mechanical behaviors of the three TV leaflets from Section 3.1 for the non-equibiaxial loading protocols.

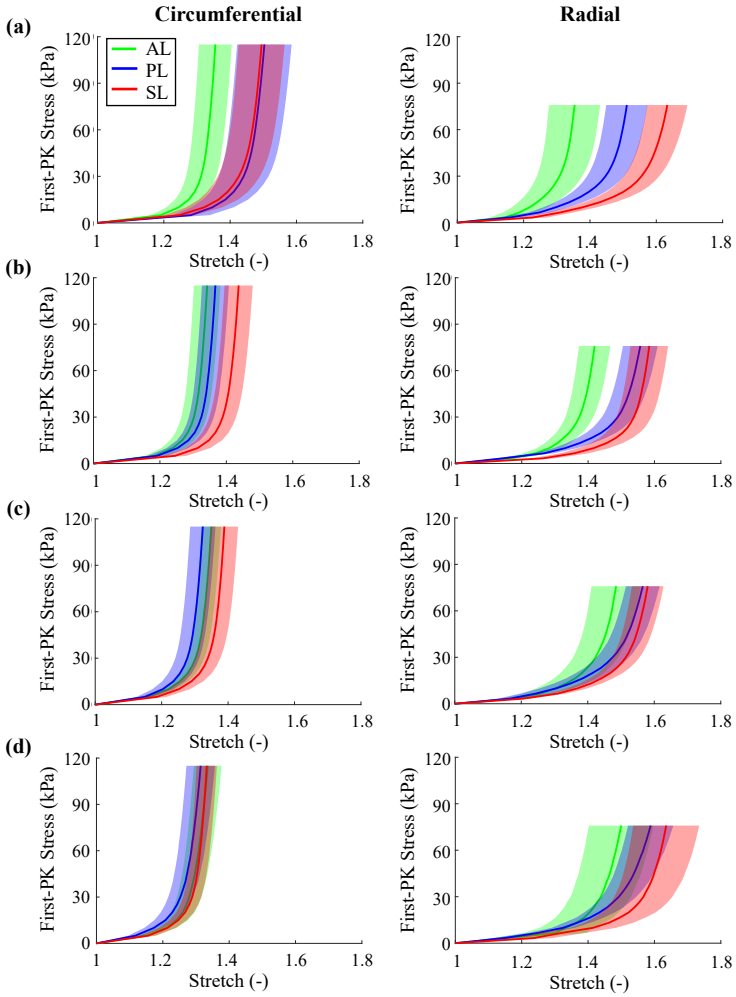

Figure B-1. Average mechanical behaviors for P_{circ}:P_{rad} =1:0.66 of the three TV leaflets for the (*left*) circumferential direction and (*right*) radial direction considering: (a) Specimen Size 1 (9×9 mm), (b) Specimen Size 2 (7.5×7.5 mm), (c) Specimen Size 3 (6×6 mm), and (d) Specimen Size 4 (4.5×4.5 mm).

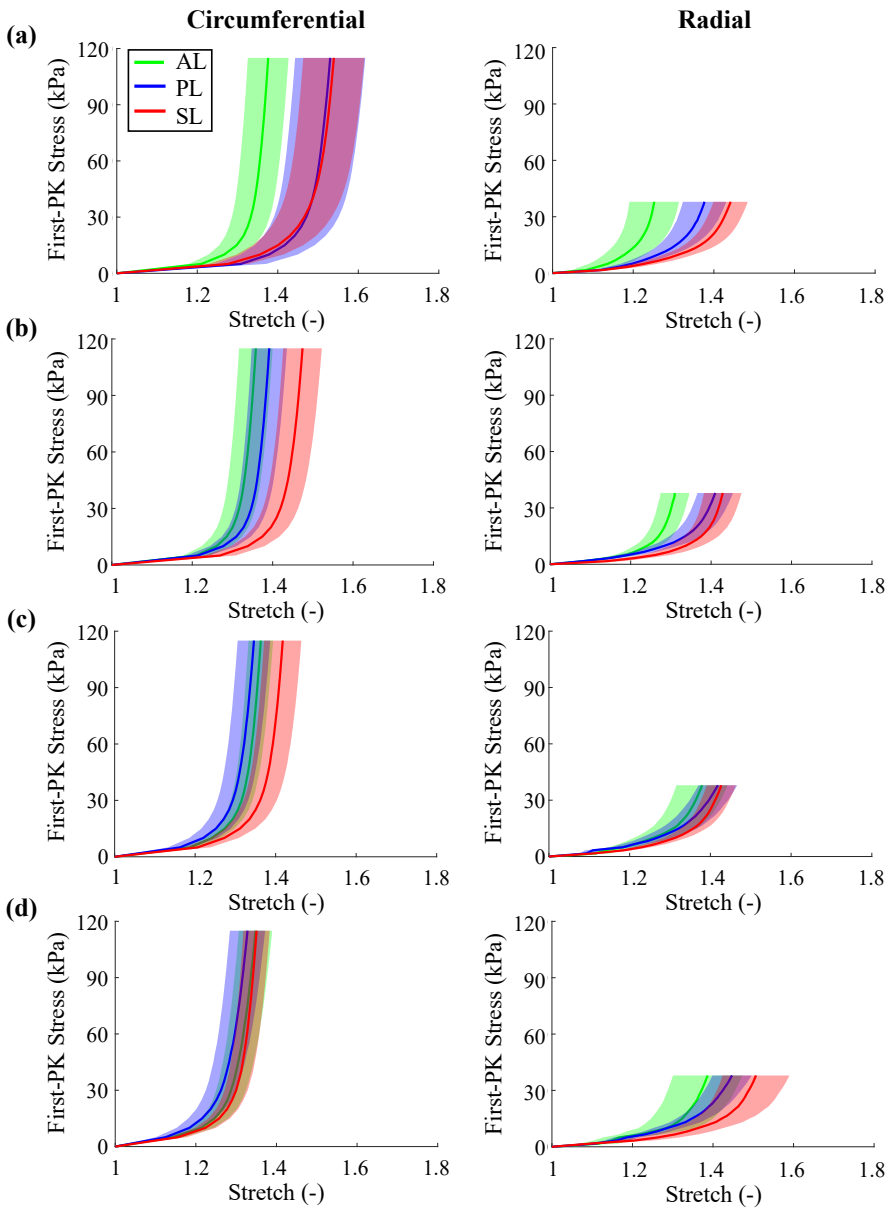

Figure B-2. Average mechanical behaviors for P_{circ}:P_{rad} =1:0.33 of the three TV leaflets for the (*left*) circumferential direction and (*right*) radial direction considering: (a) Specimen Size 1 (9×9 mm), (b) Specimen Size 2 (7.5×7.5 mm), (c) Specimen Size 3 (6×6 mm), and (d) Specimen Size 4 (4.5×4.5 mm).

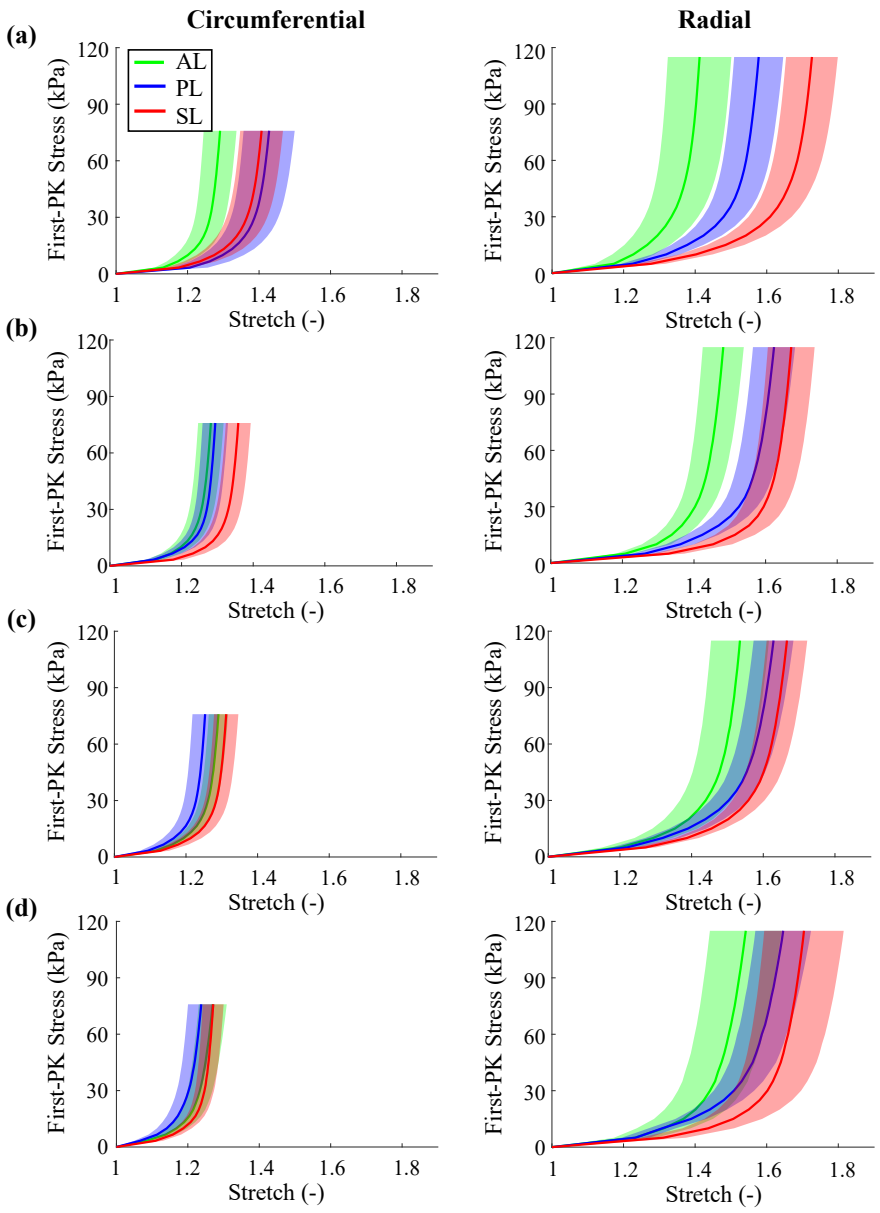

Figure B-3. Average mechanical behaviors for P_{circ}:P_{rad} =0.66:1 of the three TV leaflets for the (*left*) circumferential direction and (*right*) radial direction considering: (a) Specimen Size 1 (9×9 mm), (b) Specimen Size 2 (7.5×7.5 mm), (c) Specimen Size 3 (6×6 mm), and (d) Specimen Size 4 (4.5×4.5 mm).

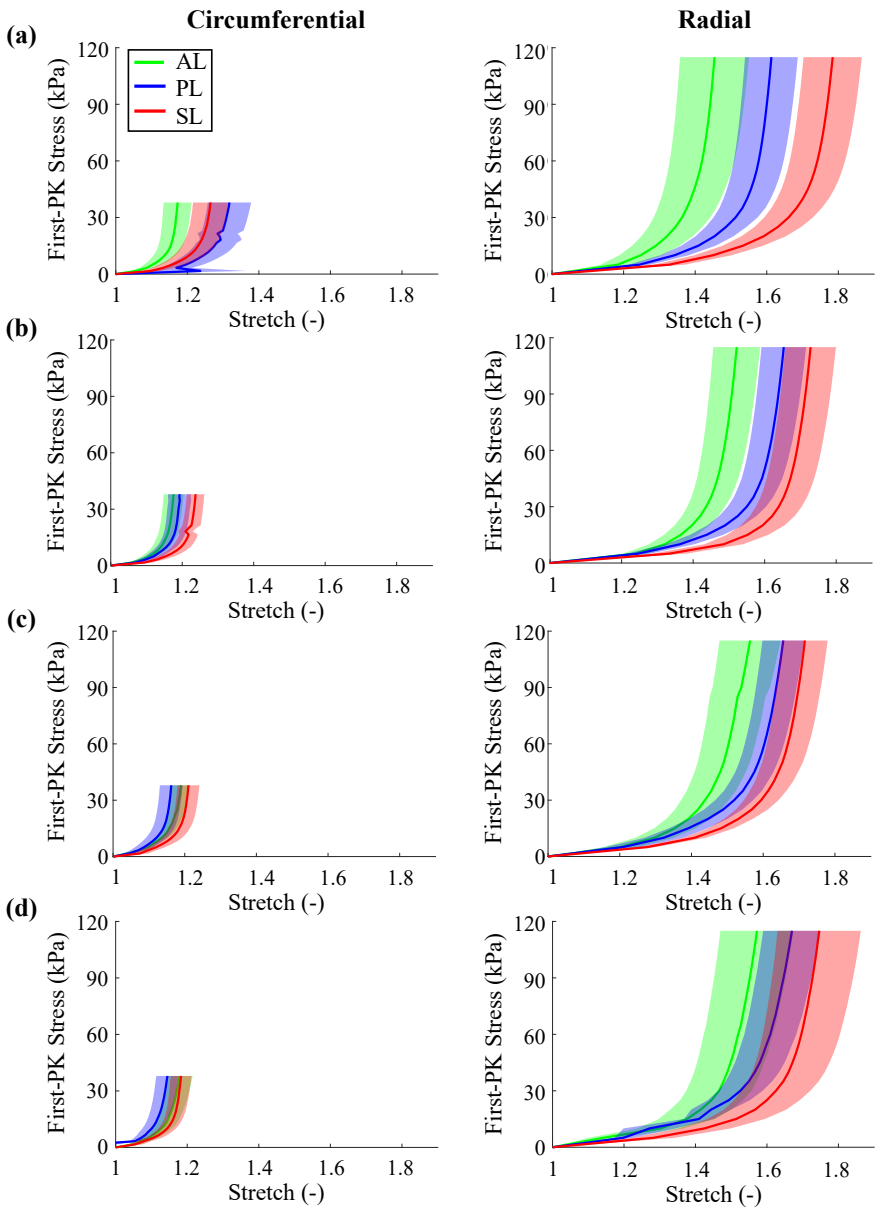

Figure B-4. Average mechanical behaviors for P_{circ}:P_{rad} =0.33:1 of the three TV leaflets for the (*left*) circumferential direction and (*right*) radial direction considering: (a) Specimen Size 1 (9×9 mm), (b) Specimen Size 2 (7.5×7.5 mm), (c) Specimen Size 3 (6×6 mm), and (d) Specimen Size 4 (4.5×4.5 mm).

APPENDIX C Tricuspid Valve Leaflet Layer Microdissection Protocol

This Appendix presents the TV leaflet layer microdissection employed in Chapter 4. Details of this Appendix were adopted from the associated publication [25].

1) ***Biaxial Mechanical Characterization***

1.1) Tissue preparation

1.1.1) Retrieve a TV leaflet from the freezer, razor blades, a surgical pen, forceps, a pipette with DI water, and a cutting mat. Thaw the TV leaflet using 2-3 drops of room-temperature DI water.

NOTE: DI water is used instead of PBS to avoid any PBS-induced difficulties for the layer microdissection.

1.1.2) Lay the specimen flat on the cutting mat with the ventricularis layer (i.e., the surface with the chordae insertions) facing upwards. Position the specimen so that the radial direction aligns with the *Y*-direction and the circumferential direction aligns with the *X*-direction.

NOTE: The circumferential direction is oriented along the circumference of the valve.

1.1.3) Examine the chordae insertion locations of the tissue. Determine an area, ideally 12×12 mm, with the least amount of large chordae insertions while also avoiding extremely thin (i.e., transparent) areas (**Figure C-1**).

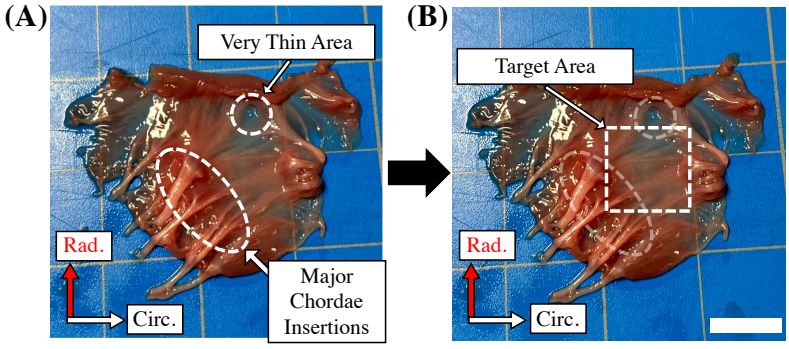

Figure C-1. Selection of microdissection area. (a) Identification of problematic areas to avoid and (b) target area for the layer microdissection. Scale bar = 10 mm.

1.1.4) Flip the specimen over so the atrial surface (i.e., the surface with no chordae insertions) is facing upwards. Ensure the circumferential and radial leaflet directions remain aligned with the *X*- and *Y*-axes, respectively.

1.1.5) Cut a square 12×12 mm specimen from the leaflet tissue that avoids the large chordae insertions or thin areas identified in step 1.1.3. Remove the trimmed portions of the leaflet tissue with the forceps and place them into a waste container.

1.1.5.1) If it is not possible to completely avoid large chordae insertions, cut the tissues so that they are along the edge of the square specimen. Avoiding chordae insertions is important as it helps prevent issues for the later microdissection.

1.1.6) Use a surgical pen to place a small dot in the top right corner to track the specimen's orientation. Allow the ink to dry for approximately 30 s.

1.1.7) Flip the specimen with the ventricular surface (i.e., the surface with chordal insertions) facing upwards. Trim the chordal attachments on the back of the tissue by stretching the chordae from the leaflet and using a razor blade to cut near its insertion location. Flip the specimen once again so the atrial surface (i.e., the smooth

surface) is facing upwards.

1.2) Thickness measurement

CAUTION: Do not shine the laser into eyes.

1.2.1) Retrieve a noncontact laser displacement sensor. Zero the displacement sensor on a flat section of the cutting mat near the trimmed tissue.

1.2.2) Position the laser over the central region of the specimen. Remove air trapped under the leaflet surface as it can cause measurement errors. To release trapped air, either use tweezers to push the bubble to the edge of the tissue or lift one corner of the tissue.

1.2.3) Record the thickness shown on the displacement sensor's display. Repeat two more measurements in other locations of the specimen.

1.2.4) Compute the average leaflet thickness using the three measurements recorded in the previous step. Use this value when creating the biaxial mechanical characterization protocols.

1.3) Biaxial tester setup and tissue mounting

1.3.1) Prepare a DI water bath at 37 °C, following the testing system's guidelines, to ensure the temperature under in vivo physiologic conditions.

1.3.2) Retrieve forceps, the tissue specimen, mounting hardware, a fine-tipped tool, liquid cyanoacrylate glue, and black-painted glass beads (diameter: 300-500 μm).

NOTE: Mounting hardware includes the tines, the mounting bridge, and the mounting rubber.

1.3.3) Mount the tissue specimen to the testing system. Ensure the circumferential direction of the tissue aligns with the *X*-direction, which can be assisted by the dot previously placed in step 1.1.6.

NOTE: The tines used here should be evenly spaced across the entire tissue edge length. The effective edge length *L* is set to be 10 mm for the intact tissue and >3.3 mm for the composite layers.

1.4) Fiducial marker placement

1.4.1) Identify the central one-third square region of the mounted tissue. Use the approximate corners of this area for the fiducial marker placement.

1.4.2) Place glass beads in an open-faced weighing boat and create a small pool of liquid cyanoacrylate glue in a separate weigh boat. Coat the top of the fine-tipped tool with a small amount of glue. Dab excess glue on the side of the weigh boat.

1.4.3) Create one corner of the central one-third square array by gently pressing the glue-coated tip onto the tissue. Using forceps, grab a glass bead and carefully place it on top of the glue dot. Use the camera of the biaxial testing device for help with the bead placement.

1.4.4) Repeat steps 1.4.2 and 1.4.3 for three additional beads until the square array is completed. Ensure the beads are securely attached and their respective glue dots are not touching or sticking together. Dry the glue before lowering the tissue into the water bath.

1.4.4.1) If the beads are stuck together, wait for the glue to dry, then use the forceps to gently grasp the bead or glue and pull it off the tissue.

1.5) Preconditioning

1.5.1) Create a force-controlled preconditioning protocol, in which the tissue with edge length L and thickness t will undergo six repetitions of equibiaxial loading to a peak membrane tension T_{peak} of 40 N/m with a preload of 3% of T_{peak} and stretch and recovery times of 30 s each.

1.5.1.1) Construct an arbitrary testing directory that will temporarily store the data for future calculations. Set the loading rate to be 4.42 N/m.

1.5.1.2) Construct a new testing parameter set with the name Preconditioning0. Set the *X*-axis and *Y*-axis control modes to force and set the control functions to step. Define the load magnitude to be the force associated with T_{peak}, i.e., $f_{peak} = T_{peak} \cdot L$. Define the preload magnitude as 3% of f_{peak} for the first repetition only and define both the stretch duration and recovery duration as 30 s. Define the number of repetitions as 10.

NOTE: The computed peak first Piola-Kirchhoff stress may exceed 200 kPa for thinner tissues, which could result in tissue tearing during testing. In these scenarios, the peak membrane tension was adjusted to a maximum first Piola-Kirchhoff stress of 200 kPa.

1.5.2) Execute the preconditioning protocol. Following preconditioning, record the current *X*- and *Y*-dimensions of the specimen for use in the biaxial testing protocols.

1.6 Creation and execution of biaxial testing protocols

1.6.1) Determine the time required to achieve the peak equibiaxial configuration from the PPC configuration with the desired displacement rate. Compute the loading times for the remaining loading ratios (i.e., $T_{XX} : T_{YY} = 1 : 0.5$ and $T_{XX} : T_{YY} = 0.5 : 1$)

considering a constant displacement rate.

1.6.2) Manually jog the linear actuators to match the target forces for a given loading ratio. Repeat this process and record the leaflet dimensions for all loading ratios.

1.6.3) Prepare a displacement-controlled testing protocol that biaxially displaces the tissue from the PPC configuration to the configurations recorded in step 1.6.2 (i.e., $T_{XX}:T_{YY}=1:1,\ 1:0.5,\ 0.5:1$) within the times determined in step 1.6.1. Ensure that each protocol has three loading/unloading cycles for repeatability of the mechanical behavior.

1.6.3.1) Construct a testing directory that will store the data for future calculations. Ensure the directory name matches the current specimen.

1.6.3.2) Construct a new testing parameter set with the name 1:1, set the *X*-axis and *Y*-axis control modes to displacement, and set the control functions to ramp. Define the stretch magnitude to be the configuration recorded in step 1.6.1. Define the preload magnitude as 3% of f_{peak} for only the first repetition and define both the stretch duration and recovery duration as the time recorded in step 1.6.1. Define the number of repetitions as 3.

1.6.3.3) Repeat step 1.6.3.2 for the remaining loading ratios (i.e., $T_{XX}:T_{YY}=1:0.5$ and $T_{XX}:T_{YY}=0.5:1$), except define the preload magnitude as not applied. Ensure the stretch magnitude, stretch duration, and recovery duration match those recorded in step 1.6.2.

NOTE: Only data from the final (third) cycle will be used for stress and strain analyses.

1.6.4) Execute the displacement-controlled protocols. After completion of biaxial testing, return the tissue to its PPC dimensions.

NOTE: The test should be immediately aborted if the tissue begins to tear.

1.7) Further characterizations

1.7.1) Leave the tissue submerged in DI water and mounted to the biaxial testing system. Perform pSFDI imaging as described in steps 2.1-2.3.

1.7.2) Unmount the tissue. If it is an intact tissue, proceed to the microdissection described in steps 3.1-3.7. If not, collect histology following step 3.7.

NOTE: The DI water bath can be used for subsequent characterizations within the same day.

1.7.3) Repeat steps 1.2-1.7 with the A/S and F/V layers acquired following the microdissection (steps 3.1-3.6).

NOTE: The repetition of the testing protocol for the layers allows for direct comparison of the intact tissue to its own layers.

1.8) Biaxial testing data post processing procedures

1.8.1) Perform DIC of the acquired biaxial testing images to determine the time-dependent marker positions. Compute the fiducial marker displacements.

1.8.2) Compute the deformation gradient $\mathbf{F}$ by considering the fiducial markers as a four-node bilinear finite element (see Section 3.1)

1.8.3) Compute the applied first Piola-Kirchhoff stress $\mathbf{P}$ (see Section 3.1)

2) ***Polarized spatial frequency domain imaging***

NOTE: The fiducial markers can be removed from the tissue prior to the following steps.

2.1) System preparation

2.1.1) Center the pSFDI device over the specimen (**Figure C-2**). Turn on the projector and illuminate the specimen with 490 nm (cyan) light.

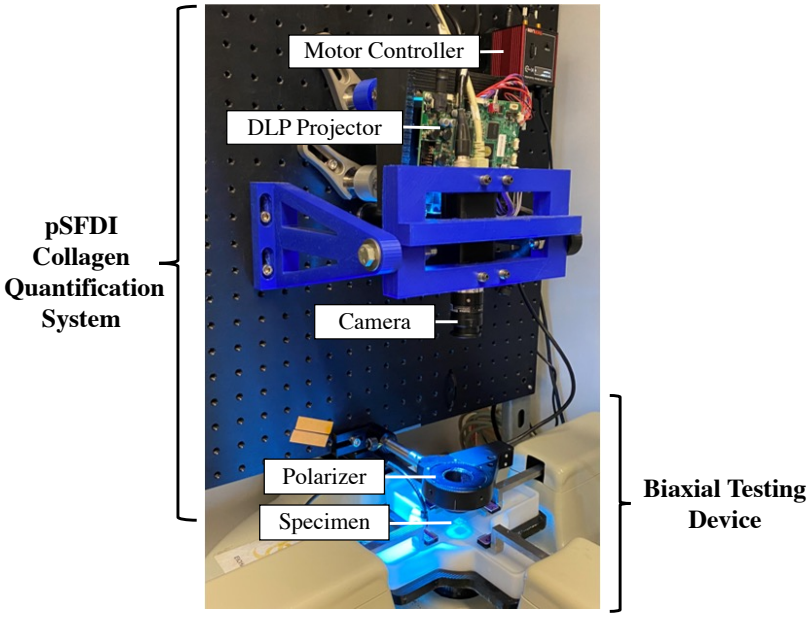

Figure C-2: The pSFDI system integrated with the biaxial testing device. Key components of both devices are labeled.

2.1.2) Open the camera software and inspect the camera's field of view. Ensure the specimen is centered in the frame and is completely contained within the field of view.

2.1.3) If the mounted specimen is an intact leaflet, adjust the digital light processing (DLP) projector brightness to ensure the tissue is fully illuminated with no glares on the

tissue surface. Do not adjust the brightness if the specimen is one of the composite layers.

2.1.4) Rotate the polarizer across its complete range of motion to detect possible glares or dirt on the polarizer lens. Carefully clean the polarizer lens with a microfiber cloth as necessary.

NOTE: The following data collection can be automated using software, such as Python.

2.2) Data collection

2.2.1) Move the polarizer to its home position—ideally aligned with one of the biaxial testing axes. Capture one grayscale image and save to the computer with the polarizer location (i.e., 0°).

2.2.2) Rotate the polarizer 5° and capture another grayscale image. Repeat this process to acquire 37 images that range from 0° to 180° with a 5° increment.

NOTE: The images from the first pSFDI imaging sequence can be preliminarily analyzed to ensure the desired optical response from the tissue. Refer to step 2.3 for instructions.

2.2.3) Repeat the pSFDI imaging sequence for other desired tissue configurations, for example, the peak configurations of the loading protocols considered for biaxial mechanical testing.

NOTE: Any preferred language (e.g., Python) may be used for the following step.

2.3) pSFDI data postprocessing procedures

2.3.1) Use the MATLAB `imread()` function to construct arrays containing the pixel-wise

intensities of the 37 acquired images. For convenience, arrange these as an *n*×*m*×37 three-dimensional array, where n and m are the number of pixels along the two axes.

2.3.2) Define the tissue ROI using the user-defined `grabit()` function.

2.3.3) Fit the intensity vs. polarizer angle data for each ROI pixel using a 3-term Fourier series:

$$I(\theta) = b_0 + b_1\cos(2\theta) + b_2\sin(2\theta) + b_3\cos(4\theta) + b_4\sin(4\theta) \qquad \text{(C.1)}$$

Herein, $I(\theta)$ is the pixel-wise intensity as a function of polarizer angle, and the b_i are the Fourier constants. Use standard linear least-squares regression to determine b_i.

2.3.4) Determine the pixel-wise fiber orientation as the polarizer angle associated with the maximum value of $I(\theta)$. Compute the degree of optical anisotropy (DOA):

$$DOA = \frac{b_0}{(b_0 + b_2 + b_4)} \qquad \text{(C.2)}$$

2.3.5) Use `plot()` and `histogram()` to visualize the acquired fiber orientation and DOA values. Save the processed results for later use.

3) ***Microdissection of tricuspid valve leaflet composite layers***

3.1) Tissue attachment to wax board

3.1.1) Gather the required materials: wax board, DI water, pipette, scalpel, micro scissors, thin forceps, curved forceps, thick forceps, and pins.

NOTE: Only use tweezers without teeth or grips, as forceps of this type can very easily rip the thin tissue of the A/S layer when performing the dissection.

3.1.2) Unmount the tissue from the biaxial tester and measure its thickness using the laser

displacement sensor as described in step 1.2. Place the tissue on the wax board.

3.1.3) Examine the ventricularis side of the tissue for large chordae insertions. Note the position of these insertions to avoid them during the dissection. Take a photograph for reference.

3.1.4) Spread the tissue flat on the wax board with the atrialis facing up. Affix the tissue to the board using the pins:

3.1.4.1) In each corner of the tissue, place one pin that is angled away from the tissue (for better viewing) and slightly pulls the tissue taut (**Figure C-3**(a)). Do this in a clockwise or counterclockwise order. Ensure that the pins are outside of the holes created by the tines when mounting the tissue.

3.1.4.2) Adjust the pin placement slightly to ensure that the tissue is taut and in a square configuration (**Figure C-3**(b)) so that the tissue lies flat and does not shift during the layer micro-dissection.

3.1.4.3) If necessary, during the dissection, place pins along the side of the tissue to stretch the tissue more. Keep in mind when placing and angling additional pins that they must be worked around during the dissection.

3.1.4.4) Remove the glass bead fiducial markers.

NOTE: The following step is optional. The added DI water helps maintain tissue hydration.

3.1.5) Using a pipette, place DI water on the surface of the tissue, so that it completely covers the tissue in a bubble-like manner. Replenish the DI water as needed throughout the dissection.

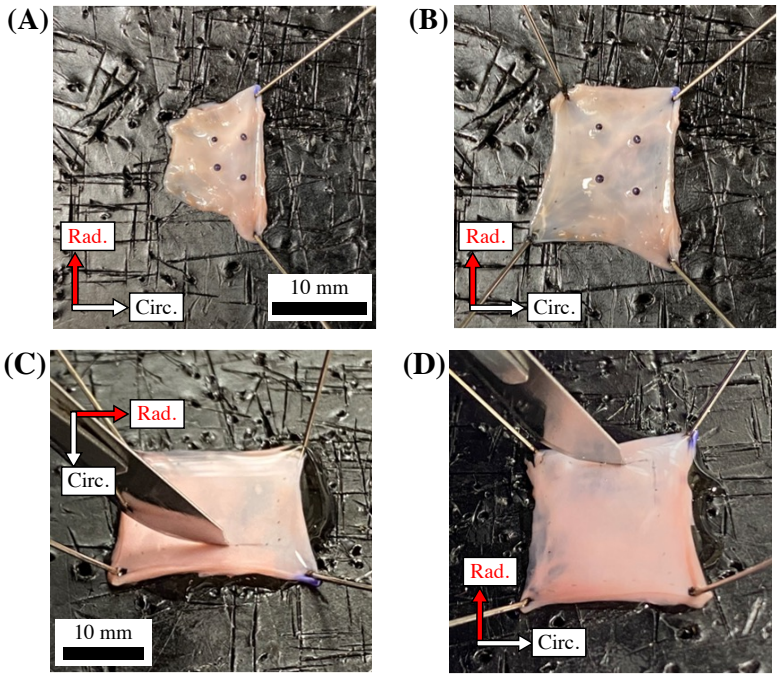

Figure C-3: Initiation of the leaflet microdissection. (a) Stretching the tissue taut while placing pins, (b) the pinned tissue ready for microdissection, (c) making the first cut into the A/S composite layer, and (d) creating the first corner of cuts into the A/S composite layer. Scale bars = 10 mm.

3.2) Make the initial corner

3.2.1) Select a corner of the pinned specimen to begin the dissection. Avoid large chordae insertions and extremely thin areas.

3.2.2) Make a cut in the A/S layer by lightly dragging the scalpel over the tissue surface along the mounting holes from mechanical testing (**Figure C-3**(c)). Ensure the cut is at least 5 mm long, and the edges of the cut start to pull apart, revealing the F/V layer underneath.

3.2.3) Use the thin forceps (without a sharp tip) to firmly rub along the cut and pull the edges of the cut apart.

3.2.3.1) If the cut in the A/S layer does not start to pull apart, lightly trace over the same cut again with the scalpel until it begins to do this. Be careful not to cut too deeply into the tissue (past the A/S composite layer) as it makes it more difficult to cleanly separate the layers.

3.2.4) Repeat steps 3.2 and 3.2.3 to make a second cut perpendicular to the first cut (**Figure C-3**(d)). Ensure that the two cuts are connected and form a corner.

3.2.4.1) If the two cuts are not connected, run the thin tweezers under the small area of tissue that is separating the two cuts. Then, carefully use the scissors to cut the tissue.

3.3) Peel the tissue from the corner

3.3.1) Rub along the cuts using the thin forceps until the tissue begins to separate from the F/V layer. As soon as a small piece of tissue is separated, grasp it by the tweezers and gently pull to further separate the composite layers.

NOTE: Always place the tip of the thin tweezers past the edge of the tissue when grasping. Otherwise, they could accidentally poke a hole into the A/S composite layer.

3.3.2) Continue to peel the tissue and rub the seam until reached the end of the two cuts made for the corner. Throughout this process, switch to larger tweezers to grasp the tissue for the peeling process to prevent undesired ripping and tearing of the A/S composite layer.

3.3.2.1) If the first corner attempted has major issues with separation, try a different corner as a starting point (go back to step 3.2).

3.4) Extend cuts, peel the tissue, and make a second corner

3.4.1) Extend the two cuts made for the first corner by placing the scalpel tip at the bottom of each cut and lightly dragging it along the tissue surface (**Figure C-4**(a)). Ensure that all extension cuts are at least 5 mm and the cut extensions connect to the original cuts and continue to follow the tine or suture holes.

NOTE: If the extension cut is too deep, then the forthcoming peeling must be closely monitored to ensure sections of the fibrosa are not separated with the A/S composite layer (**Figure C-5**(a)).

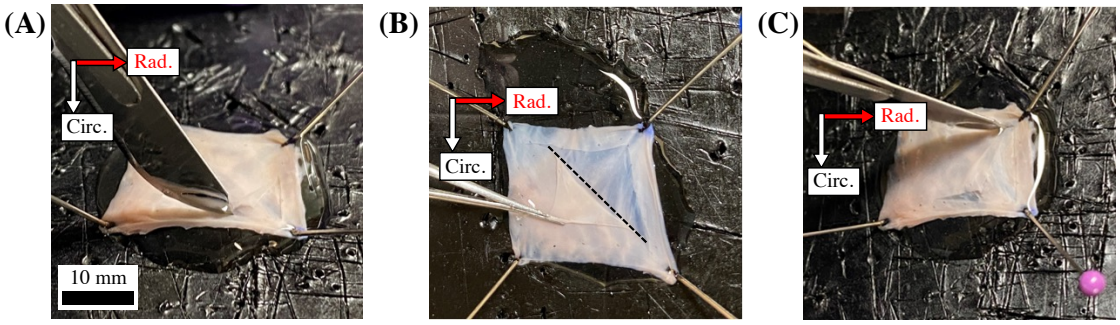

Figure C-4: Separation of the A/S composite layer. (a) Extension of the cuts into the A/S composite layer, (b) separation of the A/S composite layer via careful peeling, and (c) creation of the second corner. Scale bar = 10 mm. Abbreviations: Rad. = radial; Circ. = circumferential; A/S = atrialis/spongiosa.

3.4.2) Continue to extend the cuts and peel the top composite A/S layer back while rubbing the seam until one side is finished. Observe that the tissue will be separated completely along one cut; ensure that the seam between the A/S and F/V composite layers is straight (**Figure C-4**(b)).

3.4.3) Repeat the instructions in step 3.2 and step 3.3 to create a second corner perpendicular to the end of the fully peeled side (**Figure C-4**(c)).

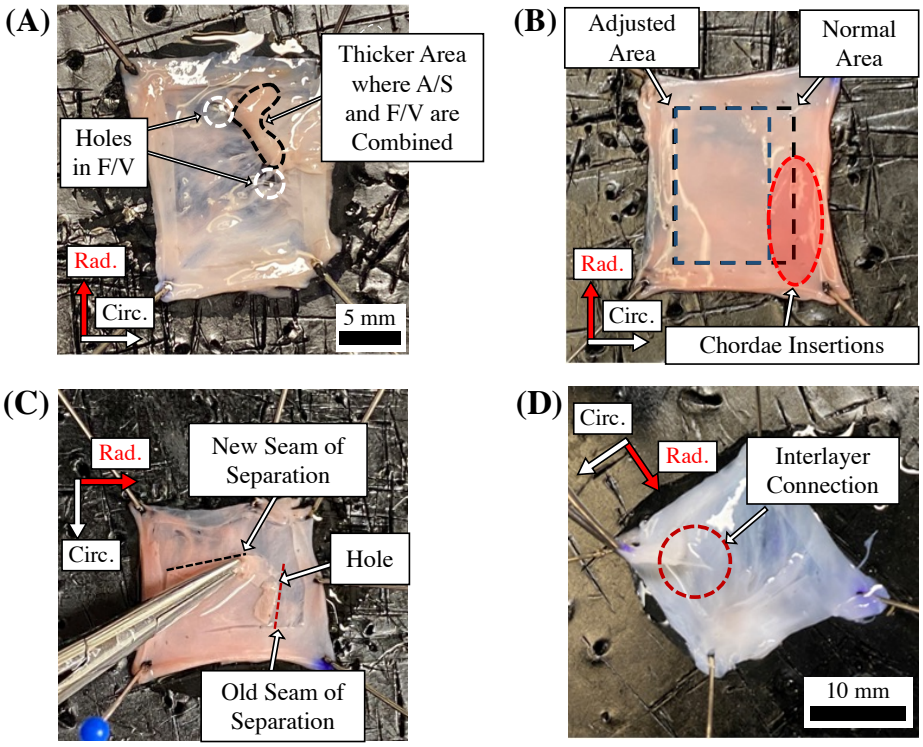

Figure C-5: Potential problems during the leaflet microdissection. (a) Unsuccessful separation of the A/S and F/V composite layers, (b) adjustment of the microdissection area to avoid chordae insertions, (c) creation of a new separation seam due to undesired hole, and (d) interlayer connection connecting the A/S and F/V composite layers. Scale bars = 5 mm (a-c), 10 mm (d).

3.5) Completely separate the A/S layer.

3.5.1) Extend the remaining cuts while avoiding large chordae insertions. Continue separating the A/S and F/V layers by using the rubbing and pulling techniques employed for the first corner. Make a note of several considerations or problems that may arise during this process:

3.5.1.1) Exclude the chordae insertions from the A/S separation area (**Figure C-5**(b)) only when this exclusion will allow for an A/S specimen large enough for experimental characterizations (>3.3 mm).

3.5.1.2) If the tissue tears or a hole forms, stop separating the tissue immediately. To prevent tweezers from being caught, place the scissors in any hole that forms and cut the tissue away from the center. If the defect forms along the seam of separation, then begin separating the tissue along another edge to prevent further tearing (**Figure C-5**(c)).

3.5.1.3) Look for interlayer connections that may appear while separating the tissue and prevent further separation of the tissue without a high risk of ripping (**Figure C-5**(d)). Observe these are thin, but strong, strands that must be carefully cut using the scissors. Avoid creating a hole in the A/S layer or cutting downwards into the F/V layer, as this would cause uneven separation.

3.5.1.4) Continue this process until the largest sample possible of the A/S layer has been separated. Mark the orientation of the sample using the surgical pen (**Figure C-6**(a)).

3.6) Finish dissection.

3.6.1) Use the scissors to cut along the seam of separation for the remaining tissue edge (**Figure C-6**(b)). Ensure this cut is as close to the seam of separation as possible.

3.6.2) Place the separated A/S composite layer flat on the cutting mat. If necessary, use the scalpel to straighten the edges of the tissue and create a square tissue shape suitable for biaxial mechanical testing. Place the A/S layer in DI water until it is ready to be tested.

3.6.3) Mark the orientation of the F/V layer that remains on the wax board. Cut the largest square possible out of the area where the A/S layer was removed (**Figure C-6**(c)), then place it in DI water.

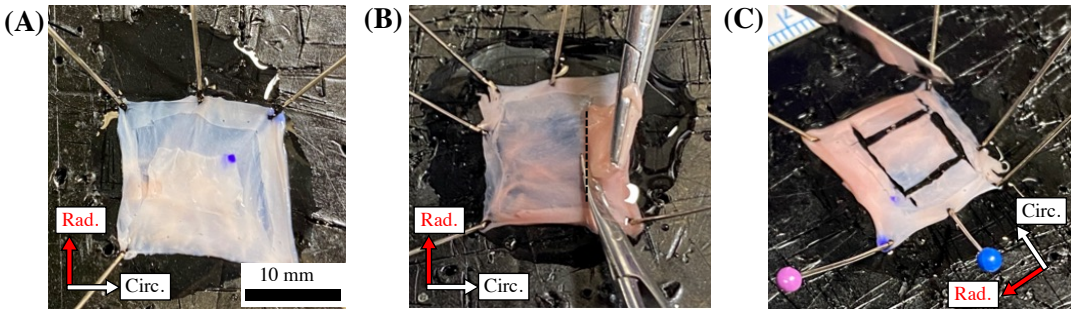

Figure C-6: Completion of the microdissection. (a) Denotation of the top-right corner for orientation, (b) separation of the A/S using scissors, and (c) retrieval of the F/V composite layer with orientation marked. Scale bar = 10 mm

3.7) Histology

3.7.1) Excise two strips of tissue—aligned with the circumferential and radial directions—for use in histology. Use different protocols for the intact and the composite layers

(i.e., A/S and F/V):

3.7.1.1) For the intact layer, take the specimens from the tissue that remains pinned to the wax board. Use the tissue outside of the tine/suture holes, as this portion of the tissue has not been dissected and will represent the intact leaflet.

3.7.1.2) For the A/S and F/V composite layers, only collect histology samples after fully completing their testing and imaging. Unmount the specimen from the biaxial testing system, lay the tissue flat on a cutting mat, and excise the circumferential and radial strips using a razor blade.

3.7.2) Place the excised strips in tissue cassettes and submerge the cassettes in 10% formalin.

3.7.3) Discard the remaining tissue. Clean the dissection tools using cleaning compound.

APPENDIX D Formulation of Locally Convex Data-Driven Solver

The Global Step of the LCDD Method

This Appendix presents the solution procedures of the global step in the proposed LCDD nonlinear solver. The associated constrained minimization problem in Eqs. (5.18)-(5.20) can be transformed into the following functional:

$$\begin{aligned} L_{DD}(\mathbf{u},\mathbf{S},\boldsymbol{\lambda}) = & \int_{\Omega^X} [d_E^2(\mathbf{E}(\mathbf{u}),\hat{\mathbf{E}}) + d_S^2(\mathbf{S},\hat{\mathbf{S}})] d\Omega \\ & + \int_{\Omega^X} \boldsymbol{\lambda} \cdot [\mathrm{DIV}(\mathbf{F}(\mathbf{u}) \cdot \mathbf{S}) - \boldsymbol{\lambda}\bar{\mathbf{b}}] d\Omega - \int_{\Gamma_t^X} \boldsymbol{\lambda} \cdot [(\mathbf{F}(\mathbf{u}) \cdot \mathbf{S}) \cdot \mathbf{N} - \bar{\mathbf{t}}] d\Gamma \end{aligned} \tag{D.1}$$

where the subscript *DD* denotes the *data-driven* computational framework, $(\hat{\mathbf{E}},\hat{\mathbf{S}})$ is the resultant data solution from the previous iteration, $\boldsymbol{\lambda}$ is the Lagrange multiplier in a proper function space. Using integration by parts and the divergence theorem, we arrived an equivalent form as follows

$$\begin{aligned} L_{DD}(\mathbf{u},\mathbf{S},\boldsymbol{\lambda}) = & \int_{\Omega^X} [d_E^2(\mathbf{E}(\mathbf{u}),\hat{\mathbf{E}}) + d_S^2(\mathbf{S},\hat{\mathbf{S}})] d\Omega \\ & - \int_{\Omega^X} [\nabla\boldsymbol{\lambda} : (\mathbf{F}(\mathbf{u}) \cdot \mathbf{S}) - \boldsymbol{\lambda}\bar{\mathbf{b}}] d\Omega + \int_{\Gamma_t^X} \boldsymbol{\lambda} \cdot \bar{\mathbf{t}} d\Gamma + \int_{\Gamma_u^X} \boldsymbol{\lambda} \cdot [(\mathbf{F}(\mathbf{u}) \cdot \mathbf{S}) \cdot \mathbf{N}] d\Gamma \end{aligned} \tag{D.2}$$

Following the standard variational approach [43], we assume $\boldsymbol{\lambda}=\mathbf{0}$ on the essential boundary Γ_u^X and the last term in the above equation can be dropped, which is analogous to the homogeneous boundary condition for the test functions used in the Galerkin approximation. The stationary condition $\delta L_{DD}(\mathbf{u},\mathbf{S},\boldsymbol{\lambda}) = 0$ with respect to $\mathbf{u}$, $\mathbf{S}$, and $\boldsymbol{\lambda}$ leads to the following three variational equations:

$$\int_{\Omega^X} \delta\mathbf{E}(\mathbf{u}) : \mathbf{M} : (\mathbf{E}(\mathbf{u}) - \hat{\mathbf{E}}) \mathrm{d}\Omega = \int_{\Omega^X} (\delta\mathbf{F}^T(\mathbf{u}) \cdot \nabla\boldsymbol{\lambda}) : \mathbf{S} \mathrm{d}\Omega \tag{D.3}$$

$$\int_{\Omega^X} \delta\mathbf{S} : (\mathbf{M}^{-1} : \mathbf{S} - \mathbf{F}^T(\mathbf{u}) \cdot \nabla\boldsymbol{\lambda}) \mathrm{d}\Omega = \int_{\Omega^X} \delta\mathbf{S} : \mathbf{M}^{-1} : \hat{\mathbf{S}} \mathrm{d}\Omega \tag{D.4}$$

$$\int_{\Omega^X} \delta\nabla\boldsymbol{\lambda} : (\mathbf{F}(\mathbf{u}) \cdot \mathbf{S}) \mathrm{d}\Omega = \int_{\Omega^X} \delta\boldsymbol{\lambda} \cdot \bar{\mathbf{b}} \mathrm{d}\Omega + \int_{\Gamma_t^X} \delta\boldsymbol{\lambda} \cdot \bar{\mathbf{t}} \mathrm{d}\Gamma := P^{\text{ext}}(\delta\boldsymbol{\lambda}) \tag{D.5}$$

From the above formulations, we can see that Eq. (D.3) relates a strain compatibility constraint on the displacement solution $\mathbf{u}$ to strain data $\hat{\mathbf{E}}$, and $\boldsymbol{\lambda}$ represents the displacement. Similarly, Eq. (D.4) relates the computational stress $\mathbf{S}$ and the measured stress data $\hat{\mathbf{S}}$. Lastly, Eq. (D.5) is a generalized equilibrium.

Remark 1: Because the LCDD framework proposed in He and Chen (2020) [54] was developed based on the weak formulation, it can be easily extended to employ other energy-conjugate strain/stress pair. For example, the Cauchy stress and its energy conjugate strain (Euler-Almansi strain) or the 1st Piola-Kirchhoff stress and its energy conjugate strain (transpose of the deformation gradient) can be used in the LCDD method as long as the experimental data expressed in the same stress-strain measures are available. If the asymmetric stress-strain measures are employed in the LCDD framework, such as $\mathbf{P}$ and $\mathbf{F}$, they lead to the increased dimension in the database and thus is less desirable. The selection of the energy-conjugate $\mathbf{S}$ and $\mathbf{E}$ employed in our study was due to the availability of the experimental information and their reference with respect to the undeformed configuration.

If the stress approximation is constructed by either static condensation at the element level or nodal integration schemes, Equation (D.4) can be further recast into independent element-wise or point-wise systems [54]:

$$\mathbf{S} = \hat{\mathbf{S}} + \mathbf{M} : (\mathbf{F}^T(\mathbf{u}) \cdot \nabla\boldsymbol{\lambda}) \tag{D.6}$$

By substituting Eq. (D.6) into Eqs. (D.3) and (D.5) and rearranging the equations, we obtained

$$\begin{aligned} J_{\mathbf{u}} = & \int_{\Omega^X} \delta\mathbf{E}(\mathbf{u}) : \mathbf{M} : \mathbf{E}(\mathbf{u}) \mathrm{d}\Omega - \int_{\Omega^X} \left(\delta\mathbf{F}^T(\mathbf{u}) \cdot \nabla\boldsymbol{\lambda}\right) : \mathbf{M} : \left(\mathbf{F}^T(\mathbf{u}) \cdot \nabla\boldsymbol{\lambda}\right) \mathrm{d}\Omega \\ & - \int_{\Omega^X} \delta\mathbf{E}(\mathbf{u}) : \mathbf{M} : \hat{\mathbf{E}} \mathrm{d}\Omega - \int_{\Omega^X} \left(\delta\mathbf{F}^T(\mathbf{u}) \cdot \nabla\boldsymbol{\lambda}\right) : \hat{\mathbf{S}} \mathrm{d}\Omega = 0 \end{aligned} \tag{D.7}$$

and

$$J_{\boldsymbol{\lambda}} = \int_{\Omega^X} (\mathbf{F}^T(\mathbf{u}) \cdot \delta\nabla\boldsymbol{\lambda}) : \mathbf{M} : (\mathbf{F}^T(\mathbf{u}) \cdot \nabla\boldsymbol{\lambda}) \mathrm{d}\Omega + \int_{\Omega^X} (\mathbf{F}^T(\mathbf{u}) \cdot \delta\nabla\boldsymbol{\lambda}) : \hat{\mathbf{S}} \mathrm{d}\Omega = P^{\text{ext}}(\delta\boldsymbol{\lambda}) \tag{D.8}$$

The weak form system in Eqns. (D.7)-(D.8) needs to be solved by the Newton-Raphson method with respect to **u** and **λ**.

To numerically solve the above weak form system, in this study the variables **u** and **λ** are approximated by the reproducing kernel (RK) shape functions [26, 98] constructed using the linear basis functions and the cubic spline kernel function. These node-based RK approximation functions are employed for better numerical performance under large deformation without experiencing mesh distortion difficulties in the conventional mesh-based methods. The 2nd Piola-Kirchhoff stress **S** is approximated by indicator functions so that it can be directly related to discrete stress data $\hat{\mathbf{S}}$ in Eq. (D.6). Furthermore, the stabilized conforming nodal integration [27] is employed for the integration of the weak form in Eqs. (D.7)-(D.8). With stabilized conforming nodal integration framework, variables **u**, **λ**, and the associated $\mathbf{E}(\mathbf{u})$ and $\mathbf{F}(\mathbf{u})$ are computed at the nodal points (instead of integration points), making it very efficient for data-driven computing where local data search are only performed at the nodal points. More details about the employed discretization scheme can be found in [54].

The Local Step of the LCDD Method

After the Green strain tensor $\mathbf{E}(\mathbf{u})$ and the 2nd Piola-Kirchhoff stress $\mathbf{S}$ are obtained (Eqs. (D.7)-(D.8)) and the weak form system (Eq. (D.8)), they are then used to update the measurement data solution $(\hat{\mathbf{E}},\hat{\mathbf{S}})$ from the experimental dataset using Eq. (5.21) via the proposed locally convexity-preserving machine learning algorithm [54]. The key procedure is to recast the minimization problem in Eq. (5.21) with a convex feasible set E_α associated with $\mathbf{z}_\alpha = (\mathbf{E}_\alpha, \mathbf{S}_\alpha)$ into the following constrained minimization problem to solve for the optimal reconstruction weights $\mathbf{w}_\alpha^* \in \sim^k$, $\forall \alpha$=1,…,m:

$$\mathbf{w}_\alpha^* = \arg\min_{\mathbf{w}\in\sim^k} \| \mathrm{z}_\alpha - \sum_{i\in \mathrm{N}_k(\mathrm{z}_\alpha)} w_i \hat{\mathrm{z}}_\alpha^i \|_{\mathbf{M}} \tag{D.9}$$

$$\text{subject to } \sum_{i\in \mathrm{N}_k(\mathrm{z}_\alpha)} w_i = 1 \text{ and } w_i \geq 0 \tag{D.10}$$

where $\hat{\mathrm{z}}_\alpha^i = (\hat{\mathbf{E}}_\alpha^i, \hat{\mathbf{S}}_\alpha^i)$ are the raw data points in the experimental dataset E, and $\mathrm{N}_k(\mathrm{z}_\alpha)$ represents the indices of the k-nearest neighboring data points to $\mathbf{z}_\alpha$. A computationally feasible algorithm based on the Lawson-Hanson method [87] for non-negative least squares problem is introduced to solve Eqs. (D.9)-(D.10) [54].

APPENDIX E Direct Linear Transformation

In this appendix, we describe the direct linear transformation used for three-dimensional photogrammetry in this study. We also detail the calibration of our stereo camera setup used in Section 6.1.3.

Direct Linear Transformation

Let us consider a point O in the 3D space, a direct linear transformation [64, 108] can be used to transform its 3D location (x, y, z) to a camera's pixel coordinates (p, q) via

$$p = \frac{Ax + By + Cz + d}{Ix + Jy + Kz + 1}, \quad q = \frac{Ex + Fy + Gz + H}{Ix + Jy + Kz + 1} \tag{E.1}$$

Herein, $\{A, B, C, \ldots, I, J, K\}$ are the camera-specific coefficients that depend on the camera's properties (e.g., focal length) and overall configuration. At least six non-coplanar points with known (x_i, y_i, z_i) are required to determine the 11 unknown coefficients $\{A, B, C, \ldots, I, J, K\}$ by solving the following overdetermined linear system of equations:

$$\begin{bmatrix} x_1 & y_1 & z_1 & 1 & 0 & 0 & 0 & 0 & -p_1x_1 & -p_1y_1 & -p_1z_1 \\ 0 & 0 & 0 & 0 & x_1 & y_1 & z_1 & 1 & -q_1x_1 & -q_1y_1 & -q_1z_1 \\ \vdots & \vdots & \vdots & \vdots & \vdots & \vdots & \vdots & \vdots & \vdots & \vdots & \vdots \\ x_n & y_n & z_n & 1 & 0 & 0 & 0 & 0 & -p_nx_n & -p_ny_n & -p_nz_n \\ 0 & 0 & 0 & 0 & x_n & y_n & z_n & 1 & -q_nx_n & -q_ny_n & -q_nz_n \end{bmatrix} \begin{Bmatrix} A \\ B \\ \vdots \\ J \\ K \end{Bmatrix} = \begin{Bmatrix} p_1 \\ q_1 \\ \vdots \\ p_n \\ q_n \end{Bmatrix} \tag{E.2}$$

The above calibration procedure is repeated for two cameras with non-planar views to obtain the coefficient sets $\{A^{[1]}, B^{[1]}, C^{[1]}, \ldots, I^{[1]}, J^{[1]}, K^{[1]}\}$ and $\{A^{[2]}, B^{[2]}, C^{[2]}, \ldots, I^{[2]}, J^{[2]}, K^{[2]}\}$.

Once these camera-specific unknown coefficients are calibrated, the pixel coordinates from the two cameras $(p_i^{[1]}, q_i^{[1]})$ and $(p_i^{[2]}, q_i^{[2]})$ for each fiducial marker can then be used to determine the fiducial marker location in the 3D space (x_i, y_i, z_i) by solving the linear equations below:

$$\begin{bmatrix} (A^{[1]} - p_i^{[1]} I^{[1]}) & (B^{[1]} - p_i^{[1]} J^{[1]}) & (C^{[1]} - p_i^{[1]} K^{[1]}) \\ (E^{[1]} - q_i^{[1]} I^{[1]}) & (F^{[1]} - q_i^{[1]} J^{[1]}) & (G^{[1]} - q_i^{[1]} K^{[1]}) \\ (A^{[2]} - p_i^{[2]} I^{[2]}) & (B^{[2]} - p_i^{[2]} J^{[2]}) & (C^{[2]} - p_i^{[2]} K^{[2]}) \\ (E^{[2]} - q_i^{[2]} I^{[2]}) & (F^{[2]} - q_i^{[2]} J^{[2]}) & (G^{[2]} - q_i^{[2]} K^{[2]}) \end{bmatrix} \begin{Bmatrix} x_i \\ y_i \\ z_i \end{Bmatrix} = \begin{Bmatrix} (D^{[1]} - p_i^{[1]}) \\ (H^{[1]} - q_i^{[1]}) \\ (D^{[2]} - p_i^{[2]}) \\ (H^{[2]} - q_i^{[2]}) \end{Bmatrix} \quad \text{(E.3)}$$

Stereo Camera Calibration

We calibrated the direct linear transformations for our two cameras using a 3D-printed half cylinder covered in gridded calibration markers (**Figure E-1**). The cylinder was placed approximately 20 cm away from each camera. One calibration image was acquired by each camera and imported into MATLAB (MathWorks, Natick, MA), in which we used the `drawpolygon()` function to determine the pixel locations of the 42 visible calibration points.

The system of equations in Eq. (E.2) requires at least six non-coplanar calibration points to determine the camera-specific coefficients $\{A, B, C, \ldots, I, J, K\}$ for each camera. However, it is not known how the number of calibration points (≥ 6) or their arrangement would influence the resulting 3D photogrammtery results. Thus, we investigated further these important considerations through the 5 calibration scenarios as depicted in **Figure E-2**. For each scenario, the camera-specific coefficients were determined using a subset of the calibration markers (denoted by the box in **Figure E-2**), which were then used to predict all other 3D locations.

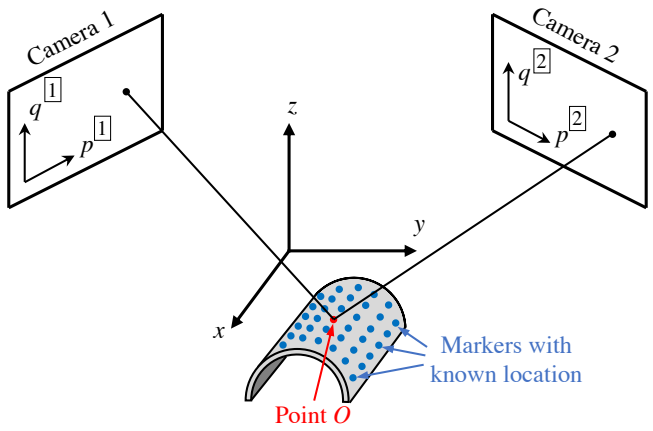

Figure E-1. Schematic of the calibration of the direct linear transformation with two cameras via a gridded cylinder.

The predicted 3D marker locations were compared with the known marker locations (determined from the given half-cylindrical geometry) to compute the average distance errors. It is clear that more than six calibration markers are needed to avoid large errors in the predicted marker locations (**Figure E-2**(a)). However, the error can be quickly minimized by increasing the number of calibrated points (**Figure E-2**(b)-(d)) or ensuring the 3D photogrammetry predictions fall within the calibration markers (**Figure E-2**(e)). We were satisfied with the minimum error for our 3D photogrammetry (0.24 mm) considering the TV tissues typically falling within or near the calibrated region. However, further investigations are warranted to explore the extrapolative capabilities of this photogrammetry method and calibration process.

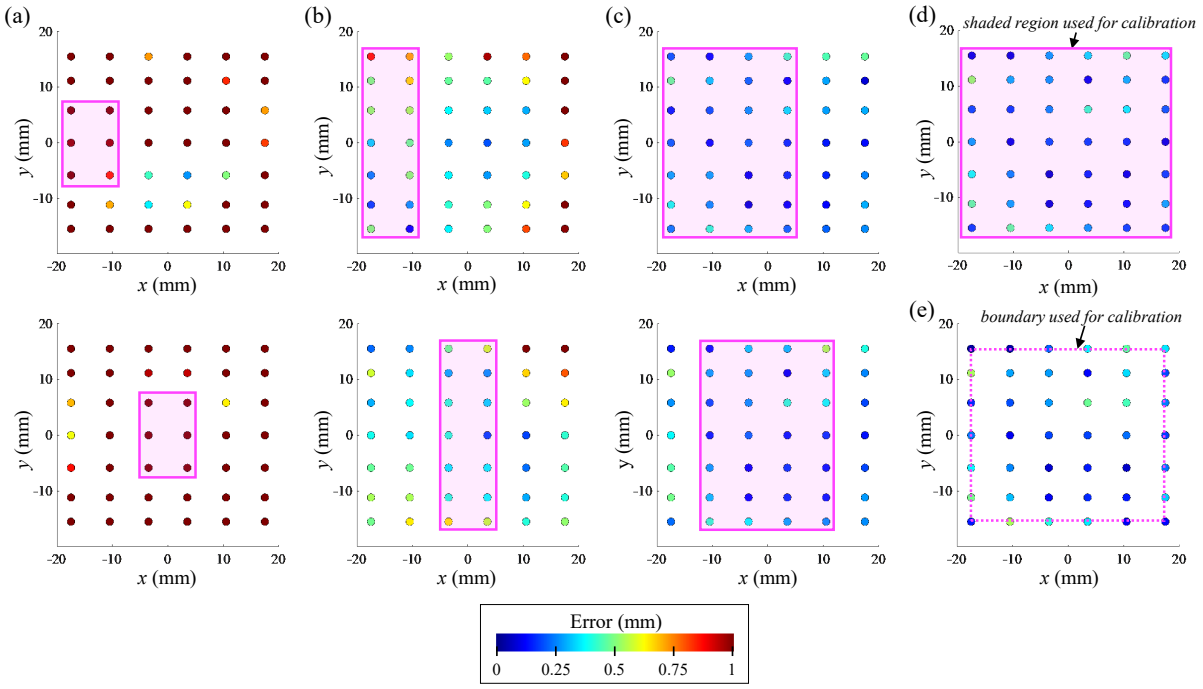

Figure E-2. Computed distance error of 42 markers on the calibration cylinder surface using a sub-set of the marks for camera-specific coefficient calibration: (a) the 6 marks (*top*) along the boundary, and (*bottom*) in the center, (b) the 14 markers (*top*) along the boundary, and (*bottom*) in the center, (c) the 28 marks (*top*) along the boundary and (*bottom*) in the center, (d) all the 42 markers, and (e) the 22 markers along the perimeter.

APPENDIX F Reproducing Kernel Shape Function

In this appendix, we describe the reproducing kernel (RK) meshfree method [26] that we used to compute the shape function derivatives in the calculation of the deformation gradient $\mathbf{F}$ (see Section 6.1.5) and the isoparametric generation of material points (i.e., visualization grid points) based on the nine fiducial markers.

Reproducing Kernel Shape Function and Approximation

The RK shape function of the I^{th} material point $\mathbf{x}_I = [x_I, y_I, z_I]$ has the form:

$$\Psi_I(\mathbf{x}) = \mathbf{H}^T(0)\mathbf{M}^{-1}(\mathbf{x})\mathbf{H}(\mathbf{x}-\mathbf{x}_I)\Phi(\mathbf{x}-\mathbf{x}_I;\mathbf{a}) \tag{F.1}$$

where $\mathbf{H}(\mathbf{x}) = [1, x, y, z]^T$ is the basis function vector of monomials (up to the first order chosen for the present study), $\Phi(\mathbf{x};\mathbf{a})$ is the kernel function with support radii $\mathbf{a} = [a_x, a_y, a_z]^T$, and $\mathbf{M}(\mathbf{x})$ is the moment matrix defined as

$$\mathbf{M}(\mathbf{x}) = \sum_{I=1}^{NP} \mathbf{H}(\mathbf{x}-\mathbf{x}_I)\mathbf{H}^T(\mathbf{x}-\mathbf{x}_I)\Phi(\mathbf{x}-\mathbf{x}_I;\mathbf{a}) \tag{F.2}$$

For the purpose of this study, $\Phi(\mathbf{x}-\mathbf{x}_I;\mathbf{a})$ is chosen as the product of one-dimensional kernel functions, i.e.,

$$\Phi(\mathbf{x}-\mathbf{x}_I;\mathbf{a}) = \frac{1}{a_x a_y a_z}\bar{\Phi}\left(\left|\frac{x-x_I}{a_x}\right|\right)\bar{\Phi}\left(\left|\frac{y-y_I}{a_y}\right|\right)\bar{\Phi}\left(\left|\frac{z-z_I}{a_z}\right|\right) \tag{F.3}$$

where the one-dimensional kernel functions for all three spatial coordinates x, y, and z take the form of a cubic spline function:

$$\bar{\Phi}(t) = \begin{cases} \dfrac{2}{3} - 4t^2 + 4t^3 & \text{for } 0 \le t \le \dfrac{1}{2} \\ \dfrac{4}{3} - 4t + 4t^2 - \dfrac{4}{3}t^3 & \text{for } \dfrac{1}{2} \le t \le 1 \\ 0 & \text{otherwise} \end{cases} \tag{F.4}$$

The partial derivatives of shape function $\Psi_I(\mathbf{x})$ with respect to the three spatial coordinates were then determined using

$$\begin{aligned} \nabla_{\mathbf{x}}\Psi_I(\mathbf{x}) = \mathbf{H}^T(\mathbf{0})[&\nabla_{\mathbf{x}}\mathbf{M}^{-1}(\mathbf{x})\mathbf{H}(\mathbf{x}-\mathbf{x}_I)\Phi(\mathbf{x}-\mathbf{x}_I;\mathbf{a}) \\ &+ \mathbf{M}^{-1}(\mathbf{x})\nabla_{\mathbf{x}}\mathbf{H}(\mathbf{x}-\mathbf{x}_I)\Phi(\mathbf{x}-\mathbf{x}_I;\mathbf{a}) + \mathbf{M}^{-1}(\mathbf{x})\mathbf{H}(\mathbf{x}-\mathbf{x}_I)\nabla_{\mathbf{x}}\Phi(\mathbf{x}-\mathbf{x}_I;\mathbf{a})]. \end{aligned} \tag{F.5}$$

In this relationship, $\nabla_{\mathbf{x}}(\bullet)$ is the gradient operator with respect to the spatial coordinates (x, y, z), $\nabla_{\mathbf{x}}\mathbf{M}^{-1}(\mathbf{x}) = -\mathbf{M}^{-1}(\mathbf{x})\nabla_{\mathbf{x}}\mathbf{M}(\mathbf{x})\mathbf{M}^{-1}(\mathbf{x})$, and $\nabla_{\mathbf{x}}\mathbf{M}(\mathbf{x})$ can be algebraically derived from Eq. (F.5).

Isoparametric Generation of Material Points

The 3×3 fiducial marker array was considered as a 9-node finite element in the parametric domain (ξ, η), equipped with the following shape functions:

$$\begin{aligned} &N_1(\xi,\eta) = \frac{1}{4}(\xi^2-\xi)(\eta^2-\eta), \quad N_2(\xi,\eta) = \frac{1}{4}(\xi^2+\xi)(\eta^2-\eta), \quad N_3(\xi,\eta) = \frac{1}{4}(\xi^2+\xi)(\eta^2+\eta) \\ &N_4(\xi,\eta) = \frac{1}{4}(\xi^2-\xi)(\eta^2+\eta), \quad N_5(\xi,\eta) = \frac{1}{2}(1-\xi^2)(\eta^2-\eta), \quad N_6(\xi,\eta) = \frac{1}{2}(\xi^2+\xi)(1-\eta^2) \\ &N_7(\xi,\eta) = \frac{1}{2}(1-\xi^2)(\eta^2+\eta), \quad N_8(\xi,\eta) = \frac{1}{2}(\xi^2-\xi)(1-\eta^2), \quad N_9(\xi,\eta) = \frac{1}{4}(1-\xi^2)(1-\eta^2) \end{aligned} \tag{F.6}$$

The shape functions of the single 9-node finite element were combined with the (x, y, z) coordinates of the nine fiducial markers to generate a 25×25 visualization grid of *material points*. These visualization grid points were used for the subsequent computations of the deformation gradient $\mathbf{F}$ in Section 6.1.5.

References

1. Aggarwal, A., An improved parameter estimation and comparison for soft tissue constitutive models containing an exponential function. *Biomechanics and Modeling in Mechanobiology*, 2017. 16(4): pp. 1309-1327.
2. Aggarwal, A., Pouch, A.M., Lai, E., Lesicko, J., Yushkevich, P.A., Gorman III, J.H., Gorman, R.C., and Sacks, M.S., In-vivo heterogeneous functional and residual strains in human aortic valve leaflets. *Journal of Biomechanics*, 2016. 49(12): pp. 2481-2490.
3. Aldea, G.S., Commentary: Tricuspid valve ring characteristics: Physiologically important, clinically relevant, or too little too late? *The Journal of Thoracic and Cardiovascular Surgery*, 2021. 161(2): pp. e209-e210.
4. Alkhouli, M., Berzingi, C., Kowatli, A., Alqahtani, F., and Badhwar, V., Comparative early outcomes of tricuspid valve repair versus replacement for secondary tricuspid regurgitation. *Open Heart*, 2018. 5(2): p. e000878.
5. Amini Khoiy, K. and Amini, R., On the biaxial mechanical response of porcine tricuspid valve leaflets. *Journal of Biomechanical Engineering*, 2016. 138(10): p. 104504.
6. Amini Khoiy, K., Asgarian, K.T., Loth, F., and Amini, R., Dilation of tricuspid valve annulus immediately after rupture of chordae tendineae in ex-vivo porcine hearts. *PLOS ONE*, 2018. 13(11): p. e0206744.
7. Amini Khoiy, K., Biswas, D., Decker, T.N., Asgarian, K.T., Loth, F., and Amini, R., Surface strains of porcine tricuspid valve septal leaflets measured in *ex vivo* beating hearts. *Journal of Biomechanical Engineering*, 2016. 138(11): p. 111006.
8. Amini, R., Eckert, C.E., Koomalsingh, K., McGarvey, J., Minakawa, M., Gorman, J.H.,

Gorman, R.C., and Sacks, M.S., On the *in vivo* deformation of the mitral valve anterior leaflet: Effects of annular geometry and referential configuration. *Annals of Biomedical Engineering*, 2012. 40(7): pp. 1455-1467.

9. Antunes, M. and Girdwood, R., Tricuspid annuloplasty: A modified technique. *The Annals of Thoracic Surgery*, 1983. 35(6): pp. 676-678.
10. Anwar, A.M., Cate, F.J.t., and Soliman, O.I., *Clinical Recognition of Tricuspid Valve Disease*, in *Practical Manual of Tricuspid Valve Diseases*. 2018, Springer. pp. 25-48.
11. Anyanwu, A.C. and Adams, D.H. *Functional Tricuspid Regurgitation in Mitral Valve Disease: Epidemiology and Prognostic Implications*. in *Seminars in Thoracic and Cardiovascular Surgery*. 2010. Elsevier.
12. Avanzini, A. and Battini, D., Integrated experimental and numerical comparison of different approaches for planar biaxial testing of a hyperelastic material. *Advances in Materials Science and Engineering*, 2016. 2016: pp. 6014129.
13. Avazmohammadi, R., Li, D.S., Leahy, T., Shih, E., Soares, J.S., Gorman, J.H., Gorman, R.C., and Sacks, M.S., An integrated inverse model-experimental approach to determine soft tissue three-dimensional constitutive parameters: Application to post-infarcted myocardium. *Biomechanics and Modeling in Mechanobiology*, 2018. 17(1): pp. 31-53.
14. Ayoub, S., Lee, C.-H., Driesbaugh, K.H., Anselmo, W., Hughes, C.T., Ferrari, G., Gorman, R.C., Gorman, J.H., and Sacks, M.S., Regulation of valve interstitial cell homeostasis by mechanical deformation: Implications for heart valve disease and surgical repair. *Journal of The Royal Society Interface*, 2017. 14(135): p. 20170580.
15. Badano, L.P., Muraru, D., and Enriquez-Sarano, M., Assessment of functional tricuspid

regurgitation. *European Heart Journal*, 2013. 34(25): pp. 1875-1885.

16. Basciano, C. and Kleinstreuer, C., Invariant-based anisotropic constitutive models of the healthy and aneurysmal abdominal aortic wall. *Journal of Biomechanical Engineering*, 2009. 131(2): p. 021009.
17. Basu, A. and He, Z., Annulus tension on the tricuspid valve: An in-vitro study. *Cardiovascular Engineering and Technology*, 2016. 7(3): pp. 270-279.
18. Belytschko, T., Liu, W.K., Moran, B., and Elkhodary, K., *Nonlinear Finite Elements for Continua and Structures*. 2014: John Wiley & Sons.
19. Billiar, K.L. and Sacks, M.S., Biaxial mechanical properties of the natural and glutaraldehyde treated aortic valve cusp—Part I: Experimental results. *Journal of Biomechanical Engineering*, 2000. 122(1): pp. 23-30.
20. Braunwald, N.S., Ross Jr, J., and Morrow, A.G., Conservative management of tricuspid regurgitation in patients undergoing mitral valve replacement. *Circulation*, 1967. 35(4s1): pp. I63-I69.
21. Buganza Tepole, A., Gart, M., Purnell, C.A., Gosain, A.K., and Kuhl, E., Multi-view stereo analysis reveals anisotropy of prestrain, deformation, and growth in living skin. *Biomechanics and Modeling in Mechanobiology*, 2015. 14(5): pp. 1007-1019.
22. Buganza Tepole, A., Gart, M., Purnell, C.A., Gosain, A.K., and Kuhl, E., The incompatibility of living systems: Characterizing growth-induced incompatibilities in expanded skin. *Annals of Biomedical Engineering*, 2016. 44(5): pp. 1734-1752.
23. Caetano, G.F., Fronza, M., Leite, M.N., Gomes, A., and Frade, M.A.C., Comparison of collagen content in skin wounds evaluated by biochemical assay and by computer-aided histomorphometric analysis. *Pharmaceutical Biology*, 2016. 54(11): pp. 2555-

2559.

24. Carpentier, A., Deloche, A., Dauptain, J., Soyer, R., Blondeau, P., Piwnica, A., Dubost, C., and McGoon, D., A new reconstructive operation for correction of mitral and tricuspid insufficiency. *The Journal of Thoracic and Cardiovascular Surgery*, 1971. 61(1): pp. 1-13.

25. Casey, K.M., Laurence, D.W., Tang, M., and Lee, C.-H., Layer Microdissection of Tricuspid Valve Leaflets for Biaxial Mechanical Characterization and Microstructural Quantification. *Journal of Visualized Experiments*, 2022(180): p. 63522.

26. Chen, J.-S., Pan, C., Wu, C.-T., and Liu, W.K., Reproducing kernel particle methods for large deformation analysis of non-linear structures. *Computer Methods in Applied Mechanics and Engineering*, 1996. 139(1-4): pp. 195-227.

27. Chen, J.S., Yoon, S., and Wu, C.T., Non-linear version of stabilized conforming nodal integration for Galerkin mesh-free methods. *International Journal for Numerical Methods in Engineering*, 2002. 53(12): pp. 2587-2615.

28. Choi, H.S. and Vito, R., Two-dimensional stress-strain relationship for canine pericardium. *Journal of Biomechanical Engineering*, 1990. 112(2): pp. 153-159.

29. Chuong, C.-J. and Fung, Y.-C., *Residual Stress in Arteries*, in *Frontiers in Biomechanics*. 1986, Springer. pp. 117-129.

30. Criscione, J.C., Douglas, A.S., and Hunter, W.C., Physically based strain invariant set for materials exhibiting transversely isotropic behavior. *Journal of the Mechanics and Physics of Solids*, 2001. 49(4): pp. 871-897.

31. Cyron, C. and Humphrey, J., Growth and remodeling of load-bearing biological soft tissues. *Meccanica*, 2017. 52(3): pp. 645-664.

32. Dabiri, Y., Yao, J., Sack, K.L., Kassab, G.S., and Guccione, J.M., Tricuspid valve regurgitation decreases after mitraclip implantation: Fluid structure interaction simulation. *Mechanics Research Communications*, 2019. 97: pp. 96-100.

33. De Vega, N., De Rabago, G., Castillon, L., Moreno, T., and Azpitarte, J., A new tricuspid repair. Short-term clinical results in 23 cases. *The Journal of Cardiovascular Surgery*, 1973: pp. 384-386.

34. de Vega Sanromán, N.G., Orueta, M., and Olivar, E., La anuloplastia selectiva, regulable y permanente. Una técnica original para el tratamiento de la insuficiencia tricúspide. *Revista Española Cardiología*, 1972. 25: pp. 555-556.

35. Dover, C.M., Goth, W., Goodbrake, C., Tunnell, J.W., and Sacks, M.S., Simultaneous wide-field planar strain–fiber orientation distribution measurement using polarized spatial domain imaging. *Annals of Biomedical Engineering*, 2022. 50: pp. 253-277.

36. Dreyfus, G.D., Corbi, P.J., Chan, K.J., and Bahrami, T., Secondary tricuspid regurgitation or dilatation: Which should be the criteria for surgical repair? *The Annals of Thoracic Surgery*, 2005. 79(1): pp. 127-132.

37. Driessen, N.J., Bouten, C.V., and Baaijens, F.P., Improved prediction of the collagen fiber architecture in the aortic heart valve. *Journal of Biomechanical Engineering*, 2005. 127(2): pp. 329-336.

38. Duginski, G.A., Ross, C.J., Laurence, D.W., Johns, C.H., and Lee, C.-H., An investigation of the effect of freezing storage on the biaxial mechanical properties of excised porcine tricuspid valve anterior leaflets. *Journal of the Mechanical Behavior of Biomedical Materials*, 2020. 101: pp. 103438.

39. Duran, C. and Gunning, A., The vascularization of the heart valves: A comparative

study. *Cardiovascular Research*, 1968. 2(3): pp. 290-296.

40. Elkin, L.A., Kay, M., Higgins, J.J., and Wobbrock, J.O. *An aligned rank transform procedure for multifactor contrast tests*. in *The 34th Annual ACM Symposium on User Interface Software and Technology*. 2021.

41. Fan, R. and Sacks, M.S., Simulation of planar soft tissues using a structural constitutive model: Finite element implementation and validation. *Journal of Biomechanics*, 2014. 47(9): pp. 2043-2054.

42. Fawzy, H., Fukamachi, K., Mazer, C.D., Harrington, A., Latter, D., Bonneau, D., and Errett, L., Complete mapping of the tricuspid valve apparatus using three-dimensional sonomicrometry. *The Journal of Thoracic and Cardiovascular Surgery*, 2011. 141(4): pp. 1037-1043.

43. Felippa, C.A., A survey of parametrized variational principles and applications to computational mechanics. *Computer Methods in Applied Mechanics and Engineering*, 1994. 113(1-2): pp. 109-139.

44. Ferruzzi, J., Vorp, D.A., and Humphrey, J., On constitutive descriptors of the biaxial mechanical behaviour of human abdominal aorta and aneurysms. *Journal of the Royal Society Interface*, 2011. 8(56): pp. 435-450.

45. Filsoufi, F., Salzberg, S.P., Coutu, M., and Adams, D.H., A three-dimensional ring annuloplasty for the treatment of tricuspid regurgitation. *The Annals of Thoracic Surgery*, 2006. 81(6): pp. 2273-2277.

46. Fukuda, S., Saracino, G., Matsumura, Y., Daimon, M., Tran, H., Greenberg, N.L., Hozumi, T., Yoshikawa, J., Thomas, J.D., and Shiota, T., Three-dimensional geometry of the tricuspid annulus in healthy subjects and in patients with functional tricuspid

regurgitation: A real-time, 3-dimensional echocardiographic study. *Circulation*, 2006. 114(1): pp. I492-I498.

47. Fung, Y.-C., *Biomechanics: Mechanical Properties of Living Tissues*. 2013: Springer Science & Business Media.

48. Fung, Y.-C., Biorheology of soft tissues. *Biorheology*, 1973. 10(2): pp. 139-155.

49. Garg, S., Singh, P., Sharma, A., and Gupta, G., A gross comparative anatomical study of hearts in human cadavers and pigs. *International Journal of Medical and Dental Sciences*, 2013. 2(2): pp. 170-176.

50. Genet, M., Rausch, M., Lee, L.C., Choy, S., Zhao, X., Kassab, G.S., Kozerke, S., Guccione, J.M., and Kuhl, E., Heterogeneous growth-induced prestrain in the heart. *Journal of Biomechanics*, 2015. 48(10): pp. 2080-2089.

51. Grashow, J.S., Sacks, M.S., Liao, J., and Yoganathan, A.P., Planar biaxial creep and stress relaxation of the mitral valve anterior leaflet. *Annals of Biomedical Engineering*, 2006. 34(10): pp. 1509-1518.

52. Grashow, J.S., Yoganathan, A.P., and Sacks, M.S., Biaixal stress–stretch behavior of the mitral valve anterior leaflet at physiologic strain rates. *Annals of Biomedical Engineering*, 2006. 34(2): pp. 315-325.

53. Gunnal, S., Wabale, R., and Farooqui, M., Morphological study of chordae tendinae in human cadaveric hearts. *Heart Views: The Official Journal of the Gulf Heart Association*, 2015. 16(1): pp. 1-12.

54. He, Q. and Chen, J.-S., A physics-constrained data-driven approach based on locally convex reconstruction for noisy database. *Computer Methods in Applied Mechanics and Engineering*, 2020. 363: pp. 112791.

55. He, Q., Laurence, D.W., Lee, C.-H., and Chen, J.-S., Manifold learning based data-driven modeling for soft biological tissues. *Journal of Biomechanics*, 2021. 117: p. 110124.

56. He, Z., Ritchie, J., Grashow, J.S., Sacks, M.S., and Yoganathan, A.P., *In vitro* dynamic strain behavior of the mitral valve posterior leaflet. *Journal of Biomechanical Engineering*, 2005. 127(3): pp. 504-511.

57. Heyden, S., Nagler, A., Bertoglio, C., Biehler, J., Gee, M.W., Wall, W.A., and Ortiz, M., Material modeling of cardiac valve tissue: Experiments, constitutive analysis and numerical investigation. *Journal of Biomechanics*, 2015. 48(16): pp. 4287-4296.

58. Holzapfel, G.A., Nonlinear solid mechanics: A continuum approach for engineering science. *Meccanica*, 2002. 37(4): pp. 489-490.

59. Huang, X., Gu, C., Men, X., Zhang, J., You, B., Zhang, H., Wei, H., and Li, J., Repair of functional tricuspid regurgitation: Comparison between suture annuloplasty and rings annuloplasty. *The Annals of Thoracic Surgery*, 2014. 97(4): pp. 1286-1292.

60. Hudson, L.T., Jett, S.V., Kramer, K.E., Laurence, D.W., Ross, C.J., Towner, R.A., Baumwart, R., Lim, K.M., Mir, A., Burkhart, H.M., and Lee, C.-H., A pilot study on linking tissue mechanics with load-dependent collagen microstructures in porcine tricuspid valve leaflets. *Bioengineering*, 2020. 7(2): p. 60.

61. Hudson, L.T., Laurence, D.W., Lau, H.M., Mullins, B.T., Doan, D.D., and Lee, C.-H., Linking collagen fiber architecture to tissue-level biaxial mechanical behaviors of porcine semilunar heart valve cusps. *Journal of the Mechanical Behavior of Biomedical Materials*, 2022. 125: p. 104907.

62. Humphrey, J., Strumpf, R., and Yin, F., Determination of a constitutive relation for

passive myocardium: I. A new functional form. *Journal of Biomechanical Engineering*, 1990. 112(3): pp. 333-339.

63. Humphrey, J. and Yin, F., A new constitutive formulation for characterizing the mechanical behavior of soft tissues. *Biophysical Journal*, 1987. 52(4): pp. 563-570.

64. Iyengar, A.K., Sugimoto, H., Smith, D.B., and Sacks, M.S., Dynamic *in vitro* quantification of bioprosthetic heart valve leaflet motion using structured light projection. *Annals of Biomedical Engineering*, 2001. 29(11): pp. 963-973.

65. Jacobs, N.T., Cortes, D.H., Vresilovic, E.J., and Elliott, D.M., Biaxial tension of fibrous tissue: Using finite element methods to address experimental challenges arising from boundary conditions and anisotropy. *Journal of Biomechanical Engineering*, 2013. 135(2): p. 021004.

66. Jang, J.Y., Heo, R., Lee, S., Kim, J.B., Kim, D.-H., Yun, S.-C., Song, J.-M., Song, J.-K., Lee, J.-W., and Kang, D.-H., Comparison of results of tricuspid valve repair versus replacement for severe functional tricuspid regurgitation. *The American Journal of Cardiology*, 2017. 119(6): pp. 905-910.

67. Jett, S., Laurence, D., Kunkel, R., Babu, A.R., Kramer, K., Baumwart, R., Towner, R., Wu, Y., and Lee, C.-H., An investigation of the anisotropic mechanical properties and anatomical structure of porcine atrioventricular heart valves. *Journal of the Mechanical Behavior of Biomedical Materials*, 2018. 87: pp. 155-171.

68. Jett, S.V., Hudson, L.T., Baumwart, R., Bohnstedt, B.N., Mir, A., Burkhart, H.M., Holzapfel, G.A., Wu, Y., and Lee, C.-H., Integration of polarized spatial frequency domain imaging (pSFDI) with a biaxial mechanical testing system for quantification of load-dependent collagen architecture in soft collagenous tissues. *Acta Biomaterialia*,

2020. 102: pp. 149-168.

69. Johnson, E.L., Laurence, D.W., Xu, F., Crisp, C.E., Mir, A., Burkhart, H.M., Lee, C.-H., and Hsu, M.-C., Parameterization, geometric modeling, and isogeometric analysis of tricuspid valves. *Computer Methods in Applied Mechanics and Engineering*, 2021. 384: p. 113960.

70. Kamensky, D., Xu, F., Lee, C.-H., Yan, J., Bazilevs, Y., and Hsu, M.-C., A contact formulation based on a volumetric potential: Application to isogeometric simulations of atrioventricular valves. *Computer Methods in Applied Mechanics and Engineering*, 2018. 330: pp. 522-546.

71. Khoiy, K.A., Pant, A.D., and Amini, R., Quantification of material constants for a phenomenological constitutive model of porcine tricuspid valve leaflets for simulation applications. *Journal of Biomechanical Engineering*, 2018. 140(9): p. 094503.

72. Kirchdoerfer, T. and Ortiz, M., Data-driven computational mechanics. *Computer Methods in Applied Mechanics and Engineering*, 2016. 304: pp. 81-101.

73. Kong, F., Pham, T., Martin, C., McKay, R., Primiano, C., Hashim, S., Kodali, S., and Sun, W., Finite element analysis of tricuspid valve deformation from multi-slice computed tomography images. *Annals of Biomedical Engineering*, 2018. 46(8): pp. 1112-1127.

74. Kramer, K.E., Ross, C.J., Laurence, D.W., Babu, A.R., Wu, Y., Towner, R.A., Mir, A., Burkhart, H.M., Holzapfel, G.A., and Lee, C.-H., An investigation of layer-specific tissue biomechanics of porcine atrioventricular valve anterior leaflets. *Acta Biomaterialia*, 2019. 96: pp. 368-384.

75. Krishnamurthy, G., Itoh, A., Bothe, W., Swanson, J.C., Kuhl, E., Karlsson, M., Miller,

D.C., and Ingels Jr, N.B., Stress–strain behavior of mitral valve leaflets in the beating ovine heart. *Journal of Biomechanics*, 2009. 42(12): pp. 1909-1916.

76. Kunzelman, K., Cochran, R., Murphree, S., Ring, W., Verrier, E., and Eberhart, R., Differential collagen distribution in the mitral valve and its influence on biomechanical behaviour. *The Journal of Heart Valve Disease*, 1993. 2(2): pp. 236-244.

77. Labrosse, M.R., Jafar, R., Ngu, J., and Boodhwani, M., Planar biaxial testing of heart valve cusp replacement biomaterials: Experiments, theory and material constants. *Acta Biomaterialia*, 2016. 45: pp. 303-320.

78. Lafçı, G., Çiçek, Ö.F., Lafçı, A., Esenboğa, K., Günertem, E., Kadiroğulları, E., Çiçek, M.C., Diken, A.İ., and Çağlı, K., A comparison of three tricuspid annuloplasty techniques: Suture, ring, and band. *Turkish Journal of Thoracic and Cardiovascular Surgery*, 2019. 27(3): p. 286.

79. Lanir, Y., Mechanistic micro-structural theory of soft tissues growth and remodeling: Tissues with unidirectional fibers. *Biomechanics and Modeling in Mechanobiology*, 2015. 14(2): pp. 245-266.

80. Lanir, Y., Lichtenstein, O., and Imanuel, O., Optimal design of biaxial tests for structural material characterization of flat tissues. *Journal of Biomechanical Engineering*, 1996. 118(1): pp. 41-47.

81. Laurence, D., *Investigations of the Tricuspid Heart Valve Function: An Integrated Computational-Experimental Approach*. 2019, M.S. Thesis, University of Oklahoma.

82. Laurence, D., Ross, C., Jett, S., Johns, C., Echols, A., Baumwart, R., Towner, R., Liao, J., Bajona, P., Wu, Y., and Lee, C.-H., An investigation of regional variations in the biaxial mechanical properties and stress relaxation behaviors of porcine

atrioventricular heart valve leaflets. *Journal of Biomechanics*, 2019. 83: pp. 16-27.

83. Laurence, D.W., Homburg, H., Yan, F., Tang, Q., Fung, K.-M., Bohnstedt, B.N., Holzapfel, G.A., and Lee, C.-H., A pilot study on biaxial mechanical, collagen microstructural, and morphological characterizations of a resected human intracranial aneurysm tissue. *Nature: Scientific Reports*, 2021. 11: p. 3525.

84. Laurence, D.W., Johnson, E.L., Hsu, M.C., Baumwart, R., Mir, A., Burkhart, H.M., Holzapfel, G.A., Wu, Y., and Lee, C.H., A pilot *in silico* modeling-based study of the pathological effects on the biomechanical function of tricuspid valves. *International Journal for Numerical Methods in Biomedical Engineering*, 2020. 36(7): p. e3346.

85. Laurence, D.W. and Lee, C.-H., Determination of a strain energy density function for the tricuspid valve leaflets using constant invariant-based mechanical characterizations. *Journal of Biomechanical Engineering*, 2021. 143(12): p. 121009.

86. Laurence, D.W., Lee, C.-H., Johnson, E.L., and Hsu, M.-C., An *in-silico* benchmark for the tricuspid heart valve–Geometry, finite element mesh, Abaqus simulation, and result data set. *Data in brief*, 2021. 39: p. 107664.

87. Lawson, C.L. and Hanson, R.J., *Solving Least Squares Problems*. 1995: SIAM.

88. Lee, C.-H., Amini, R., Gorman, R.C., Gorman III, J.H., and Sacks, M.S., An inverse modeling approach for stress estimation in mitral valve anterior leaflet valvuloplasty for in-vivo valvular biomaterial assessment. *Journal of Biomechanics*, 2014. 47(9): pp. 2055-2063.

89. Lee, C.-H., Laurence, D.W., Ross, C.J., Kramer, K.E., Babu, A.R., Johnson, E.L., Hsu, M.-C., Aggarwal, A., Mir, A., and Burkhart, H.M., Mechanics of the tricuspid valve—From clinical diagnosis/treatment, in-vivo and in-vitro investigations, to patient-

specific biomechanical modeling. *Bioengineering*, 2019. 6(2): p. 47.

90. Lee, C.-H., Oomen, P.J., Rabbah, J.P., Yoganathan, A., Gorman, R.C., Gorman, J.H., Amini, R., and Sacks, M.S. *A High-Fidelity and Micro-Anatomically Accurate 3D Finite Element Model for Simulations of Functional Mitral Valve*. in *International Conference on Functional Imaging and Modeling of the Heart*. 2013. Springer.

91. Lee, C.-H., Rabbah, J.-P., Yoganathan, A.P., Gorman, R.C., Gorman III, J.H., and Sacks, M.S., On the effects of leaflet microstructure and constitutive model on the closing behavior of the mitral valve. *Biomechanics and Modeling in Mechanobiology*, 2015. 14(6): pp. 1281-1302.

92. Lee, C.-H., Zhang, W., Feaver, K., Gorman, R.C., Gorman III, J.H., and Sacks, M.S., On the *in vivo* function of the mitral heart valve leaflet: Insights into tissue–interstitial cell biomechanical coupling. *Biomechanics and Modeling in Mechanobiology*, 2017. 16(5): pp. 1613-1632.

93. Lee, C.-H., Zhang, W., Liao, J., Carruthers, C.A., Sacks, J.I., and Sacks, M.S., On the presence of affine fibril and fiber kinematics in the mitral valve anterior leaflet. *Biophysical Journal*, 2015. 108(8): pp. 2074-2087.

94. Lee, P.-Y., Yang, B., Hua, Y., Waxman, S., Zhu, Z., Ji, F., and Sigal, I.A., Real-time imaging of optic nerve head collagen microstructure and biomechanics using instant polarized light microscopy. *Experimental Eye Research*, 2022. 217: p. 108967.

95. Liao, J., Yang, L., Grashow, J., and Sacks, M.S., The relation between collagen fibril kinematics and mechanical properties in the mitral valve anterior leaflet. *Journal of Biomechanical Engineering*, 2007. 129(1): pp. 78-87.

96. Lim, K.O., Mechanical properties and ultrastructure of normal human tricuspid valve

chordae tendineae. *The Japanese Journal of Physiology*, 1980. 30(3): pp. 455-464.

97. Lim, K.O., Boughner, D.R., and Perkins, D.G., Ultrastructure and mechanical properties of chordae tendineae from a myxomatous tricuspid valve. *Japanese Heart Journal*, 1983. 24(4): pp. 539-548.

98. Liu, W.K., Jun, S., and Zhang, Y.F., Reproducing kernel particle methods. *International Journal for Numerical Methods in Fluids*, 1995. 20(8-9): pp. 1081-1106.

99. Livens, P., Muyshondt, P.G., and Dirckx, J.J., Prestrain in the rabbit eardrum measured by digital image correlation and micro-incisions. *Hearing Research*, 2021. 412: p. 108392.

100. Loerakker, S., Obbink-Huizer, C., and Baaijens, F., A physically motivated constitutive model for cell-mediated compaction and collagen remodeling in soft tissues. *Biomechanics and Modeling in Mechanobiology*, 2014. 13(5): pp. 985-1001.

101. Loerakker, S., Ristori, T., and Baaijens, F.P., A computational analysis of cell-mediated compaction and collagen remodeling in tissue-engineered heart valves. *Journal of the Mechanical Behavior of Biomedical Materials*, 2016. 58: pp. 173-187.

102. Madhurapantula, R.S., Krell, G., Morfin, B., Roy, R., Lister, K., and Orgel, J.P., Advanced methodology and preliminary measurements of molecular and mechanical properties of heart valves under dynamic strain. *International Journal of Molecular Sciences*, 2020. 21(3): p. 763.

103. Mathur, M., Jazwiec, T., Meador, W., Malinowski, M., Goehler, M., Ferguson, H., Timek, T., and Rausch, M., Tricuspid valve leaflet strains in the beating ovine heart. *Biomechanics and Modeling in Mechanobiology*, 2019. 18(5): pp. 1351-1361.

104. Mathur, M., Meador, W.D., Jazwiec, T., Malinowski, M., Timek, T.A., and Rausch,

M.K., Tricuspid valve annuloplasty alters leaflet mechanics. *Annals of Biomedical Engineering*, 2020. 48(12): pp. 2911-2923.

105. May-Newman, K. and Yin, F., Biaxial mechanical behavior of excised porcine mitral valve leaflets. *American Journal of Physiology*, 1995. 269(4): pp. H1319-H1327.

106. May-Newman, K. and Yin, F., A constitutive law for mitral valve tissue. *Journal of Biomechanical Engineering*, 1998. 120(1): pp. 38-47.

107. Meador, W.D., Mathur, M., Sugerman, G.P., Jazwiec, T., Malinowski, M., Bersi, M.R., Timek, T.A., and Rausch, M.K., A detailed mechanical and microstructural analysis of ovine tricuspid valve leaflets. *Acta Biomaterialia*, 2020. 102: pp. 100-113.

108. Miller, N.R., Shapiro, R., and McLaughlin, T.M., A technique for obtaining spatial kinematic parameters of segments of biomechanical systems from cinematographic data. *Journal of Biomechanics*, 1980. 13(7): pp. 535-547.

109. Mooney, M., A theory of large elastic deformation. *Journal of Applied Physics*, 1940. 11(9): pp. 582-592.

110. Nathanson, M.H. and Saidel, G.M., Multiple-objective criteria for optimal experimental design: Application to ferrokinetics. *American Journal of Physiology-Regulatory, Integrative and Comparative Physiology*, 1985. 248(3): pp. R378-R386.

111. Nishimura, R.A., Otto, C.M., Bonow, R.O., Carabello, B.A., Erwin, J.P., Fleisher, L.A., Jneid, H., Mack, M.J., McLeod, C.J., and O'Gara, P.T., 2017 AHA/ACC focused update of the 2014 AHA/ACC guideline for the management of patients with valvular heart disease: A report of the American College of Cardiology/American Heart Association Task Force on Clinical Practice Guidelines. *Journal of the American College of Cardiology*, 2017. 70(2): pp. 252-289.

112. Otsu, N., A threshold selection method from gray-level histograms. *IEEE Transactions on Systems, Man, and Cybernetics*, 1979. 9(1): pp. 62-66.

113. Pant, A.D., Thomas, V.S., Black, A.L., Verba, T., Lesicko, J.G., and Amini, R., Pressure-induced microstructural changes in porcine tricuspid valve leaflets. *Acta Biomaterialia*, 2018. 67: pp. 248-258.

114. Pham, T., Sulejmani, F., Shin, E., Wang, D., and Sun, W., Quantification and comparison of the mechanical properties of four human cardiac valves. *Acta Biomaterialia*, 2017. 54: pp. 345-355.

115. Pham, T. and Sun, W., Material properties of aged human mitral valve leaflets. *Journal of Biomedical Materials Research Part A*, 2014. 102(8): pp. 2692-2703.

116. Pierlot, C.M., Lee, J.M., Amini, R., Sacks, M.S., and Wells, S.M., Pregnancy-induced remodeling of collagen architecture and content in the mitral valve. *Annals of Biomedical Engineering*, 2014. 42(10): pp. 2058-2071.

117. Pokutta-Paskaleva, A., Sulejmani, F., DelRocini, M., and Sun, W., Comparative mechanical, morphological, and microstructural characterization of porcine mitral and tricuspid leaflets and chordae tendineae. *Acta Biomaterialia*, 2019. 85: pp. 241-252.

118. Pozzoli, A., Elisabetta, L., Vicentini, L., Alfieri, O., and De Bonis, M., Surgical indication for functional tricuspid regurgitation at initial operation: Judging from long term outcomes. *General Thoracic and Cardiovascular Surgery*, 2016. 64(9): pp. 509-516.

119. Prot, V. and Skallerud, B., Nonlinear solid finite element analysis of mitral valves with heterogeneous leaflet layers. *Computational Mechanics*, 2009. 43(3): pp. 353-368.

120. Prot, V. and Skallerud, B., Contributions of prestrains, hyperelasticity, and muscle fiber

activation on mitral valve systolic performance. *International Journal for Numerical Methods in Biomedical Engineering*, 2017. 33(4): p. e2806.

121. Prot, V., Skallerud, B., Sommer, G., and Holzapfel, G.A., On modelling and analysis of healthy and pathological human mitral valves: Two case studies. *Journal of the Mechanical Behavior of Biomedical Materials*, 2010. 3(2): pp. 167-177.

122. Rabbah, J.-P., Saikrishnan, N., and Yoganathan, A.P., A novel left heart simulator for the multi-modality characterization of native mitral valve geometry and fluid mechanics. *Annals of Biomedical Engineering*, 2013. 41(2): pp. 305-315.

123. Rausch, M.K., Famaey, N., Shultz, T.O.B., Bothe, W., Miller, D.C., and Kuhl, E., Mechanics of the mitral valve. *Biomechanics and Modeling in Mechanobiology*, 2013. 12(5): pp. 1053-1071.

124. Rausch, M.K. and Kuhl, E., On the effect of prestrain and residual stress in thin biological membranes. *Journal of the Mechanics and Physics of Solids*, 2013. 61(9): pp. 1955-1969.

125. Reddy, J.N., *An Introduction to Continuum Mechanics*. 2013: Cambridge University Press.

126. Rego, B.V. and Sacks, M.S., A functionally graded material model for the transmural stress distribution of the aortic valve leaflet. *Journal of Biomechanics*, 2017. 54: pp. 88-95.

127. Rego, B.V., Wells, S.M., Lee, C.-H., and Sacks, M.S., Mitral valve leaflet remodelling during pregnancy: Insights into cell-mediated recovery of tissue homeostasis. *Journal of The Royal Society Interface*, 2016. 13(125): p. 20160709.

128. Rivlin, R.S., Large elastic deformations of isotropic materials IV. Further

developments of the general theory. *Philosophical Transactions of the Royal Society of London. Series A, Mathematical and Physical Sciences*, 1948. 241(835): pp. 379-397.

129. Ross, C., Laurence, D., Wu, Y., and Lee, C.-H., Biaxial mechanical characterizations of atrioventricular heart valves. *Journal of Visualized Experiments*, 2019(146): p. e59170.

130. Ross, C.J., Hsu, M.-C., Baumwart, R., Mir, A., Burkhart, H.M., Holzapfel, G.A., Wu, Y., and Lee, C.-H., Quantification of load-dependent changes in the collagen fiber architecture for the strut chordae tendineae-leaflet insertion of porcine atrioventricular heart valves. *Biomechanics and Modeling in Mechanobiology*, 2021. 20(1): pp. 223-241.

131. Ross, C.J., Laurence, D.W., Echols, A.L., Babu, A.R., Gu, T., Duginski, G.A., Johns, C.H., Mullins, B.T., Casey, K.M., and Laurence, K.A., Effects of enzyme-based removal of collagen and elastin constituents on the biaxial mechanical responses of porcine atrioventricular heart valve anterior leaflets. *Acta Biomaterialia*, 2021. 135: pp. 425-440.

132. Ross, C.J., Laurence, D.W., Hsu, M.-C., Baumwart, R., Zhao, Y.D., Mir, A., Burkhart, H.M., Holzapfel, G.A., Wu, Y., and Lee, C.-H., Mechanics of porcine heart valves' strut chordae tendineae investigated as a leaflet–chordae–papillary muscle entity. *Annals of Biomedical Engineering*, 2020. 48(5): pp. 1463-1474.

133. Ross, C.J., Laurence, D.W., Richardson, J., Babu, A.R., Evans, L.E., Beyer, E.G., Childers, R.C., Wu, Y., Towner, R.A., and Fung, K.-M., An investigation of the glycosaminoglycan contribution to biaxial mechanical behaviours of porcine

atrioventricular heart valve leaflets. *Journal of the Royal Society Interface*, 2019. 16(156): p. 20190069.

134. Ross, C.J., Mullins, B.T., Hillshafer, C.E., Mir, A., Burkhart, H.M., and Lee, C.-H., Evaluation of affine fiber kinematics in porcine tricuspid valve leaflets using polarized spatial frequency domain imaging and planar biaxial testing. *Journal of Biomechanics*, 2021. 123: pp. 110475.

135. Sacks, M.S., Biaxial mechanical evaluation of planar biological materials. *Journal of Elasticity and the Physical Science of Solids*, 2000. 61(1): pp. 199-246.

136. Sacks, M.S., Enomoto, Y., Graybill, J.R., Merryman, W.D., Zeeshan, A., Yoganathan, A.P., Levy, R.J., Gorman, R.C., and Gorman III, J.H., In-vivo dynamic deformation of the mitral valve anterior leaflet. *The Annals of Thoracic Surgery*, 2006. 82(4): pp. 1369-1377.

137. Sacks, M.S. and Yoganathan, A.P., Heart valve function: A biomechanical perspective. *Philosophical Transactions of the Royal Society B: Biological Sciences*, 2007. 362(1484): pp. 1369-1391.

138. Salinas, S.D., Clark, M.M., and Amini, R., Mechanical response changes in porcine tricuspid valve anterior leaflet under osmotic-induced swelling. *Bioengineering*, 2019. 6(3): p. 70.

139. Salinas, S.D., Clark, M.M., and Amini, R., The effects of − 80° C short-term storage on the mechanical response of tricuspid valve leaflets. *Journal of Biomechanics*, 2020. 98: p. 109462.

140. Sigaeva, T., Destrade, M., and Di Martino, E.S., Multi-sector approximation method for arteries: The residual stresses of circumferential rings with non-trivial openings.

Journal of the Royal Society Interface, 2019. 16(156): p. 20190023.

141. Silver, M., Lam, J., Ranganathan, N., and Wigle, E., Morphology of the human tricuspid valve. *Circulation*, 1971. 43(3): pp. 333-348.

142. Simon-Allue, R., Cordero, A., and Pena, E., Unraveling the effect of boundary conditions and strain monitoring on estimation of the constitutive parameters of elastic membranes by biaxial tests. *Mechanics Research Communications*, 2014. 57: pp. 82-89.

143. Singh-Gryzbon, S., Sadri, V., Toma, M., Pierce, E.L., Wei, Z.A., and Yoganathan, A.P., Development of a computational method for simulating tricuspid valve dynamics. *Annals of Biomedical Engineering*, 2019. 47(6): pp. 1422-1434.

144. Smith, K., Mathur, M., Meador, W., Phillips-Garcia, B., Sugerman, G., Menta, A., Jazwiec, T., Malinowski, M., Timek, T., and Rausch, M., Tricuspid chordae tendineae mechanics: Insertion site, leaflet, and size-specific analysis and constitutive modelling. *Experimental Mechanics*, 2021. 61(1): pp. 19-29.

145. Stankovic, I., Daraban, A.M., Jasaityte, R., Neskovic, A.N., Claus, P., and Voigt, J.-U., Incremental value of the *en face* view of the tricuspid valve by two-dimensional and three-dimensional echocardiography for accurate identification of tricuspid valve leaflets. *Journal of the American Society of Echocardiography*, 2014. 27(4): pp. 376-384.

146. Stella, J.A. and Sacks, M.S., On the biaxial mechanical properties of the layers of the aortic valve leaflet. *Journal of Biomechanical Engineering*, 2007. 129(5): pp. 757-766.

147. Stevanella, M., Votta, E., Lemma, M., Antona, C., and Redaelli, A., Finite element modelling of the tricuspid valve: A preliminary study. *Medical Engineering & Physics*,

2010. 32(10): pp. 1213-1223.

148. Sun, W., Sacks, M.S., and Scott, M.J., Effects of boundary conditions on the estimation of the planar biaxial mechanical properties of soft tissues. *Journal of Biomechanical Engineering*, 2005. 127(4): pp. 709-715.

149. Sun, W., Sacks, M.S., Sellaro, T.L., Slaughter, W.S., and Scott, M.J., Biaxial mechanical response of bioprosthetic heart valve biomaterials to high in-plane shear. *Journal of Biomechanical Engineering*, 2003. 125(3): pp. 372-380.

150. Sun, Y.-P. and O'Gara, P.T., Epidemiology, anatomy, pathophysiology and clinical evaluation of functional tricuspid regurgitation. *Minerva Cardioangiologica*, 2017. 65(5): pp. 469-479.

151. Tchantchaleishvili, V., Rajab, T.K., and Cohn, L.H., Posterior suture annuloplasty for functional tricuspid regurgitation. *Annals of Cardiothoracic Surgery*, 2017. 6(3): pp. 262.

152. Thomas, V.S., Lai, V., and Amini, R., A computational multi-scale approach to investigate mechanically-induced changes in tricuspid valve anterior leaflet microstructure. *Acta Biomaterialia*, 2019. 94: pp. 524-535.

153. Tong, P. and Fung, Y.-C., The stress-strain relationship for the skin. *Journal of Biomechanics*, 1976. 9(10): pp. 649-657.

154. van Kelle, M., Rausch, M., Kuhl, E., and Loerakker, S., A computational model to predict cell traction-mediated prestretch in the mitral valve. *Computer Methods in Biomechanics and Biomedical Engineering*, 2019. 22(15): pp. 1174-1185.

155. Vesely, I. and Lozon, A., Natural preload of aortic valve leaflet components during glutaraldehyde fixation: Effects on tissue mechanics. *Journal of Biomechanics*, 1993.

26(2): pp. 121-131.

156. Vesely, I. and Noseworthy, R., Micromechanics of the fibrosa and the ventricularis in aortic valve leaflets. *Journal of Biomechanics*, 1992. 25(1): pp. 101-113.

157. Wells, S.M., Pierlot, C.M., and Moeller, A.D., Physiological remodeling of the mitral valve during pregnancy. *American Journal of Physiology-Heart and Circulatory Physiology*, 2012. 303(7): pp. H878-H892.

158. Wobbrock, J.O., Findlater, L., Gergle, D., and Higgins, J.J. *The Aligned Rank Transform for Nonparametric Factorial Analyses Using Only ANOVA Procedures*. in *Proceedings of the SIGCHI Conference on Human Factors in Computing Systems*. 2011.

159. Young, A., Legrice, I., Young, M., and Smaill, B., Extended confocal microscopy of myocardial laminae and collagen network. *Journal of Microscopy*, 1998. 192(2): pp. 139-150.

160. Yu, W.-J., Shen, M., Chen, W.-N., Zhan, Z.-H., Gong, Y.-J., Lin, Y., Liu, O., and Zhang, J., Differential evolution with two-level parameter adaptation. *IEEE Transactions on Cybernetics*, 2013. 44(7): pp. 1080-1099.

161. Zhang, W., Ayoub, S., Liao, J., and Sacks, M.S., A meso-scale layer-specific structural constitutive model of the mitral heart valve leaflets. *Acta Biomaterialia*, 2016. 32: pp. 238-255.

162. Zhang, W., Sommer, G., Niestrawska, J.A., Holzapfel, G.A., and Nordsletten, D., The effects of viscoelasticity on residual strain in aortic soft tissues. *Acta Biomaterialia*, 2022. 140: pp. 398-411.